DISS. ETH NO. 28834

CONTRIBUTION OF ICE CLIFFS TO THE MELT OF DEBRIS-COVERED GLACIERS IN HIGH MOUNTAIN ASIA

A thesis submitted to attain the degree of

DOCTOR OF SCIENCES of ETH ZURICH

(Dr. sc. ETH Zurich)

presented by

Marin Colin Pierre KNEIB

MSc in Executive Engineering, Mines Paristech

born on 12.05.1995

Accepted on the recommendation of

Prof. Dr. Peter Molnar, examiner

Dr. Francesca Pellicciotti, co-examiner

Dr. Patrick Wagnon, co-examiner

Prof. Dr. Duncan Quincey, co-examiner

Prof. Dr. Paolo Burlando, co-examiner

2022

'Come on kids, you can play extinction later'

The Ice Age

Abstract

One third of the ice in the ablation area of glaciers in High Mountain Asia (HMA) is covered by a layer of rock debris of a few centimetres to several metres thickness. This supraglacial debris insulates the ice, therefore reducing melt, but the effect is partly compensated by the presence of supraglacial ice cliffs which enhance melt locally by a factor 2 to 30. The contribution of ice cliffs to the mass balance of these debris-covered glaciers is highly uncertain and depends on the local meteorology, the surrounding debris thickness, the ice cliff distribution across the surface of the glacier and their interactions with debris and the supraglacial hydrology (streams and ponds). In this thesis, I have been expanding observations of ice cliffs at very high spatio-temporal resolution using time-lapse photogrammetry, and at the very large scale using novel remote sensing techniques. These observations, combined with advanced energy-balance modelling and a novel stochastic birth-death cliff population model, enable a better understanding of the local processes and how these influence the large-scale distribution and evolution patterns of ice cliffs.

First, I have quantified for four cliffs in Central Nepal and Eastern Tibet the importance of the different energy fluxes for melt, as well as the impact of debris redistribution on top of their ice faces during the monsoon season. These results highlight the importance of very thin debris in enhancing melt at the surface of the cliffs due to albedo reduction, while slightly thicker or patchy debris reduces it by 30-60%. Most importantly, these observations show the very strong temporal variability in cliff area, which is highly coupled to the influence of streams and ponds.

Second, I have developed two novel semi-automated cliff mapping approaches for high-resolution (<10m) multispectral satellite images. These approaches display high performance metrics and are transferable from image to image and glacier to glacier, which makes them suitable to study the evolution and distribution of ice cliffs at the large scale.

Third, I have developed an algorithm to track the evolution of ice cliffs automatically over time and applied it to yearly observations of the cliff population of four debris-covered glaciers in HMA over a period of 10 years. This has highlighted the very high cliff birth and death rates at all these sites, which results in the cliff relative area changing commonly by up to +/-20% from year to year. However, using a novel stochastic birth-death model, we also showed that the cliff relative area is constrained, and depends on a variety of controls, and especially the supraglacial hydrology.

Fourth, I have derived the cliff population of 86 glaciers across HMA and combined it with a number of large-scale datasets, as well as with complementary observations from multi-temporal Unsupervised Aerial Vehicle (UAV) surveys. This has enabled me to quantitatively link the state of ice cliffs and their density with the supraglacial hydrology, and therefore with glacier dynamics and debris thickness, i.e. with the evolution state of debris-covered glaciers.

Ultimately, this work provides crucial insights into the underlying processes of ice cliff evolution from the cliff to the glacier scale. These results are a major advance in the assessment of the large-scale ice cliff contribution to glacier mass balance.

Résumé

Un tiers de la glace située dans la zone d'ablation des glaciers des Hautes Montagnes d'Asie (HMA) est recouvert d'une couche de débris rocheux allant de quelques centimètres à plusieurs mètres d'épaisseur. Ces débris isolent la glace, réduisant ainsi la fonte, mais cet effet est partiellement compensé par la présence de falaises de glace qui augmentent localement la fonte d'un facteur 2 à 30. La contribution des falaises de glace au bilan de masse de ces glaciers couverts de débris est très incertaine et dépend de la météorologie locale, de l'épaisseur des débris environnants, de la distribution des falaises à la surface des glaciers et de leurs interactions avec les débris ainsi qu'avec les rivières et chenaux supraglaciaires. Dans cette thèse, j'ai poussé les observations des falaises de glace à très haute résolution spatiale et temporelle en utilisant de la photogrammétrie time-lapse, et à très grande échelle spatiale à l'aide de nouvelles techniques de télédétection. Ces observations, combinées à une modélisation avancée du bilan énergétique et à un nouveau modèle stochastique de la population de ces falaises, permettent de mieux comprendre les processus locaux et la façon dont ils influencent la distribution et l'évolution à grande échelle des falaises de glace.

Dans une première partie, j'ai quantifié pour quatre falaises du centre du Népal et de l'est du Tibet l'importance des différents flux d'énergie pour la fonte, ainsi que l'impact de la redistribution des débris sur ces falaises pendant la mousson. Ces résultats mettent en évidence l'importance d'une fine couche de poussière dans l'augmentation de la fonte à la surface des falaises en raison de la réduction de l'albédo, tandis que les débris légèrement plus épais ou parcellaires la réduisent de 30 à 60%. D'autre part, ces observations montrent la très forte variabilité temporelle de la superficie des falaises, qui est fortement couplée à l'influence des chenaux et lacs supraglaciaires.

Dans une seconde partie, j'ai développé deux nouvelles méthodes semi-automatiques de cartographie des falaises à partir d'images satellites multi-spectrales à haute résolution (<10m). Ces méthodes performantes sont applicables à différentes images et différents glaciers, ce qui les rend particulièrement utiles pour étudier l'évolution et la distribution des falaises de glace à grande échelle.

Dans une troisième partie, j'ai développé un algorithme pour suivre automatiquement l'évolution des falaises de glace dans le temps et je l'ai appliqué aux observations annuelles de la population de falaises de quatre glaciers couverts de débris des HMA sur une période de 10 ans. Cela a mis en évidence les taux très élevés d'apparition et de disparition des falaises sur tous ces glaciers, ce qui a pour conséquence que la superficie totale des falaises change aisément de +/-20% d'une année sur l'autre. Néanmoins, en utilisant un nouveau modèle stochastique d'évolution de ces falaises, nous avons également pu montrer que cette superficie totale est limitée et dépend d'un certain nombre de facteurs, et en particulier de l'hydrologie supraglaciaire.

Dans une quatrième partie, j'ai cartographié la population de falaises de 86 glaciers à travers les HMA et combiné ces observations avec des observations multi-temporelles réalisées à l'aide de drones. Cela m'a permis de relier quantitativement les caractéristiques et la densité des falaises de glace avec l'hydrologie supraglaciaire, et donc avec la dynamique des glaciers et l'épaisseur des débris, c'est-à-dire avec l'état d'évolution des glaciers couverts de débris.

Ce travail a fourni des informations cruciales sur les processus sous-jacents de l'évolution des falaises de glace, de l'échelle de la falaise à celle du glacier. Ces résultats constituent une avancée majeure dans l'évaluation de la contribution des falaises de glace au bilan de masse des glaciers à grande échelle.

Acknowledgements

Contents

Preface: The debris-covered glacier environment

When I first met Francesca to discuss the topic of this PhD, I did not really comprehend what debris-covered glaciers or ice cliffs were. Coincidentally, a few weeks after this first interview I found myself with Thomas, my cousin and partner-in-crime, trudging up the lower tongue of Inylchek Glacier in Eastern Kyrgyzstan, one of the largest glaciers outside the poles and extensively debris-covered. With 25 kilos of climbing gear in our backpacks, including 10 days' worth of food, we casually made our first steps on this lunar landscape, outskirting ice cliffs and supraglacial ponds, finding a way of least resistance through roller-coaster hills of unstable rocks and tackling steep scree slopes (two steps up, one step down). It was fun the first hour. After a full day of navigating this particularly unstable terrain and a number of falls and uncontrolled slides, we had only progressed 7 km up-glacier, four times less than expected. We pitched our tent next to a supraglacial pond and collapsed on our sleeping mats. This is when Thomas looked at me: 'So… That's what you'll be doing for the next four years?'... The next morning, the pond had drained. The weather was bad, so we went out under the rain to check out some of the massive ice cliffs that stood around our camp (Fig. 1.1, 1.2). Walking on the bouldery crest, staring down on the smooth ice face falling straight in a massive pond, 40m below… 'Well this is pretty cool!?'.

Figure 1.1: *first steps on a debris-covered glacier. Inylchek Glacier, Eastern Kyrgyzstan, 2018.*

Chapter 1: Introduction

1.1. Motivation

In recent decades, mountain glaciers have been retreating and losing mass globally at an accelerated rate due to anthropogenic warming (Hugonnet et al., 2021; Zemp et al., 2019, 2015) and are projected to keep following this trajectory until at least the end of the century (IPCC, 2019; Marzeion et al., 2020; Radić et al., 2014). This will have a number of consequences, some of which are already observable. Beyond the contribution to sea-level rise, which cannot compare with the future contribution from the Greenland and Antarctic ice sheets (Gardner et al., 2013), the depletion of the water storage that represents mountain glaciers could directly impact downstream ecosystems (Cauvy-Fraunié and Dangles, 2019; Huss et al., 2017; Huss and Hock, 2018; Milner et al., 2017) as well as the livelihoods of millions of people living in vulnerable basins (Immerzeel et al., 2020). Indeed, water discharge from the glaciers is expected to peak by 2100 for all glacierized drainage basins, and this peak is thought to have already been reached in more than half of them (Bliss et al., 2014; Huss and Hock, 2018). In basins with high water demand and dry summer climates, the reduction of this resource could become problematic, especially during episodes of drought (Pritchard, 2019). This is especially true in parts of High Mountain Asia (HMA), where diminishing water towers are combined with a growing demand on water resources (Bolch et al., 2012; Immerzeel et al., 2020; Kraaijenbrink et al., 2017; Miles et al., 2020; Pritchard, 2019; Viviroli et al., 2020).

Such general trends are harder to disentangle for smaller catchments limited to a few glaciers, as there is a strong variability in response between individual glaciers (Bolch et al., 2011; Ragettli et al., 2016a; Thakuri et al., 2014), which requires much more sophisticated sets of tools to understand and model (Ayala et al., 2016; Burger et al., 2018; Ragettli et al., 2016b, 2015). At this spatial scale, it becomes necessary to take into account the specific processes underlying glacier accumulation and ablation to understand the past and future evolution of glaciers and water resources. Such complex glacio-hydrological models require to be informed by high spatio-temporal resolution observations to comprehend the physics of the processes influencing the glacier mass balance (Ragettli et al., 2016b).

Glaciers show a variety of thinning patterns depending on morphological characteristics or the presence of a layer of rock debris in their ablation area (Brun et al., 2019; Scherler et al., 2011). Such glaciers are identified as 'debris-covered', and the rock debris extents and thicknesses at their surface can vary considerably (Kirkbride and Deline, 2013; Pellicciotti et al., 2015). They are common throughout the world (Herreid and Pellicciotti, 2020a), and the presence of a few centimetres of debris is enough to considerably influence their dynamics and melt patterns (Anderson and Anderson, 2016; Nicholson and Benn, 2013, 2006). Indeed, debris thicker than a few centimetres will reduce the melt of the underlying ice exponentially with debris thickness (Mattson, 1993; Ostrem, 1959), thus allowing debris-covered glaciers to extend to lower elevations than clean-ice glaciers (Scherler et al., 2011). However, beyond this simple relationship, regional-scale remote sensing studies have also shown that thinning patterns of debris-covered glaciers remained similar to those of debris-free glaciers at similar elevations, an apparent paradox often referred to as the 'debris-cover anomaly' (Brun et al., 2018; Gardelle et al., 2013; Kääb et al., 2012; Pellicciotti et al., 2015; Rounce et al., 2021). Debris-covered glaciers are indeed more complex than they appear when just considering the 'Ostrem' curve. Debris influences the ice dynamics, leading to long stagnating debris-covered tongues, which favour the development of peculiar

supraglacial features such as supraglacial streams, ponds and ice cliffs (Benn et al., 2012; Miles et al., 2020).

These ice cliffs are exposed ice faces amid the debris-covered ice, cleared of debris usually because their slope exceeds the local angle of repose (Fig. 1.3, Moore, 2018; Sakai et al., 1998). As supraglacial cliffs are directly exposed to incoming radiation, including to the longwave radiation emitted from the debris, they act as melt 'hotspots.' Despite their relatively low areal density at the glacier surface, they contribute considerably to the melt of debris-covered glaciers (Buri et al., 2021, 2016a; Immerzeel et al., 2014; Miles et al., 2022; Sakai and Takeuchi, 2000). This is also the case for supraglacial ponds, which store energy and redistribute it in the glacier at the pond margins and when they drain into the glacier (Miles et al., 2018b, 2022). As such, it has been hypothesised that ice cliffs and ponds could be partly responsible for the enhanced melt of debris-covered glaciers and could explain their accelerated thinning (Anderson et al., 2021a; Gardelle et al., 2013; Kääb et al., 2012; Pellicciotti et al., 2015; Ragettli et al., 2016a). However, despite some detailed studies at scales from individual cliffs to individual glaciers, there are still major unknowns related to the distribution and dynamics of such features that prevent assessing their contribution at the scale of HMA.

17
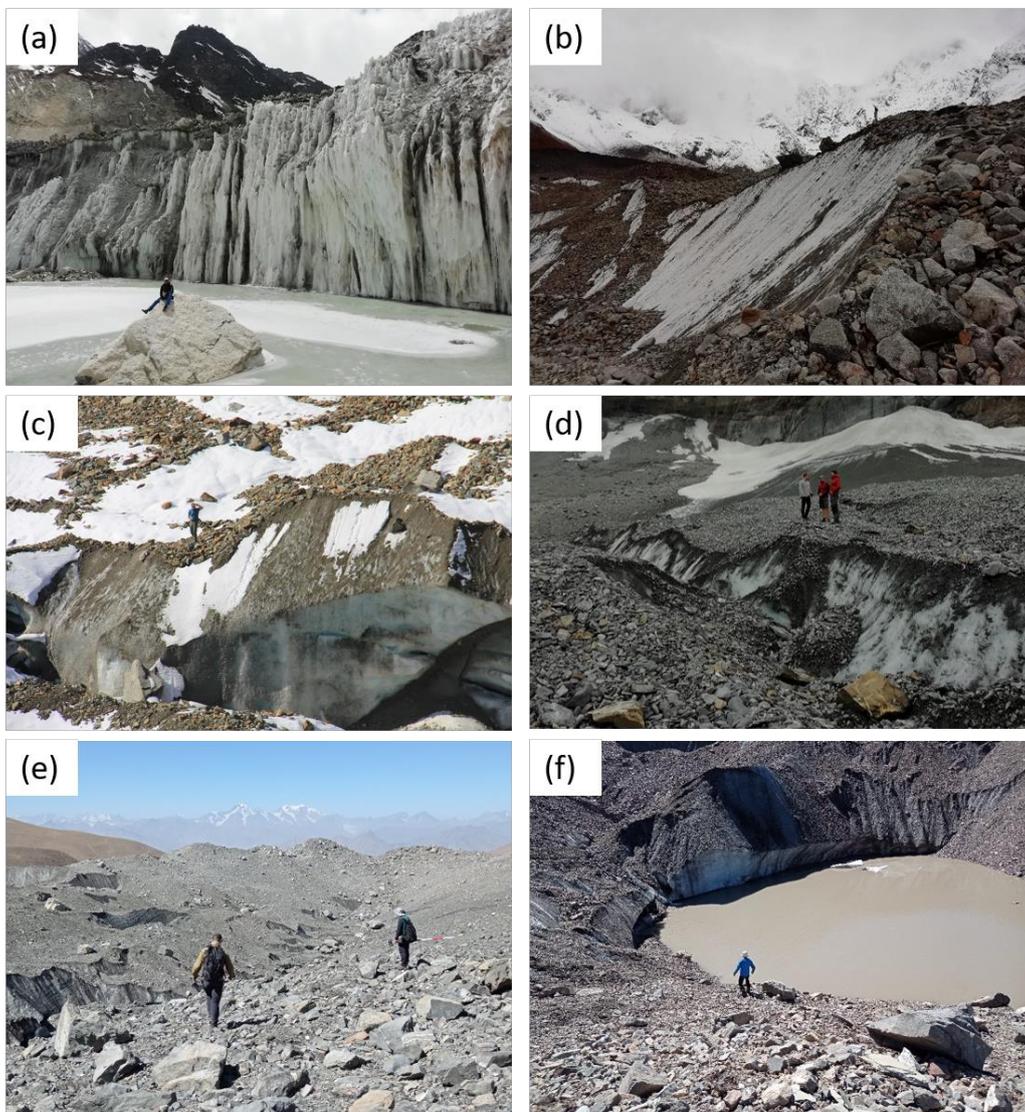
Figure 1.3: Supraglacial ice cliffs on (a) Langtang Glacier (Central Nepal), (b) 24K Glacier (Eastern Tibet), (c) Zmutt Glacier (Swiss Alps), (d) Im Gries (Swiss Alps), (e-f) Kyzylsu Glacier (Western Pamir). Image credit: Fabienne Meier (c) and Marin Kneib (a-b, d-f).

1.2. State of the art

1.2.1. Melt and thinning patterns of debris-covered glaciers

1.2.1.1. Debris on glaciers

Debris-covered glaciers are commonly observed in all major mountain ranges, and at the global scale 7.3% of the mountain glacier area is debris-covered (Herreid and Pellicciotti, 2020a; Scherler et al., 2018). They are particularly concentrated in HMA where more than 30% of the ice in the ablation area is covered with debris (Herreid and Pellicciotti, 2020a; Kraaijenbrink et al., 2017; Scherler et al., 2018). Debris cover has been observed to increase in several locations in the Alps and HMA in the past decades (Bhambri et al., 2011; Deline, 2005; Kamp et al., 2011; Mölg et al., 2019; Thakuri et al., 2014; Xie et al., 2020), due to a combination of enhanced melting and progressive glacier slowdown (Anderson and Anderson, 2018; Dehecq et al., 2019). This upward expansion of debris is therefore linked to climate warming and glaciers are expected to develop more extensive and thicker debris cover in the near future (Compagno et al., 2022; Herreid and Pellicciotti, 2020a; Thakuri et al., 2014).

Rock debris enters the glacier system from avalanches, rock falls, and subglacial erosion. While a large portion is exported subglacially, the rest is entrained englacially and melts out of the ice in the ablation zone (Goodsell et al., 2005; Kirkbride and Deline, 2013; McCarthy et al., 2021; Miles et al., 2020; Orr et al., 2021). Debris develops progressively in medial moraines which expand laterally due to debris creep driven by differential ablation (Anderson, 2000; Glazyrin, 1975; Kirkbride and Deline, 2013; Moore, 2021). Lower down-glacier, these lateral moraines merge and a continuous debris cover develops (Herreid and Pellicciotti, 2020a). As a result of progressive melt-out of debris, debris thickness increases down-glacier and generally towards glacier margins and can reach a few metres near the terminus (Anderson and Anderson, 2018; Nicholson et al., 2018).

At the local scale, the debris thickness can be very heterogeneous due to varying debris sources, from localized rockfall events to the melting out of medial moraines (Van Woerkom et al., 2019). This heterogeneity is further enhanced by differential melt under the debris (Moore, 2021; Sharp, 1949). Indeed, higher melt rates under thinner debris promotes surface lowering relative to zones of thicker debris. These topographic lows can progressively accumulate debris, which leads to a strong melt reduction and an inversion of the melt patterns, ultimately leading to a topographic inversion (Moore, 2021; Thompson et al., 2016). Glacier hummocks are symptomatic of such differential melt patterns and are predominant features of thickly debris-covered glacier tongues (Bartlett et al., 2020).

This heterogeneous debris distribution is confirmed by field and remote sensing observations. Debris thickness is usually measured directly by manual excavation, direct measurements at the top of ice cliffs or ground penetrating radar measurements (McCarthy et al., 2017; Nicholson and Mertes, 2017; Nicholson et al., 2018). Methods to estimate debris thickness have been developed using drone or satellite thermal imagery, exploiting either a direct empirical relationship or the surface energy balance (Foster et al., 2012; Herreid, 2021; Mihalcea et al., 2008; Ragettli et al., 2015; Rounce et al., 2018; Stewart et al., 2021). When the incoming energy to the glacier surface and the relationship between melt and debris thickness are known, surface mass balance patterns can also be inverted to compute debris thickness at the large scale (McCarthy et al., 2021; Ragettli et al., 2015; Rounce et al., 2018). A

combination of thermal and mass balance inversion has also been used to derive debris thickness for all glaciers in the world (Rounce et al., 2021). Such products reflect the thickening debris down-glacier, inform on the relative debris thickness from glacier to glacier, enable to study the controls of debris-cover development, and are particularly useful for large-scale glacier modelling (Compagno et al., 2022). However, their relatively coarse resolution (50-100m) condenses the local melt signal and the heterogeneous melt patterns from varying debris thicknesses as well as supraglacial melt hotspots (McCarthy et al., 2021; Rounce et al., 2021).

1.2.1.2. Effect of debris on ice

Local observations at stake locations have shown that for debris thicker than a few centimetres, melt is exponentially reduced with increasing debris thickness (Mattson, 1993; Nicholson and Benn, 2006; Ostrem, 1959; Fig. 1.4). This relationship results from the complex interaction between the atmosphere and the glacier surface, with the energy from the surface being conducted through the debris layer and contributing to ice melt (Nicholson and Benn, 2006; Reid and Brock, 2010).
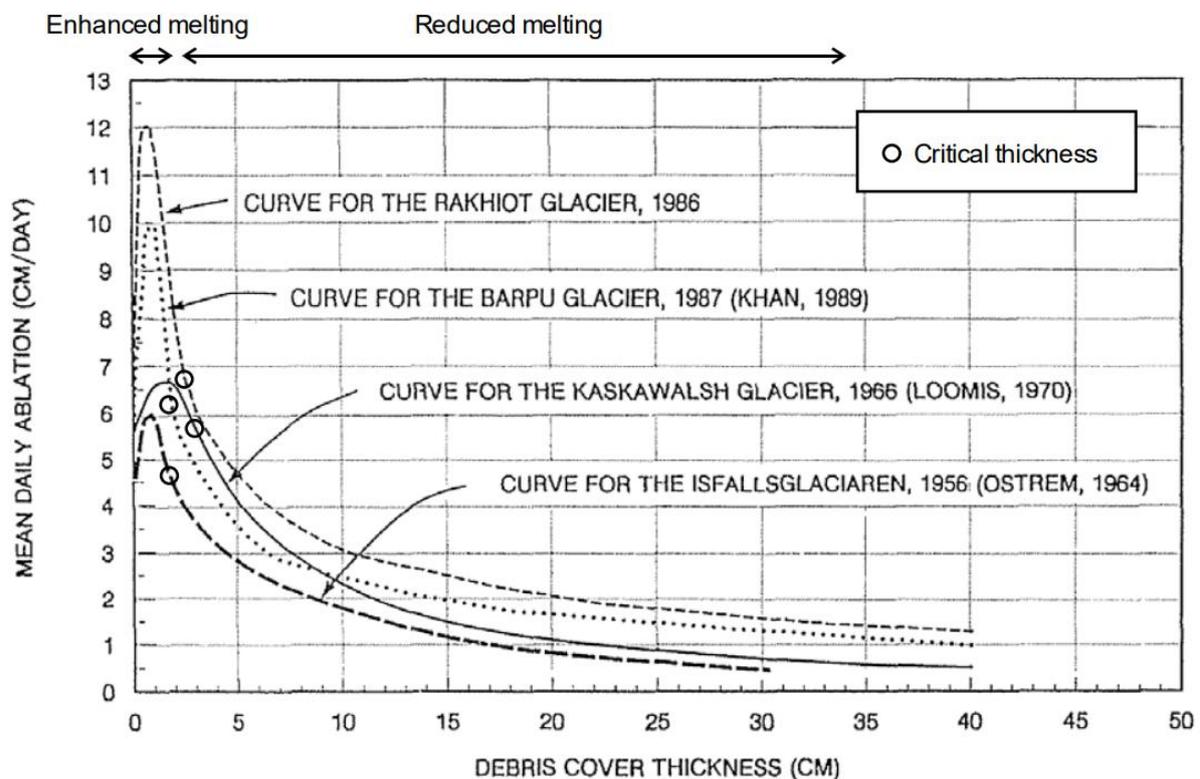
Figure 1.4: *Examples of field measurements of the relationship between ice ablation and debris thickness. The critical thickness is the thickness below which the ablation is enhanced relative to clean ice. Figure from McCarthy (2018), adapted from Mattson (1993).*

On the contrary, for debris thinner than a few centimetres, sub-debris melt is enhanced relative to clean ice. This can be explained by the fact that very thin debris is often patchy, with some ice with very low albedo values being exposed (Mattson, 1993; Fig. 1.4), and that as debris thickens there is a reduction in the evaporative heat flux, leaving more energy for melt (Evatt et al., 2015). This results in enhanced melt in the transition zone between ice and debris (Fyffe et al., 2020a).

1.2.1.3. Dynamics of debris-covered glaciers

Glaciers throughout the world are currently undergoing major changes due to increasing temperatures. This typically results in an up-glacier migration of the glacier equilibrium line, which corresponds to the transition between the accumulation and ablation area of a glacier (Cuffey and Paterson, 2010; Fig. 1.5). Such rising equilibrium lines and decreasing ratios of accumulation area versus ablation area are visible throughout HMA (Miles et al., 2021).
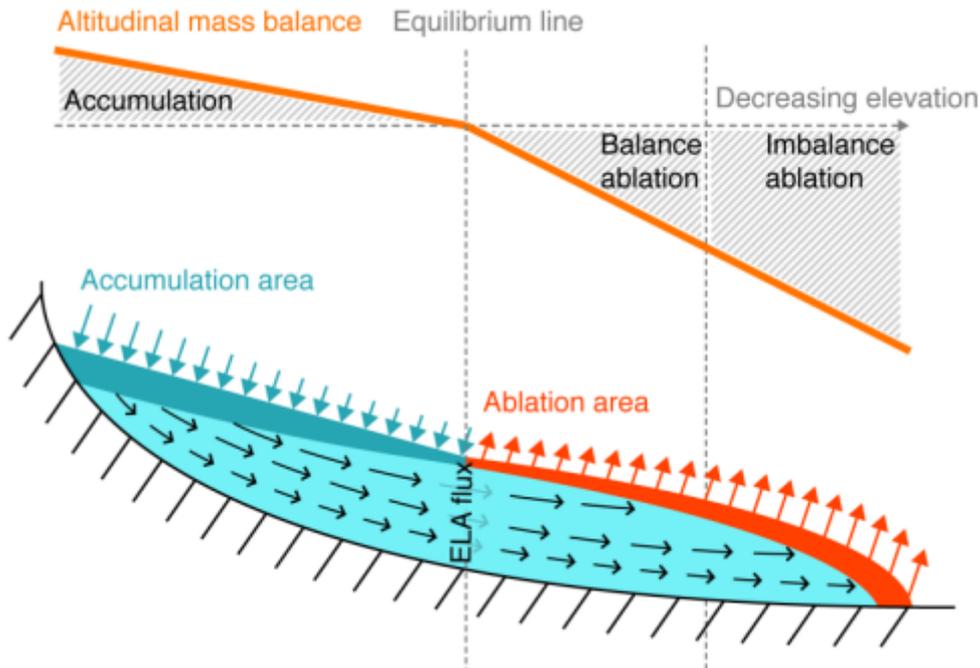
Figure 1.5: *Synthetic depiction of glacier accumulation, flow and ablation as a function of decreasing elevation. For an imbalanced glacier, more ice is lost in the ablation area than is gained in the accumulation area. Figure from Miles et al. (2021).*

While in general for clean-ice glaciers the melt decreases with elevation due to decreasing temperatures, the main control on debris-covered glacier melt comes from the debris thickness (Banerjee, 2017). The progressive thickening of debris down-glacier results in an inversion of the melt gradient in the ablation area of these glaciers (Benn and Lehmkuhl, 2000). This down-glacier ablation pattern can in addition be highly heterogeneous due to varying debris thicknesses as well as local mass inputs from avalanches, which are usually more important as a mass supply mechanism on debris-covered glaciers (Benn and Lehmkuhl, 2000; Brun et al., 2019; Laha et al., 2017; Scherler et al., 2011).

Higher melt rates at the transition from clean to debris-covered ice and the thickening of debris down-glacier means that debris-covered glaciers usually maintain extensive tongues at low elevations, which are characterised by low velocities due to a reduction in ice discharge (Anderson and Anderson, 2016; Ferguson and Vieli, 2021). As such, extensively debris-covered glaciers tend to react to climate change more slowly than clean-ice glaciers (Banerjee, 2017; Ferguson and Vieli, 2021; Rowan et al., 2015). Such modelling results are confirmed by observations of glacier slow-down at the regional scale (Dehecq et al., 2019), as well as by the long-term persistence of debris-covered ice at low altitude despite the rising equilibrium lines (Mölg et al., 2019; Nainwal et al., 2016). In the long-term, the slow-down of the ice supply to the debris-covered tongue and the enhanced thinning at higher elevations may additionally result in the complete detachment of the stagnating debris-covered tongue from its ice supply (Rowan et al., 2021).

Large-scale geodetic mass balance studies have compared the thinning patterns of debris-covered glaciers with those of debris-free glaciers located at the same elevation. Despite the presence of debris and its effect on the glacier surface mass balance, these observations showed similar thinning rates (Gardelle et al., 2013; Kääb et al., 2012) and glacier-wide mass balance patterns (Brun et al., 2019) for debris-covered and debris-free glaciers. Similar studies with higher spatial resolution products and conducted at the catchment scale (Bolch et al., 2011, 2008; Pellicciotti et al., 2015; Ragettli et al., 2016a) highlighted very heterogeneous thinning patterns across a glacier and between different glaciers and confirmed that at this scale debris-cover alone could not be considered to be a primary control of glacier mass balance.

This 'debris-cover anomaly' could be due to a number of debated factors that eventually add up to compensate for the debris insulating effect. As mentioned above, debris-covered glaciers tend to be less dynamic than debris-free glaciers, which may result in reduced ice flux in the ablation zone, including in its vertical component, also known as emergence velocity (Fig. 1.5). If one neglects the mass gain and loss processes occurring englacially and subglacially, for any particular section of a glacier, annual rates of elevation change (*dH/dt*) can be expressed as the sum of the annual surface mass balance ($\dot{b}$) and the vertical component of the ice flux, or flux divergence ($\nabla * \boldsymbol{q}$), accounting for the density (ρ) for each quantity (Cuffey and Paterson, 2010):

$$\frac{\rho_{dH}}{\rho_{H2O}}\frac{dH}{dt} = \dot{b} - \frac{\rho_{\nabla q}}{\rho_{H2O}}\nabla * \boldsymbol{q} \qquad \text{(Eq. 1.1)}$$

Therefore, a reduction in the emergence will result in increased thinning, which could partly explain the debris-cover 'anomaly' (Anderson et al., 2021a; Brun et al., 2018; Rounce et al., 2021). The other explanations relate to the other term of the equation ($\dot{b}$), which encompasses all the mass gains and loss at the glacier surface (including accumulation from snow, and melt). Indeed, enhanced melt at the location of supraglacial ice cliffs, ponds, or even streams, often described as melt 'hotspots', could balance to some extent the debris insulation effect (Buri et al., 2021; Kääb et al., 2012; Miles et al., 2018b; Pellicciotti et al., 2015; Thompson et al., 2016). Additionally, very thin or patchy debris can also enhance melt and could have a non-negligible effect at the regional scale (Fyffe et al., 2020a).

1.2.2. Ice cliffs

1.2.2.1. Melt patterns

1.2.2.1.1.   Measuring ice cliff melt

Ice cliffs act as melt 'hotspots' at the surface of debris-covered glaciers, as they undergo much higher ablation rates than the surrounding debris-covered ice. Due to their steep surface slopes and the redistribution of debris from the top to the bottom, these ice cliffs have a large lateral melt component and therefore appear to be backwasting as they melt (as opposed to 'downwasting'). Measurements of this backwasting or melt rates have been conducted using direct field measurements or aerial or terrestrial remote sensing approaches.

Direct measurements of ice cliff melt can be undertaken using traditional ablation stakes drilled into the ice, perpendicular to their surface, as this is also the direction of the melt vector (Buri et al., 2016a; Han

et al., 2010; Juen et al., 2014; Reid and Brock, 2014; Sakai et al., 2002; Steiner et al., 2015). Ice cliff backwasting has also been quantified by repeat measurements of the distance between benchmark boulders and the cliffs' crests (Anderson et al., 2021a; Han et al., 2010; Sakai et al., 1998). These approaches lead to point measurements that are relatively difficult and time-consuming to make, but with the advantage that they directly measure melt (or backwasting) as they are not affected by ice dynamics.

Distributed melt of ice cliffs can be assessed using Digital Elevation Models (DEMs) produced from terrestrial or aerial 'Structure-from-Motion' photogrammetry surveys, as well as from satellite stereo pairs (Brun et al., 2016; Immerzeel et al., 2014; Thompson et al., 2016; Watson et al., 2017b). The differencing of DEMs results in a thinning map, which can be used to extract the thinning patterns at the ice cliff location, assuming that the cliff outlines are known (Thompson et al., 2016). This method however ignores glacier motion, which can be problematic when the ice is not stagnant (Thompson et al., 2016). Accounting for glacier flow requires estimating the surface velocity of the ice (x, y components) as well as the emergence (z component) at the location of the cliffs (Brun et al., 2018). The surface velocity can be measured in a variety of ways, from point measurements of boulders on the glacier, to distributed measurements using cross correlation techniques (e.g. Messerli and Grinsted, 2015). The emergence velocity can be estimated using a mass conservation scheme, which requires to know the surface velocity, the ice thickness and to make assumptions on how velocity scales with depth (Cuffey and Paterson, 2010). Once the three components of the ice velocity have been calculated, the glacier surface can be corrected, also accounting for the glacier slope at the cliff location (Fig. 1.6; Brun et al., 2018; Miles et al., 2021, 2018b; Mishra et al., 2021; Westoby et al., 2020).
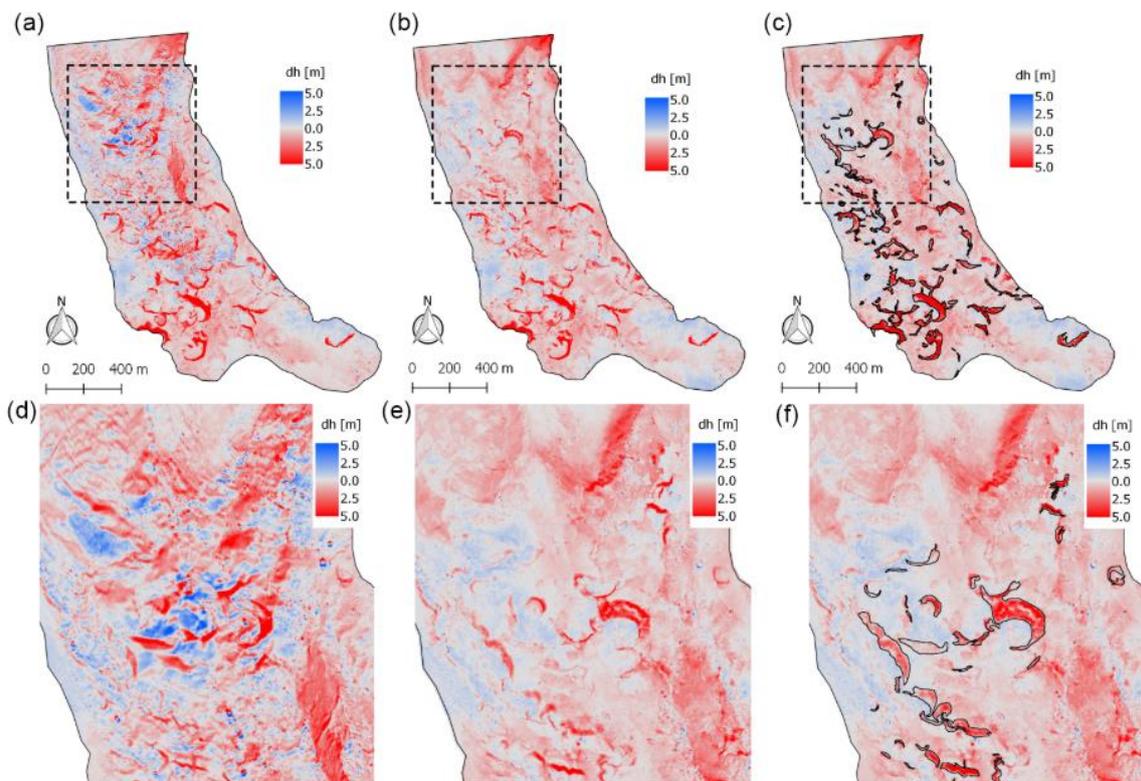
Figure 1.6: *Panels showing thinning maps from Unsupervised Aerial Vehicle (UAV) DEMs (a, d) before and (b, c, e, f) after flow correction over the period 23 November 2015–16 November 2016 on Changri Nup Glacier, Nepal. Black outlines on panels (c) and (f) are the cliff footprints. Panels (d), (e) and (f) are close-ups of the panels (a), (b) and (c). Figure from Brun et al., 2018.*

Even when all these steps have been followed, there remains important considerations on how to define ice cliff melt. Indeed, as discussed in the following sections, ice cliffs are (a) difficult to outline and (b) their outlines can change considerably within a few months. This approach based on DEM differencing also has limitations when the cliffs are very steep or even overhanging (Brun et al., 2016; Kraaijenbrink et al., 2016b; Watson et al., 2017b). Moreover, to account for ice cliff backwasting and avoid overestimating the cliff ablation, the melt needs to be calculated perpendicular to the surface of the cliff (Mishra et al., 2021). This has led to the use of point clouds rather than DEMs to extract the melt at the cliff location (Brun et al., 2016; Watson et al., 2017b; Mishra et al., 2021), using tailored algorithms such as the M3C2 (Lague et al., 2013).

1.2.2.1.2.   *Ice cliff enhancement factor*

Once the cliff melt is known, it can be compared to the melt of the surrounding debris-covered ice to estimate the cliff enhancement factor, which is generally understood as the cliff melt rate relative to the sub-debris melt rate. There are various ways of defining this enhancement factor, which adds to the number of ways there are to estimate ice cliff melt (which can be measured in a distributed way or at the point scale, but also modelled, and often needs to be extrapolated). There is no consensus for either of these approaches, so the definition varies from study to study.

A classic way of defining enhancement factor f_C of ice cliffs (or sometimes ice cliffs and ponds together) is to divide the total cliff melt $\dot{b}_C$ by the total melt in the debris-covered area $\dot{b}_T$ (Sakai et al., 1998, 2002; Thompson et al., 2016; Buri et al., 2021):

$$f_C = \frac{\dot{b}_C}{\dot{b}_T} \qquad \text{(Eq. 1.2)}$$

Other studies remove the cliff contribution from the total melt in the debris-covered area (Brun et al., 2018):

$$f_C = \frac{\dot{b}_C}{\dot{b}_{NC}} \qquad \text{(Eq. 1.3)}$$

But the enhancement factor can also be calculated at the point-scale, by comparing modelled or measured melt rates with melt rates from debris-covered ice in the same meteorological settings, or better, clean ice, since sub-debris melt strongly depends on debris thickness which is often unknown and very site-specific (Rounce et al., 2021; Miles et al., 2022).

Despite all these variations, all the studies that derived enhancement factors agree that ice cliffs melt considerably faster than the surrounding debris-covered ice (Fig. 1.7; Table 1.1). The enhancement factors indeed vary between 1.5 and 35 at the glacier scale but are mostly centred between 3 and 4 (Fig. 1.7.a; Table 1.1). The large spread can be explained by the different approaches used to derive cliff area and melt as well as their respective uncertainties, but also by the variety of climatic conditions and debris thicknesses of the glaciers considered. The only study to have calculated enhancement factors at a variety of sites across the world in a consistent way used point-scale energy-balance modelling to compare cliff, pond, debris-covered and debris-free ice melt and still found that the enhancement factor of ice cliffs relative to clean ice varied between 2 and 3, and 2 and 30 relative to debris-covered ice (Miles et al., 2022; Fig. 1.7.b).
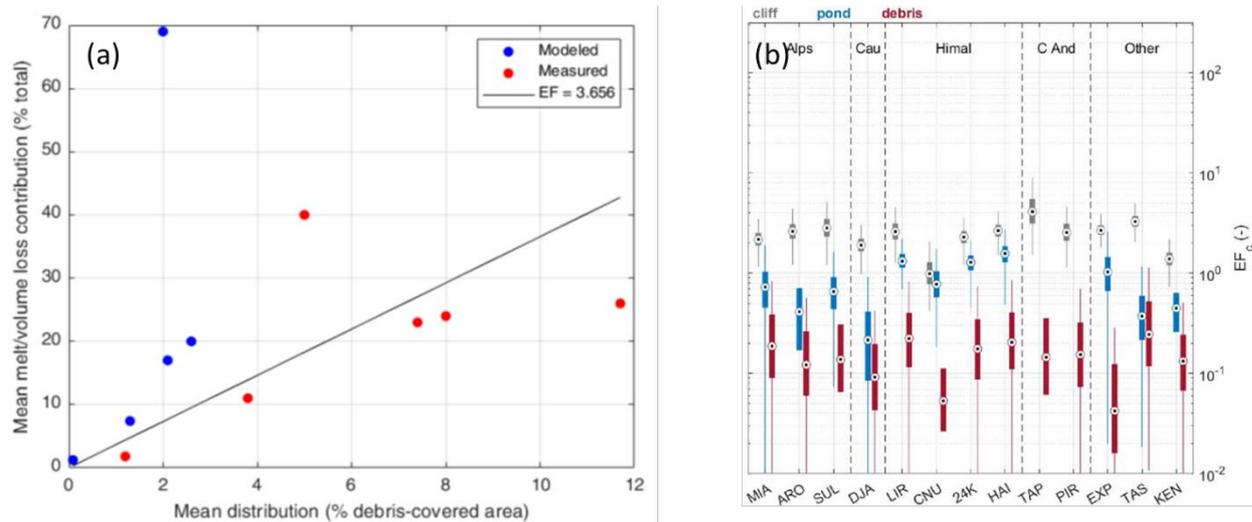
Figure 1.7: *(a) Literature values of ice cliff enhancement factors from the mean distribution of cliffs and their mean melt or volume loss contribution (modelled or measured). One glacier is located in Alaska, 2 are in the Alps and 8 in HMA (Sakai et al., 1998, 2002; Reid and Brock, 2014; Immerzeel et al., 2014; Thompson et al., 2016; Buri et al., 2016a, 2021; Brun et al., 2018; Mölg et al., 2019; Mishra et al., 2021). (b) Cliff, pond and debris enhancement factors relative to clean ice and calculated from point energy-balance modelling at various on-debris AWSs around the world. Figure from Miles et al., 2022.*

Table 1.1: *Literature values for ice cliff density, contribution to melt (or thinning patterns) and enhancement factor on debris-covered glaciers. The yellow, blue, orange and green shading show the sites in HMA, the European Alps, Alaska and Patagonia, respectively.*

Study	Distribution (% of planimetric study area)	Melt/thinning contribution (%)	EF	Glaciers	Comments
Sakai et al., 1998	1.8	69	38	Lirung Glacier (HMA)	**Melt** calculated from energy-balance modelling.
Sakai et al., 2002	2.6	20	7.7	Khumbu Glacier (HMA)	**Melt** calculated from energy-balance modelling.
Immerzeel et al., 2014	8	24	3	Lirung Glacier (HMA)	Combined contribution of cliffs and ponds measured from 0.2 m-resolution UAV-derived **thinning patterns**
Juen et al., 2014	1.7	12	7	Koxkar Glacier (HMA)	**Melt** calculated from energy-balance modelling.

Reid and Brock, 2014	1.3	7.4	5.7	Miage Glacier (European Alps)	**Melt** calculated from energy-balance modelling.
Thompson et al., 2016	5	40	8	Ngozumpa Glacier (HMA)	Contribution measured from **thinning patterns** from 1 m-resolution GeoEye and WorldView DEMs
Buri et al., 2016a	0.09	1.23	13.7	Lirung Glacier (HMA)	**Melt** calculated from distributed modelling of 2 ice cliffs
Watson et al., 2017	3-8	NA	NA	14 glaciers in the Khumbu region (HMA)	Extrapolated from ice cliff upper edges
Brun et al., 2018	7-8	23 +/- 0.5	3.1+/-0.6	Changri Nup Glacier (HMA)	**Melt** contribution measured from flow-corrected 0.2 m-resolution UAV DEMs
Steiner et al., 2019	1.2-2.7	NA	NA	5 glaciers in the Langtang region (HMA)	
Mölg et al., 2019	<1.8	<5	1.2 - 1.7	Zmutt Glacier (European Alps)	Contribution measured from **thinning patterns** from <5m-resolution DEMs
Mishra et al., 2021	3.78	11	3.9	Annapurna III Glacier (HMA)	**Melt** contribution measured from flow-corrected 0.1 m-resolution UAV DEMs
Anderson et al., 2021	11.7	26	2.2	Kennicott Glacier (Alaska)	Average values. **Melt** extrapolated from measurements of cliff backwasting rates
Stefaniak et al., 2021	1.13	NA	4.1-8.4	Miage Glacier (European Alps)	Average values
Falaschi et al., 2021	0.6-5.5	NA	NA	San Lorenzo region (Patagonia)	Average values
Sato et al., 2021	4.7-7.1	NA	NA	Trakarding Glacier (HMA)	

Buri et al., 2021	NA	NA	6+/-3 - 13+/-4	5 glaciers in the Langtang region (HMA)	**Melt** calculated from energy-balance modelling (using cliff outlines from Steiner et al., 2019)
Loriaux and Ruiz, 2021	0.51-2.7	NA	NA	Verde Glacier (Patagonia)	
Miles et al., 2022			2-30	20 on-glacier AWS locations around the world	**Melt** from energy-balance point-scale modelling
Racoviteanu et al., 2022	1.0-1.35	NA	NA	Ponkar Glacier (HMA)	

1.2.2.2. Energy balance

1.2.2.2.1.   Development of ice cliff energy-balance models

Ice cliffs consist of bare ice emerging among debris-covered ice and directly exposed to incoming radiations. In general ice cliffs are relatively steep (> 30°), thus preventing the debris from accumulating at their surface.

The energy balance at the cliff surface can be written as (Buri et al., 2016a; Han et al., 2010; Reid and Brock, 2014; Steiner et al., 2015):

$$Q_m = I_n + L_n + LE + H$$
(Eq. 1.4)

Where Q_m is the energy available for melt, I_n the contribution from the net shortwave radiation, L_n from net longwave, LE and H the latent and sensible heat fluxes, respectively. The heat from precipitation as well as the conductive heat flux into the ice are usually considered to be negligible (Reid and Brock, 2014).

The calculation of the different terms of this equation has been iteratively refined since its first known application to ice cliffs by Sakai et al., (1998). It indeed has strong implications for the melt contribution of ice cliffs on debris-covered glaciers but also for the evolution of the cliffs, to the degree that their evolution is controlled by the melt patterns at their surface (Watson et al., 2017b).

Initially, these fluxes were calculated at the point scale for a few cliffs of Lirung Glacier, in Nepal (Sakai et al., 1998; 2002). The parametrization used to account for solar radiation on a cliff slope was further improved and tested on Koxkar Glacier, China (Han et al., 2010), which confirmed that the main energy flux controlling the melt was the net shortwave radiation. A further application of this point-scale model to ice cliffs on Miage Glacier, Italy, accounted for the heating of the debris relative to the air temperature to calculate the longwave radiation emitted by the debris, and included a debris view factor to account for nearby debris mounds obscuring the cliff (Reid and Brock, 2014). This study benefited from a high resolution DEM (1m) for its calculations which helped model the total melt contribution of ice cliffs to the ablation on Miage Glacier. This model was further developed using new data from Lirung Glacier and including local shading effect on shortwave radiation, which highlighted

the strong spatio-temporal variability in ice cliff melt (Steiner et al., 2015). This most advanced formulation of this energy-balance model was then implemented in a distributed way (Buri et al., 2016a) and further expanded in a dynamic model accounting for cliff expansion or reburial as well as the influence of supraglacial ponds (Buri et al., 2016b). These last two steps strongly benefited from the use of multi-temporal UAV data to constrain the 3D evolution of the cliffs (Immerzeel et al., 2014), while the previous versions used stake data for validation. All the versions of the model were forced using on-glacier Automated Weather Stations (AWS) data with measured on-glacier temperature lapse rates to expand the model to cliffs across the whole glacier (Reid and Brock, 2014; Steiner and Pellicciotti, 2020).

1.2.2.2.2. Current formulation of the ice cliff energy-balance

This section gives a brief description of the different components of the energy-balance model as implemented in the most recent and advanced version, in a distributed way (Buri et al., 2016a).

The model uses a high resolution DEM (usually <1m) of the cliff and its surroundings (within a 200 m window) and a coarser DEM (~30 m) for the far-field (the whole glacier catchment). For each cliff pixel the debris and sky horizons (using the coarse DEM for shortwave, and the high-resolution DEM for longwave) are calculated with a 1° interval. These are then integrated to calculate the sky view factors V_{sI} and V_{sL} for shortwave and longwave, respectively, and the debris view factor V_d.

The net shortwave radiation is calculated as:

$$I_n = (I_s + D_s + D_t)(1 - \alpha_i) \qquad \text{(Eq. 1.5)}$$

where I_s is direct solar radiation, D_s is diffuse irradiance from the sky and D_t is incoming radiation reflected from the terrain (all fluxes in Wm–2). α_i (dimensionless) is the albedo of the ice. I_s, D_s and D_t are calculated from the incoming shortwave radiation measured at the AWS I_0 following (Reindl et al., 1990).

The net longwave is expressed as:

$$L_n = V_{s,L} \times L_{in} + V_d \times L_d + L_o \qquad \text{(Eq. 1.6)}$$

where L_{in} is the incoming longwave radiation from the atmosphere for a horizontal, unobstructed location, L_d is the longwave radiation emitted by the debris and L_o is the outgoing longwave radiation emitted by the ice surface.

L_{in} can be calculated following the Stefan-Boltzmann relation:

$$L_{in} = \varepsilon_a \sigma T_a^4 \qquad \text{(Eq. 1.7)}$$

where σ is the Stefan–Boltzmann constant and ε_a (dimensionless) is the effective emissivity of the sky, estimated with the parameterizations of Dilley and O'Brien (1998) for clear sky and Unsworth and Monteith (1975) for cloudy conditions. T_a is the air temperature in Kelvins.

The longwave radiation emitted by the surrounding debris is calculated as:

$$L_d = \varepsilon_d \sigma T_s^4 \qquad \text{(Eq. 1.8)}$$

where ε_d (dimensionless) is the emissivity and T_s (K) is the surface temperature of the debris.

The outgoing longwave radiation is also calculated with the Stefan–Boltzmann relation, using the emissivity of ice, ε_i, and the ice surface temperature, T_i (K), assumed to be equal to zero °C:

$$L_o = \varepsilon_i \sigma T_i^4 \qquad \text{(Eq. 1.9)}$$

The turbulent sensible (H) and latent heat (LE) are calculated using the bulk aerodynamic model (Han et al., 2010).

The net shortwave represents the most important energy flux, and it is dominated by the diffuse shortwave from sky (Fig. 1.8). The net longwave contributes to a lesser extent, and the longwave from the debris is also a minor component of the net longwave. The turbulent fluxes usually account for a very small portion of the energy-balance, although they have the highest uncertainty due to the difficulty of estimating the surface roughness and its variability at the cliffs' surface (Bonekamp et al., 2020; Miles et al., 2017b; Steiner et al., 2015).
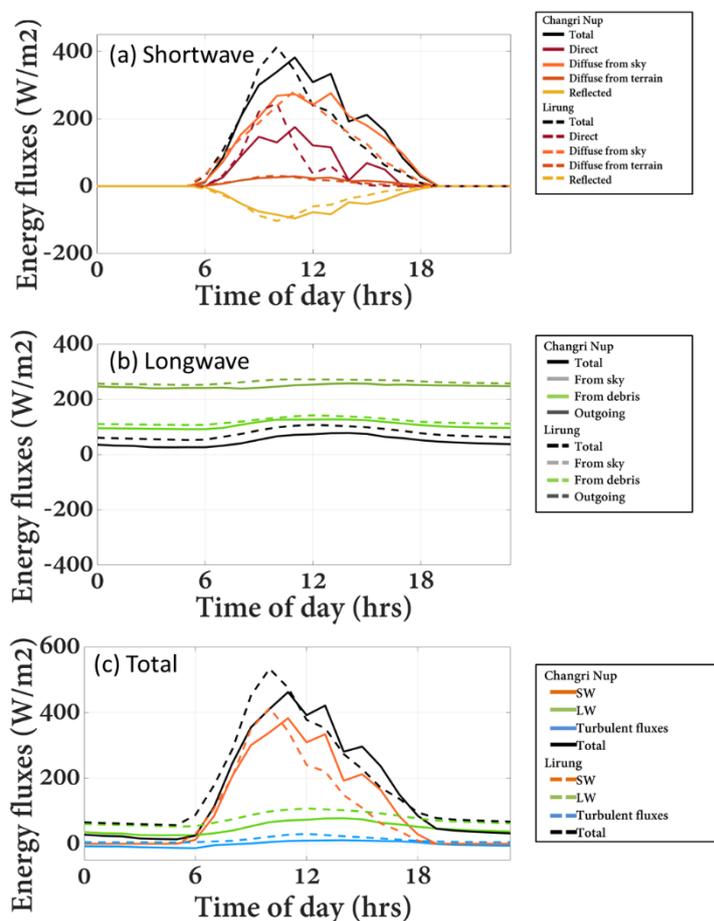
Figure 1.8: *Comparison of daily energy fluxes over Lirung Cliff 2 south-facing forced with Changri Nup 2017 and Lirung 2013 AWS data averaged over 15 days (July 19 to August 2). Figure presented at IUGG, 2019.*

1.2.2.2.3. Influence of supraglacial hydrology on ice cliff melt

Ice cliffs are often found in the vicinity of supraglacial ponds (Steiner et al., 2019; Watson et al., 2017a), which also contribute to the cliff melt and energy-balance. Being directly exposed to incoming radiation, ponds also act as melt hotspots, as they accumulate energy during the melt season and redistribute it to melt the ice (Sakai et al., 2000). This results in melt of the ice in contact with the water, and in the event of a pond drainage, which is frequent (Miles et al., 2017c), will contribute to the internal melt of the glacier (Miles et al., 2016). As a result, ponds are often found to be undercutting ice cliffs (Benn et al., 2001; Röhl, 2008, 2006), and in the case of very large ice cliffs this can sometimes lead to calving (Röhl, 2006, 2008). Additional melt from supraglacial ponds has been implemented in the dynamic version of the cliff energy-balance model by prescribing an additional constant melt contribution to the pixels in contact with a lake, based on model results from one particular pond (Buri et al., 2016b).

Ice cliffs are also regularly found in the vicinity of supraglacial streams, which shape the glacier surface by incising into the debris-covered ice and forming supraglacial valleys (Mölg et al., 2019; 2020). The streams tend to undercut the debris-covered slopes, which can destabilise the debris and lead to the formation of ice cliffs, which then also receive an additional melt contribution at their base from the flowing streams. This process has however never been taken into account in ice cliff melt models.

1.2.2.2.4. Implications of the energy-balance for ice cliff evolution

Several studies based on remote sensing observations have highlighted the fact that ice cliffs are preferentially oriented polewards (Sakai et al., 1998; Thompson et al., 2016; Watson et al., 2017a; Steiner et al., 2019). The first implementation of an ice cliff energy-balance model already made Sakai et al. raise the idea that this was caused by the gradient in shortwave radiation at the cliffs' surface, which is much higher for the south-facing cliffs than for the north-facing ones in the Northern Hemisphere (Sakai et al., 1998). Indeed, the sky view factor increases from the base of the cliff to the top, which results in a strong gradient in net shortwave contribution for the south-facing cliffs, and their progressive flattening (and therefore reburial). These results were confirmed by artificially rotating two ice cliffs to face different aspects and modelling the distributed energy balance at their surface. The south-facing cliffs disappeared almost entirely within the course of a season while the north-facing ones maintained a self-similar geometry (Buri and Pellicciotti, 2018).

1.2.2.2.5. Implications for ice cliff contribution to melt

The development of such ice cliff energy-balance models has been a major advance for the understanding of the contribution of ice cliffs to the melt of debris-covered glaciers.

Applying the cliff dynamic model to all the cliffs of a catchment, the Langtang catchment in Central Nepal comprising four debris-covered glaciers, it was possible to estimate the cliff enhancement factor at the catchment scale (Buri et al., 2021). This enhancement factor varied between 6 +/- 3 and 13 +/- 4 from glacier to glacier, and overall the ice cliffs contributed to 17 +/- 4% of the melt of these four debris-covered glaciers. The application of such a model is however computationally very expensive and at the regional scale, ice cliff contribution to glacier melt has only been accounted for in a very simplistic way by prescribing a constant enhancement factor in a degree-day model (Kraaijenbrink et

al., 2017). Such a model prescribes a linear relationship between melt and the sum of daily average temperatures above 0°C (Kraaijenbrink et al., 2017).

These model developments recently enabled the comparison of melt contributions of ice cliffs, ponds, debris-free and debris-covered ice for a large number of sites around the world, thus allowing the comparison of glaciers in very different climatic settings (Miles et al., 2022). The rigorous uncertainty estimates based on Monte Carlo simulations in this study demonstrated the importance of additional measurements to constrain the cliffs geometry, which is just as important for the melt estimation as getting the incoming energy fluxes right (Miles et al., 2022).

1.2.2.3. Ice cliff distribution

Ice cliff contribution to melt scales with the cliff density at the glacier scale. As a result, knowing the distribution of ice cliffs on debris-covered glaciers, and therefore their density in various locations at the glacier to the regional scale is a key component of understanding the contribution of ice cliffs to glacier melt.

1.2.2.3.1.   Ice cliff mapping

Prior to this thesis, ice cliffs had been mapped only on a handful of glaciers around the world. Most studies, especially those focusing on the ice cliff energy balance, had focused on <10 ice cliffs on five glaciers in different regions of the world (3 in HMA, 2 in the Alps). Some first larger-scale efforts had managed to manually map ice cliffs at the catchment scale (5-13 glaciers) using high resolution (<5m) satellite data (Watson et al., 2017a; Steiner et al., 2019) and some first studies had proposed approaches to map ice cliffs automatically using slope and spectral characteristics from UAV and satellite data (Kraaijenbrink et al., 2016; Herreid and Pellicciotti, 2018).

The development of a large ice cliff database to study their distribution patterns and their dynamics was hindered by the small size and steep slope of these features, requiring very high spatial resolution data, and their variable surface characteristics (a mixture of clean ice, thin debris and meltwater), requiring very accurate and highly resolved spectral data. Delineating ice cliffs manually based on expert knowledge has been the most common approach used, as being the most robust and trustworthy, the downside being the large amount of time and efforts it requires, especially if a validation by other operators is undertaken (Brun et al., 2018; Racoviteanu et al., 2022; Steiner et al., 2019; Watson et al., 2017a). Slope-based approaches have been limited by the changing slope characteristics between ice cliffs, at least partly due to the interactions between cliffs and debris (Herreid and Pellicciotti, 2018), while thermal-based approaches are limited by the coarse resolution of the sensors preventing mapping at the large-scale (Herreid, 2021). On the other hand, high spatial resolution multi-spectral data from UAV or satellites has been increasingly used to derive cliff outlines in a (semi-)automated way and has been the direction taken by many groups to extract ice cliff distribution at the glacier scale (Anderson et al., 2021a; Kraaijenbrink et al., 2016b; Mölg et al., 2019).

1.2.2.3.2.   Formation mechanisms

While the death of ice cliffs by slope flattening is fairly well understood and represented in cliff dynamic models, there exist only a few hypotheses on how they form in the first place, based on qualitative observations from a few glaciers. These formation mechanisms could however be important elements to understand the distribution of ice cliffs on glaciers. These mechanisms are expected to be responsible

for a more or less rapid local slope steepening, leading to debris instability and evacuation. The main hypotheses suggested to date, of unknown importance, would be:

- the collapse of englacial conduits, leading to steep circular slopes forming around a topographic low likely to be filled by a pond (Benn et al., 2012; Immerzeel et al., 2014; Ragettli et al., 2016a; Reid and Brock, 2014; Sakai and Takeuchi, 2000)

- differential melt under the debris due to different debris thicknesses on a hummocky debris-covered glacier (Sharp, 1949) or along medial moraines and glacier margins (Reid and Brock, 2014), leading to progressive slope steepening (Moore, 2021)

- crevasse opening, where the upper sides of the crevasses would evolve into cliffs due to enhanced melt leading to backwasting (Reid and Brock, 2014)

- supraglacial ponds or streams undercutting the debris-covered slopes (Röhl, 2006), enhancing melt at the margins (Miles et al., 2017a, 2017c, 2016; Röhl, 2008; Sakai and Takeuchi, 2000) and in some cases promoting fluvial transport (Moore, 2018), sometimes leading to accelerated steepening from calving (Röhl, 2006, 2008; Benn et al., 2012; Immerzeel et al., 2014). All of these effects are expected to either steepen the debris-covered slope in contact or destabilize the debris on the slope (Moore, 2018).

1.2.2.3.3. *Distribution patterns*

Ice cliff density on glaciers varies between 1 and 12% and in addition to this glacier-to-glacier variability, there is also a strong spatial variability within each glacier (Fig. 1.9a; Table 1.1; Watson et al., 2017b; Steiner et al., 2019).

The proximity of cliffs to supraglacial ponds has been documented at the local cliff scale as well as at the large scale (Brun et al., 2016; Steiner et al., 2019; Watson et al., 2017a, 2017b). Indeed, for the Khumbu region of Nepal, 49% of the cliffs had an adjacent pond, while 77% of the ponds had an adjacent cliff (Watson et al., 2017b). This has led to the hypothesis that supraglacial ponds promote the long-term survival of cliffs (Brun et al., 2016; Watson et al., 2017b), and possibly their formation (Sakai and Takeuchi, 2000). A detailed study of Zmutt Glacier in the Swiss Alps found the same preferential distribution of ice cliffs in the supraglacial valleys controlled by streams (Mölg et al., 2019), and such a feedback between streams and cliffs was also highlighted on Kennicott Glacier in Alaska (Anderson et al., 2021b) and Trakarding Glacier in Nepal (Sato et al., 2021).

The controls of the ice cliff distribution should therefore be related to those of the supraglacial hydrology. For example, ponds mainly develop in low gradient, stagnating glacier tongues with a relatively thick debris cover (Benn et al., 2012; Miles et al., 2017c; Racoviteanu et al., 2021; Reynolds, 2000; Watson et al., 2016). Stream distribution on the other hand is less well constrained. Streams need input meltwater flowing into a catchment (Benn et al., 2017) and their rate of incision needs to be higher than that of the debris-covered ice but not too high, as in this case they would disappear englacially via cut-and-closure mechanisms (Gulley et al., 2009). Both streams and ponds are unlikely to be found very high up glacier, where stronger flow dynamics mean that crevasses are more frequent and prone to deviate meltwater subglacially or englacially (Benn et al., 2017). As a result, conceptually, crevasses would be found in the upper reaches of the debris-covered area of a glacier, with streams developing in the steeper mid-elevation tongue and ponds in the lower, thickly debris-covered, stagnating tongue (Miles et al., 2020, Fig. 1.9a). This repartition of the supraglacial hydrology is also expected to constrain

the ice cliff distribution and characteristics, depending on whether they are controlled by crevasse opening, ponds or streams (Reid and Brock, 2014; Watson et al., 2017a).
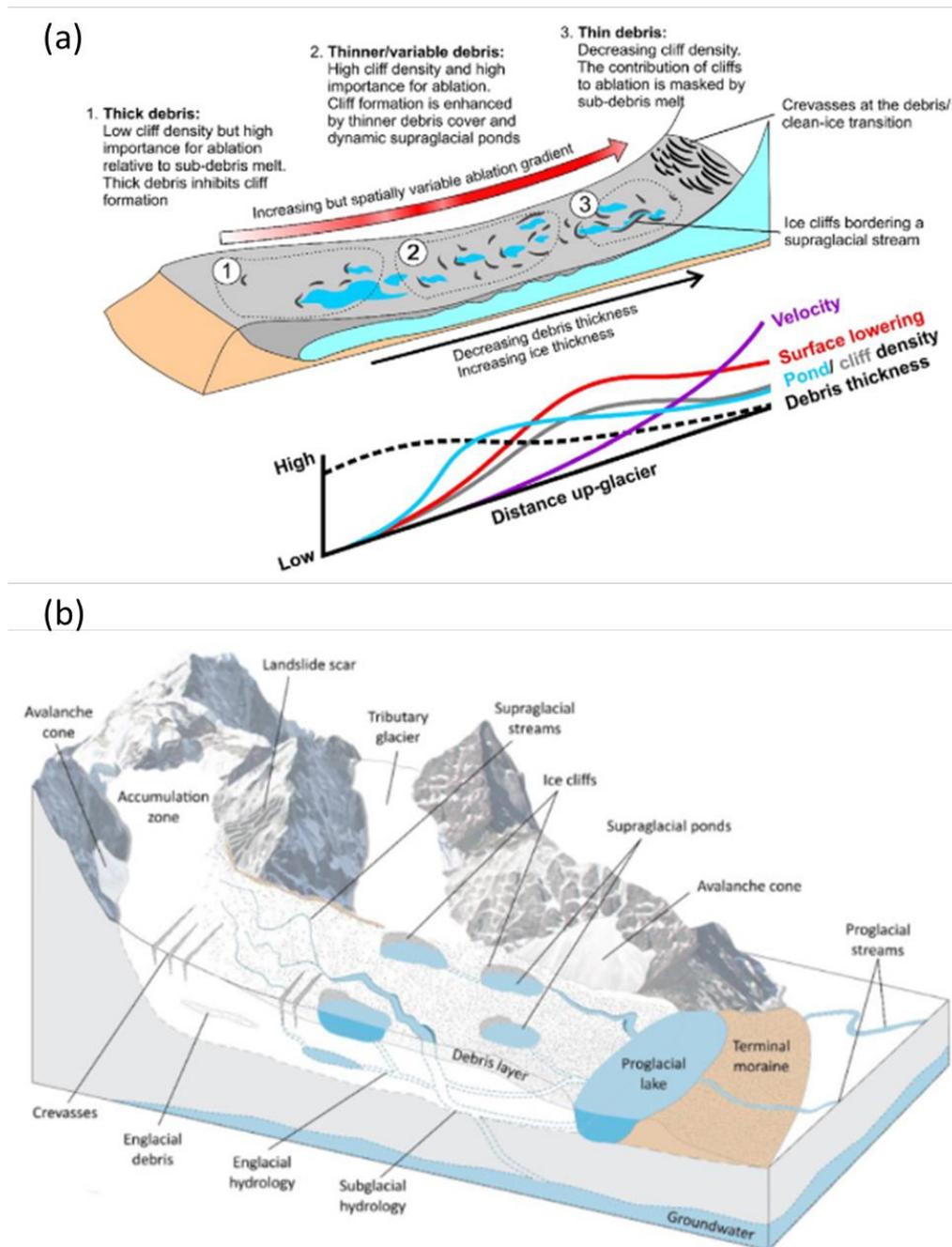
Figure 1.9: *Conceptual depictions of (a) ice cliff distribution on a glacier (Watson et al., 2017a) and of (b) the hydrology of a debris-covered glacier (Miles et al., 2020).*

Based on these various observations, it seems that there should be a link between the development of ice cliffs and the glacier dynamics and state of evolution (Benn et al., 2012; Watson et al., 2017a; Mölg et al., 2019; Fig. 1.9b). Several studies of ice cliff distribution have highlighted a correlation between ice cliff density and compressive strain rate (Anderson et al., 2021b; Benn et al., 2012; Kraaijenbrink et al., 2016b). Beyond the implications on the supraglacial hydrology, the hypothesis retained in this case was that the compression would lead to non-uniform debris thickness patterns, enhancing differential melt and allowing debris to slide off steep slopes (Anderson et al., 2021b). Slightly contradictory with this hypothesis, authors have also formulated the development of ice cliffs to be

conditioned by driving stress, with the assumption that a debris-covered glacier needs to be relatively stagnant to develop enough of these features to have an effect on glacier melt (Ferguson and Vieli, 2021). The threshold values used were however quite arbitrarily defined from one particular glacier and were in disagreement with other large-scale observations (Watson et al., 2017a; Anderson et al., 2021b). These conflicting theories call for a better understanding of the controls of ice cliff distribution (Ferguson and Vieli, 2021).

1.2.2.4. Ice cliff evolution

1.2.2.4.1.   General large-scale patterns

Contrary to supraglacial ponds, which strongly vary seasonally due to meltwater accumulation at the surface at the start of the melt season and subsequent drainage as the englacial conduits get reactivated (Miles et al., 2017c; Narama et al., 2017; Steiner et al., 2019; Watson et al., 2017a), the seasonal variability in ice cliff area is less obvious. It has been hypothesised based on limited observations that ice cliffs should be more dynamically active during the melt season and that combined with additional water enabling debris mobilisation, this should lead to a seasonal increase in ice cliff size (Steiner et al., 2019).

While these seasonal variations lack validation, ice cliffs have been observed to be very dynamic at the interannual scale (Watson et al., 2017a; Steiner et al., 2019), with the cliff density varying between 1.4+/-0.4 % and 3.4+/-0.9 % in the Langtang catchment (Steiner et al., 2019). The controls of this temporal variability remain however unclear, and this represents a relatively large uncertainty for melt modelling.

1.2.2.4.2.   Ice cliff interactions with hydrology

Ice cliffs combined with streams have been shown to have a considerable impact on the topography of debris-covered glaciers. Two decades of observations on Zmutt Glacier in the Alps have shown that small streams initiating between medial moraines in low-relief zones quickly developed small ice cliffs which, due to their high backwasting rates, enabled to widen and deepen these so-called 'cryo-valleys'. Stream meandering and formation of further ice cliffs resulted in the formation of high relief zones and in the reworking of the glacier topography and debris distribution (Mölg et al., 2020). Ultimately, the surface became hummocky enough that the streams could not efficiently drain across the surface, an environment which could favour the formation of supraglacial ponds (Fyffe et al., 2019).

Examples from Langtang Glacier have also shown that supraglacial ponds and ice cliff complexes may evolve together over the years if the pond is able to maintain contact with the cliff (Steiner et al., 2019). When they first form, these ice cliffs often present a circular shape, highlighting that the formation mechanism may play a role in the cliffs' characteristics and their evolution.

1.2.2.4.3.   Influence of debris

At the glacier scale debris can be considered to be passively transported on top of the flowing ice (Anderson and Anderson, 2016; Anderson et al., 2018). However, debris also moves relative to the ice, as soon as the local slope gets steeper than a few degrees (Fyffe et al., 2020). In such configuration, debris moves downslope or in the sunward direction when the slope is very low. Indeed, differential

melt leads to an ice pedestal forming under the individual debris, which will ultimately fall, resulting in a horizontal displacement independent of glacier motion. This debris 'topple-walk' has been described to explain the development and widening of medial moraines (Anderson, 2000), the evolution of 'cryo-valleys' on Zmutt Glacier (Mölg et al., 2020), differential melt on a hummocky surface (Moore, 2021), but also the formation of ice sails (Fowler and Mayer, 2017). Other mechanisms leading to debris displacement are related to water seepage within the debris, but also simply gravitational redistribution when the slope becomes steep enough that the debris is destabilised, and the 'topple-walk' description becomes irrelevant (Moore, 2018, 2021).

A recent framework has been developed to assess the stability of supraglacial debris on glaciers, which depends not only on the ice slope but also on the slope configuration and the water content in the debris (Moore 2018). This framework has been shown to identify reasonably well the zones where debris is unstable (Moore et al., 2019; Westoby et al., 2020). It fails however to represent debris transport and the rates at which it occurs. In such situations, parametrizations of gravitational mass transport provide interesting pathways to explore debris redistribution (Van Woerkom et al., 2019).

Debris motion on glaciers is likely important for the evolution of ice cliffs. Differential melt under debris can lead to high relief zones (Bartlett et al., 2020; Moore, 2021) with steep slopes. Combined with the influence of streams or ponds, these slopes are likely to enable ice cliff formation. Similarly, the redistribution of debris from the top to the bottom of the cliff may result in differential debris thicknesses that could influence the local energy-balance. The most recent version of the ice cliff dynamic model considers sub-debris melt to be constant and does not represent debris transport, except by removing debris on slopes steeper than a given threshold. This limits the applicability of the cliff dynamic model to represent the cliff evolution for periods longer than one melt season (Buri et al., 2016b).

1.3. Research gaps

Three major research gaps emerge to understand the melt contribution of ice cliffs to glaciers:

1. The interactions between ice cliffs, supraglacial hydrology and debris need to be described in more detail to understand the influence of the cliffs' energy-balance and on their evolution for periods longer than a few months. Some of the main limitations here come from the lack of high spatio-temporal observations of ice cliffs and their surroundings.

2. There is a data paucity on ice cliff distribution and evolution from the glacier to the regional scale. The few studies that have looked into ice cliff distribution patterns have been hindered by low data quality, images irregularly spaced in time, and above all, mapping difficulties. Moving forward requires robust techniques to automatically derive cliff outlines from remote sensing products and the development of consistent ice cliff databases.

3. Despite a number of hypotheses and observations, it is still unclear what controls ice cliff formation and distribution at the surface of debris-covered glaciers. The respective roles of climate, ice dynamics and debris-cover stage and the feedbacks from ice cliff formation and melt are still unclear and prevent the understanding of the long-term glacier evolution.

1.4. Research questions

Based on the research gaps described above, I formulated the following research questions, which I answer in the four following chapters (Fig. 1.10). This is a cumulative thesis, and the different sections build on each other. The local field observations and understanding of the cliff energy-balance are necessary steps to understand the large-scale cliff distribution and evolution, while the newly-developed methods used to semi-automatically delineate cliffs in satellite images are used to answer each other research question.

(RQ 1) What processes control the seasonal evolution and melt of ice cliffs at the local scale?

All previous studies have been based on measurements of cliff geometry before and after the melt season. Therefore, little is known about the local scale processes controlling the short-term evolution of the cliffs and how these influence their sub-seasonal melt patterns.

To address this question, I needed very high spatio-temporal observations of ice cliff evolution throughout the monsoon season. One of the challenges was the extensive cloud cover and difficult weather conditions, which prevented satellite observations or extensive fieldwork. I therefore used arrays of custom-built time-lapse cameras to reconstruct the 3D topography of two glaciers in Nepal and Eastern Tibet (including 4 ice cliffs) at weekly time-steps. The glacier motion was accounted for using a mass conservation scheme (e.g. Miles et al., 2018), which meant that I could derive intra-seasonal melt rates at the surface of the cliffs, in addition to tracking their changes in shape, size, slope and aspect. I compared these results with a cliff energy-balance model (Buri et al., 2016a) to characterise the importance of changing albedo and debris accumulation, as well as the role of supraglacial ponds and streams on the cliffs.

This research question is addressed in Chapter 2.

(RQ 2) Can high-resolution multi-spectral satellite images be used for the automated mapping of ice cliffs on debris-covered glaciers?

Previous large-scale remote sensing studies of ice cliff distribution are based on manual delineation of these features, which implies major time constraints and limitations in terms of objectivity, reproducibility and transferability. There is a need for automated, transferable and objective mapping approaches to better understand the distribution and evolution of ice cliffs on glaciers.

This question was addressed by testing two new methods to extract ice cliffs from two different satellite multi-spectral images, the Pléiades (2m resolution, 4 spectral bands) and Sentinel-2 (10m resolution, 10 spectral bands) satellites. The first method uses a band-ratio type of approach, while the second method was derived from Linear Spectral Unmixing. I tested the methods for three different glaciers in HMA and compared them with other existing approaches. The performance of each method was assessed against manually outlined ice cliffs by calculating the Dice coefficient of the outlines derived automatically (Dice, 1945).

This research question is addressed in Chapter 3.

(RQ 3) How variable are ice cliffs on an interannual scale and what controls this evolution?

The total melt of ice cliffs on a glacier is given by integrating their net ablation across the entire cliff area. Previous studies have assumed this area to be constant in time but remote sensing observations have hinted that it could vary from year to year and even seasonally. There is therefore a need to better quantify the long-term evolution of ice cliffs and understand its controls.

To answer this question, I mapped ice cliffs across four different debris-covered glaciers at yearly intervals and over a period of 10 years. The mapping was done manually and used RapidEye satellite images (5m resolution). Each individual cliff was tracked automatically and its evolution from year to year characterised in terms of area change, splitting or merging. The cliffs' birth and death events could therefore be automatically identified and characterised. I then developed a stochastic birth-death model applied to the whole cliff population of each glacier to determine the variability range in terms of cliff area and number. In the last step I added external controls (climate, glacier dynamics, ponding) to explain some of the observed variability.

This research question is addressed in Chapter 4.

(RQ4) What controls the distribution of ice cliffs at the surface of a glacier and how is this related to ice cliff formation mechanisms?

There has been some observations across a few sets of glaciers or single glaciers that have highlighted the variability in cliff distribution and density from glacier to glacier. However, as they all focused on glaciers in a similar evolution stage, they have not been able to propose unifying controls and mechanisms explaining this diversity. This is a key missing link to be able to represent and model the distribution and density of ice cliffs at the surface of glaciers.

This question was addressed by deriving 37537 ice cliffs and their characteristics (slope, aspect, size) on 86 glaciers of HMA using high-resolution (2m) Pléiades satellite DEMs and multi-spectral images. The seasonality of supraglacial ponds was accounted for by automatically deriving pond extents across all Sentinel-2 scenes acquired during the preceding monsoon season. These observations were complemented by large-scale products of glacier surface velocity, debris and ice thickness, as well as a detailed analysis of 202 ice cliff formation events derived from multi-temporal UAV datasets. This unprecedented dataset enabled linking the mechanisms underlying ice cliff formation and distribution.

This research question is addressed in Chapter 5.
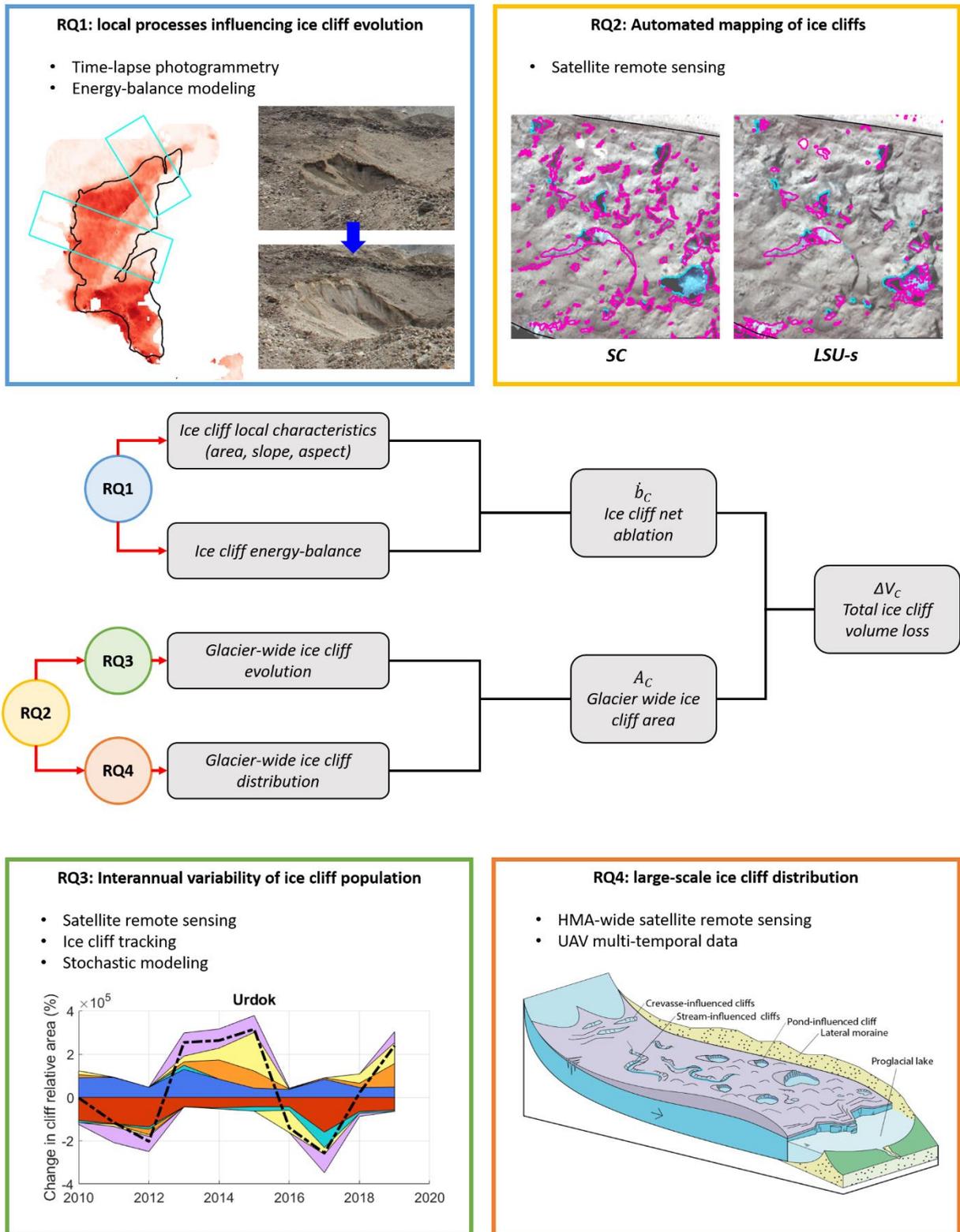
Figure 1.10: *Research questions with the different approaches used to address them. RQ1 (Chapter 2) looks at the local processes influencing the local characteristics and melt patterns of ice cliffs. RQ2 (Chapter 3) aims to develop an automated method for the mapping of ice cliffs, to address RQ3 and RQ4. RQ3 (Chapter 4) focuses on the interannual variability of ice cliffs at the glacier scale. RQ4 (Chapter 5) deals with the controls of ice cliff distribution at the large scale. All these research*

questions aim to improve the evaluation of the total contribution of ice cliffs to glacier mass balance (ΔV_C) from their net ablation ($\dot{b}_C$) and distribution (A_C).

Chapter 2: Sub-seasonal variability of supraglacial ice cliff melt rates and associated processes from time-lapse photogrammetry

 Marin Kneib[1,2], Evan S. Miles[1], Pascal Buri[1], Stefan Fugger[1,2], Michael McCarthy[1] , Thomas E. Shaw[1], Zhao Chuanxi[3], Martin Truffer[4], Matthew J. Westoby[5], Wei Yang[3], Francesca Pellicciotti[1,5]

[1] High Mountain Glaciers and Hydrology Group, Swiss Federal Institute, WSL, Birmensdorf, 8903, Switzerland.

[2] Institute of Environmental Engineering, ETH Zürich, Zürich, 8092, Switzerland

[3] Key Laboratory of Tibetan Environment Changes and Land Surface Processes, Institute of Tibetan Plateau Research, Chinese Academy of Sciences, Beijing, 100045, China

[4] Geophysical Institute and Department of Physics, University of Alaska Fairbanks, Fairbanks, AK 99775, USA 10

[5] Department of Geography and Environmental Sciences, Northumbria University, Newcastle upon Tyne, NE1 8ST, UK

Author contribution

MK, ESM and FP designed the study. MK, ESM designed the time-lapse setup. MK, ESM, SF, MM conducted the fieldwork on Langtang and MK, ESM, SF, TES, ZC, MT, MJW, WY on 24K. PB provided the cliff energy-balance model and helped in applying it. ESM provided the codes to flow-correct the different DEMs and helped in applying them. MK completed all the analysis and composed the manuscript. FP supervised the study. All authors aided in the reviewing and editing of the manuscript.

Key points

- Weekly high-resolution DEMs (0.2m) of four ice cliffs on 24K and Langtang Glaciers from time-lapse photogrammetry enable quantifying the spatio-temporal variability in ice cliff melt
- Ice cliff albedo, and therefore melt, is influenced by the presence of dust and single-clast debris on the cliff surface, regularly washed away by liquid precipitation
- Patchy debris accumulating on cliff surfaces has a melt reducing effect
- Streams, ponds and undercuts at the base of the cliffs promote debris evacuation and therefore lateral cliff expansion

2.1. Abstract

Melt from supraglacial ice cliffs is an important contributor to the mass loss of debris-covered glaciers. However, ice cliff contribution is difficult to quantify as they are highly dynamic features, and the paucity of observations of melt rates and their variability leads to large modeling uncertainties. We quantify monsoon season melt and 3D evolution of four ice cliffs over two debris-covered glaciers in High Mountain Asia (Langtang Glacier, Nepal, and 24K Glacier, China) at very high resolution using terrestrial photogrammetry applied to imagery captured from time-lapse cameras installed on lateral moraines. We derive weekly flow-corrected DEMs of the glacier surface with a maximum vertical bias of +/- 0.2 m for Langtang Glacier and +/- 0.05 m for 24K Glacier and use change detection to determine distributed melt rates at the surfaces of the ice cliffs throughout the study period. We compare the measured melt patterns with those derived from a 3D energy balance model to derive the contribution of the main energy fluxes. We find that ice cliff melt varies considerably throughout the melt season, with maximum melt rates of 5 to 8 cm.day^{-1}, and their average melt rates are 11-14 (Langtang) and 4.5 (24K) times higher than the surrounding debris-covered ice. Our results highlight the influence of redistributed supraglacial debris on cliff melt. At both sites, ice cliff albedo is influenced by the presence of thin debris at the ice cliff surface, which is largely controlled on 24K Glacier by liquid precipitation events that wash away this debris. Slightly thicker or patchy debris reduces melt by 1-3 cm.day^{-1} at all sites. Ultimately, our observations show a strong spatio-temporal variability in cliff area at each site, which is controlled by supraglacial streams and ponds and englacial cavities that promote debris slope destabilization and the lateral expansion of the cliffs. These findings highlight the need to better represent processes of debris redistribution in ice cliff models, to in turn improve estimates of ice cliff contribution to glacier melt and the long-term geomorphological evolution of debris-covered glacier surfaces.

2.2. Introduction

Ice cliffs are one of the main contributors to the mass loss of debris-covered glaciers and are likely to contribute to the 'debris-cover anomaly', which describes the tendency of debris-covered glaciers to display similar ablation rates to clean ice glaciers at the same elevation despite the insulating effect of debris (Gardelle et al., 2013; Pellicciotti et al., 2015; Buri et al., 2021). Similar to supraglacial ponds, the surfaces of ice cliffs are directly exposed to energy fluxes from the atmosphere, these cliffs therefore act as 'melt hotspots' relative to the surrounding debris-covered ice (Steiner et al., 2015; Buri et al., 2016a; Miles et al., 2016). Indeed, beyond a few centimeters of debris, melt rates reduce exponentially with increasing debris cover thickness (Ostrem, 1959; Nicholson and Benn, 2006; Reid and Brock, 2010). A series of studies based on high-resolution remote sensing data acquired from unoccupied aerial vehicles (UAVs) and satellite sensors have shown that ice cliffs enhance melt relative to their surrounding debris-covered area by a factor of 1.2 to 14 (Immerzeel et al., 2014; Juen et al., 2014; Mölg et al., 2019; Thompson et al., 2016; Brun et al., 2018; Mishra et al., 2021; Reid and Brock, 2014) and ponds by a factor of 4 to 8 (Stefaniak et al., 2021; Salerno et al., 2017). Similarly, modeling studies using energy balance models at the scale of an entire glacier or catchment have estimated the melt enhancement factors to be between 6 and 13 for ice cliffs (Buri et al., 2021) and between 9 and 17 for ponds (Miles et al., 2018) for specific locations. Both remote sensing and modeling based approaches to quantify ice cliff melt have limitations. Remote sensing approaches typically focus on deriving melt estimates from 'hot spots' of high thinning identified in maps of elevation change, and which need to be corrected to account for glacier flow (Brun et al., 2018; Miles et al., 2021, 2018b; Mishra et al., 2021; Vincent et al., 2016). However, attributing the melt to the cliffs is non-trivial as they are particularly

difficult to map from remote sensing data, either manually, or using automated methods (Herreid and Pellicciotti, 2018; Kneib et al., 2020). Once the cliff outlines at the start and the end of a focus period are known, there are various ways of extrapolating the melt between the two digital elevation models (DEMs) that may lead to varying results (Brun et al., 2016; Mishra et al., 2021), while the cliff outlines may have varied considerably within a few months (Watson et al., 2017b). Wet and cloudy conditions during the monsoon season, when ice cliffs are the most active, present additional challenges for acquiring time series observations of Himalayan debris-covered glaciers using satellite sensors.

The modeling of the cliff energy balance is another way to tackle the problem of the cliff contribution to glacier melt. It has evolved in the past two decades from the point scale (Han et al., 2010; Reid and Brock, 2014; Sakai et al., 2002; Steiner et al., 2015) to a distributed representation of the energy balance at the cliff surface (Buri et al., 2016a). Accounting for the cliff energy balance to dynamically update the cliff geometry (Buri et al., 2016a) has led to a better understanding of the controls of ice cliff evolution, including aspect (Buri and Pellicciotti, 2018), and to the estimation of ice cliff melt contribution at the catchment scale (Buri et al., 2021). This complex modeling framework is, however, still limited in the representation of the interaction of ice cliffs with their surroundings. For example, the model presented by Buri et al. (2016b) accounts for debris redistribution by removing debris on slopes solely based on a fixed slope threshold, and, for ice cliffs which are attached to a pond, uses a fixed value of pond melt at the cliff base. Moreover, the model parameters have only been evaluated using a small sample of cliffs, where data has been collected over short time-scales using ablation stakes, by measuring the backwasting rate of the cliff edge (Buri et al., 2016a; Han et al., 2010; Reid and Brock, 2014; Sakai et al., 1998, 2002; Steiner et al., 2015), and, more recently, using measured volume changes (Buri et al., 2016a). Ultimately, fully distributed energy balance models require knowledge of meteorological and surface variables over the cliffs surface and the surrounding debris slopes, such as albedo, which are difficult to determine, and which vary much in time and space.

These limitations highlight the need for detailed and quantitative observations of cliff melt and evolution during the melt season. This is particularly challenging as ice cliffs are dynamic features which can grow, shrink, appear or disappear within the course of a single season (Sato et al., 2021; Kneib et al., 2021), which results in the ice cliff area regularly changing by up to 20% from year to year (Kneib et al., 2021; Watson et al., 2017a; Steiner et al., 2019; Falaschi et al., 2021; Sato et al., 2021; Anderson et al., 2021). This high variability can be explained by the strong influence of local processes such as pond undercutting, filling and drainage (Kraaijenbrink et al., 2016; Watson et al., 2017b), stream undercutting (Mölg et al., 2020) and debris redistribution (Moore, 2018; Westoby et al., 2020). To improve process understanding and, in turn, inform the refinement of numerical models, observations of ice cliff evolution therefore need to: 1) be captured during the melt season, when ice cliff activity is at its highest; 2) be of high spatiotemporal resolution and, in turn, 3) be suitable for quantifying surface changes both across ice cliffs, and on adjacent local topography and features, including debris-covered ice, and supraglacial streams and ponds.

In the past decade, advances in modern 'structure-from-motion' (SfM) photogrammetry have enabled the reconstruction of 3D topography from images acquired from multiple, converging viewing angles (Westoby et al., 2012). A primary use of SfM-based approaches has been to map glacier surfaces from UAV, enabling the detailed study of debris-covered glaciers and their supraglacial features (Brun et al., 2018; Immerzeel et al., 2014; Kraaijenbrink et al., 2016b; Mishra et al., 2021; Westoby et al., 2020). Topographic reconstruction can also be achieved through terrestrial photogrammetric survey, which can enable the accurate mapping of steep and overhanging features which are common at ice cliff locations (Brun et al., 2016; King et al., 2020; Watson et al., 2017b), and can be occluded in imagery acquired from nadir-oriented aerial surveys. The combination of high-frequency time-lapse image

capture and photogrammetric processing is therefore highly promising for generating quantitative observations of the dynamics of fast-changing cryospheric landscapes. While still limited by the amount of processing required and the logistical aspects of deploying arrays of time-lapse cameras, time-lapse photogrammetry has been used successfully to precisely monitor thaw slump activity (Armstrong et al., 2018), lava flows (James and Robson, 2014a), snow melt (Filhol et al., 2019) and calving dynamics (Mallalieu et al., 2017).

Here we apply time-lapse SfM photogrammetry to study the subseasonal melt of four ice cliffs on two different glaciers of the Himalayan range, at weekly intervals during a full melt season. **We aim to quantify ice cliff subseasonal melt and identify the local processes controlling its variability.** To this end, we derive weekly flow-corrected DEMs of the ice cliffs and calculate spatially distributed melt over the study period. We compare these results with estimates of melt generated by a 3D energy balance model to isolate the main energy fluxes and identify the local processes that cause modeled melt to deviate from our measurements.

2.3. Data

2.3.1. Study sites

We installed time-lapse camera arrays on two Himalayan debris-covered glaciers with distinct glaciological and climatic characteristics (Fig. 1). Langtang Glacier is located in Central Nepal (85.72°E, 28.27°N) and has a 15 km-long debris-covered tongue, with an estimated density of supraglacial ice cliffs (ponds) ranging between 2.1% and 4.7% (0.9% and 2.5%) of the debris-covered area (Kneib et al., 2020, 2021; Steiner et al., 2019; Miles et al., 2017b). The debris thickness increases down-glacier and exceeds 2 m in the lower portion of the glacier (McCarthy et al., 2021), where our survey domain was located (Fig. 1c). 24K Glacier (hereafter '24K') is located in Eastern Tibet (95.72°E, 29.76°N), is also extensively debris-covered but is much smaller than Langtang Glacier; it has a 2 km-long debris-covered tongue, and debris cover is thinner (at most 0.5 m in the lower portion of the glacier) (Fig. 1d). The debris-covered area of 24K is much steeper (9.8°) than for Langtang (3.4°), which may partly explain the scarcity of ponds at its surface, and the presence of a number of supraglacial streams in its central area which have led to the development of so-called 'cryo-valleys' bounded by ice cliffs, and similar to those described on Zmutt Glacier in Switzerland (Mölg et al., 2020).

We installed an array of eight time-lapse cameras on the lateral moraine of Langtang Glacier, overlooking a small domain of the lower portion of the debris-covered tongue and comprising a number of North-East to North-West facing ice cliffs, three of which are connected to a pond (Fig. 2.1a). An additional array of four time-lapse cameras was installed on 24K, overlooking a large stream-influenced North-facing cliff (Fig. 2.1b).
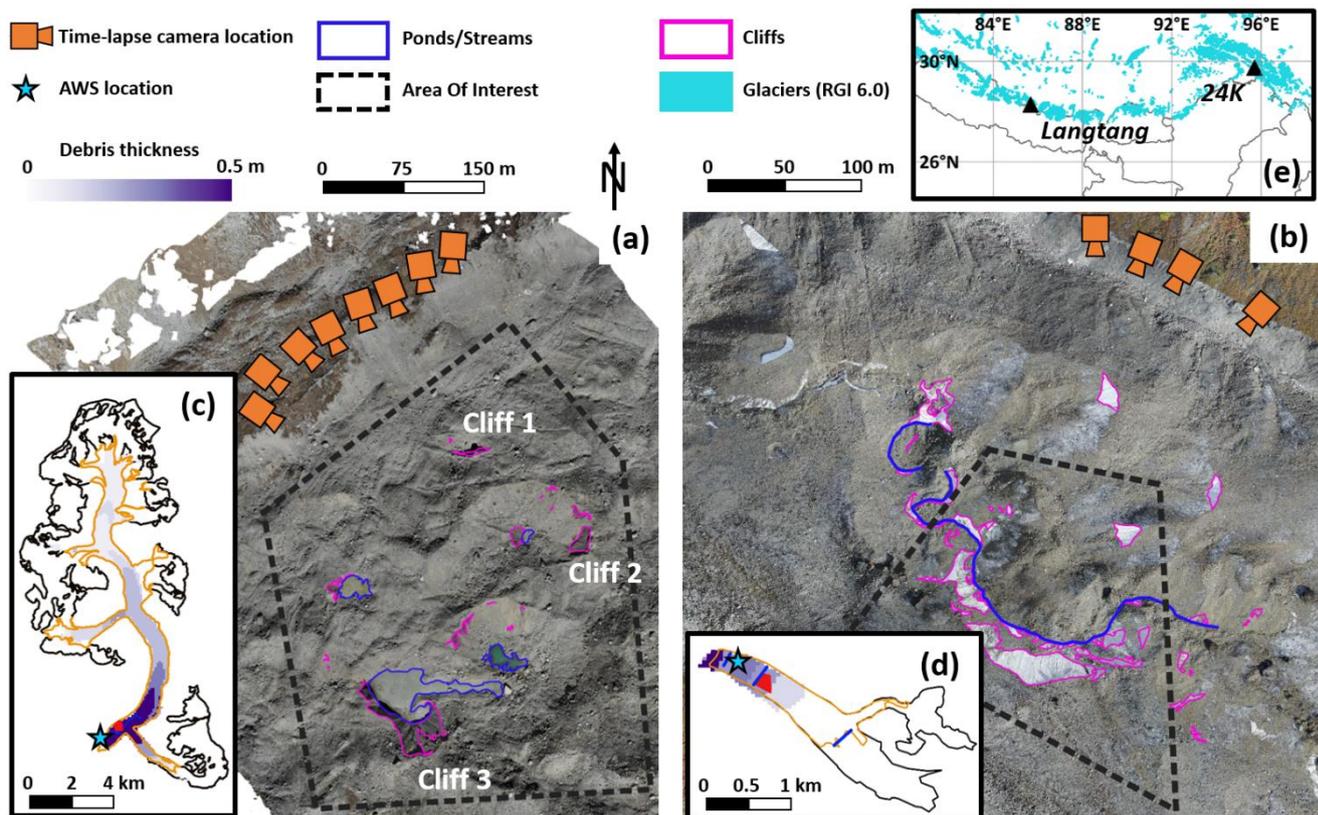
Figure 2.1: *Survey domains of Langtang (a) and 24K (b) Glaciers. Background is the UAV orthoimage from 02/11/2019 (Langtang) and 11/10/2019 (24K), with the outlines of cliffs (pink), ponds and streams (blue). (c-d) Glacier (black) and debris-cover (orange) outlines of Langtang and 24K with the location of the areas of interest (AOIs)(red), automatic weather stations (AWSs) and ground penetrating radar (GPR) measurements (blue). Background shows the distributed debris thickness from McCarthy et al. (2021). (e) Location of the two sites in the Himalaya.*

2.3.2. Time-lapse camera arrays

The time-lapse cameras were mounted directly on stable boulders along lateral moraine crests of the two glaciers (Fig. 2.1a, b). The custom time-lapse rigs consisted of a Canon EOS 2000D camera (24.1 MP) with an 18-25 mm lens. The cameras took photographs at a consistent 2-hour interval for the whole duration of the melt season, triggered by an intervalometer. The cameras were powered by a 5W solar panel, a 12V 7Ah lead-acid battery and an ECO-N-T solar charge controller (Fig. 2.2a). These elements were assembled in a weather-proof box (Bixibox) which was mounted on a 1.5 m-long aluminum mast bolted vertically to the rock (Fig. 2.2b, c). All camera stations ran without data gaps from 12/05/2019 to 01/11/2019 (6 months) for Langtang, and from 08/06/2019 to 12/10/2019 (4.1 months) for 24K.The focal length of all cameras was manually set to 18 mm to ensure the widest viewing angle. The xyz position of each time-lapse camera was measured using a differential GPS (dGPS), and the three viewing angles were measured at the beginning and at the end of the time-lapse period.
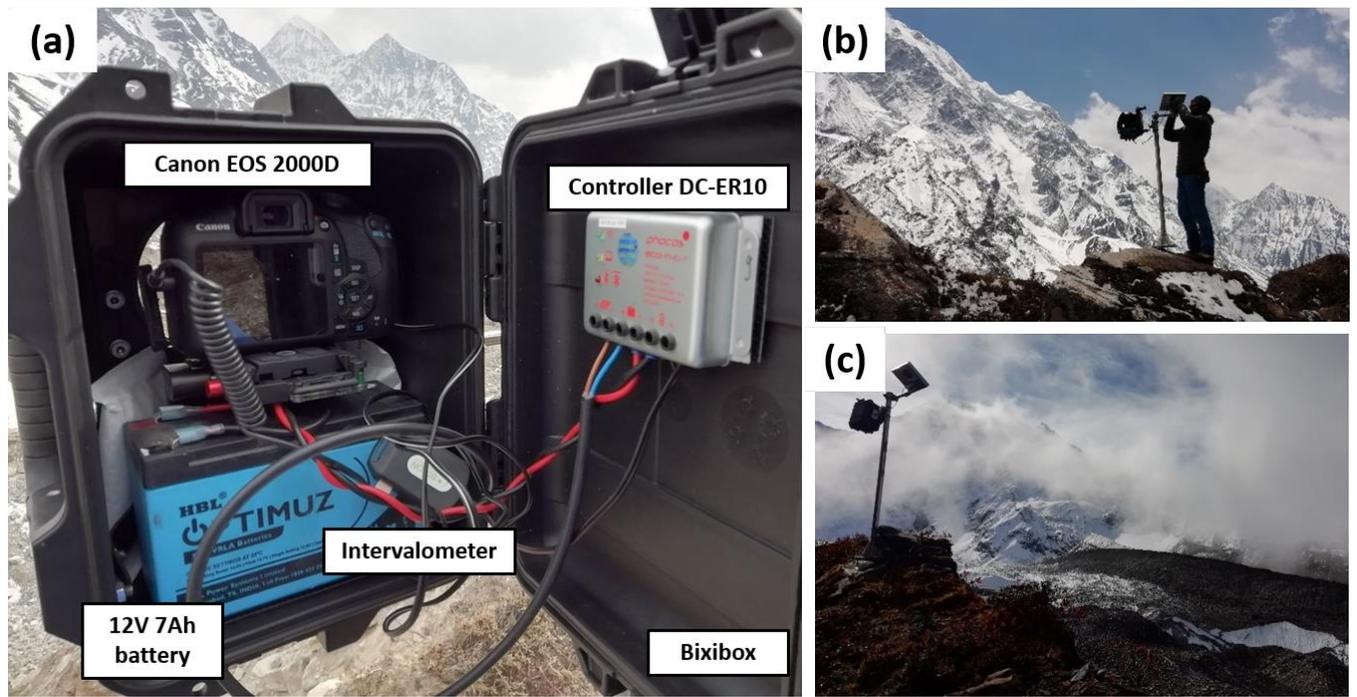
Figure 2.2: *(a) Different elements of the time-lapse camera setup inside the Bixibox. (b) Mounting of a time-lapse camera on the moraine of Langtang Glacier. (c) Time-lapse camera overlooking the ice cliffs of the 24K study domain.*

2.3.3. UAV flights and remote sensing imagery

We carried out a UAV survey of the study domain at the start and the end of the monitoring period on 24K. On Langtang, a flight was only possible at the end of the study period (Table 2.1). The initial and final conditions for Langtang were instead constrained with two Pléiades stereo images taken within a month of the start and the end of the time-lapse recording period (Table 2.1).

The UAV images were taken nadir-oriented at a fixed elevation of 70 to 120 m above the glacier surface with a lateral overlap of 70% and a forward overlap of ≥80%. Additional oblique images of the survey domain, which have been proven to mitigate against the introduction of systematic model deformation (James and Robson, 2014b), were taken manually, depending upon UAV battery limits.

Between 15 and 18 ground control points (GCPs) were laid out across the survey domain around the main features of interest (ice cliffs, ponds and streams), with a good distribution between topographic lows and highs (Fig. 2.4), and consistent coverage at margins of the study area. GCPs were visible in photographs captured by the time-lapse cameras, and from the UAV. The xyz positions of the GCPs were measured with a single-band dGPS system (10 cm accuracy) within 48 hours of the UAV flights.

Table 2.1: *Pre- and post-monsoon remote sensing observations from UAV and satellite surveys.*

Platform	Model	Site	Date	Orthoimage & DEM Resolution (m)
UAV quadcopter	Mavic 2 Enterprise	24K	10/06/2019	0.12

UAV fixed-wing	eBee PLUS	24K	11/10/2019	0.12
UAV quadcopter	Mavic 2 Enterprise	Langtang	02/11/2019	0.2
Satellite stereo	Pléiades 1A	Langtang	14/06/2019	2
Satellite stereo	Pléiades 1A	Langtang	22/10/2019	2

2.3.4. GPR measurements

We conducted ice thickness measurements using a Kentech ground penetrating radar (GPR) monopulse generator with 20 m dipole antennas (~2.5 MHz) along four transects on 24K Glacier in October 2019 (Fig. 2.1b). For Langtang, we used the measurements from Pritchard et al. (2020) conducted in the vicinity of the survey domain (Fig. 2.1a). These measured ice thicknesses were used to bias-correct the consensus ice thicknesses from Farinotti et al. (2019) using a linear regression of the ice thickness for Langtang and of the bed altitude for 24K to obtain a distributed estimate of ice thickness for each survey area. These corrections led to the reduction of the mean bias from 15.8 to 0.1 m and from 94.1 to 1.7 m for Langtang and 24K, respectively.

2.3.5. Field observations of supraglacial ponds

Two of the cliffs in the Langtang survey domain had a pond at their base in May 2019, at the start of the recording period. We monitored the two pond water level changes using HOBO pressure transducers and recorded the water surface temperature using a HOBO thermistor attached to a float. The pond at the base of one cliff drained almost entirely during the study period and it was not possible to retrieve its pressure transducer, which got buried by a thick layer of debris. The thermistor was, however, still accessible and its temperature record combined with the observations from the time-lapse cameras clearly shows the timing of the drainage.

2.3.6. Meteorological observations

Each glacier was equipped with an on-glacier automatic weather station (AWS), which was installed in the vicinity of the survey domain (<100 m of elevation difference) and recorded, among other variables, air temperature, relative humidity, incoming and outgoing longwave and shortwave radiation and wind speed at 5 minute intervals over the study period (Fugger et al., 2022). Precipitation measurements were acquired using a HOBO tipping bucket at the AWS site for 24K and on the lateral moraine, ~500 m away from the AWS, for Langtang (Steiner et al., 2021). The air temperature measured at the AWS location was lapsed considering the mean above-debris lapse rates (-0.0088°C m^{-1}) following Shaw et al. (2016). All other variables were left unadjusted for input to the energy balance model (Section 2.6.7).

2.4.   Methods

2.4.1. Processing of UAV and Pléiades images

The Langtang Pléiades satellite images were stereo-processed to generate 2 m-resolution DEMs and 0.5 m-resolution orthoimages from the panchromatic band using Rational Polynomial Coefficients (RPCs) within the NASA AMES Stereo Pipeline (Beyer et al., 2018; Kneib et al., 2020; Shean et al., 2016).

The Langtang and 24K UAV images were imported to Agisoft Metashape Professional (v1.7.2). Initial bundle adjustment was performed using only the UAV GPS geotags. We then incorporated the xyz positions of the GCPs to refine this adjustment and improve camera location and pose estimation, and the location of image tie points (Westoby et al., 2020). We then generated dense point clouds, which were used to produce DEMs and orthoimages (0.2 m resolution for the Langtang survey, 0.12 m for the 24K survey).

Co-registration of the Langtang Pléiades DEMs was performed over off-glacier stable terrain with slopes between 10 and 45°, following the approach detailed in Nuth and Kääb, (2011). For the 24K UAV flights, we used the fixed position of the time-lapse cameras, which we measured during each dGPS survey, to correct for vertical and horizontal shifts in the position of the on-glacier GCPs. After the initial co-registration of the UAV DEMs, there remained some non-linear distortions (tilts) that were removed using additional natural off-glacier control points (boulders) on both sides of the glacier from the June flight to rerun the bundle adjustment of the October flight, which improved the co-registration.

For both sites we estimated the vertical uncertainty as the standard deviation of the DEM difference over off-glacier stable terrain (Mishra et al., 2021), 0.53 m for Langtang and 0.50 m for 24K.

2.4.2. DEM processing with time-lapse photogrammetry

The overall workflow for generating DEMs from the time-lapse images broadly follows that described by Mallalieu et al. (2017) (Fig. 2.3). The time-lapse lasted from 12/05/2019 to 01/11/2019 (173 days) for Langtang, and from 08/06/2019 to 12/10/2019 (126 days) for 24K, resulting in ~2100 images per camera for Langtang and ~1550 images per camera for 24K, at 24.1 MP resolution.

In the first step (step 1, Fig. 2.3) we manually removed all the images taken during night time, with water or snow in front of the lens, or with poor visibility due to clouds or precipitation. We then grouped the images from the different cameras taken at each site within 2.5-hour periods to account for offsets in the image acquisition time of the different cameras. If one or more images were missing, we ignored all the images in that set. After this pre-selection, there remained 781 image sets for Langtang and 357 for 24K.
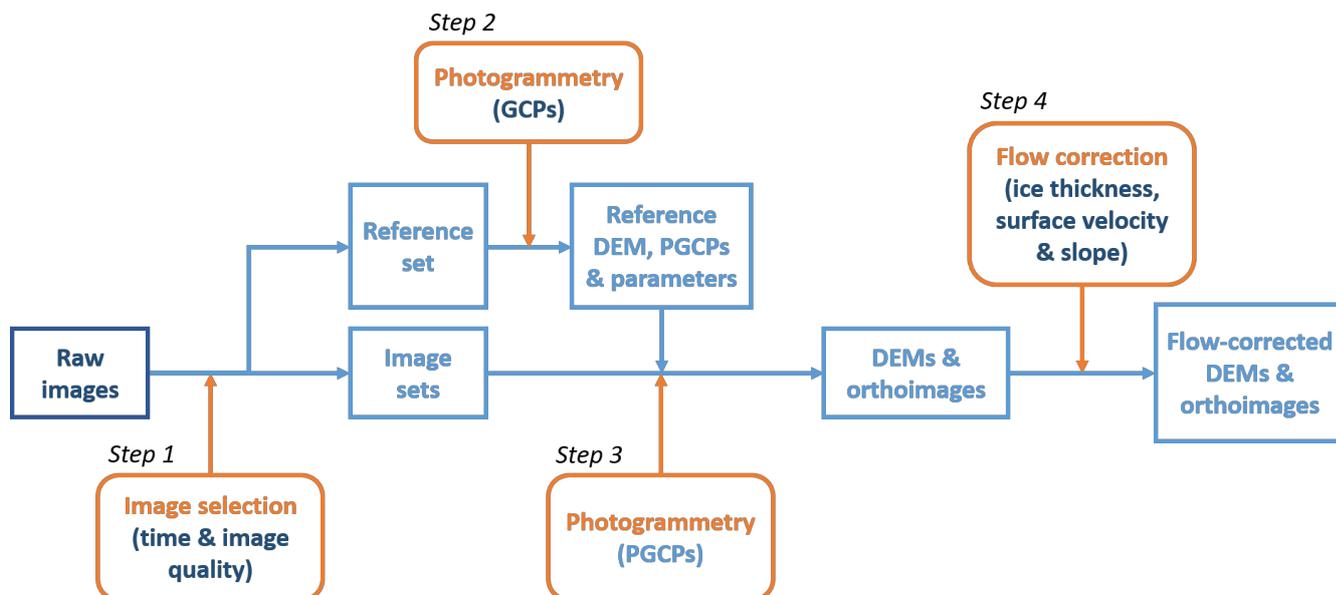
Figure 2.3: *Processing workflow of the time-lapse images, indicating the initial data (dark blue), processing steps (orange), intermediate and final outputs (light blue).*

We used the image sets of 01/11/2019 14:00 for Langtang and 08/06/2019 14:00 for 24K as 'reference' sets, as they were taken within a few hours of the GCP surveys conducted in the survey domain (Fig. 4). In step 2, the reference image sets were imported to Agisoft Metashape Professional (v1.7.2) and we used the dGPS-measured position and viewing angles of the cameras in the initial bundle adjustment and then used the GCP coordinates for subsequent optimization of the lens parameters prior to generation of the dense point cloud (Fig. 3). These reference sets were used to define 'pseudo' GCPs (PGCPs), which, combined with their camera parameters, were used to process the weekly images sets (step 3; Section S1; Fig. 3, 4).

We established the relative accuracy of the output DEMs by computing the mean and standard deviation values of elevation change relative to the reference DEM calculated over background stable terrain (Fig. 4, orange outline). The mean elevation change over this area of the background moraine was generally <0.2 m for Langtang and <0.05 m for 24K. Higher values were obtained when the illumination conditions in a given image set differed substantially from the reference image set, or when some of the images were slightly blurred from rain or mist. In these instances, we used other, higher quality image sets taken within a few days from the target date.

Ultimately, we produced 25 time-lapse DEMs and orthoimages for Langtang (0.20 m resolution) and 19 DEMs and orthoimages for 24K (0.24 m resolution), covering the full study period at an approximately weekly interval (Table 2.S3).

We used the orthoimages to manually delineate the ice cliff outlines at each weekly time-step, which we considered to be the exposed ice sections free of debris. This was sometimes difficult in the case of patchy debris, which was included in the cliff outlines when the underlying ice was still visible. Oblique viewing angles combined with a complex glacier surface led to gaps in the orthoimages and DEMs caused by topographic shadowing. Despite this limitation, we still resolved the larger portion of three cliffs on Langtang and of the 24K cliff (Fig. 2.4a, b).
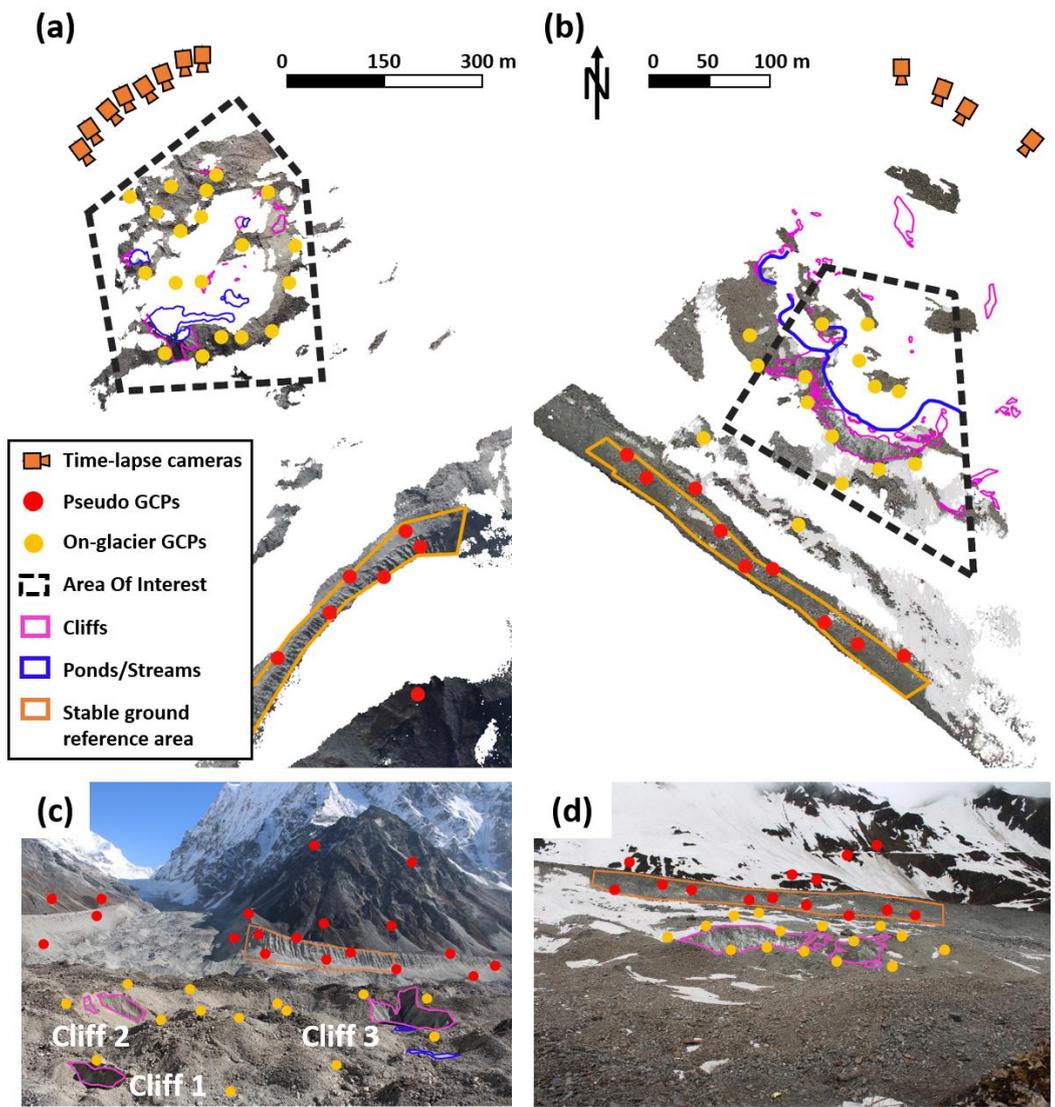
Figure 2.4: *Survey areas with Pseudo GCPs (red), on-glacier GCPs used for the reference image sets (yellow), stream, ponds and cliff outlines, from the perspective of the orthoimages (a-b) and the reference time-lapse images (c-d), on Langtang (a & c) and 24K (b & d).*

2.4.3. Glacier flow corrections

In a fourth step (step 4, Fig. 2.3), all the DEMs except a reference DEM for each glacier were corrected to account for glacier flow (horizontal surface velocity and emergence) following the approach described by Mishra et al. (2021), using estimates of distributed surface velocity and ice thickness to calculate the ice flux through a flux gate, and, in turn, an implied ice emergence velocity. We calculated distributed surface velocity fields over the lower portion of the glaciers, including the survey domains, by applying a normalized cross-correlation approach to the Pléiades (for Langtang) and UAV (for 24K) DEM hillshades using ImGRAFT (Messerli and Grinsted, 2015). We filtered these velocity fields by removing values with a low signal-to-noise ratio (<2), low correlation score (<0.5) or unrealistically high values (>3 m for Langtang, >8 m for 24K over the study period) and interpolated the remaining results with a cubic spline interpolation (Mishra et al., 2021).

We used these velocity fields to correct the x-y displacements between the different DEMs (time-lapse, UAV, Pléiades) and the reference time-lapse DEMs, assuming a constant velocity over the study period. In this step we also accounted for vertical displacement due to the downslope advection of the surface using the slope from the AW3D 30 m-resolution DEM (Tadono et al., 2014) of each study area, smoothed using a 30-pixel Gaussian filter (Brun et al., 2018; Miles et al., 2018b; Mishra et al., 2021).

We calculated emergence velocity in the lower portion of the glaciers (including the survey domains) by estimating the flux through a flux gate located immediately upstream from the survey domains, taking into account the surface velocity and the adjusted ice thickness at this location (Brun et al., 2018; Miles et al., 2018b; Mishra et al., 2021; Vincent et al., 2016) at a 8 m resolution for Langtang, 4 m for 24K, and assuming that basal sliding accounts for 50% of the surface motion (but considered the full 0-100% range in the uncertainty calculation). We integrated the flux across the cross section with a simple-shear assumption to calculate the column-averaged velocity (Huss et al., 2007) and assumed that this flux is uniformly distributed as emergence downstream from the flux gate.

We estimated the surface velocity uncertainty as the normalized median absolute deviation of its x and y components over off-glacier terrain, equal to 0.84 m (0.6 cm.day^{-1}) for Langtang and 0.35 m (0.3 cm.day^{-1}) for 24K over the full study period. We obtained an emergence velocity of 0.39 +/- 0.16 m (0.3 +/- 0.1 cm.day^{-1}) for Langtang and 0.66 +/- 0.16 m (0.5 +/- 0.1 cm.day^{-1}) for 24K. As for the x-y displacements, we used these emergence values to correct the different DEMs (time-lapse, UAV, Pléiades) relative to the reference time-lapse DEMs assuming a constant emergence over time. Similarly to the DEMs, the cliff outlines were flow-corrected for the surface displacements in the x and y directions.

2.4.4. Estimating melt from DEM differencing

In this study we were interested in calculating distributed melt patterns at the surface of the cliffs, which correspond to the normal displacement of the cliff surface (Buri et al., 2016a). A number of studies used the M3C2 algorithm (Lague et al., 2013; Mishra et al., 2021; Watson et al., 2017b) directly applied to the point clouds to calculate this normal displacement. However, here we aimed to compare our results with a gridded ice cliff energy balance model (Buri et al., 2016a, 2016b), which uses the cliff DEM for the distributed energy balance calculations. We therefore estimated the melt from two time-lapse DEMs (DEM1 and DEM2) by calculating for each pixel of DEM1 the local normal based on its eight neighboring pixels and finding the intersection of the normal with DEM2. The melt was then equal to the distance between the DEMs along this normal (Fig. 2.S1). This approach is similar to the M3C2 algorithm but using DEMs and 3x3 neighborhoods.

2.4.5. Uncertainty estimation

To estimate the uncertainty in melt rate, we combined the uncertainties from the flow correction σ_{flow} with an estimation of the uncertainty of the calculation of melt distance from the DEMs σ_{DEM}.

We conservatively assumed the melt distance uncertainty σ_{DEM} to be equal to the uncertainty in elevation change as this removes the dependence on the terrain aspect and slope. Indeed, in the case of two DEMs with the same slope parallel to one another, which we considered to be the most common short-term change due to ice melt, the elevation difference should be larger than the melt distances (e.g. Mishra et al., 2021), and the same should be true for their uncertainties. In the case of our study areas

with complex geometries and viewing angles, we expected these uncertainties to vary with slope and aspect, as well as with the number of overlapping images, the distance from the time-lapse cameras, and the time difference with the reference DEMs (James and Robson, 2014b; Mallalieu et al., 2017; Armstrong et al., 2018; Filhol et al., 2019). We also expected elevation change uncertainties to increase with time from the reference image set and distance from the time-lapse cameras, except in the very near-field where less overlap of the images should lead to higher uncertainties (Mallalieu et al., 2017).

The uncertainty from the melt distances σ_{DEM} comprises a systematic error $\sigma_{DEM,sys}$ given by the absolute mean elevation change over stable terrain, and a random error $\sigma_{DEM,rand}$ given by the standard deviation of elevation change over stable terrain. Depending on the evolution of the uncertainties in space, this relationship can be scaled by a factor f:

$$\sigma_{DEM} = \frac{1}{f} \times \sqrt{\sigma_{DEM,sys}{}^2 + \sigma_{DEM,rand}{}^2} \tag{1}$$

We therefore estimated the melt uncertainties in the cliff domain by analyzing the mean and standard deviation of elevation change over the moraine (Fig. 2.4). Indeed, the moraine was the closest feature to the survey domain that could be considered relatively 'stable', at least over a period of a few months. Furthermore, it had similar slopes and aspects to those of the cliffs in the survey domain, but was located in the background of the survey area, making it a good but conservative proxy for the features analyzed (Fig. 2.4). We conducted two different tests to estimate the melt uncertainties in the cliff domain. The first test (1) was to look at the evolution of the mean and standard deviation of the elevation changes relative to the reference DEMs over the moraine with time (Fig, 2.5a, b). The second test (2) was to look at the evolution of the mean and standard deviation of the elevation changes with distance for time-lapse DEMs taken within a few days from each other (Fig. 5c, d).

The mean value remained between +/-0.2 m for Langtang, where the moraine was ~800 m away from the cameras (Fig. 2.5a), and between +/-0.05 m for 24K, where the moraine was ~400 m away from the cameras (Fig. 2.5b). Using a factor 2 to account for positive and negative biases, we obtained $\sigma_{DEM,sys} = 0.4\ m$ for Langtang and $\sigma_{DEM,sys} = 0.1\ m$ for 24K (Table 2.2). $\sigma_{DEM,rand}$, given by the standard deviation, increased with time during the first two months of the time-series for Langtang, until it reached a value of ~1 m, while it remained stable around 0.6 m for 24K during the whole period. For (2), we took the DEM the furthest away in time from the reference DEM and processed the image pairs taken within 48 hours of this new reference DEM, only keeping the resulting DEMs with a mean elevation change relative to the reference DEM lower than 0.2 m for Langtang (4 remaining DEMs) and 0.05 m for 24K (7 remaining DEMs) (Fig. 2.5a, b, dashed lines). The elevation change patterns of these near-contemporaneous DEMs highlighted a factor $f = 2$ increase in standard deviation with distance between the cliff domain and the moraine for Langtang and $f = 1.7$ for 24K (Fig. 2.5c, d). As a result, for Langtang $\sigma_{DEM} = 0.5\ m$ and for 24K $\sigma_{DEM} = 0.4\ m$ (Table 2.2). These are the same values as if we had calculated them from the random errors only, which means that the systematic errors can be considered negligible.

We also needed to account for the uncertainties related to the flow correction, which we assumed to be equal to the quadratic sum of the 1σ surface velocity uncertainty σ_{xy}, the 1σ emergence velocity

uncertainty σ_b estimated following the approach and assumptions described by Miles et al., 2018, and the uncertainty from the slope correction σ_{Slope} (all in m.day^{-1}):

$$\sigma_{flow} = \sqrt{\sigma_{xy}{}^2 + \sigma_b{}^2 + \sigma_{Slope}{}^2}. \tag{2}$$

Where:

$$\sigma_{Slope} = \sigma_{xy}\tan(\alpha) + \frac{d\alpha}{\cos^2\alpha}u_s \approx u_s d\alpha \tag{3}$$

Where α is the mean glacier slope in the survey domain, and u_s the mean velocity. For the uncertainty on the slope correction, we assumed a $d\alpha = 2° = 0.03\ rad$ uncertainty in the slope angle, which results in $\sigma_{Slope} = 0.03$ cm.day^{-1} for Langtang and 0.06 cm.day^{-1} for 24K. As a result, the 1σ uncertainty from flow correction was equal to 0.007 m.day^{-1} for Langtang and 0.004 m.day^{-1} for 24K.

The 1σ melt uncertainty for each pixel could be expressed as:

$$\sigma_{Melt} = \sqrt{\sigma_{DEM}{}^2 + \left(\sigma_{flow} \times dt\right)^2}, \tag{4}$$

where dt is the number of days over which the melt is calculated. Ultimately, we calculated melt on a tri-weekly basis for Langtang and a bi-weekly basis for 24K to reduce the uncertainties relative to the measured melt rates. This meant that the uncertainty from flow was an order of magnitude lower for these domains and could therefore be neglected: $\sigma_{Melt} = \sigma_{DEM} = 0.5\ m\ (0.02\ m/day)$ for Langtang and $\sigma_{Melt} = \sigma_{DEM} = 0.4\ m\ (0.03\ m/day)$ for 24K over their respective tri- and bi-weekly melt periods (Table 2.2).

Based on this, in all that follows we used the standard deviation of melt at the cliff location to represent these uncertainties, as it directly accounts for 1) the random error from the DEMs and 2) the melt variability at the surface of the cliffs. We note however that assuming a Gaussian error for independent measurements, the random error from the DEMs becomes negligible (<0.05 m) for the average melt when the number of pixels considered is greater than 100, which is always the case here.

Uncertainties as a function of time

Uncertainties as a function of distance

Langtang

24K
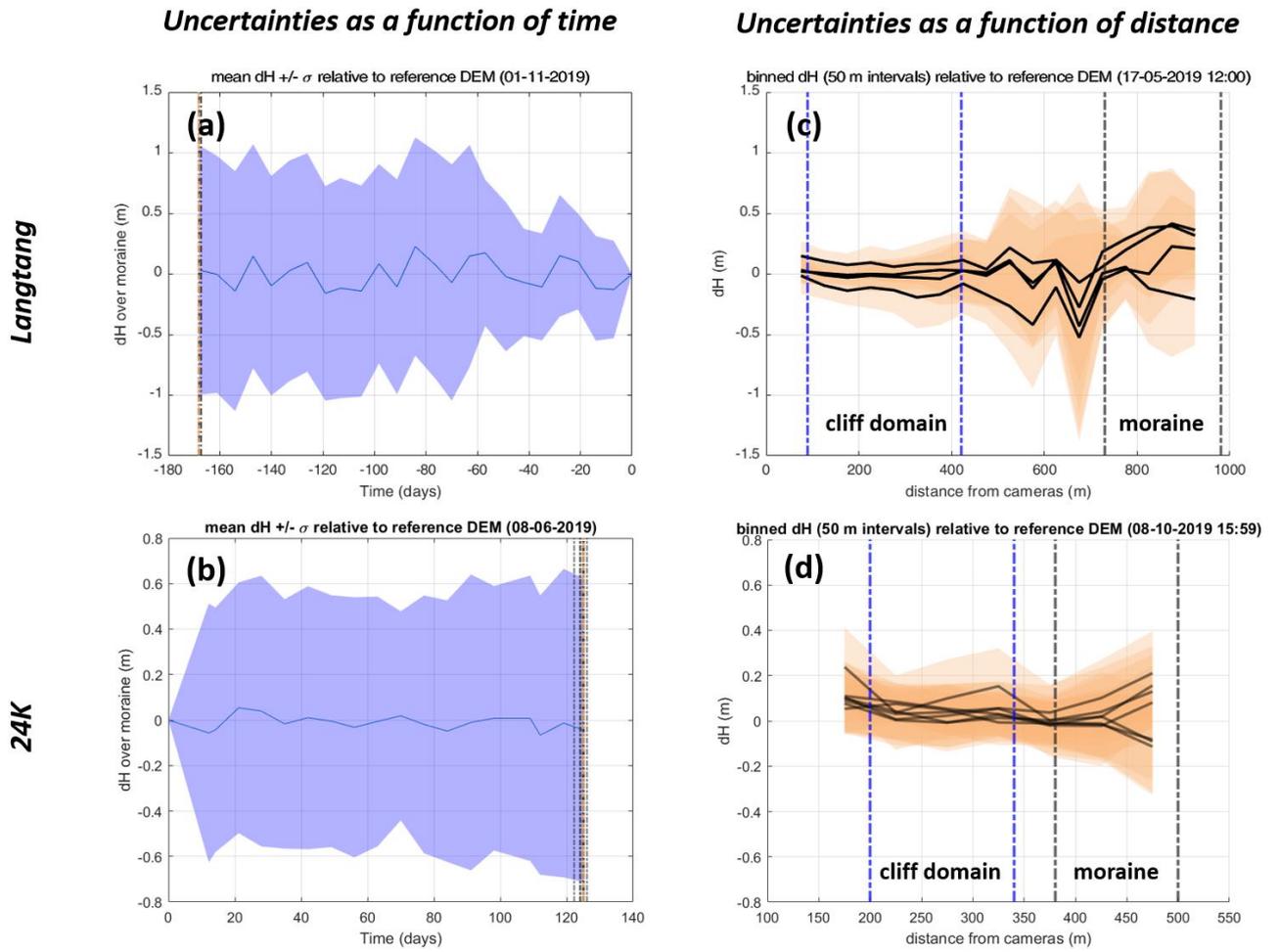
Figure 2.5: *(a-b) dH patterns of all considered time-lapse DEMs relative to the reference DEM assessed over stable terrain as a function of time. The dotted lines indicate the DEMs furthest away in time, considered to test the uncertainty as a function of distance. (c-d) dH patterns relative to the DEM furthest away in time from the reference DEM and four (Langtang) and seven (24K) DEMs less than four days away, as a function of distance.*

Table 2.2: *Uncertainty estimations for Langtang and 24K.*

Glacier	Random DEM uncertainty $\sigma_{DEM,rand}$ (m)	Systematic DEM uncertainty $\sigma_{DEM,sys}$ (m)	Scaling factor f (-)	Flow correction uncertainty σ_{flow} (m/day)	Averaging period dt (days)	Final uncertainty σ_{Melt} (m)	Final uncertainty σ_{Melt} (m/day)
Langtang	1	0.4	2	0.007	21	0.5	0.02
24K	0.6	0.1	1.7	0.004	14	0.4	0.03

2.4.6. Cliff brightness and snow events

For 24K we found the brightness of the cliffs to change substantially with time. We estimated this brightness for each set of images (781 for Langtang, 357 for 24K), by taking the average value of the blue band in a 200 x 100 px domain at the center of Cliff 1 (Langtang) and of the main 24K ice cliff (Fig. 2.S2). We normalized this brightness value by the mean value of the blue band in a domain of the same size over a debris-covered slope with similar slope and aspect characteristics, giving a basic proxy for apparent changes in ice cliff albedo insensitive to illumination differences between scenes. We used the blue band as when comparing the visible spectra of cliffs and debris of different brightnesses, this was the band that highlighted the strongest differences. We took a single brightness value for all cliffs with different slopes and aspects in the domain, as the brightness appeared to evolve in a similar way across all cliffs (Fig. 2.S2).

We additionally looked at the daily influence of snow events on ice cliff melt at both sites. We considered that there was a snow event when 1) the daytime shortwave albedo at the AWS location was higher than 0.3, or 2) when snowfall or fresh snow cover on the glacier could be observed in at least one of the time-lapse images on a given day.

2.4.7. Energy balance model

We compared our tri- to bi-weekly melt patterns with the melt obtained over the same period using a static cliff energy balance model (Buri et al., 2016a). The model calculates the energy inputs from shortwave, longwave and turbulent fluxes in a distributed way across the cliff surface. The static version of the model that we used (Buri et al., 2016a) has been described extensively in the past literature, which we invite the reader to refer to for further details (Buri et al., 2016a; Steiner et al., 2015). We used the exact same parameters as Buri et al. (2016a) at both sites, and did not conduct any further calibration.

The model was run over the exact same periods over which we calculated melt from DEM differencing, without simulating surface geometry changes. We used the static version of the model to focus on the contribution of the different energy-fluxes only, thus removing the influence of the modeled geometry updates. Indeed, the cliff dynamic model was designed to represent changes over long periods (entire melt season or monthly intervals), for which the melt rates are high relative to the model's spatial resolution. Due to the limited data available for the model development, the processes influencing the

cliff dynamics (debris redistribution, additional melt from ponds) were also represented by rather simple parametrizations lumping together distinct physical processes. While this dynamic model is appropriate to estimate bulk changes over long periods (Buri et al., 2021; Buri and Pellicciotti, 2018; Buri et al., 2016b), we considered it to be too simple to represent all the complexity of changes occurring on a weekly time-scale, and therefore less reliable to understand the local energy-balance.

We used the gap-filled time-lapse DEMs as the reference surface over which to calculate the energy-fluxes and the debris-viewing angles and near-field horizon calculations. We filled the gaps using the UAV DEMs corrected with the elevation change signal from the Pléiades (for Langtang) and UAV (for 24K) DEMs. To reduce computation time, the DEMs were resampled to 0.6m. We used the 30m AW3D DEMs (Tadono et al., 2014) of the area for the far-field horizon calculations and did not include debris redistribution or additional melt from the ponds.

We used data from the nearby on-glacier AWSs as meteorological forcing for the ice cliff model, and estimated debris surface temperature, which is an additional model input, from the outgoing longwave radiation at those AWSs. Importantly, we assumed a fixed albedo of 0.15 for debris and 0.2 for ice, which were the same values used in the original studies, calibrated on Lirung Glacier, which is located in the vicinity of Langtang Glacier (Buri et al., 2016a; Steiner et al., 2015).

2.5. Results

2.5.1. General measured and modeled patterns

2.5.1.1. Site-scale melt patterns

Elevation change patterns between the pre- and post-monsoon period from the UAV and Pléiades DEMs alike showed enhanced surface lowering at the location of the ice cliffs (Fig. 6a, b). Elevation change patterns displayed some variability in the non-cliff area of the domain, and this was especially visible with the higher resolution data from 24K (Fig. 6b). Sub-debris melt on 24K, where the debris cover was thinner (Fig 1; McCarthy et al., 2021), also appeared to be higher than on Langtang (Fig. 6b). In both domains, cliff backwasting is evident (Fig. 6a, b), varying from cliff to cliff and site to site, between 0 and 5 cm.day^{-1} on Langtang and 4 and 9 cm.day^{-1} on 24K. There were also signs of cliff expansion (e.g. Cliff 3 on Langtang) and reburial (e.g. 24K main cliff). The mean and standard deviation of the sub-debris melt calculated from the flow-corrected Pléiades and UAV DEMs and for snow- and cliff-free (including a 5 m buffer around the initial and final cliff outlines) zones were -0.3 +/- 0.4 cm.day^{-1} for Langtang and -1.1 +/- 0.5 cm.day^{-1} for 24K, 11-14 (resp. 4.5) times less than the average cliff melt measured from the time-lapse DEMs (Fig. 6).

The high temporal resolution of this dataset enables one to precisely estimate the total and spatially-averaged melt of ice cliffs, while the estimates from the Pléiades and UAV DEMs are usually 5 to 80% off depending on the method used to extract these values (Table S4, S5), due to the mixing of ice cliff and sub-debris melt contributions for less temporally-resolved data.

To disentangle the different components of the ice cliffs' evolution, we focused the analysis of the sub-seasonal patterns on six transects of the three main Langtang cliffs and four transects of the 24K cliff, which kept similar aspect and slope during the whole study period (Fig. 2.6a, b), and were all west to north-east facing. The mean measured and modeled melt were comparable for each of those transects,

with ≤25% difference and no consistent bias, even though there was a higher variability in measured melt (Fig. 2.6c). The observed daily cliff melt was in general higher (3.9-5.1 cm.day^{-1}) for 24K than for Langtang (2.9-4.3 cm.day^{-1}). At the seasonal scale there did not appear to be a control of slope or aspect on melt (Fig. 2.6C, S3).
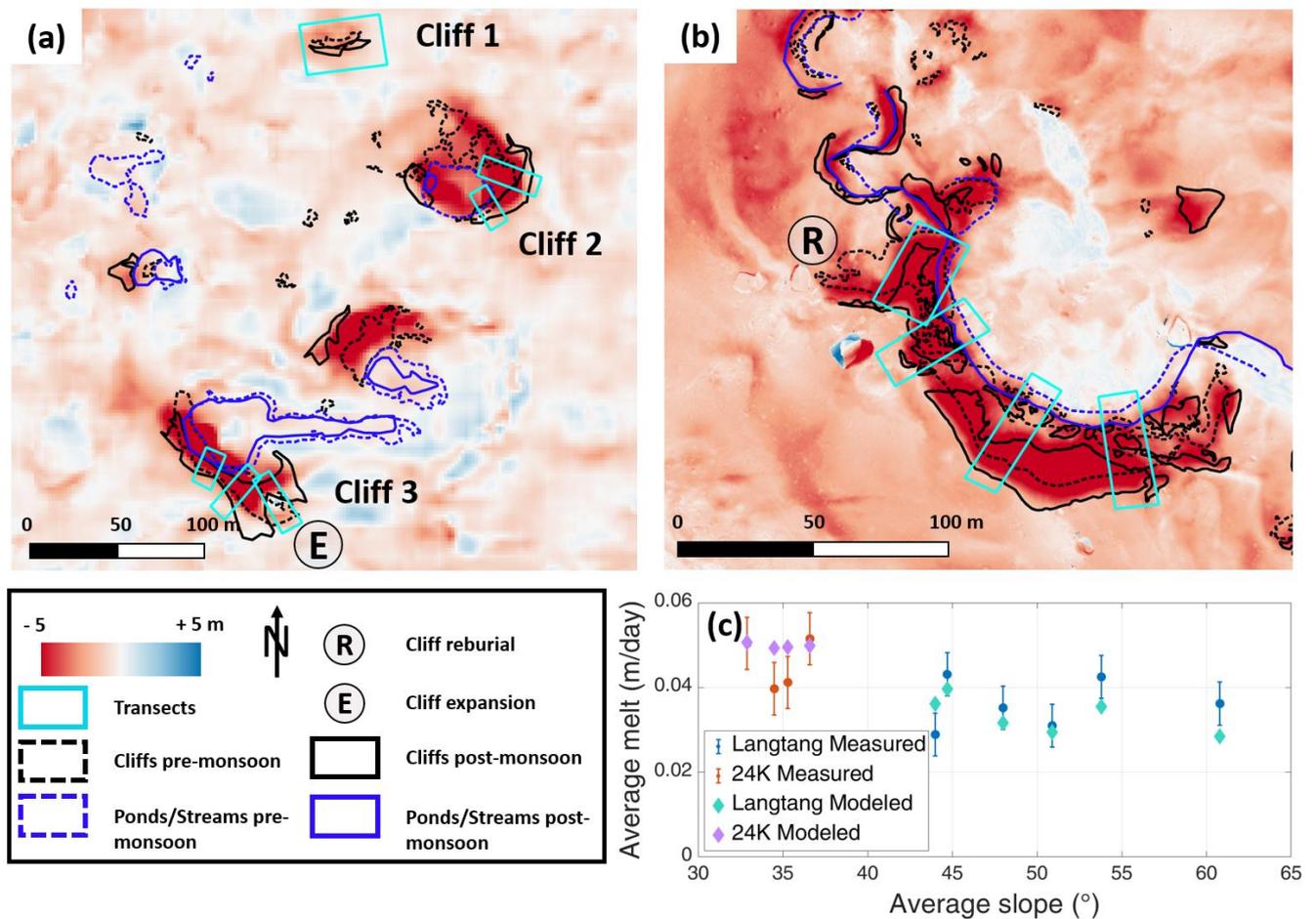
Figure 2.6: (a) Elevation change from the Langtang flow corrected Pléiades DEMs (22/10/2019 - 14/06/2019). (b) Elevation change from the 24K flow corrected UAV DEMs (11/10/2019 - 10/06/2019). (c) Average measured and modeled melt from the time-lapse camera data as a function of the average slope from the time-lapse DEMs over the full study period for all blue transects in (a) and (b). The bars indicate the uncertainty of the measured melt rates.

2.5.1.2. Melt patterns as a function of time

The time-lapse observations at both sites started a few days after the ice cliffs became snow-free, and ended after the first snowfalls. Overall, air temperatures were higher at 24K by 4-5 °C, but this difference was partly compensated by higher incoming shortwave radiation on Langtang (Fig. 2.2 c, d). The incoming longwave radiations were of similar values, and plateaued during the whole monsoon season. Melt patterns at the two sites differed considerably. Melt was higher at the start of the study period (pre-monsoon; 3.4 +/-1.5 cm.day^{-1} for Langtang, 6.7 +/- 2.1 cm.day^{-1} for 24K) than at the end (post-monsoon; 0.7 +/- 1.1 cm.day^{-1} for Langtang, 1.1 +/- 1.0 cm.day^{-1} for 24K) (Fig. 2. 7), and exhibited similar variability over the study period at both sites (coefficient of variation of 0.37 for Langtang Cliff 3, and 0.34 for the 24K cliff). The peak in melt was reached in the last week of June and

first week of July on Langtang (6.4 +/- 1.9 cm.day^{-1}) and around mid-August on 24K (7.3 +/- 1.8 cm.day^{-1}). This peak in melt on Langtang corresponded with the timing of the peak in air temperature, but while air temperature stabilized between early July and early September, melt started to decrease from early July, coinciding with the decrease in incoming shortwave radiation and increase in longwave radiation at the start of the monsoon period (Fig. 2.7c). The peak in melt at 24K also corresponded to the maximum air temperature, but similar to Langtang, the incoming shortwave radiation had a direct influence on this melt pattern (Fig. 2.7d). The observed melt behaviors were well represented by the modeled melt but with slightly smaller amplitudes.
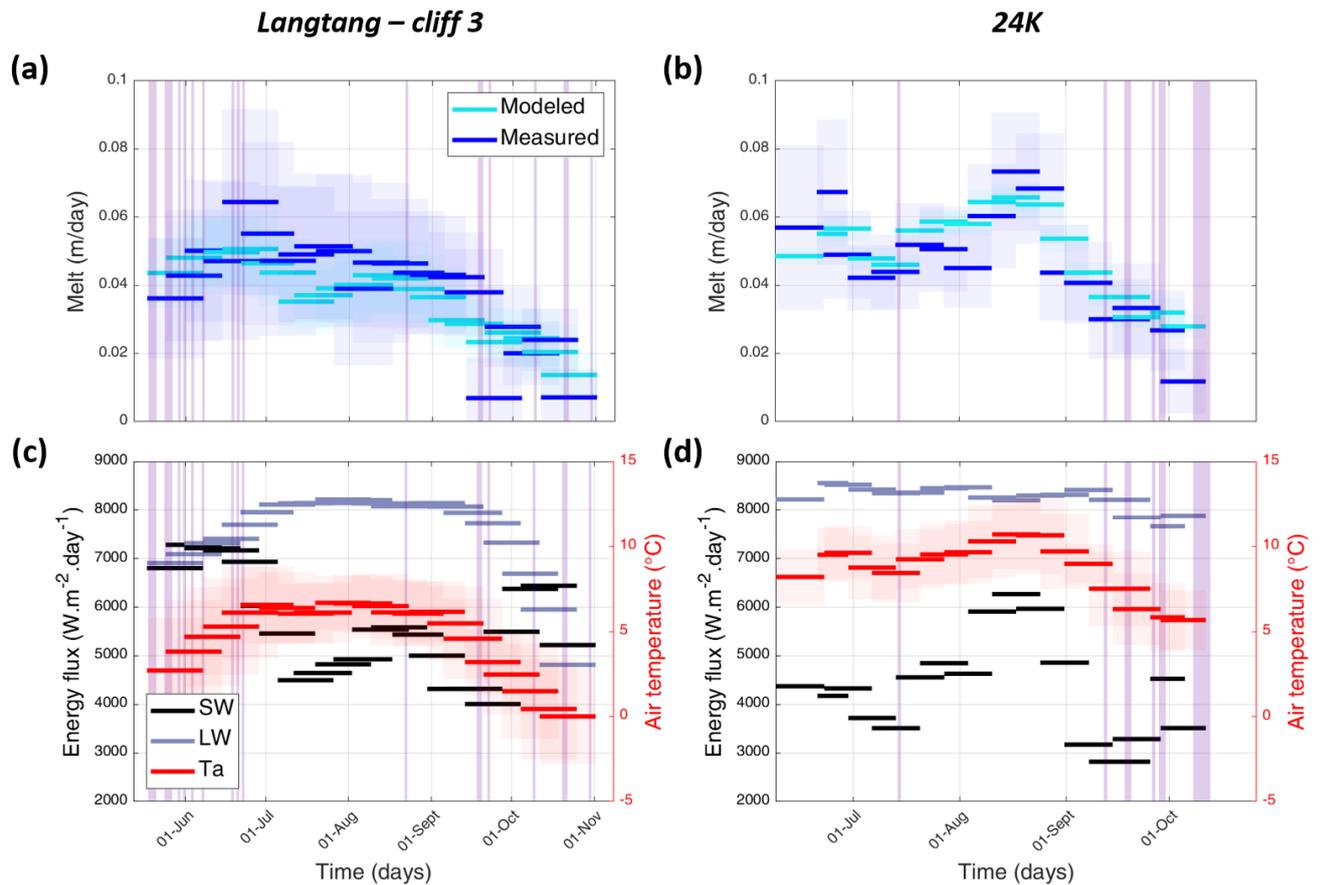
Figure 2.7: *Observed sub-seasonal measured and modeled melt patterns of Cliff 3 on Langtang (a) and of the 24K cliff (b). The lines show the spatially-averaged cliff melt over the different periods and the shaded areas represent the standard deviation. (c-d) Average daily incoming shortwave and longwave radiations and mean and standard deviation of air temperature over the same time periods at the AWS locations. The purple bars show the days with snow events.*

2.5.2. Processes occurring at each cliff

For the detailed analysis of the melt patterns of Langtang Cliffs 2 and 3 and the 24K cliff, we used transects perpendicular to the cliff outlines to derive average values across different vertical sections of the cliffs (Fig. 10-14).

Langtang Cliff 1 was a relatively small (5-10 m tall, 30-40 m wide) north-facing cliff (Fig. 8, 9). In July, it expanded a few meters to the east, resulting in enhanced melt rates at this location, but the new section got re-buried relatively quickly in August. Indeed, the small cavity at the base of the cliff (visible at the start of the study period, Fig. 8a) increased in size as the cliff backwasted, debris falling from the top of the cliff accumulated in the cavity slowly reburying this section of the cliff, which by the end of the period had become very shallow (Fig. 8f). The measured melt displayed a similar signal to that of Langtang Cliff 3 (Fig. 7a, 8f) and was relatively homogeneous across the cliff surface, except for higher values at the location of the cliff expansion (Fig. 8h). The large boulder standing on top of the cliff did not seem to influence the melt (Fig. 8d-f). The modeled fluxes showed a strong contribution of shortwave radiation to the cliff energy balance, with an increase in the contribution of net turbulent fluxes from 9 to 36% between the end of May and mid-July when the net shortwave decreased by 38% with the arrival of the monsoon (Fig. 9d). The net longwave radiation contributed negatively to the cliff's energy balance.
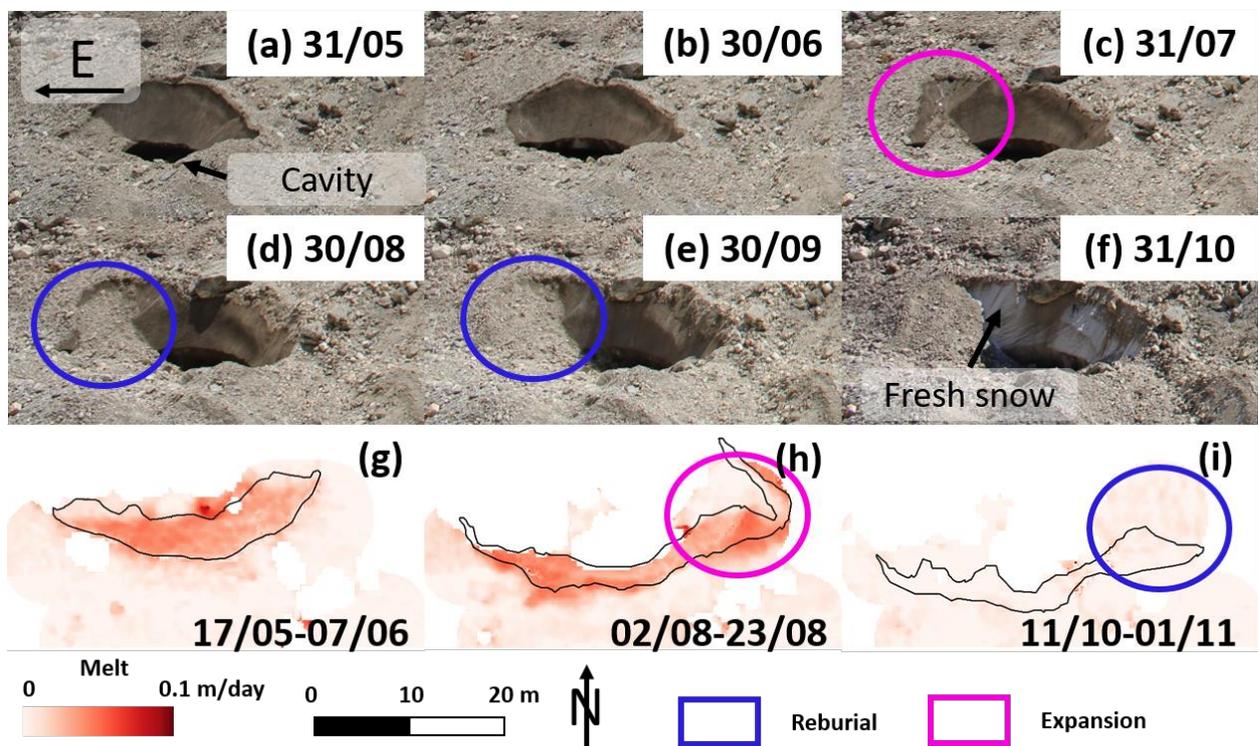
Figure 2.8: *(a-f) Evolution of Langtang Cliff 1 throughout the study period from the time-lapse camera images. The pictures were all taken at the same time of day (11:45). The black horizontal arrow in (a) indicates east. (g-i) Tri-weekly observed melt patterns at the start, in the middle and at the end of the study period. Cliff outlines corresponding to the start of the period are shown in black.*
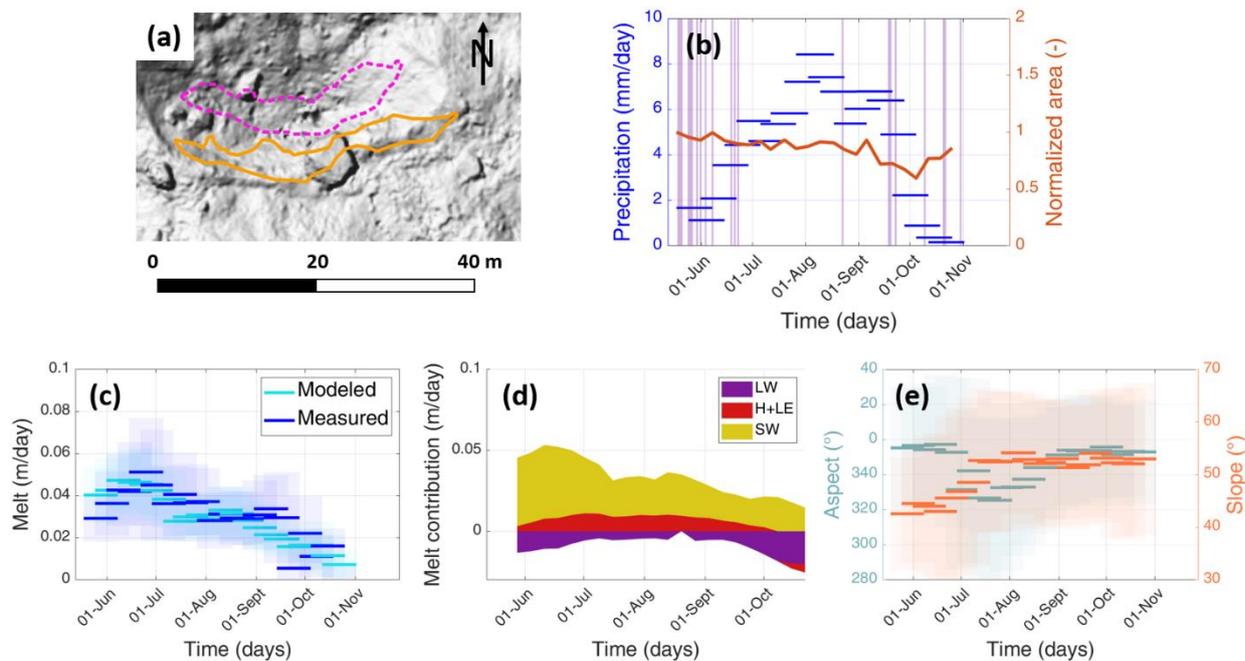
Figure 2.9: *(a) Langtang Cliff 1 at the start (pink dashed lines) and the end (orange full lines) of the study period. Background is the hillshade of the 02/11/2019 UAV DEM. (b) Average precipitation over each time-lapse period and cliff planimetric area evolution normalized by the initial cliff area. The purple shaded areas correspond to days with snow events. (c) Observed and modeled melt as a function of time. The lines show the average value over the different periods and the shaded areas the standard deviation. (d) Modeled net energy fluxes represented by the central value of each period. (e) Measured slope and aspect as a function of time.*

2.5.2.2. Langtang Cliff 2

Langtang Cliff 2 was a medium size (10-20 m tall, 35-45 m wide) west-facing cliff that was attached to a pond at the start of the study period (Fig. 2.10, 2.11) and displayed higher melt rates than at Cliff 1. The time-lapse images showed that the pond partly drained between 02/07 and 05/07. This was confirmed by the pond surface temperature data (Fig. 2.11c), which showed much stronger temperature variations after the end of June, proof that the sensor had become grounded on the debris. The vertical step left by the pond at the cliff base after draining got progressively reburied and had disappeared by mid-August (Fig. 2.10c, d). The cliff had a concave shape at the start of the study period, being steeper at the top than at the bottom. End of June, **triggered by the cliff backwasting, part of the debris-covered slope above the cliff slumped, thus expanding the cliff upwards, at a lower angle** (Fig. 2.10, 2.S6). This upper debris-free area expanded laterally in July, enhancing the **sharp transition between the lower steeper portion that was progressively reburied after the drainage of the pond, and the upper shallower portion of the cliff that became predominant with time**. This reburial of the lower steeper section and expansion of the upper shallower section led to the cliff doubling in size in July and then returning to its initial size by early September.

In parallel, melt increased from 3.0 +/- 0.7 (3.2 +/- 1.0) cm.day⁻¹ at the end of May to more than double - 6.8 +/- 1.7 (6.5 +/- 0.8) cm.day⁻¹ - at the end of July for transect 1 (transect 2). These values were substantially higher than the melt predicted by the energy balance model and mostly due to the higher measured melt on the upper, shallower section of the cliff (Fig. S5). However, for both

transects there was a sharp reduction in melt synchronous with the progressive reburial of the cliff (Fig. 11). Melt then plateaued around 2.7 +/- 2.7 cm.day^{-1} for transect 1 and 3.3 +/- 1.3 cm.day^{-1} for transect 2 and finally decreased to almost null values in October.
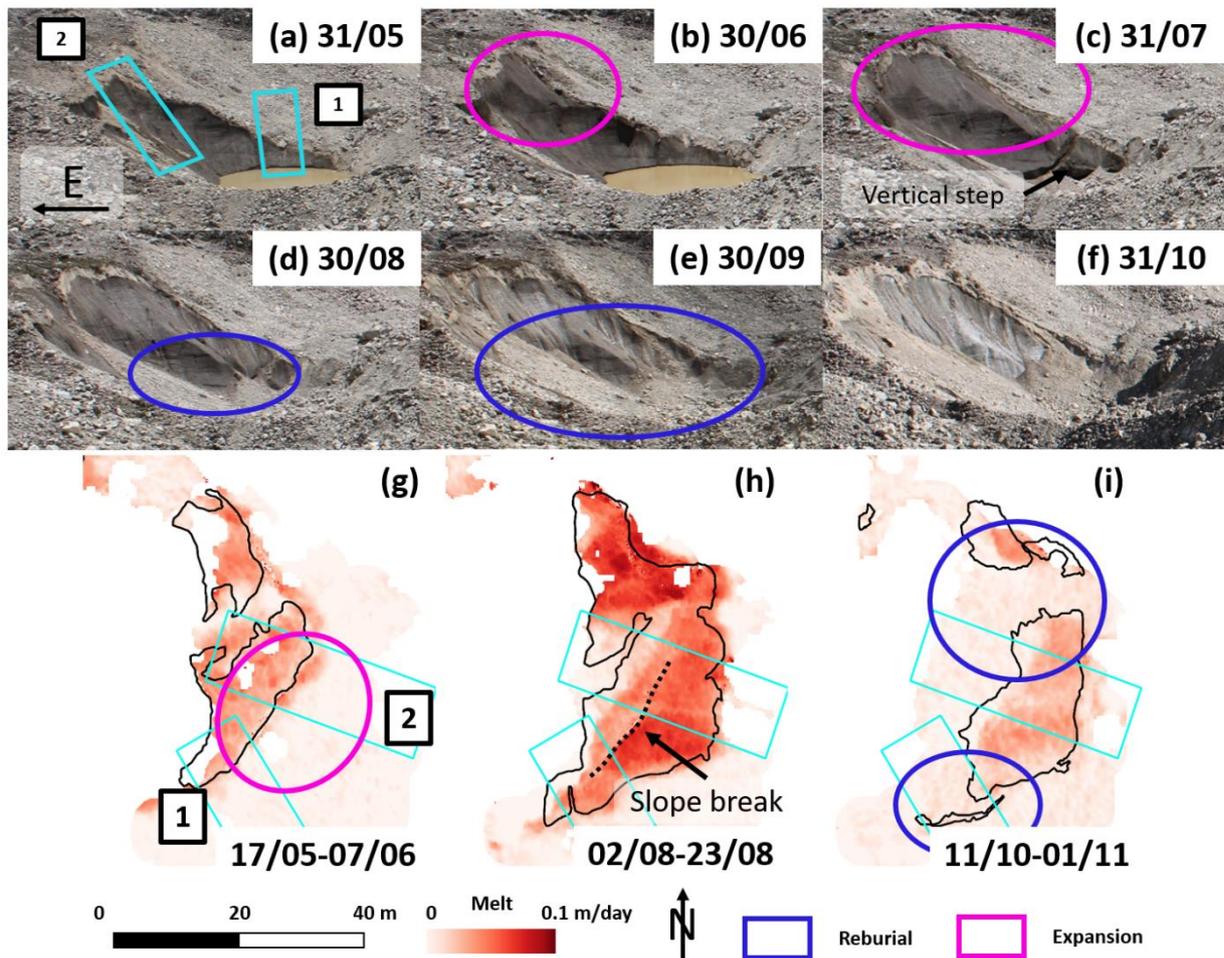
Figure 2.10: (a-f) Evolution of Langtang Cliff 2 throughout the study period from the time-lapse camera images. The pictures were all taken at the same time of day (11:45). The black horizontal arrow in (a) indicates east. (g-i) Tri-weekly observed melt patterns at the start, in the middle and at the end of the study period. Cliff outlines corresponding to the start of the period are shown in black and the focus transects in light blue.
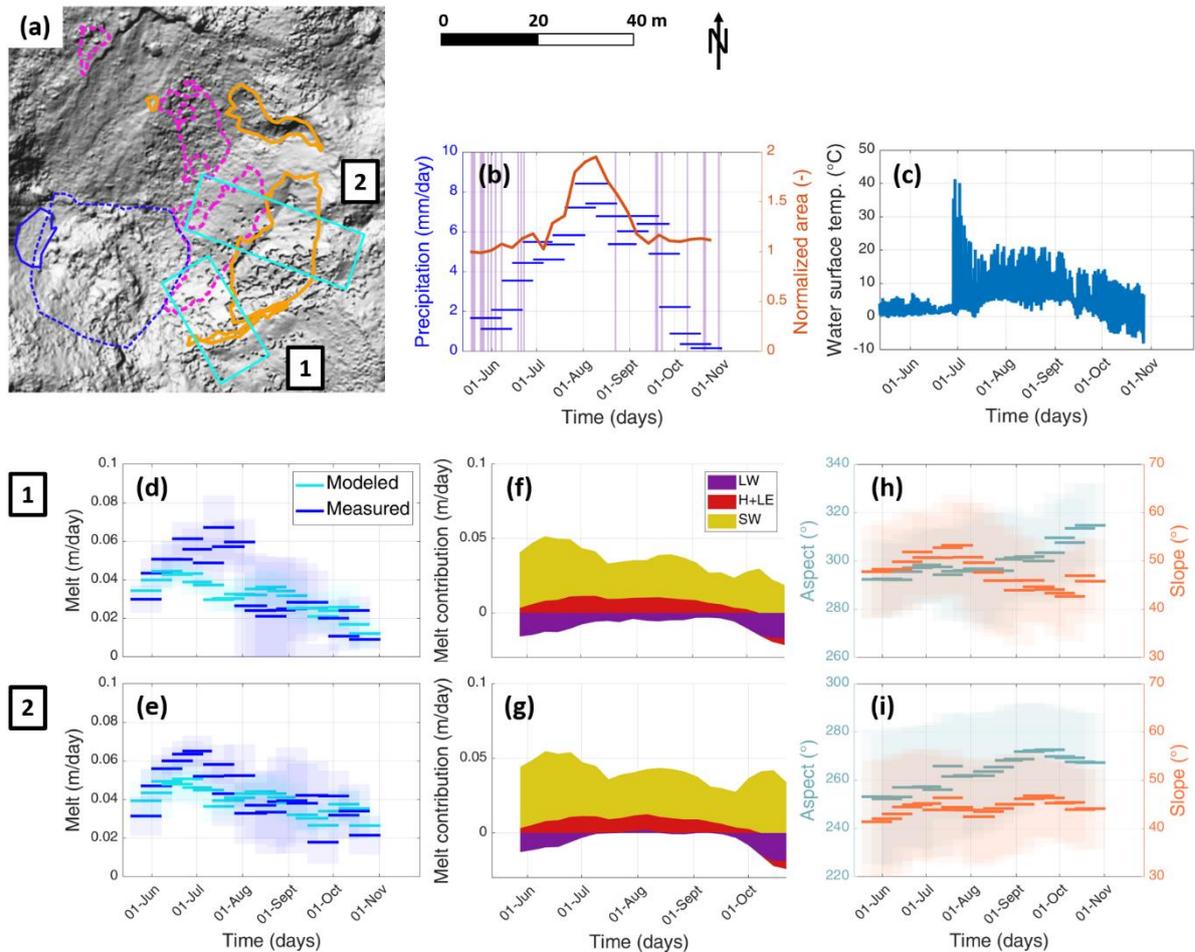
Figure 2.11: *(a) Langtang Cliff 2 at the start (pink dashed lines) and the end (orange full lines) of the study period. Background is the hillshade of the 02/11/2019 UAV DEM. The light blue rectangles are the cliffs' two main study transects. (b) Average precipitation over each time-lapse period and cliff planimetric area evolution normalized by the initial cliff area. The purple shaded areas correspond to days with snow events. (c) Pond surface temperature. (d-i) For each transect, the measured and modeled melt (d-e), modeled net energy fluxes represented by the central value of each period (f-g), and measured slope and aspect (h-i) as a function of time.*

2.5.2.3.   Langtang Cliff 3

Cliff 3 was a relatively large cliff (20-30 m tall, 70-100 m wide) which was predominantly north-east facing at the start of the period but expanded to north-facing slopes during the study period (Fig. 12). There was a large pond at the base of the cliff for the whole study period, which persisted throughout the season but also slowly drained by a total of 1.7 m (Fig. 13c), leaving a notch at the base (Fig. 12a-f). Most of the drainage occurred in July. The north-facing debris-covered slope to the east of the cliff steepened in June and July and started slumping at the end of July, when the notch appeared under the debris, revealing that the pond had also been undercutting this slope. The slumping accelerated and the slope was mostly debris-free by the end of August, leading to a doubling of the cliff area between the end of July and the end of September (Fig. 13b). Despite a decrease in shortwave radiation at the end of August for transect 1, melt increased in August synchronously with a reduction in slope linked

60

with the slumping of the north-facing slope (Fig. S8). Most of the backwasting occurred at the shallower section of the cliff that was disconnected from the pond until the end of July, while the steeper (50-65°) section of the cliff in contact with the pond displayed lower backwasting rates.
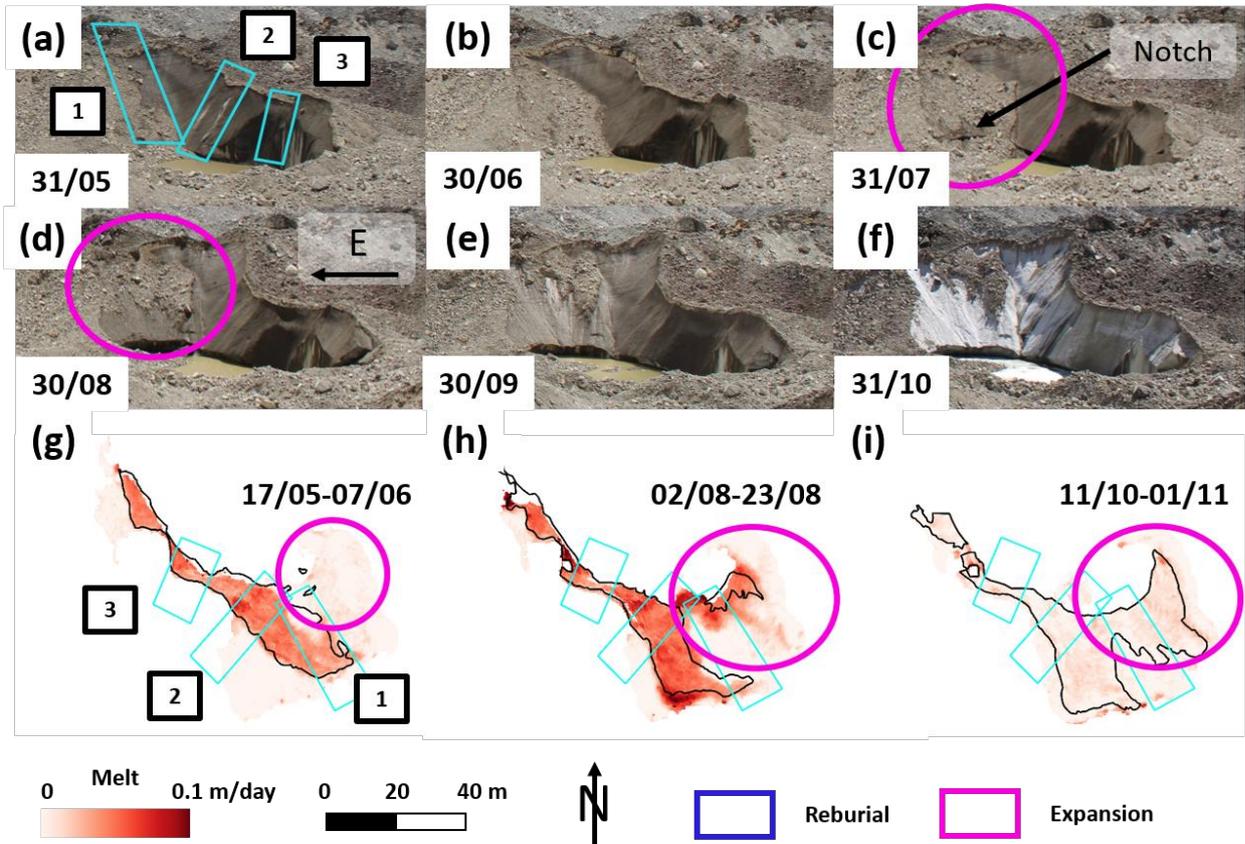
Figure 2.12: *(a-f) Evolution of Langtang Cliff 3 throughout the study period from the time-lapse camera images. The pictures were all taken at the same time of day (11:45). The black horizontal arrow in (d) indicates east. (g-i) Tri-weekly observed melt patterns at the start, in the middle and at the end of the study period. Cliff outlines corresponding to the start of the period are shown in black and the focus transects in light blue.*
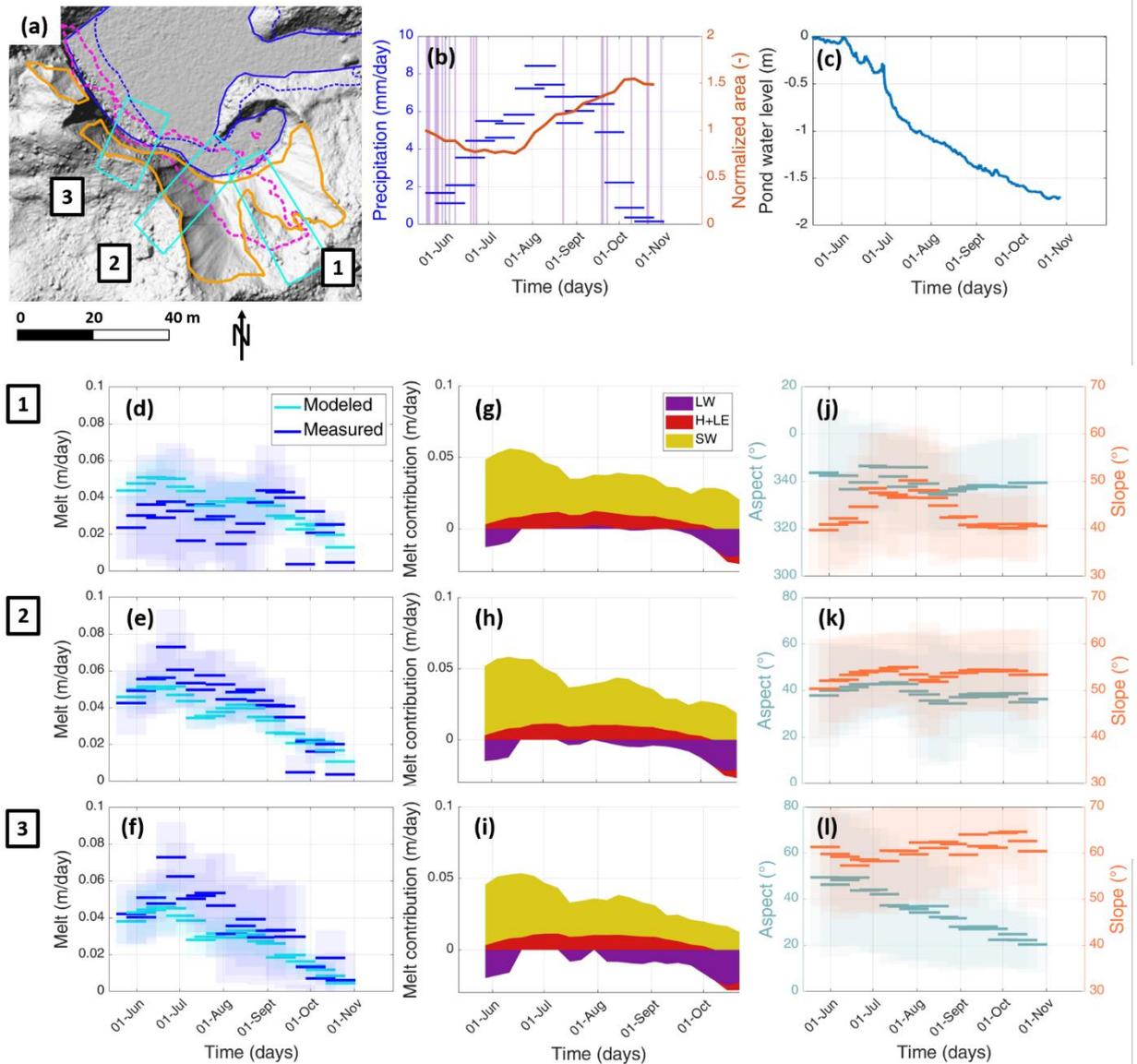
Figure 2.13: *(a) Langtang Cliff 3 at the start (pink dashed lines) and the end (orange full lines) of the study period. Background is the hillshade of the 02/11/2019 UAV DEM. The light blue rectangles are the cliffs' three main study transects. (b) Average precipitation over each time-lapse period and cliff planimetric area evolution normalized by the initial cliff area. The purple shaded areas correspond to days with snow events. (c) Pond water level. (d-l) For each transect, the measured and modeled melt (d-f), modeled net energy fluxes represented by the central value of each period (g-i), and measured slope and aspect (j-l) as a function of time.*

2.5.2.4. 24K Cliff

On 24K we focused on a set of linked cliffs at the center of the survey domain, 130 m wide and 10-20 m tall (Fig. 2.14, 15). These cliffs, which could also be regarded as one single cliff split by patches of thin debris, **occupied the slopes of the outer bend of a supraglacial stream, which was flowing directly at the base of the ice cliffs**, sometimes undercutting the ice slopes. The center of the bend was steeper and was occupied by a large continuous cliff, while the sides displayed a **changing combination of debris patches and bare ice** (Fig. 2.14). This configuration remained throughout the study period

62

except on the west side of the meander (transect 1), where the **stream disconnected from the ice cliff during the study period** (Fig. 2.15a), **causing a progressive reburial of this outer section in July and August** (Fig. 2.14). This was just a small portion of the cliff and overall the cliff area did not change by more than 10% over the whole study period, and the aspect and slope of the different transects remained consistent (Fig. 2.S10).

The different transects displayed comparable temporal melt and energy balance patterns (Fig. 2.7), with an increase from June to the mid-August peak followed by a steeper decrease until the end of the study period in early October, characterized by close to zero melt values and regular snow falls (Fig. 2.7b). The melt variability was driven by net shortwave radiation, which also represented more than 50% of the energy budget during the whole study period. Contrary to Langtang, the net longwave contributed positively to the cliff energy balance due to higher air temperatures and therefore higher incoming longwave from the atmosphere (Fig. 2.7). Transects 1, 3 and 4 displayed high (7-8 cm.day^{-1}) melt values at the very start of the study period, which were not represented by the energy balance model. **These high values exceeding modeled melt at the start and at peak melt, as well as the general patterns throughout the season also followed an inverse pattern with cliff brightness** (Fig. 2.15c), **which was itself correlated with precipitation** (Fig. 2.15b). **Transects 2 and 4 were the ones where measured and modeled melt disagreed the most** (up to 25% difference), with generally lower measured melt rates than predicted by the model, and **also the ones with the most patchy debris**, where outlining the cliff extents was particularly difficult.
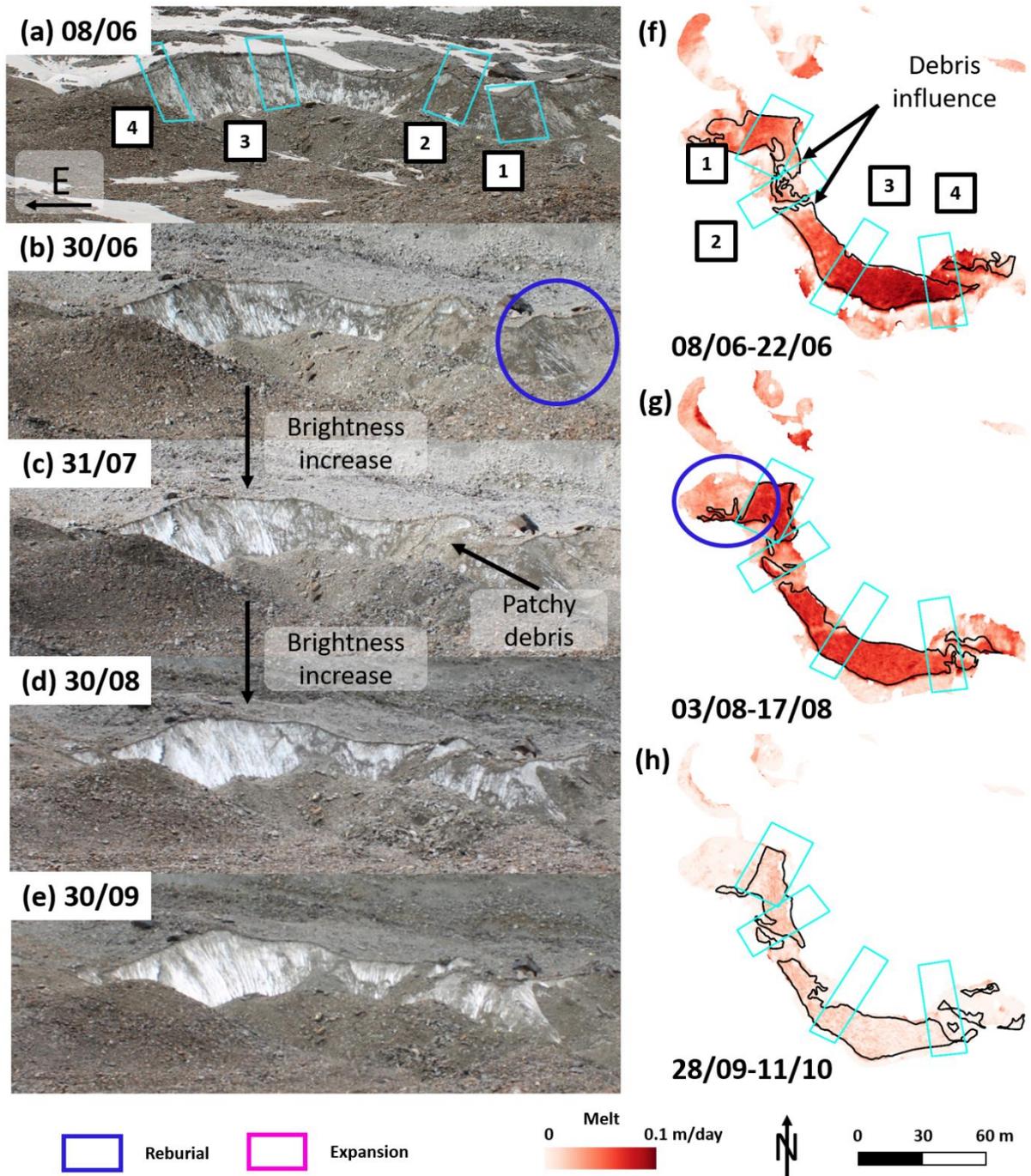
Figure 2.14: (a-e) Evolution of the 24K cliff throughout the study period from the time-lapse camera images. The pictures were all taken at the same time of day (10:00). The black horizontal arrow in (a) indicates east. (f-h) Bi-weekly observed melt patterns at the start, in the middle and at the end of the study period. Cliff outlines corresponding to the start of the period are shown in black and the focus transects in light blue.
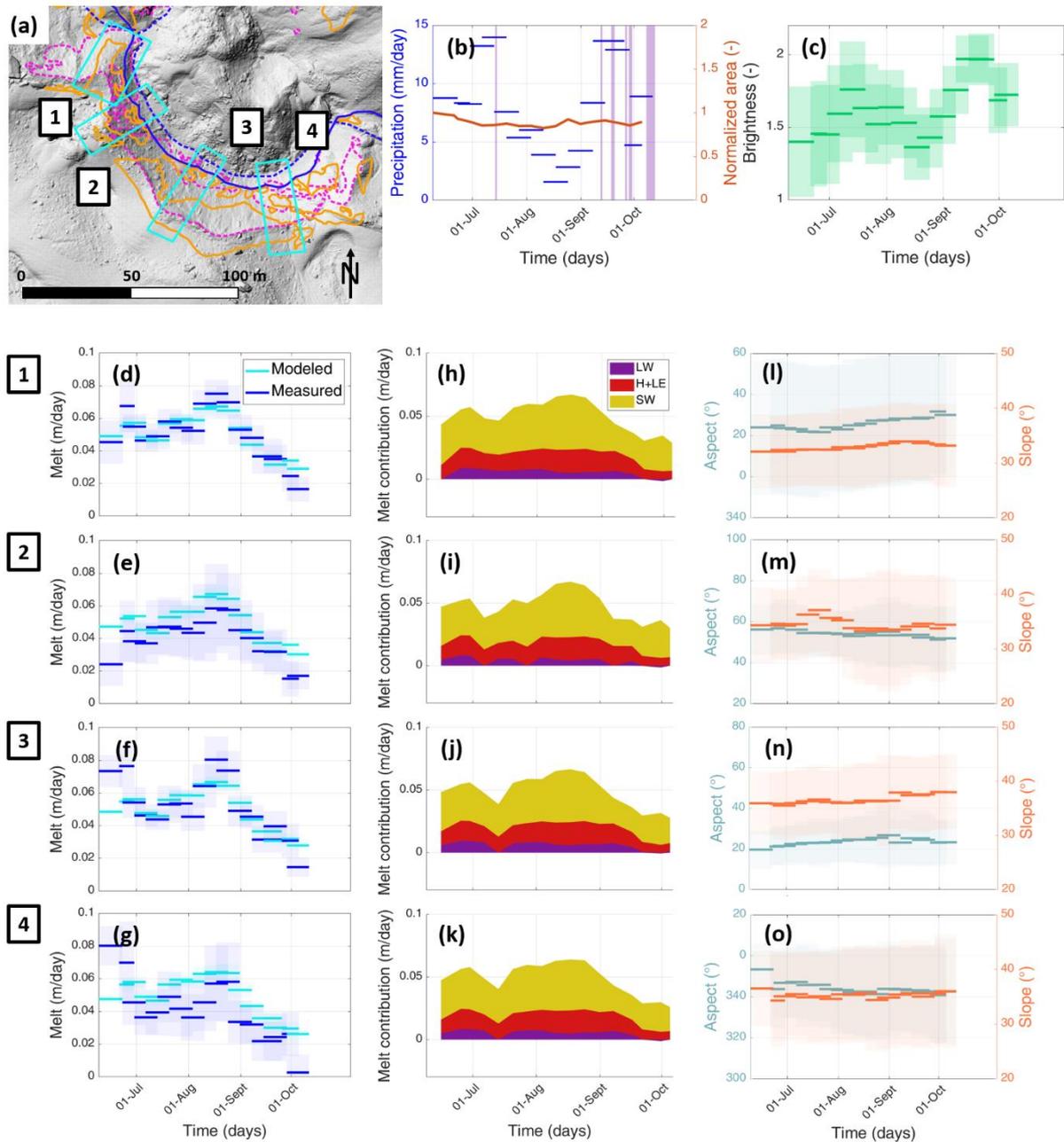
Figure 2.15: *(a) 24K cliff at the start (dashed lines) and the end (full lines) of the study period. Background is the hillshade of the 11/10/2019 UAV DEM. The light blue rectangles are the cliffs' four main study transects on which we focus. (b) Average precipitation over each time-lapse period and cliff planimetric area evolution, normalized by the initial cliff area. The purple shaded areas correspond to days with snow events. (c) Cliff brightness. (d-o) For each transect, observed and modeled melt (d-g), modeled net energy fluxes (h-k) and measured slope and aspect (l-o) as a function of time during the full study period.*

2.6. Discussion

The sub-seasonal observations of ice cliff melt, evolution and the underlying processes were made possible thanks to the use of time-lapse photogrammetry, which enabled the semi-automated production of weekly DEMs of the survey area with an estimated uncertainty of +/- 20 cm (+/- 6 cm) for Langtang

(24K). This is a novel approach, the advantages and drawbacks of which we discuss in detail in the supplementary Section 2.13.11 (Use of time-lapse photogrammetry approach). Here we discuss instead the main findings that the new setup allowed, in terms of understanding cliff melt rates and contribution to mass losses (Section 2.8.1), as well as the processes that control their evolution and are not yet included in current models (Section 2.8.2). The different mechanisms outlined here are indicated in Figure 16, which represents one possible evolution pathway for a set of idealized cliffs.

2.6.1. Controls on ice cliff melt variability

The studied cliffs displayed melt rates at 4.5 times higher than the surrounding debris-covered ice on 24K and 6-38 times higher on Langtang, where thick debris (>0.5 m) in the lower portion of the glacier prevents almost any sub-debris melt (McCarthy et al., 2021; Miles et al., 2021), thus promoting the melt-generating role of cliffs. While the cliff melt values are comparable to previous estimates for other debris-covered glaciers based on cliff volume loss and backwasting rates (e.g. Sakai et al., 1998; Juen et al., 2014; Brun et al., 2016; Mishra et al., 2021), the high temporal resolution estimates are more accurate, as they allow calculations of melt over strongly varying cliff geometries. Changes in cliff melt rates over time from the time-lapse DEMs ranged between 0 and 8 cm.day^{-1}, and captured the progressive changes in cliff area and shape (Fig. 2.8-15), thus enabling a new, more precise estimate of cliff melt compared to the values extracted from the beginning and end of season DEMs (Pléiades and UAV DEMs) (Table 2.S4). This is the first time that the sub-seasonal variability of ice cliff melt has been quantified, and it shows that use of only beginning and end of season cliffs' geometries, neglecting the history of area and geometry changes over a melt season, can lead to an underestimation of about 50% in melt rates (Table 2.S4).

Exchange of energy with the atmosphere controlled cliffs' evolution at both sites. Cliff melt rates varied substantially over the melt season and displayed similar patterns for all cliffs, with an overall trend of increase, peaking and then decline, on which a smaller-order variability was superimposed, controlled by snow and liquid precipitation. Cliff melt variability was driven by the combination of short- and longwave radiation, and turbulent fluxes which contributed considerably during the monsoon on Langtang, when incoming shortwave was reduced (Buri et al., 2016a). Differences in air temperature at the two sites led to a general negative net longwave radiative flux on Langtang and positive on 24K. This demonstrates the need to account for the whole energy balance to estimate cliff melt.

The ice cliffs of the two study sites were generally north-facing and received little direct illumination during the study period. As a result, the aspect controls on ice cliff evolution described in previous studies (Buri and Pellicciotti, 2018; Sakai et al., 1998) were not evident when analyzing the ice cliff patterns (Fig. 2.S3), and contrary to previous observations and model tests, no evidence of melt gradient was visible at the cliff surface (Fig. 2.S4, 5, 7, 9; Buri et al., 2016a; Watson et al., 2017b).

At both sites, the measured melt was more spatially variable than predicted by the model (Fig. 2.S4, 5, 7, 9), which used a constant albedo and therefore was not able to account for the influence of debris on the cliff energy-balance (Table 2.2). Two effects were visible:

- **Melt reduction from patchy debris**: 40-80% lower measured melt values evident at the foot of the Langtang Cliffs 2 and 3 (Fig. 2.10, 2.12, 2.S5 d-f, S7 a-c) were likely caused by the active reburial of these sections of the cliffs during shorter time intervals than the 2-3 week period over which melt was integrated. This influence of debris was also visible on the 24K cliff where the two transects which had the higher proportion of 'dirty' ice, and where it was

most difficult to outline the ice cliff relative to the patchy debris, experienced reduced melt. At this location, the debris on the ice cliff was thick enough to reduce melt (Fig. 2.14-15, S9). This melt reduction effect generally accounted for 1-3 cm.day^{-1} relative to the locations on the cliffs that remained debris-free.

- **Melt enhancement from thin dust layers**: The 10-60% higher melt values on the upper and shallower cliff slopes that had recently become free of debris of Langtang Cliffs 2-3 (Fig. 2.S5 d-f, S7 a-f) were likely caused by lower albedo values due a higher concentration of dust particles at the surface (Fyffe et al., 2020a). Similarly, transect 3 of the 24K cliff was affected by small debris clasts and thin debris (Fig. 2.14), but these did not reduce melt and more likely led to higher melt rates due to lower albedo values.

This effect of thin debris dust on albedo was particularly visible on 24K, where cliff brightness, which we considered as a proxy for albedo, followed an inverse pattern to that of cliff melt, and was therefore likely responsible for some of the observed differences between the measured and modeled melt. Indeed, a sensitivity test conducted for transect 3 on 24K showed that a 0.1 change in cliff albedo led to a 5-10% change in melt (Fig. 2.S11). Lower albedo values from this surface dust, unaccounted for in the model, could therefore partly explain measured melt rates 20-40% higher than predicted by the model at the start of the study period and at peak melt on 24K. Interestingly, for the 24K cliff, changes to cliff brightness seemed to be controlled by liquid precipitation, which promoted the 'washing' of the small debris clasts that accumulated at the surface of the cliffs, thereby removing the thin surface dust layer and increasing the albedo (Fig. 2.14, Fyffe et al., 2020). This effect was not visible on the darker, steeper and drier cliffs of Langtang, but for glaciers like 24K it could lead to a decrease in cliff melt with the increase in occurrence of wet precipitation events at high elevation (Jouberton et al., 2022).

On the contrary, snow events at both sites in the pre- and post-monsoon periods likely reduced melt at the cliff surface. Indeed, while the snow on the debris surface usually melted away within hours after the snowfall, these north-facing steep ice slopes had the tendency to retain the snow much longer (Fig. 2.8f), and up to a full day on Langtang, thereby increasing the cliff albedo and interrupting ice melt until all the snow had melted. Such effects were also not represented in the model.

Table 2.3: *Behaviours of the different cliffs studied and their controlling factors.*

Cliff	Behavior	Controlling factors	
		From surrounding topography	**At the surface of the cliff**
Langtang Cliff 1	Expansion followed by reburial	Cavity at the cliff base	
Langtang Cliff 2	• Expansion followed by reburial • Heterogeneous melt patterns	• Draining pond at the cliff base • Cliff backwasting and propagation to upper slopes	• Deposition of dust (low angle sections) • Patchy debris
Langtang Cliff 3	• Expansion • Heterogeneous melt patterns	Pond incision	• Deposition of dust (low angle sections) • Patchy debris

24K cliff	• Central portion maintained • Partial reburial at the edge • Heterogeneous melt patterns	Stream incision		• Deposition of dust and patchy debris (low angle sections) • Cliff 'washing' effect

2.6.2. Controls on ice cliff area variability

One of the main results of this work was that debris local dynamics are a key influence on cliffs evolution. Debris accumulating at the surface of the cliffs influenced melt, reducing it when enough patches of debris clasts had accumulated at the surface but also darkening the cliff, therefore reducing its albedo. Debris also had an influence on cliff area and slope (Table 2.2, Fig. 2.16). Debris is constantly moving on the debris-covered surface and this motion is enhanced by slope, liquid precipitation, moisture content but also debris evacuation at the base of a slope (Fyffe et al., 2020a; Moore, 2018; Nicholson et al., 2018; Westoby et al., 2020). Additional debris redistribution during the wet monsoon season has even been hypothesized to increase the cliff relative area at the glacier scale (Steiner et al., 2019). While our dataset did not encompass enough cliffs to test this hypothesis, we observed considerable debris motion and areal changes at all the studied cliffs (Fig. 2.11b, 13b, Table 2.2). The planimetric area of the 24K cliff and the Langtang Cliff 1 did not change by more than 20% during the study period despite evidence of cliff lateral expansion and reburial, but Langtang Cliffs 2 and 3 experienced dramatic expansion and reburial, leading to doubling in size of Cliff 2 within the course of a month and a reduction to its initial size one month later (Fig. 2.11b, Table 2.3). Langtang Cliff 3 also underwent a 100% areal increase in 2 months (Fig. 2.13b). These changes demonstrate the strong temporal variability of ice cliffs at the sub/seasonal scale, which underlines the interannual dynamics of ice cliff population at the glacier scale (M. Kneib et al., 2021; Steiner et al., 2019). Ultimately, not accounting for these geometry changes results in 5 to 80% discrepancies in terms of total and area-weighted cliff melt (Table 2.S4, 2.S5), which has important consequences for the estimation of cliff contribution at the glacier scale, in case the overall cliff area would consistently increase or decrease.

Debris evacuation at the base of the slope was the main controlling factor of all the cliff area change events. For Langtang Cliffs 2 and 3, the presence of a pond and its undercutting of the cliff base, led to the instability of shallow debris-covered slopes in the vicinity of the cliff, which sustained debris evacuation from the lower portion of the cliff. On the contrary, when the pond drained at the base of Cliff 2, and thermo-erosional melt and instability of the cliff base ceased, this led to rapid reburial of the lower portion of the cliff. The same events were visible at Cliff 1 where a cavity at the cliff base led to debris evacuation, while its absence prevented any lateral cliff expansion. For the 24K cliff, partial cliff reburial was triggered by the disconnection of the supraglacial stream from the base of the cliff, which effectively 'switched off' this sediment evacuation pathway. For the remainder of the cliff, a connection between the cliff and the stream served to maintain and sometimes steepen the slope. Undercuts at the base of ice cliffs are indeed common even without the presence of a pond (Kraaijenbrink et al., 2016b; Miles et al., 2016; Röhl, 2006; Watson et al., 2017b), and streams and

crevassing have been shown to promote ice cliff development by serving as mechanism for the removal of debris at their base (Mishra et al., 2021; Mölg et al., 2020; Westoby et al., 2020).
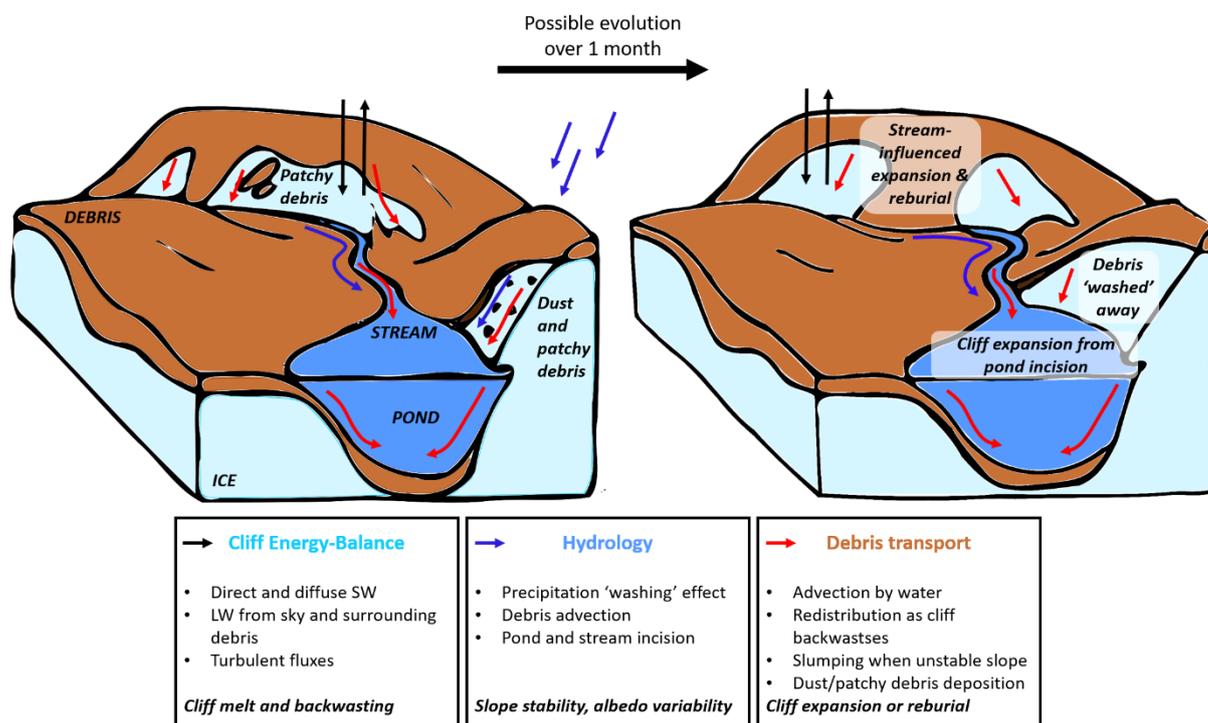
Figure 2.16: *Interactions between cliff energy balance, hydrology and debris transport at the surface of a debris-covered glacier highlighted by the time-lapse observations.*

2.6.3. Avenues for future research

Despite the small number of cliffs covered, their similarity in aspect and the relatively short duration of the observations (one melt season), this study has highlighted the variability in ice cliff characteristics and behaviors. It has also confirmed the robustness of the Buri et al. (2016a) ice cliff energy balance model to derive cliff melt estimates for a given slope and aspect over a period of 2-3 weeks. The model, which was mostly developed and evaluated using data obtained from the Langtang catchment (Steiner et al., 2015; Buri et al., 2016a), performed well when applied to 24K, a glacier located in a very different climatic setting (Fugger et al., 2022). We could also show that using a fully static version of the model generally resulted in better melt estimates than when deriving these from pre- and post-monsoon flow corrected Pléiades or UAV DEMs (Table 2.S4, 2.S5). This confirmed the suitability of the model to explore the melt contribution of ice cliffs at the large scale. However, beyond a period of one month, the variability in cliff area may lead to considerable changes in cliff extents, aspect and slope, and thus a need to better account for these aspects of cliff evolution in the model, even in a simplistic way (Table 2.S5, Buri et al., 2016b, 2021). With the growing availability of high-quality multi-temporal observations of debris-covered glacier surfaces (Westoby et al., 2020; Sato et al., 2021), including from time-lapse photogrammetry, future model developments in this direction should attempt to reconcile mechanisms of cliff backwasting that are driven primarily by the cliff energy balance with debris redistribution processes and the influence of supraglacial hydrology. Models of debris redistribution exist and have been applied to understand the evolution of debris thickness patterns on debris-covered glaciers (Moore, 2021, 2018; Nicholson et al., 2018; Westoby et al., 2020). Their integration into sub-

debris and ice cliff melt models, along with the representation of the influence of streams and ponds, would represent a key improvement in the numerical representation of the long-term patterns of debris-covered glacier surface evolution and melt (Bartlett et al., 2020; Ferguson and Vieli, 2021). This shows the need for the continued collection of high spatio-temporal resolution data of ice cliff complexes (including south-facing cliffs) and their surroundings (varying debris thicknesses). Furthermore, the cliff energy balance model would also benefit from better constraints of the characteristics and temporal variability of key parameters such as debris and ice cliff emissivity and albedo (Fig. 2.S11), as well as a more robust interpolation of wind from the AWS to the cliff surface (Bonekamp et al., 2020). Indeed, a major uncertainty of the cliff energy balance model outlined in previous studies comes from the turbulent fluxes (Steiner et al., 2015) which are notoriously difficult to constrain on debris-covered glaciers (Miles et al., 2017a; Steiner et al., 2018). A step forward in the representation of cliff albedo variability could also be to extract it from the brightness observations of the time-lapse images (Corripio, 2004) and the precipitation patterns, although the difficulty here will be the transferability of such a relationship from glacier to glacier.

2.7. Conclusions

This study considerably improved our understanding of ice cliff evolution by using terrestrial time-lapse photogrammetry to quantify the weekly evolution of four ice cliffs on two climatically contrasting Himalayan debris-covered glaciers. Notably, the time-lapse camera DEMs enabled a precise quantification of the cliff melt by accounting for sub-seasonal cliff geometry changes, which are ignored when extracting melt from pre- and post-monsoon or annual DEMs. Prior to our work, cliffs had been observed only at the beginning and end of the melt season (because of logistical and field challenges), but never during this period, when most of the ablation occurs.

We found that the sub-seasonal variability in cliff melt was high, and was driven mainly by shortwave radiation, while air temperature was the determining factor for the sign of the net longwave contribution. Overall, the modeled melt agreed with the observations. On the other hand, the interaction of the cliffs with surrounding debris cover was found to be particularly crucial, and increased the spatial variability of the cliff melt by causing very strong changes in the cliff geometry. At the cliff surface, it had two main effects:

- The presence of small clasts or thin layers of dust reduced the cliff albedo (resulting in increased melt). Liquid precipitation events were effective at 'washing' this thin debris cover from the cliff surface and increasing its albedo, whilst snow events had a similar effect.
- The presence of slightly thicker, often patchy debris at the cliff surface and the active reburial of parts of the cliffs reduced melt via the debris insulating effect.

Ultimately, our results confirmed that the connectivity between ice cliffs and supraglacial hydrology (streams, ponds) exerts an important control on rates and patterns of cliff expansion and reburial, and that the relevant processes and feedbacks need to be accounted for in contemporary ice cliff energy balance models to better constrain cliff melt and the long-term surface evolution of debris-covered glaciers.

2.8.   Code availability

The Python scripts to automate the processing of the time-lapse images to DEMs, and the R scripts to calculate melt will be made available on Zenodo and GitHub upon acceptance of the manuscript.

2.9.   Data availability

DEMs, orthoimages and melt rasters will be made available on Zenodo upon acceptance of the manuscript.

2.10. Author contribution

MK, ESM and FP designed the study. MK, ESM designed the time-lapse setup. MK, ESM, SF, MM conducted the fieldwork on Langtang and MK, ESM, SF, TES, ZC, MT, MJW, WY on 24K. PB provided the cliff energy-balance model and helped in applying it. ESM provided the codes to flow-correct the different DEMs and helped in applying them. MK completed all the analysis and composed the manuscript. FP supervised the study. All authors aided in the reviewing and editing of the manuscript.

2.11. Competing interests

The authors declare that they have no conflict of interest.

2.12. Acknowledgements

2.13. Supplementary material

2.13.1. Workflow of the DEM processing with time-lapse photogrammetry

From the reference image sets we exported all optimized camera information (xyz position, pose and lens parameters) as well as the camera-specific, pixel-based locations of a series of 'pseudo' GCPs (PGCPs) which took the form of boulders and other distinctive features located on stable background terrain (Fig. 4). We used 21 PGCPs for Langtang and 14 for 24K. A majority of these PGCPs were located on the inside of the opposite lateral moraine of each glacier, as this was the closest 'stable' terrain to the survey domains. We were careful to select boulders that showed limited movement by ensuring that the distance in the images between the boulder and crest did not change over the time-lapse period. This therefore limited the possible influence of moraine collapse or slumping on the robustness of these features in the SfM workflow (Van Woerkom et al., 2019).

The accuracy of the PGCP position and camera parameters (location and pose) are important for the uncertainty of the final results. We optimized these accuracy values to minimize the bias in elevation over background stable terrain (Table S1, S2). As an initial estimate, we used the values provided by Agisoft Metashape (for PGCP position accuracy and lens parameters) and measurements of camera positions (with dGPS) and viewing angles conducted at the start and the end of the survey periods. The vertical position of the camera along the mast did not change by more than five centimeters, and the camera pose parameters by less than 5°, although this may have been temporarily exceeded during the observation period if wind speeds were very high.

In step 3 (Fig. 3), all the weekly image sets were processed semi-automatically in Agisoft Metashape, using the Agisoft Python API, following a 3-step workflow. In the first (fully automated) step the image sets were imported, along with the reference camera parameters, and underwent an initial bundle adjustment and camera lens parameter optimization without PGCPs. In a second (manual) step, the PGCP positions and their associated accuracies were imported and the position of the PGCPs was manually adjusted in each image. In the third (fully automated) step the camera parameters were optimized after incorporating PGCP locations, and the final estimates of camera location and pose were used to build a final dense point cloud, which was then used to create a DEM and orthoimage.

Table 2.S1: Optimized accuracy of the different camera parameters for DEM processing with Agisoft Metashape.

Site	Number of cameras	Optimized position accuracy (m)		Camera pose parameters accuracy (°)		
		X, Y	Z	Yaw	Pitch	Roll
24K	4	0.1	0.5	5	5	5
Langtang	8	0.1	0.5	5	5	10

Table 2.S2: Optimized accuracy of the PGCP position for DEM processing with Agisoft Metashape. The accuracy of the PGCPs is interpreted as a weighing coefficient describing the confidence we have in the PGCP position, therefore only the relative value between control points matters.

Site	Number of PGCPs	Optimized X, Y, Z position accuracy range (m)
24K	14	[0.1;0.5]
Langtang	21	[0.1;50]

Table 2.S3: Characteristics of the DEM time-series for Langtang and 24K.

Site	Number of cameras	Survey period	Number of DEMs	DEM resolution (m)	Maximum bias over background stable terrain (m)
24K	4	08/06/2019-12/10/2019	19	0.24	0.05
Langtang	8	12/05/2019-01/11/2019	25	0.20	0.2
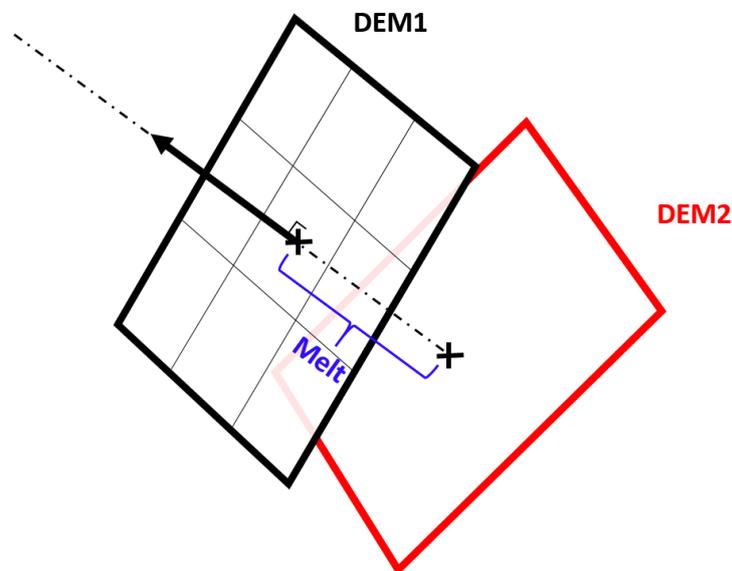
Figure 2.S1: Melt calculation from two DEMs.
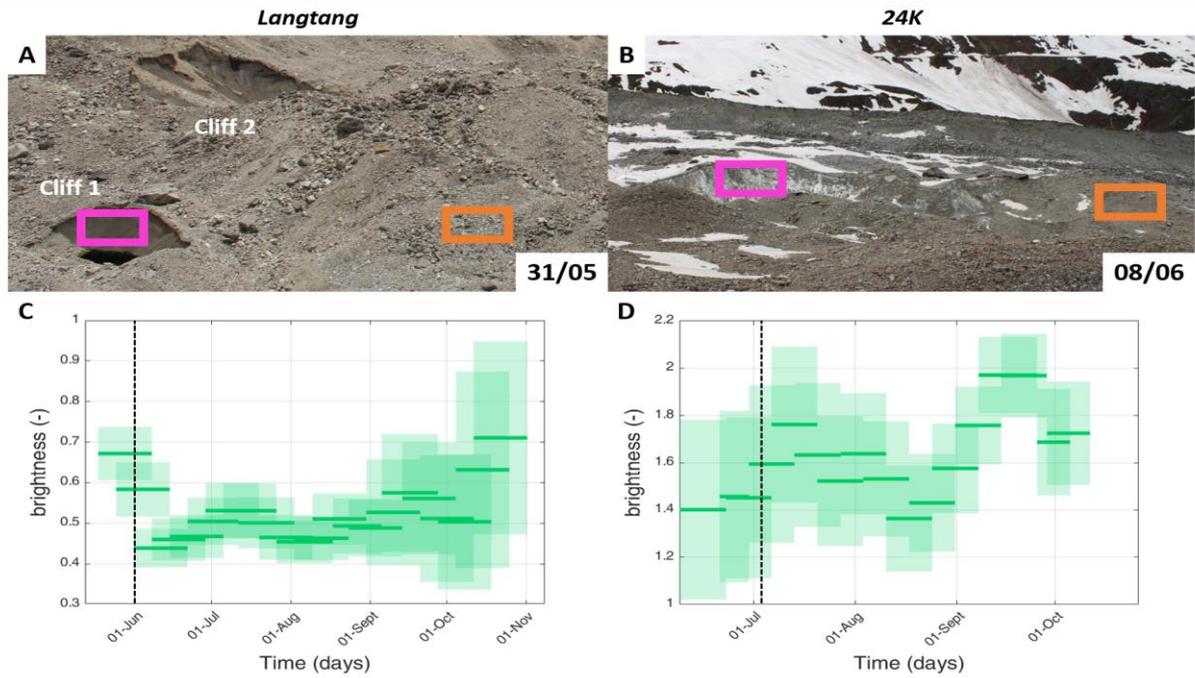
Figure 2.S2*: Brightness calculation for Langtang (A, C) and 24K (B, D). The boxes in the images represent the area over which the cliff brightness was calculated (pink) relative to the debris (orange). (C-D) Resulting brightness patterns averaged tri-weekly for Langtang and bi-weekly for 24K. The lines show the average brightness over the different periods and the shaded areas represent the standard deviation. Higher values at the beginning and the end of the study period on Langtang coincide with a higher frequency of snow events. The vertical dashed lines show when the images were taken.*

Table 2.S4*: Average cliff daily melt rate (m w.e.day⁻¹) for each surveyed cliff from the flow-corrected Pléiades (for Langtang), UAV (for 24K), as well as from the measured and modeled melt from the time-lapse time series. The UAV and Pléiades melt was calculated perpendicular to the slope of the initial DEM, as described in Section 5.4. Melt values were then integrated spatially (and temporally for the melt derived from the time-lapse), accounting for the cliffs' slope, to calculate the total volume losses. For the pre- and post-monsoon DEMs this spatial integration was conducted over 4 different domains: 1) the intersection of the cliff outlines in the pre and post-monsoon, 2) the pre-monsoon outlines only, 3) their union and 4) their union with a 4m buffer. The modeled melt was calculated using a fully static model and using the static model with the geometry update from the time-lapse DEMs. The total volumes were then normalized by the domain area, and by the mean cliff planimetric area for the time-lapse values.*

Melt (m w.e.day⁻¹)	Pre- and post-monsoon DEMs (Langtang: 2m Pléiades, 24K: 0.12m UAV)				Time-lapse DEMs		
	Intersection	*Initial outlines*	*Union*	*Union + 4m*	*Modeled (static)*	*Measured*	*Modeled*

	Intersection	Initial outlines	Union	Union + 4m buffer	Modeled (static)	Measured	Modeled
				buffer			
Langtang Cliff 1	0.020 -49%	0.019 -51%	0.017 -56%	0.017 -56%	0.031 -21%	0.039 0%	0.041 +5%
Langtang Cliff 2	0.041 -16%	0.042 -14%	0.037 -24%	0.033 -33%	0.037 -24%	0.049 0%	0.049 0%
Langtang Cliff 3	0.045 -4%	0.044 -6%	0.034 -28%	0.032 -32%	0.031 -34%	0.047 0%	0.046 -2%
24K Cliff	0.053 +4%	0.046 -10%	0.041 -20%	0.037 -27%	0.045 -12%	0.051 0%	0.053 +4%

Table 2.S5: *Total cliff daily melt rate (m^3 w.e.day^{-1}) for each surveyed cliff from the flow-corrected Pléiades (for Langtang), UAV (for 24K), as well as from the measured and modeled melt from the time-lapse time series. The UAV and Pléiades melt was calculated perpendicular to the slope of the initial DEM, as described in Section 5.4. Melt values were then integrated spatially (and temporally for the melt derived from the time-lapse), accounting for the cliffs' slope, to calculate the total volume losses. For the pre- and post-monsoon DEMs this spatial integration was conducted over 4 different domains: 1) the intersection of the cliff outlines in the pre and post-monsoon, 2) the pre-monsoon outlines only, 3) their union and 4) their union with a 4m buffer. The modeled melt was calculated using a fully static model and using the static model with the geometry update from the time-lapse DEMs.*

Melt (m^3 w.e.day^{-1})	Pre- and post-monsoon DEMs (Langtang: 2m Pléiades, 24K: 0.12m UAV)				Time-lapse DEMs		
	Intersection	*Initial outlines*	*Union*	*Union + 4m buffer*	*Modeled (static)*	*Measured*	*Modeled*
Langtang Cliff 1	0.4 -90%	2.0 -49%	3.7 -5%	5.3 +36%	5.3 +36%	3.9 0%	4.2 +8%
Langtang Cliff 2	2.5 -91%	23.5 -15%	36.5 +33%	47.0 +71%	20.3 -26%	27.5 0%	27.7 +1%

Langtang Cliff 3	23.3	51.2	68.5	78.7	35.4	38.2	36.9
	-39%	*+34%*	*+79%*	*+106%*	*-7%*	*0%*	*-3%*
24K Cliff	51.9	118.5	172.2	225.9	128.8	98.0	102.6
	-47%	*-8%*	*+78%*	*+131%*	*+31%*	*0%*	*+5%*
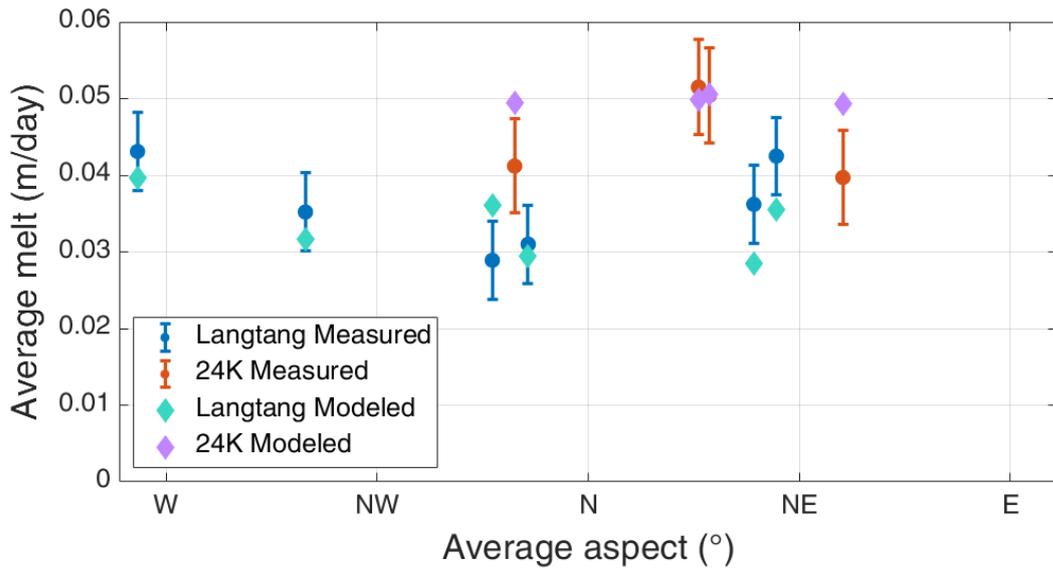
Figure 2.S3: *Average observed and modeled melt from the time-lapse camera data as a function of mean aspect from the time-lapse DEMs over the full study period for all the cliff focus areas. The bars indicate the uncertainty of the measured melt rates.*
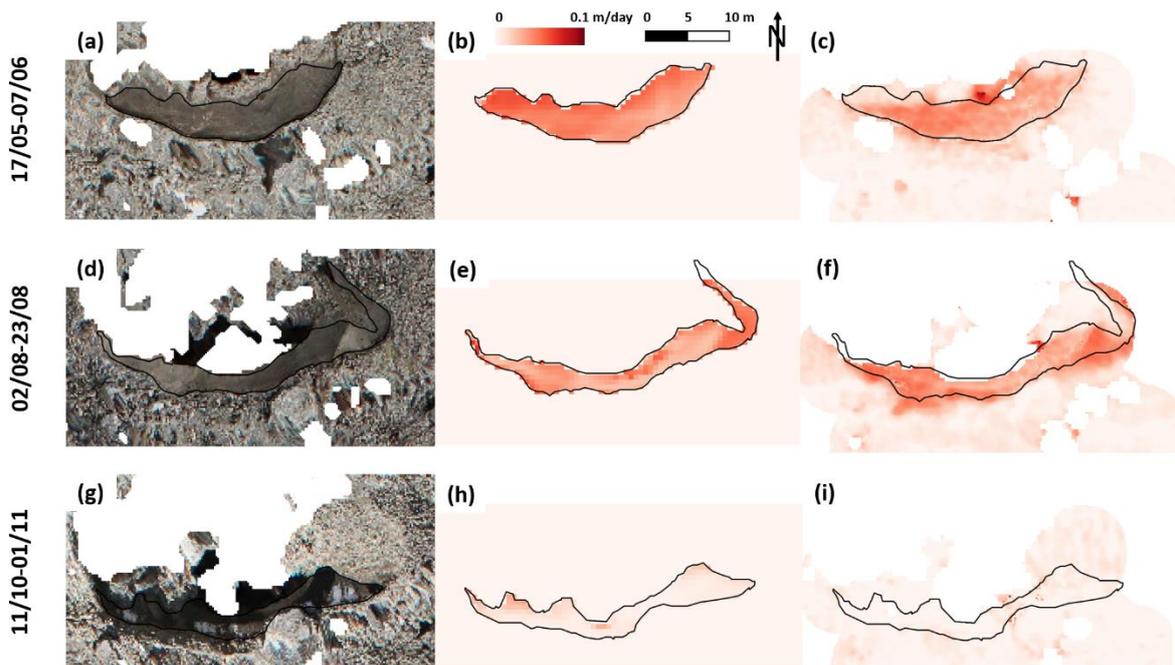
Figure 2.S4: *Orthoimages (left panels), modeled (central panels) and observed (right panels) melt patterns at the surface of Langtang cliff 1 (outlines in black) for the periods 17/05/2019 - 07/06/2019, 02/08/2019 - 23/08/2019 and 11/10/2019 - 01/11/2019.*
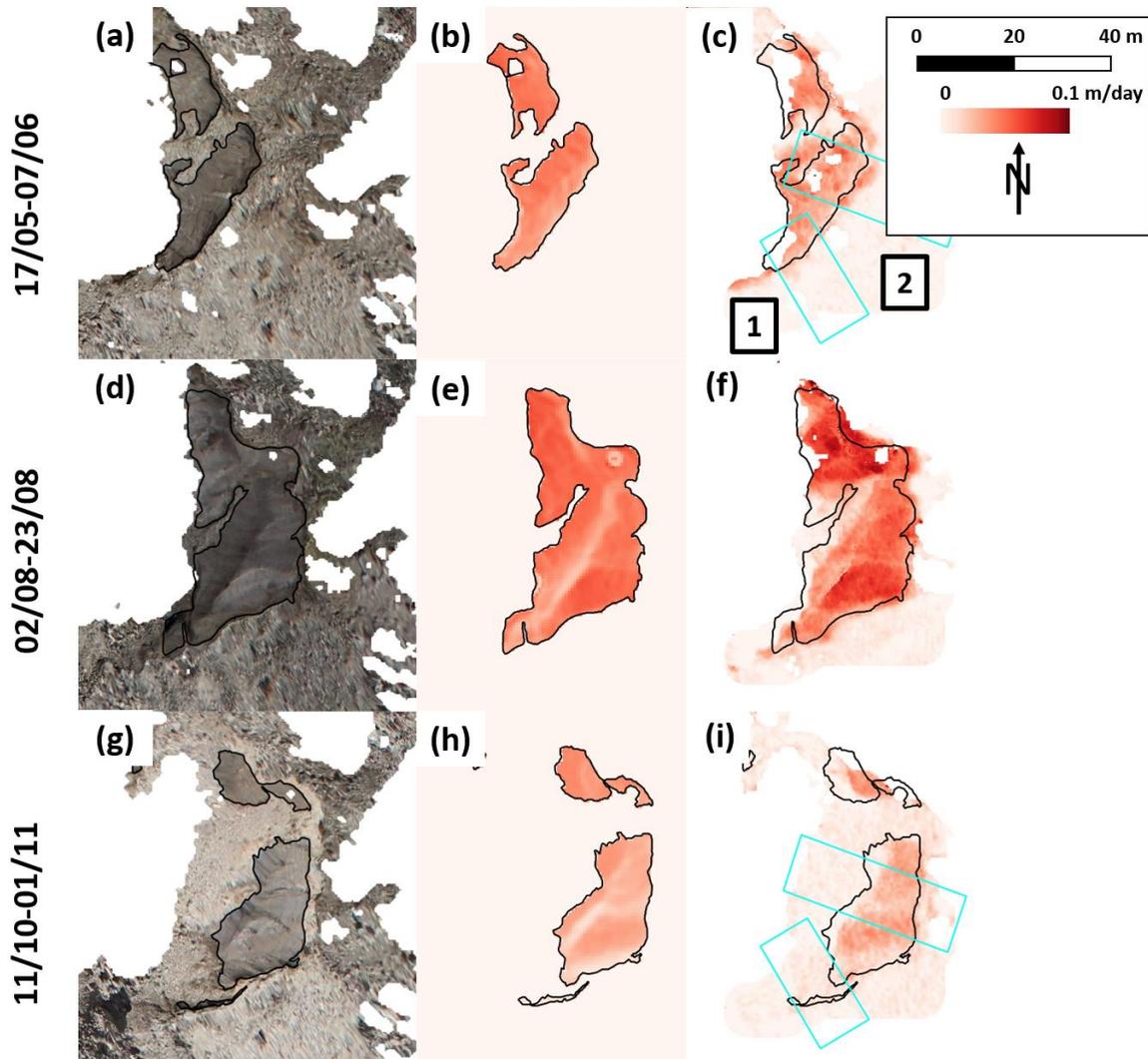
Figure 2.S5: *Orthoimages (left panels), modeled (central panels) and observed (right panels) melt patterns at the surface of Langtang cliff 2 (outlines in black) for the periods 17/05/2019 - 07/06/2019, 02/08/2019 - 23/08/2019 and 11/10/2019 - 01/11/2019.*
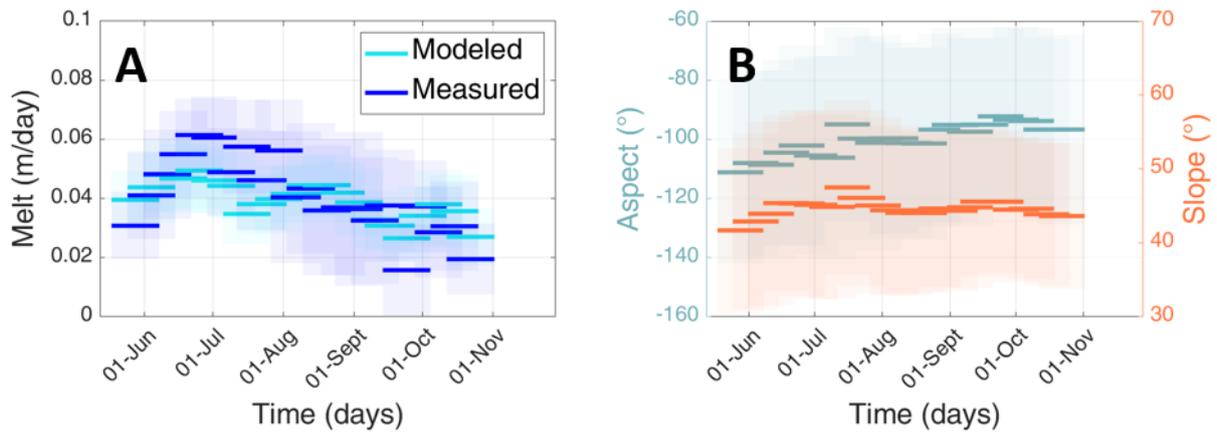
Figure 2.S6*: Measured and modeled melt (A) and aspect and slope (B) evolution of Langtang Cliff 2.*
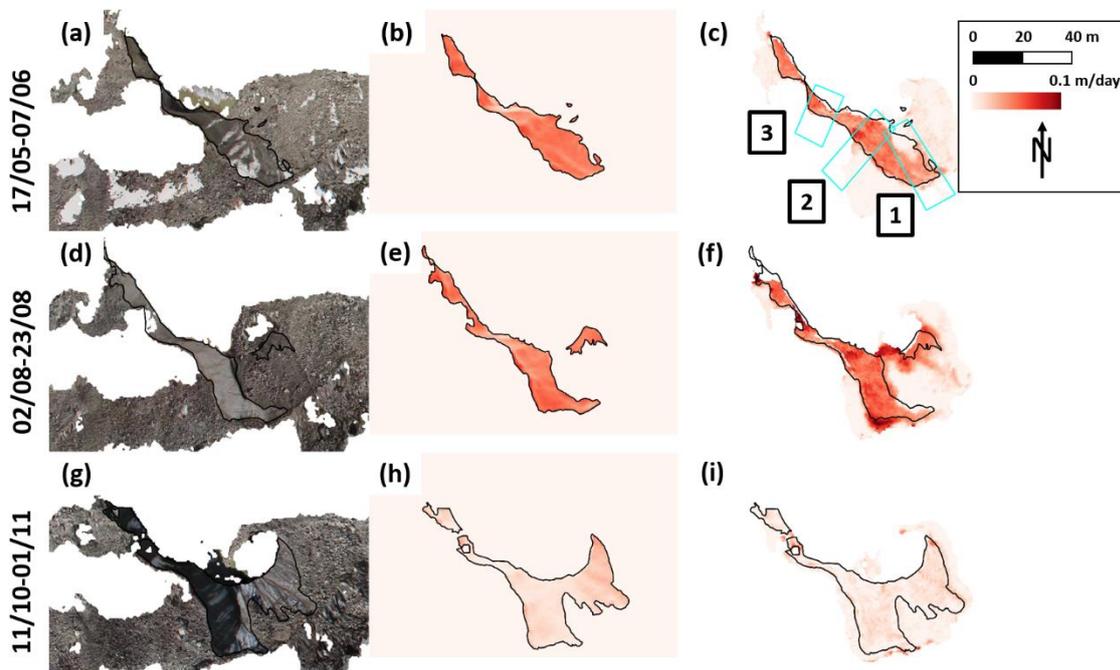
Figure 2.S7*: Orthoimages (left panels), modeled (central panels) and observed (right panels) melt patterns at the surface of Langtang cliff 3 (outlines in black) for the periods 17/05/2019 - 07/06/2019, 02/08/2019 - 23/08/2019 and 11/10/2019 - 01/11/2019.*
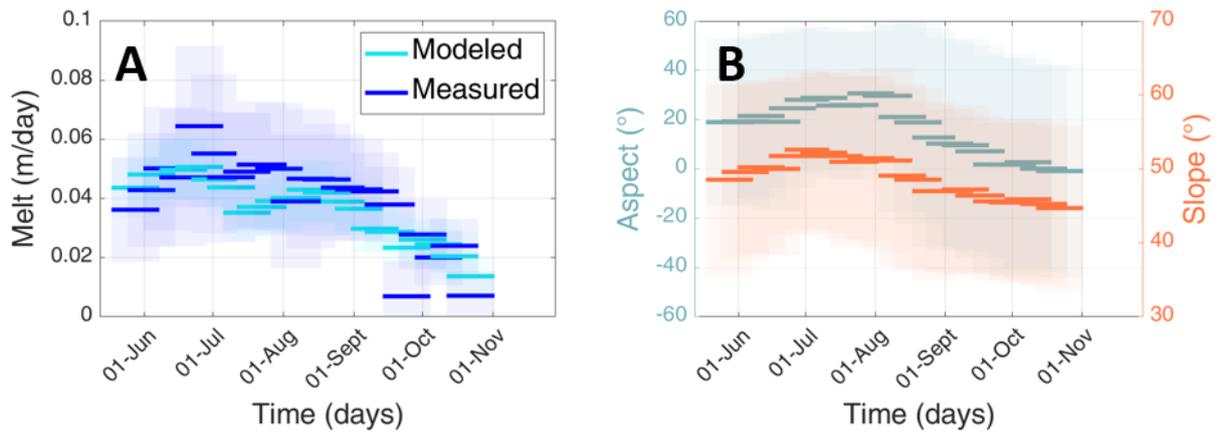
Figure 2.S8: *Measured and modeled melt (A) and aspect and slope (B) evolution of Langtang Cliff 3.*
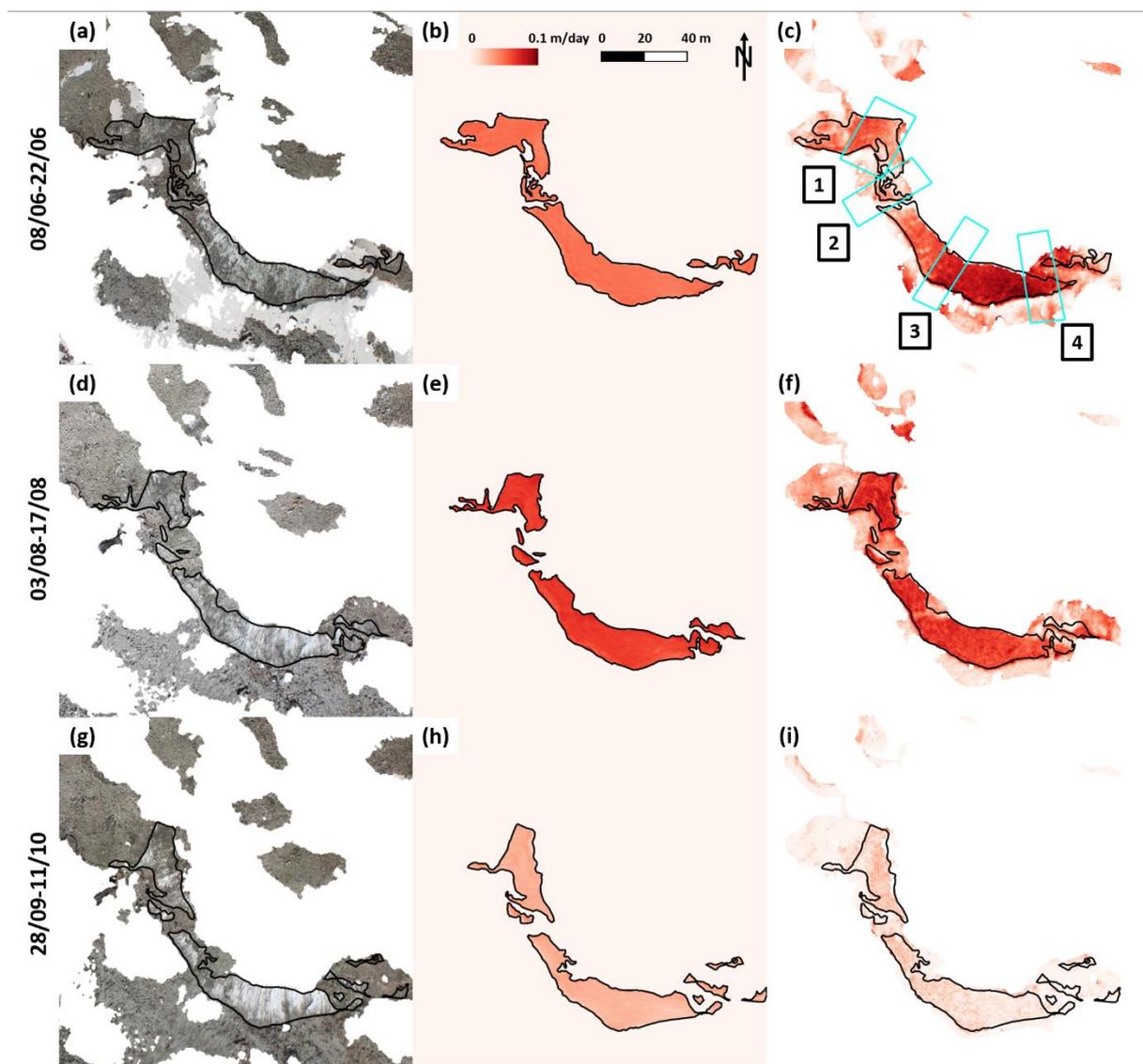
Figure 2.S9: *Orthoimages (left panels), modeled (central panels) and observed (right panels) melt patterns at the surface of the 24K cliff (outlines in black) for the periods 08/06/2019 - 22/06/2019, 03/08/2019 - 17/08/2019 and 28/09/2019 - 11/10/2019.*
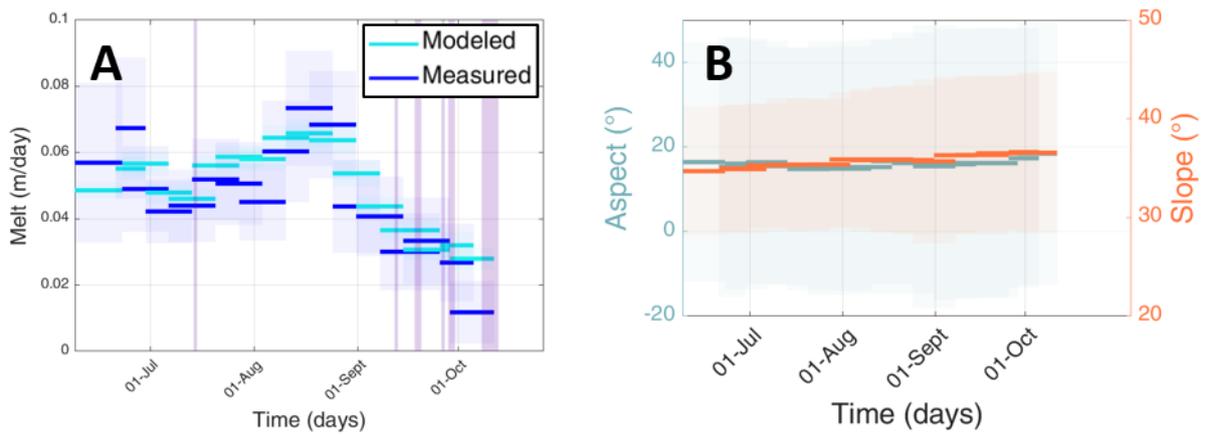
Figure 2.S10: Measured and modeled melt (A) and aspect and slope (B) evolution of the 24K cliff.
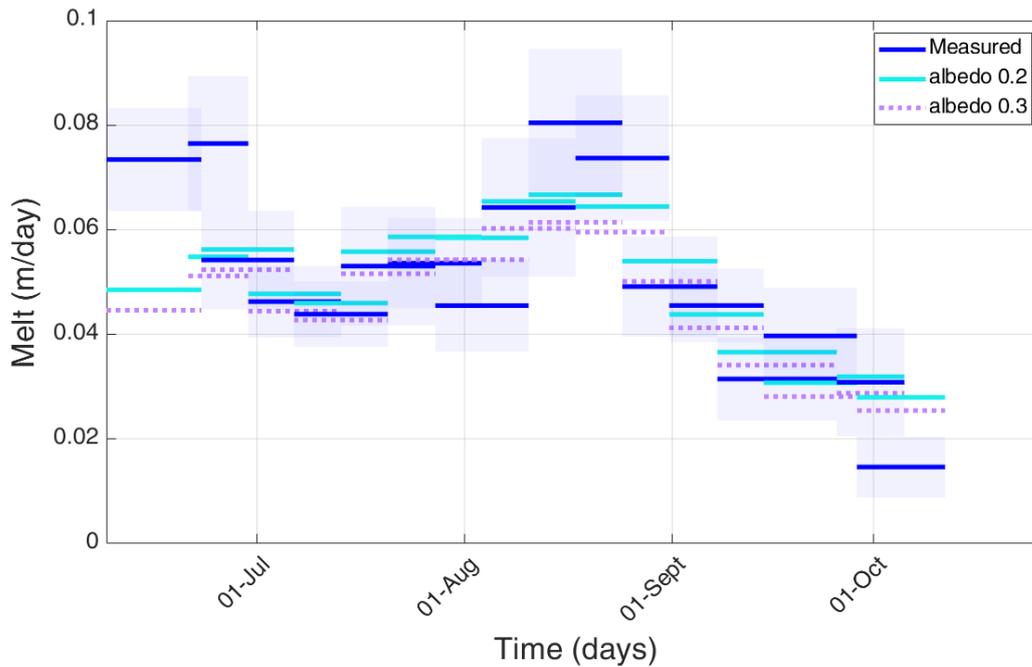
Figure 2.S11: Observed (dark blue) and modeled melt rates of the 24K transect 3 during the whole study periods with fixed cliff albedo values of 0.2 (light blue full lines) and 0.3 (purple dashed lines). The dark blue patches show the standard deviation of the measured melt rates.

2.13.2.   Use of time-lapse photogrammetry approach

We assembled a custom-built weather-proof time-lapse setup, designed to run fully autonomously for several months while taking high-quality images. The setup was relatively expensive (~1900 € per camera), with the additional constraint of weight in the field, as each setup represented ~15 kg to carry to installation location. These logistical aspects, in addition to the structure-from-motion considerations (Mallalieu et al., 2017), constrained the choice of the survey areas considerably. The setup was

relatively easy and quick to install in the field once all elements had been brought to the installation site, each camera requiring 2-3 hours to be deployed. The cameras all ran without interruption during the whole study period, and even longer for the 24K cameras. These were indeed left to run as 'fixed' stations and were still in excellent condition when last checked in summer 2021, two years after their initial installation, despite some observation gaps in the winter due to power shortages caused by limited direct sun illumination and snow accumulation on the solar panels.

The processing of the image sets was fully automated except for the identification of the PGCPs, and followed the general workflow proposed by Mallalieu et al., 2017 in Agisoft Metashape. Once all the scripts were running in an automated way, the processing of an image set to the DEM and orthoimage took between 1 and 1.5 hours, with the main constraint being the manual positioning of the PGCPs (Mallalieu et al., 2017). As was to be expected, the measurement errors depended on the distance from the cameras, time since the reference image set (Fig. 5), and to some extent the illumination and atmospheric conditions (Mallalieu et al., 2017; Smith and Vericat, 2015). Indeed, images with strong direct illumination or those which were blurred by local rain events or low clouds usually resulted in high biases relative to the reference image sets. However, the higher number of cameras on Langtang did not seem to reduce this error, possibly because the viewing angles were too similar (Bemis et al., 2014). While the spread in the elevation data had a limited influence on our results, we found that the systematic error, which we estimated to be +/- 20 cm (+/- 6 cm) at the cliff site for Langtang (24K), was the main constraint to study the cliff changes at high temporal frequency. These 1:1500 to 1:5000 errors are in the low range of previous time-lapse photogrammetry surveys, which were between 1:650 (Smith and Vericat, 2015), 1:1000 (James and Robson, 2012; Mallalieu et al., 2017) and 1:3500 (Filhol et al., 2019), which is likely at least partly related to the quality of the sensors.

The high-quality DEMs and elevation change measurements resulting from the time-lapse survey confirm the robustness of such a setup to monitor surface changes relative to other more expensive devices such as TLS (Bemis et al., 2014; Piermattei et al., 2015).

Chapter 3: Mapping ice cliffs on debris-covered glaciers using multispectral satellite images

[1] High Mountain Glaciers and Hydrology (HIMAL), Swiss Federal Research Institute WSL, 8903 Birmensdorf, Switzerland

[2] Institute of Environmental Engineering, ETH Zurich, 8093 Zurich, Switzerland

[3] School of Geography & Sustainable Development, University of St. Andrews, Scotland, KY16 9AL, UK.

[4] COMET, School of Earth and Environment, University of Leeds, Leeds, LS2 9JT, UK

[5] School of Geography, University of Leeds, Leeds, LS2 9JT, UK

[6] Department of Geography, Northumbria University, Newcastle, NE1 7RU, UK

Author contribution

MK, ESM and FP designed the study. MK, SJ and ESM prepared the calibration and validation datasets and developed the cliff mapping methods. MK, ESM, PB and SH conducted the comparison analysis with other published studies. AB, SCW, TB and DQ provided the Khumbu and Satopanth Pléiades images. MK composed the manuscript. FP and ESM supervised the study. All authors aided in the reviewing and editing of the manuscript.

Highlights

- Transferable and automated mapping of ice cliffs using multi-spectral imagery
- Mapping cliffs with Spectral Curvature performs well with fine resolution Pléiades.
- Cliff distribution can be assessed with high confidence from Sentinel-2 images.
- Objective mapping of cliffs identifies small features that escape manual delineation.

3.1. Abstract

Ice cliffs play a key role in the mass balance of debris-covered glaciers, but assessing their importance is limited by a lack of datasets on their distribution and evolution at scales larger than an individual glacier. These datasets are often derived using operator-biased and time-consuming manual delineation approaches, despite the recent emergence of semi-automatic mapping methods. These methods have used elevation or multi-spectral data, but the varying slope and mixed spectral signal of these dynamic features makes the transferability of these approaches particularly challenging. We develop three semi-automated and objective new approaches, based on the Spectral Curvature and Linear Spectral Unmixing of multi-spectral images, to map these features at a glacier to regional scale. The transferability of each method is assessed by applying it to three sites in the Himalaya, where debris-covered glaciers are widespread, with varying lithologic, glaciological and climatic settings, and encompassing different periods of the melt season. We develop the new methods keeping in mind the wide range of remote sensing platforms currently in use, and focus in particular on two products: we apply the three approaches at each site to near-contemporaneous atmospherically-corrected Pléiades (2 m resolution) and Sentinel-2 (10 m resolution) images and assess the effects of spatial and spectral resolution on the results. We find that the Spectral Curvature method works best for the high spatial resolution, four band Pléiades images, while a modification of the Linear Spectral Unmixing using the scaling factor of the unmixing is best for the coarser spatial resolution, but additional spectral information of Sentinel-2 products. In both cases ice cliffs are mapped with a Dice coefficient higher than 0.48. Comparison of the Pléiades results with other existing methods shows that the Spectral Curvature approach performs better and is more robust than any other existing automated or semi-automated approaches. Both methods outline a high number of small, sometimes shallow-sloping and thinly debris-covered ice patches that differ from our traditional understanding of cliffs but may have non-negligible impact on the mass balance of debris-covered glaciers. Overall these results pave the way for large scale efforts of ice cliff mapping that can enable inclusion of these features in debris-covered glacier melt models, as well as allow the generation of multiple datasets to study processes of cliff formation, evolution and decline.

3.2. Keywords

Debris-covered glaciers; Supraglacial ice cliffs; Linear Spectral Unmixing; Sentinel-2; Pléiades; Automated delineation; Ice cliff inventory

3.3. Introduction

Debris-covered glaciers are found in all mountain ranges of the world. Despite the insulating effect of a thick debris layer (Nicholson and Benn, 2006; Ostrem, 1959) the mass losses of debris-covered glaciers have been shown to be higher than predictions from melt models (Anderson et al., 2019a; Brun et al., 2019; Gardelle et al., 2013; Kääb et al., 2012; Nuimura et al., 2012; Ragettli et al., 2016a). This enhanced mass loss has been partially attributed to the supraglacial features specific to these glaciers, namely supraglacial ice cliffs and ponds (Pellicciotti et al., 2015; Salerno et al., 2017). These features act as enhanced energy exchange zones, as they are directly exposed to incoming shortwave radiations from the sky and longwave radiations from their surroundings (Buri et al., 2016a; Miles et al., 2016), unlike the surrounding debris-covered ice. Supraglacial ice cliffs stand out at the surface of debris-covered glaciers, appearing in the rocky landscape as steep ice slopes sometimes covered by a thin layer

of wet dust. Both empirical and numerical modeling studies have shown that ice cliffs melt at an enhanced rate (Anderson et al., 2019b; Brun et al., 2018; Buri et al., 2016a, 2016b; Han et al., 2010; Juen et al., 2014; Reid and Brock, 2014; Sakai et al., 1998; Steiner et al., 2015; Watson et al., 2017b). Cliffs have been observed to melt between 2.5 (Brun et al., 2018) and 35 (Sakai et al., 1998) times more than the surrounding debris-covered ice. As a result, they are important contributors to the mass loss of debris-covered glaciers, and can account for 20-40% of melt in the debris-covered area despite typically covering less than 10% of this area (Anderson et al., 2019b; Brun et al., 2019; Immerzeel et al., 2014; Pellicciotti et al., 2015; Sakai et al., 2002; Thompson et al., 2016). Ice cliffs are active features and can evolve, appear or disappear rapidly (Buri and Pellicciotti, 2018; Steiner et al., 2019), and past studies to assess their distribution have been challenged by the difficulty of mapping these features (Steiner et al., 2019; Watson et al., 2017a). Improved understanding of the spatial distribution and temporal evolution of cliffs is required to assess their role and melt contribution at the glacier and regional scales, but requires a mapping scheme that is consistent, automated and transferable.

The availability of a growing number of satellite images of different spatial resolution and spectral properties now allows the development of new methods based on multi-spectral analysis. Here we test three new methods based on multi-spectral images with the aim to map ice cliffs at the surface of debris-covered glaciers in an automated, transferable and objective way. Transferability between sites and images is assessed by applying all three methods to three debris-covered glaciers of the Central and Eastern Himalaya with varying lithology, altitude range and climatic settings. The images used correspond to distinct periods of the monsoon-affected melt season (Shea et al., 2015) to ensure transferability of the methods between different climatic conditions. We also test transferability between sensors by comparing results from near-contemporaneous Pléiades and Sentinel-2 scenes for each site. Finally, we compare our three approaches with existing semi-automated and automated mapping methods.

3.4. Background

Despite their implications for ablation, few studies have assessed ice cliff characteristics, spatial distribution and temporal evolution at the scale of an entire glacier (Steiner et al., 2019; Thompson et al., 2016; Watson et al., 2017a). Most previous studies have identified cliffs using manual delineation, which is the most common cliff mapping approach (Brun et al., 2018; Buri and Pellicciotti, 2018; Han et al., 2010; Juen et al., 2014; Steiner et al., 2019; Thompson et al., 2016; Watson et al., 2017a), and is also needed to train and evaluate semi-automated and automated mapping approaches (Anderson et al., 2019a; Herreid and Pellicciotti, 2018; Kraaijenbrink et al., 2016b). Manual delineation of cliffs is based on the expert knowledge of the operator who can identify cliffs with varying shapes and surface characteristics reasonably accurately. However, it is a repetitive and time-consuming task and one that can be biased by an erroneous representation of a cliff leading to misinterpretation of the information contained in the remote sensing product, and can therefore be qualified as subjective. Furthermore, the quality of the manual cliff outlines will vary across a scene due to operator fatigue, surface properties and illumination. It sometimes requires several operators to validate the outlines and reduce the delineation bias (e.g. Anderson et al., 2019a; Steiner et al., 2019). The manual delineation suffers from variability in cliff illumination, which partly conceals the cliffs in their own shadows. This can be dealt with by delineating only the top of the cliffs (Thompson et al., 2016; Watson et al., 2017a), but results in reduced information regarding their geometries.

More objective and less time consuming methods have been sought using classification criteria based on the slope (Herreid and Pellicciotti, 2018; Reid and Brock, 2014) or on the spectral signatures (Anderson et al., 2019b; Kraaijenbrink et al., 2016b) of ice cliffs. The slope-based approaches rely on elevation data from a Digital Elevation Model (DEM) and are based on the assumption that debris cannot be sustained above a certain slope value. This threshold can be taken as a fixed value (Reid and Brock, 2014), but the stability of supraglacial debris depends on many other factors including water content, shape of the slope or status of the base of the slope (Moore, 2018). Surface slope thresholds thus depend on the glacier, climatic and geomorphological settings, and the transferability of this approach from site to site can be improved by automatically selecting threshold values (Herreid and Pellicciotti, 2018). Due to the steep, sometimes overhanging cliff faces and their narrow shapes, this approach requires fine resolution DEM products ($\leq$ 5m) and will be affected by DEM spatial resolution, even though efforts have been made to take into account areas at the ends of the cliffs where the slope signal is saturated (Herreid and Pellicciotti, 2018).

Alternatively, studies have tried to reproduce the classification of cliffs as made by the expert's eye by disentangling the spectral signature of cliffs from the surrounding debris and supraglacial ponds (Anderson et al., 2019b; Kraaijenbrink et al., 2016b). These approaches are challenged by the varying and often heterogeneous nature of the cliff surface, from thinly debris-covered to bright bare ice and penitents (Fig. 3.1). An attempt was made using object-based image analysis (OBIA) applied to high spatial resolution UAV data (Kraaijenbrink et al., 2016b). Although the OBIA results are promising, they were limited to a small portion of Langtang glacier with homogeneous cliff surface characteristics (Fig. 3.1). Transferability of the complex training and classification scheme to other sites or coarser data is thus questionable, and probably requires new training datasets for each new scene (Kraaijenbrink et al., 2016b). The OBIA approach is initiated by the segmentation of the image into near-homogeneous groups of pixels, and Mölg et al., (2020, 2019) exploited this initial segmentation to reduce the subjectivity and workload of the manual delineation approach, even though considerable work remains to identify the cliff objects and adjust the outlines. A simpler approach successfully used the changes in brightness to pick out cliffs from the surrounding debris on one Alaskan glacier (Anderson et al., 2019a), but this requires scenes with little shading and new training data for each new scene due to the varying nature of the cliffs and debris, even at the scale of one glacier (Fig. 3.1). Furthermore, this method is based on the assumption that cliff brightness is lower than the brightness of the surrounding debris, which is not the case when there is bare ice at the cliff surface, or when the debris is wetted (Fig. 3.1, Anderson et al., 2019). All these approaches can be qualified as 'semi-automated' since they rely on empirical thresholds that are optimized for a scene and may be more or less transferable to other scenes, as compared with the adaptive slope threshold approach which determines threshold values internally and is therefore fully automated (Herreid and Pellicciotti, 2018).
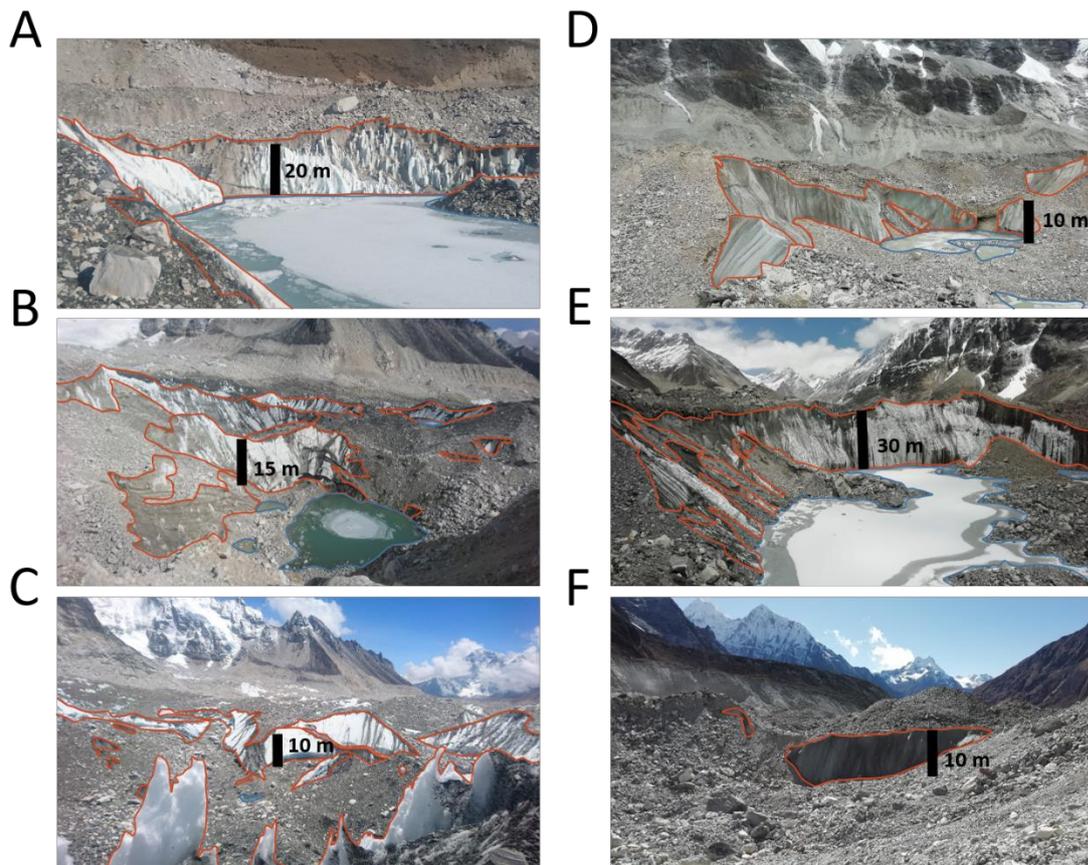
Figure 3.1. *Examples of ice-cliffs on Khumbu (A-C) and Langtang glaciers (D-F), highlighting the variability in surface character. The outlines show supraglacial cliffs (orange) and ponds (blue).*

Here, we start from the hypothesis that multi-spectral information can be exploited in alternative ways to map cliffs in a robust manner that is transferable, objective and semi-automated. Spectral indices based on simple band ratios have a rich history in producing binary maps of target features, and have proven successful for snow or ice (e.g. Girona-Mata et al., 2019; Paul et al., 2016), water bodies (e.g. Huggel et al., 2002; Watson et al., 2018) and debris (e.g. Casey et al., 2012; Pope and Rees, 2014) in similar environments. Linear spectral unmixing (LSU), an approach that decomposes the measured spectrum of each pixel of an image as a linear combination of the spectral end-members of its constituent surfaces, can make use of the increasing amount of information contained in modern satellite products for improved mapping (e.g. Keshava and Mustard, 2002). This method has been especially successful when applied to features with a highly mixed signal (e.g. Kopačková and Hladíková, 2014; Vikhamar and Solberg, 2003).

Cliff mapping is needed at different spatial and temporal scales. At the glacier scale, fine spatial resolution imagery is preferable to accurately assess cliff distribution and evolution, in order to understand the cliff dynamics in detail. At the larger scale, such as as required to inform regional melt modeling, an estimate of cliff coverage from coarser imagery may be adequate, if its bias is known. This dataset needs to rely on images that are freely available over large areas. Here we develop and assess the potential of methods that can be used for both research questions. Two distinct types of multi-spectral satellite imagers are suited to these distinct objectives: commercial platforms with a limited number of spectral bands but an extremely fine spatial resolution such as WorldView (Anderson et al., 2019b) or Pléiades (e.g. Berthier et al., 2014) , and freely available products with coarser spatial resolution but more spectral information, like Landsat or Sentinel-2. To address these objectives in a

manner that allows comparison between methods we use near-contemporaneous scenes from Pléiades and Sentinel-2 and consider the tradeoffs of spatial and spectral resolution between these data sources.

3.5. Data and Methods

3.5.1. Multi-spectral data

We first apply the cliff delineation methods to three Pléaides acquisitions covering three different areas of the Himalaya encompassing one or more debris-covered glaciers (Fig. 3.2). One scene is from the pre-monsoon (May), one is from the beginning of the monsoon (June) and the third one is from the post-monsoon season (September, Fig. 3.2). We also apply the cliff delineation to three Sentinel-2 images taken within a week of the Pléiades scenes to avoid major changes in conditions and in the surface topography of the glacier, and using the same extents (Fig. 3.2, Table 3.S1). Snow- and cloud-covered areas are discarded manually from the analysis (Fig. 3.2). The Pléiades and Sentinel-2 sensors sample the visible and near infrared spectrum, with a few observations at longer wavelengths in the case of Sentinel-2. Pléiades has a ground resolution of ~2 m for the multi-spectral orthoimages. For Sentinel-2 we use the four 10 m resolution bands that coincide with the four Pléiades bands in terms of central wavelength, as well as the six 20 m resolution bands (Table 3.S2).
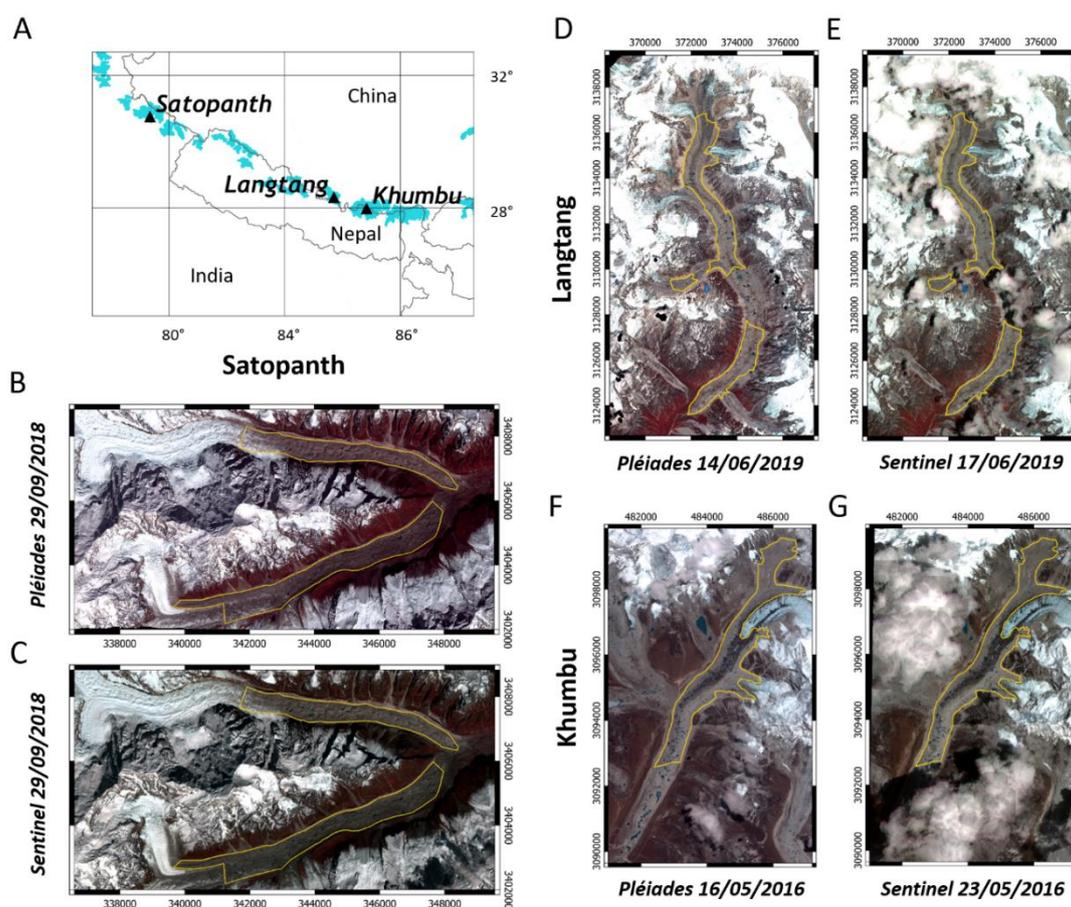
Figure 3.2. *False-color composites of the six scenes used in this study. In the lower left, Pléiades (B) and Sentinel-2 (C) images of Satopanth (to the south) and Bhagirati Kharak (to the north) Glaciers. In*

the upper right, Pléiades (D) and Sentinel-2 (E) images of Langtang Glacier. In the lower right, Pléiades (F) and Sentinel-2 (G) images of Khumbu Glacier. Areas where we apply the delineation methods are outlined in yellow, and correspond to snow- and cloud-free debris-covered areas in the corresponding Pléiades and Sentinel-2 scenes. Pléiades, 16 May 2016, 29 Sep 2018, 14 Jun 2019 © CNES (2016, 2018, 2019), and Airbus DS (2016, 2018, 2019), all rights reserved.

The Pléiades images were stereo-processed to generate 2 m resolution DEMs and orthorectified multi-spectral images using Rational Polynomial Coefficients (RPCs) with the AMES stereo pipeline (Beyer et al., 2018; Shean et al., 2016) for the Langtang scene, and with the Semi Global Matching (SGM) correlation algorithm (Hirschmüller, 2007) for the Satopanth scene. The Khumbu Pléiades image (16/05/2016) was processed to a 2 m resolution orthorectified multi-spectral image using the photogrammetry module of ERDAS Imagine 2015 software. The acquisition was not stereo so it was orthorectified using an earlier DEM generated from stereo Pléiades imagery (07/10/2015). The image RPCs and eight ground control points were used for georeferencing. The multi-spectral images were then processed to surface reflectance using the GRASS GIS (Neteler et al., 2012) i.atcorr tool, which uses the 6S radiative transfer algorithm (Kotchenova et al., 2006; Vermote et al., 1997). For the Sentinel-2 data, the images were corrected to surface reflectance using the MAJA atmospheric correction processor (Hagolle et al., 2015).

3.5.2. New cliff mapping approaches

We develop three new approaches (Fig. 3.3) to map cliffs on debris-covered glaciers. As cliffs are often associated with supraglacial ponds (Steiner et al., 2019; Watson et al., 2017a), mapping them successfully also requires the separation of partially frozen ponds from cliffs, and careful delineation of the cliff-pond boundary in joint systems. Therefore, supraglacial ponds are also delineated as part of each approach. As the shape and size of cliffs can vary widely (Fig. 3.1), we avoid excessive morphological filtering that could bias the results and use the same basic morphological filters for all approaches to make the results directly comparable. We discard cliffs and ponds of size less than or equal to 5 pixels (20 m^2) for the Pléiades and 1 pixel (100 m^2) for the Sentinel-2 imagery, reflecting likely spectral mapping errors (Salerno et al., 2012; C. S. Watson et al., 2016). We also morphologically fill the ponds, to account for partially frozen ponds with ice in the center.
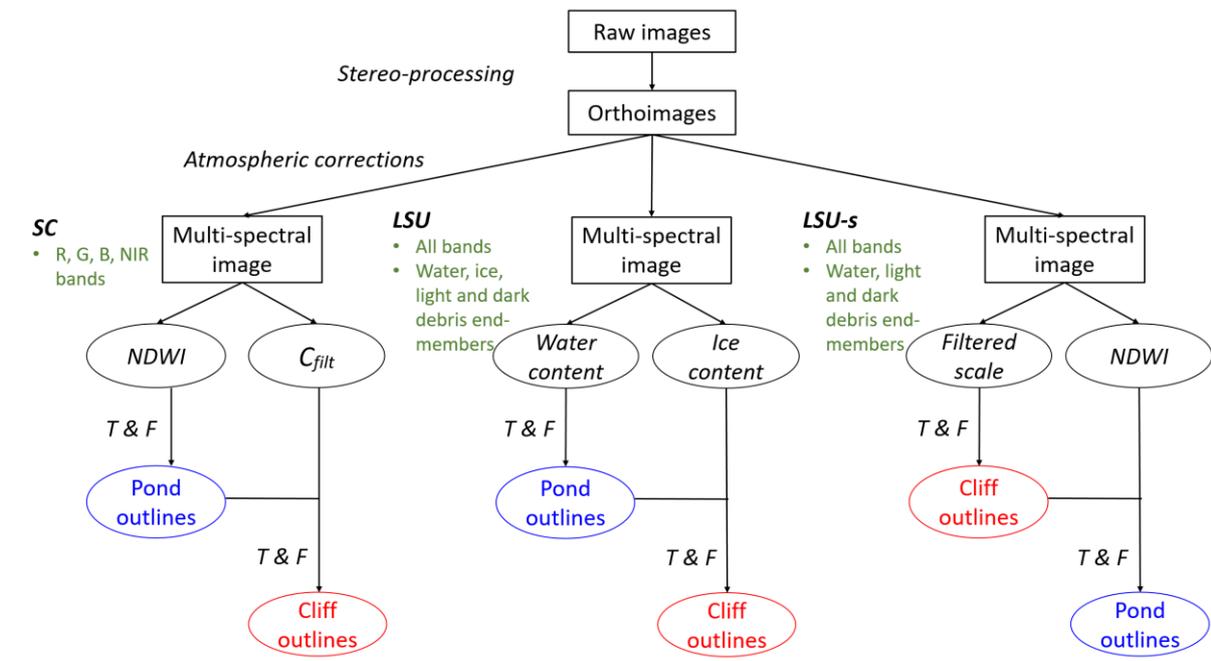
Figure 3.3. Flowcharts of the Spectral Curvature (SC), Linear Spectral Unmixing (LSU) and Linear Spectral Unmixing with scale (LSU-s) cliff delineation approaches. T & F stands for thresholding and morphological filtering. The Sentinel-2 images are not stereo-processed.

3.5.2.1.   Spectral Curvature (SC)

Ice cliffs can be highly variable in their surface condition (Herreid and Pellicciotti, 2018). Although literature tends to characterize them as 'exposed' glacier ice, they are often covered by a thin veneer of debris. They also experience enhanced melt when not covered by snow, leading to a wetted, dirty ice appearance in the melt season (Fig. 3.1). We therefore expect the spectra of the cliffs' pixels to be a mixture of 'pure' spectra of ice, water and debris in varying proportions. The rock debris component can also have varying reflectance values depending on factors such as its composition or water content. A study of the mineral content of the debris on the Ngozumpa and Khumbu glaciers showed varying values of reflectance depending on the lithology (Casey et al., 2012, Fig. 3.4), but the spectra of rock debris in the visible and near infra-red are generally relatively flat with a small positive slope (Fig. 3.4). This contrasts strongly with the spectra of ice and water, which despite different reflectance values, both have a concave shape in the visible range (Fig. 3.4). The values for ice are typically higher than for water, although varying turbidity of supraglacial ponds can increase brightness (Kraaijenbrink et al., 2016b; Wessels et al., 2002), confounding simple classifiers. The shape and values of the cliff spectra may vary considerably depending on its surface characteristic, water content, and mineral composition of the debris veneer (Fig. 3.1). A cliff with a bare ice surface should have high reflectance values for visible bands but lower reflectance in the near infra-red wavelengths, as for glacier ice (Paul et al., 2016), while this contrast can be attenuated if the cliff is covered by a thin debris layer (Fig. 3.4).
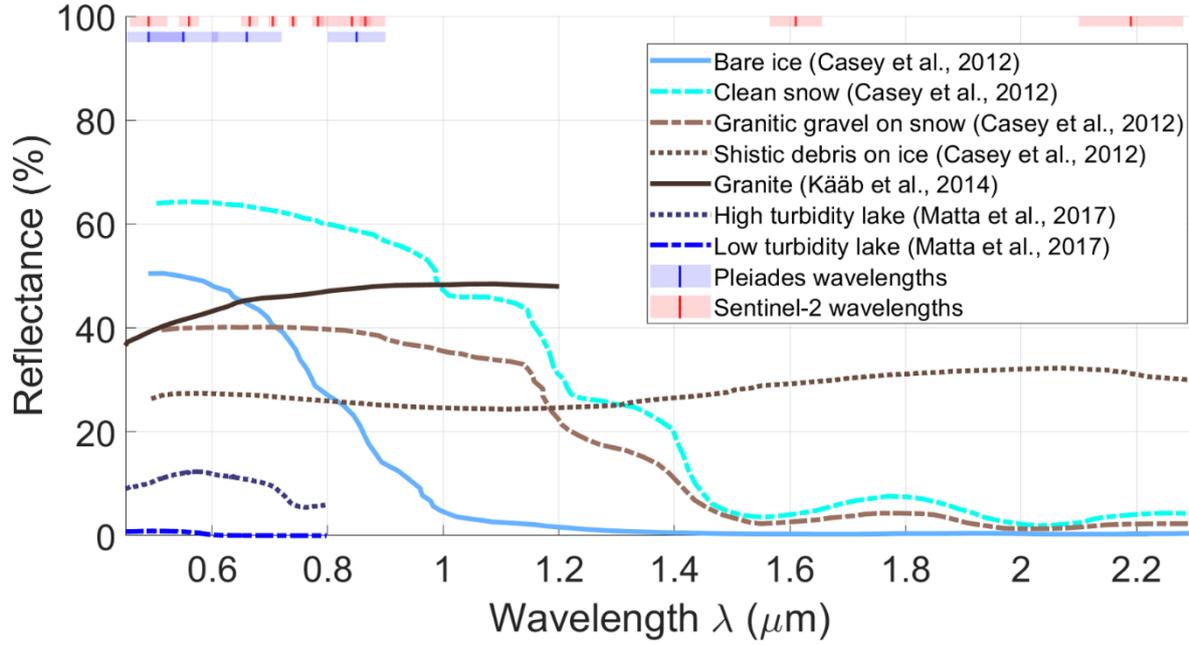
Figure 3.4. *Spectra of various surface types encountered on debris-covered glaciers, digitized from Casey et al., 2012; Kääb et al., 2014; Matta et al., 2017. The blue and red shaded zones correspond respectively to the Pléiades and Sentinel-2 bands with the central wavelength outlined.*

We first take advantage of the 0.6 µm reflectance peak that is evident in the spectral signature of water in the visible range (Fig. 3.4) to map the supraglacial ponds using the Normalized Difference Water Index (NDWI) (Fig. 3.5), a metric used to map water bodies (McFeeters, 1996) and that was previously applied successfully to map lakes and ponds on debris-covered glaciers (Bolch et al., 2008; Gardelle et al., 2011; Huggel et al., 2002; Liu et al., 2015; Miles et al., 2018a; Watson et al., 2018; Wessels et al., 2002):

(Eq. 3.1) $$\text{NDWI} = \frac{R(\lambda_2) - R(\lambda_4)}{R(\lambda_2) + R(\lambda_4)}$$

Where $R(\lambda_i)$ is the reflectance value at the central wavelength λ_i. λ_1, λ_2, λ_3, λ_4 correspond to the four Pléiades bands in an ascending order and to the corresponding Sentinel-2 Bands 2, 3, 4 and 8 (Fig. 3.4, Table 3.S2). Water bodies have higher NDWI values than cliffs because the reflectance in the near infrared is lower than for ice. We define the supraglacial ponds as the pixels with a NDWI higher than a certain threshold T_{NDWI}, which is optimized for each scene (see Section 3.5.3):

(Eq. 3.2) $$\text{Ponds} = \text{NDWI} > T_{NDWI}$$

We then assess if the remaining pixels correspond to debris or cliffs by using the curvature C of the ice cliff spectra (Jia et al., 2019; Lee and Carder, 2000; Fig. 3.5), which is less pronounced than for pure ice or water but highlights the curved cliff spectra relative to the flat debris spectra (Fig. 3.4):

(Eq. 3.3) $$C = \frac{R(\lambda_4) + R(\lambda_1) - (R(\lambda_2) + R(\lambda_3))}{\sum_{i=1}^{4} R(\lambda_i)}$$

Since the absolute value of the curvature varies across the glacier depending on the cliff characteristics, we first filter the curvature by calculating the difference to the median over a moving window of 100 by 100 meters. The size of the area is chosen so that a majority of pixels within this zone are debris-covered. We then identify the cliffs as the pixels with a filtered curvature C_{filt} lower (more negative) than a certain threshold T_{curv}, which is optimized for each scene (see Section 3.5.3):

(Eq. 3.4) $$\text{Cliffs} = C_{\text{filt}} < T_{\text{curv}}$$
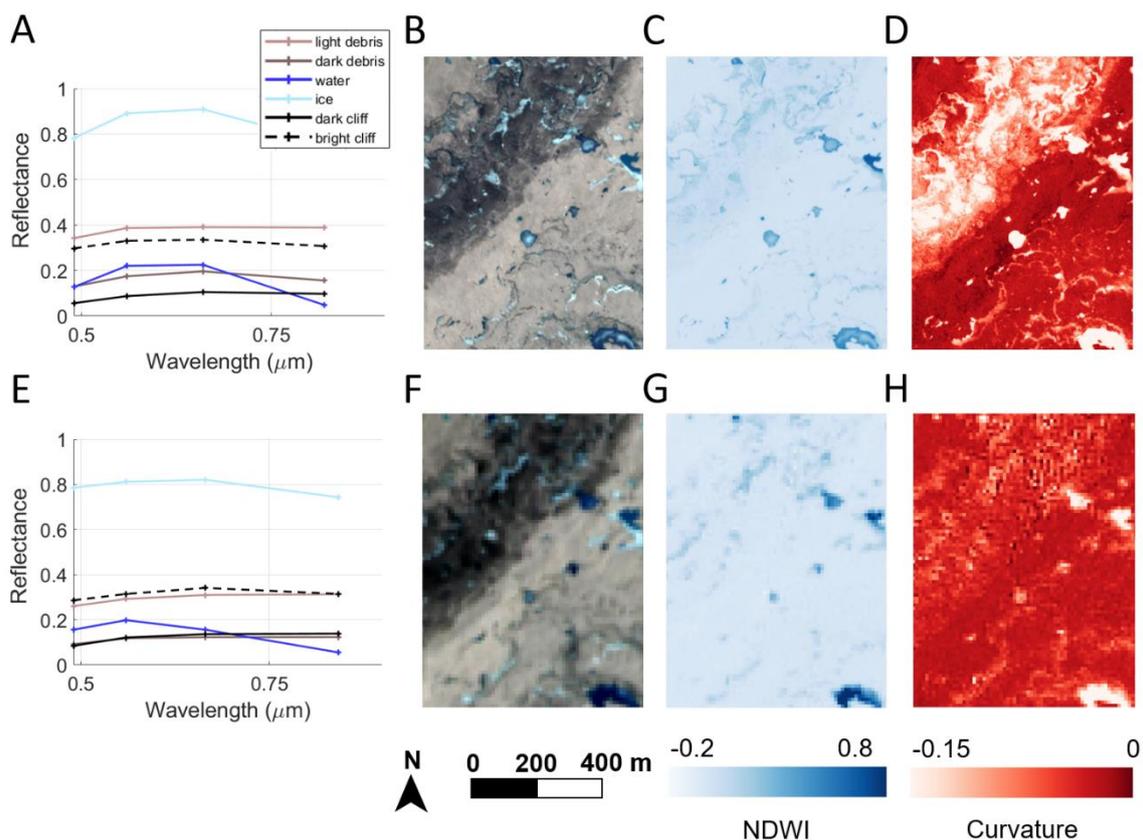
Figure 3.5. *Sampled spectra of ice, water, light and dark debris from the Khumbu Pléiades (A) and Sentinel-2 (E) images for the red, green, blue and near infrared bands. The black lines correspond to the spectra of two randomly chosen dark (plain line) and bright (dashed line) cliffs. We also show a subset of the Pléiades false color composite image (blue, green and near infrared bands) (B) along with its NDWI (C) and Curvature (D) maps and the Sentinel-2 false color composite image (blue, green and near infrared bands) of the same area (F) with its NDWI (G) and Curvature (H) maps.*

3.5.2.2.   Linear Spectral Unmixing

The LSU approach aims to provide the composition of each pixel based on its spectral signature, and can make use of the information contained in a large number of bands, while an approach using spectral indices is usually limited to three or four bands. In the case of Sentinel-2, additional information can be obtained from the six 20 m resolution bands, Bands 5, 6, 7, 8A, 11 and 12 (Fig. 3.4, Table 3.S2). For this purpose, we re-sample these to 10 meters using a nearest-neighbor approach, and apply the LSU to the ten resulting bands.

The LSU decomposes the spectrum of each pixel in the image as a linear combination of a set of pure spectral end-members. The coefficients of the linear combination can be interpreted as the abundance values of each of the spectral end-members in the image (Keshava and Mustard, 2002; Kopačková and Hladíková, 2014; Vikhamar and Solberg, 2003). These spectral end-members can be hand-picked directly from within a scene, at locations where it is assumed that the pixel is only composed of one of these pure elements. These surface reflectance values should be identical from one image to the other, and differences should reflect differences in surface composition. In all the following LSU and LSU

with scale (LSU-s) delineations applied to the Pléiades images we use the same spectral end-members extracted from the May 2016 Khumbu image. Similarly, for all Sentinel-2 scenes we use the same spectral end-members extracted in the Khumbu May 2016 Sentinel-2 image, at the same locations as the Pléiades spectral end-members. To extract these spectral end-members we manually select five pixels for each of the pure elements as our spectral end-points and take the average after confirming that the reflectance values are consistent between samples (Vikhamar and Solberg, 2003). For water, we sample non-frozen lakes outside of the glacier extents to avoid variations due to turbidity. Shallower lakes and presence of ice at the bottom can lead to a 60% increase in surface reflectance for on-glacier lakes (Fig. 3.S1A), but the shape of the spectrum is preserved, so the impact on the LSU is assumed to be limited. For ice, we sample bare ice patches in the ablation area with no identifiable surface dust. We use two spectral end-members for the debris to represent distinct lithologies, one for the light brown granitic debris that covers much of Khumbu Glacier and across the region (Hambrey et al., 2009) and one for the darker schistic debris which is predominant in the upper central area of Khumbu Glacier (Casey et al., 2012) and in some locations of the Langtang and Satopanth glaciers (Fig. 3.2, Fig. 3.S1C). For the light debris, we sample the side moraines and dry debris deposits while for the dark debris we sample the debris in the upper central area of Khumbu.

The spectrum of each pixel in a multi-spectral image can be expressed as a linear combination of these spectral end-members (Keshava and Mustard, 2002; Kopačková and Hladíková, 2014; Vikhamar and Solberg, 2003). For each pixel, the reflectance of each band can be expressed as the weighted sum of the reflectance values of the spectral end-members for this wavelength (Kopačková and Hladíková, 2014):

(Eq. 3.5) $$R(\lambda_i) \ = \ \sum_{j\,=\,1}^{n} \alpha_j r_j(\lambda_i)$$

Where $R(\lambda_i)$ is the reflectance at central band wavelength λ_i, n is the number of spectral end-members, $r_j(\lambda_i)$ are the reflectance values of end-members j at band λ_i and the coefficients α_j are calculated using a linear least squares approach to solve the system. The choice of the best coefficients α_j is constrained by imposing positive values:

(Eq. 3.6) $$\alpha_j \geq 0$$

The result is characterized by an error equal to the difference of the initial and calculated spectra. The coefficients α_j of the linear spectral unmixing are scaled so that the sum of the coefficients is equal to one:

(Eq. 3.7) $$\sum_{j=1}^{n} \alpha_j{'} = 1$$

Where:

(Eq. 3.8) $$\alpha_j{'} \ = \ \frac{\alpha_j}{\sum_{k\,=\,1}^{n} \alpha_k}$$

The final coefficients $\alpha_j{'}$ can then be interpreted as the abundance values of each pure element composing the pixel spectrum. The scaling factor $s = \sum_{j=1}^{n} \alpha_j$ gives information on the absolute reflectance values in the pixel relative to the reflectance values of the spectral end-members. A high scaling factor means that the reflectance values of the initial spectrum are high compared to the reflectance values of the spectral end-members that fit the shape best. This would be the case for example for a turbid pond (Fig. 3.4), which would be mapped as water but with a high scaling factor to account for its higher reflectance.

Thus, the results of the linear spectral unmixing are maps of the proportion of each spectral end-member within each pixel (Fig. 3.6). We use the water map to delineate supraglacial ponds using a threshold value of water T_{water} over which the pixels are considered to be ponds:

(Eq. 3.9) $$Ponds = water\ content > T_{water}$$

Once the ponds are delineated, we use a threshold value of ice T_{ice} to map ice cliffs:

(Eq. 3.10) $$Cliffs = ice\ content > T_{ice}$$

Both thresholds are optimized for each scene (Section 3.5.3). The ponds often have a non-negligible signature of ice in their spectrum so it is important to map them first to avoid them being mapped as cliffs.
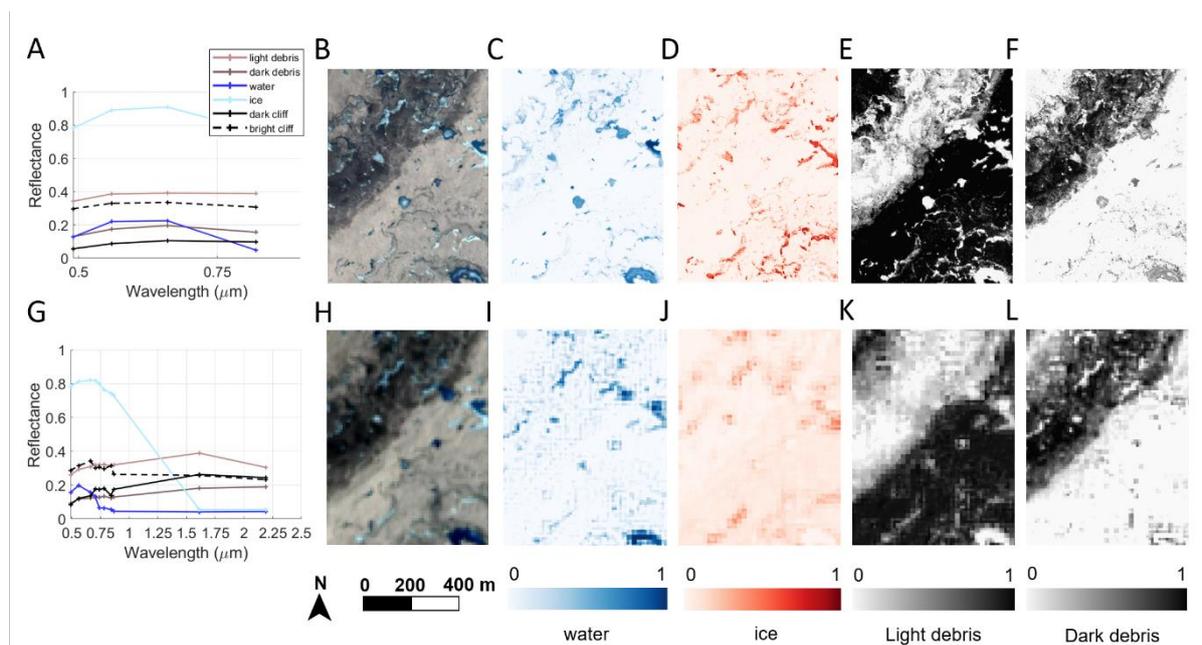
Figure 3.6. *Sampled spectra of ice, water, light and dark debris from the Khumbu Pléiades (A) and Sentinel-2 (G) images for all bands. The black lines correspond to the spectra of randomly chosen dark (plain line) and bright (dashed line) cliffs. (B). We also show a subset of the Pléiades false color composite image (B) along with its water (C) ice (D), light (E) and dark (F) debris content and the Sentinel-2 false color composite image of the same area (H) with its water (I) ice (J), light (K) and dark (L) debris content.*

3.5.2.3.   Linear Spectral Unmixing with scale

Mapping cliffs with the LSU approach can be challenging, as the 'ice' component of the cliff area can be small due to their mixed surface composition (Fig. 3.5), and the 'water' and 'ice' spectral end-members are not independent (Fig. 3.4). Furthermore, the reflectance values obtained for bare ice can change by more than 100% from site to site depending on the amount of englacial debris, and differences in foliation, orientation or density (Fig. 3.S1B). Thus, in this alternative implementation of LSU, we consider ice cliffs as falling into two categories: one in which cliffs consist of bare ice and snow, exhibiting high reflectance values, and one in which they are lightly debris covered and wet, and thus exhibit very low reflectance values. In both cases, the resulting cliff spectrum can be described as a combination of water and debris spectral end-members, but only by removing the constraint that

subpixel components must sum to one (Eq. 3.7). In the case of bright cliffs, the required combination would sum to much greater than one, corresponding to a high scale factor s while dark, thinly debris-covered cliffs scale factor s would be very low.

Therefore, in this linear spectral unmixing with scale (LSU-s) approach, we only use the pure spectra of water, light debris and dark debris for the unmixing, and use the scale map s as an additional criterion to map cliffs (Fig. 3.7). As s varies proportionally to one, we take the logarithm of its value and filter it similarly to the Spectral Curvature by subtracting the value of the median calculated over a 100 by 100 meters moving window. The cliffs are then delineated first, using two scale thresholds, T_{bright} for the bright cliffs and T_{dark} for the dark cliffs:

(11) $$Cliffs = (ln(s) < T_{dark}) \mid (ln(s) > T_{bright})$$

In a second step, the ponds are delineated using a NDWI threshold. A simple water threshold based on the ratio of the near infrared and the green bands was also tested for the ponds but the results were never as good as those obtained with the NDWI.
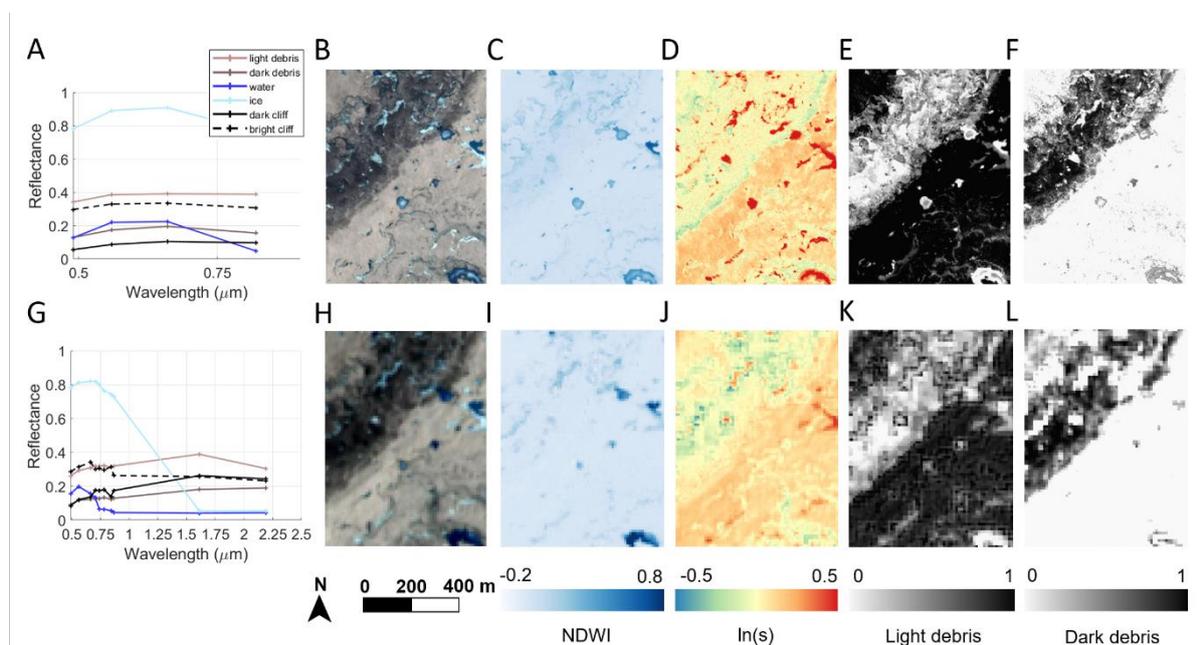
Figure 3.7*. Sampled spectra of ice, water, light and dark debris from the Khumbu Pléiades (A) and Sentinel-2 (G) images for all bands. The black lines correspond to the spectra of randomly chosen dark (plain line) and bright (dashed line) cliffs. (B). We also show a subset of the Pléiades false color composite image (B) along with its NDWI (C) filtered scale (D) maps, light (E) and dark (F) debris content and the Sentinel-2 false color composite image of the same area (H) with its NDWI (I) filtered scale (J) maps, light (K) and dark (L) debris content.*

3.5.3. Optimization

We evaluate the results of the different mapping methods against a set of manually delineated cliffs and ponds. In each of the Pléiades scenes, we manually outline a subset of 20-40 cliffs and 25-30 ponds of different surface characteristics to serve as a validation dataset. Illumination conditions or high-density cliff zones make it difficult to pick out the individual features, so we only outline features for which our

confidence in the manual delineation is high (Fig. 3.8B). We then define a test area with a fifty-meter buffer around all mapped features and manually map the remaining features within this buffer zone (Fig. 3.8C). These buffers maintain a balance between the proportion of cliff or pond and debris in the area tested. The outlines were checked independently by a second operator who modified them when deemed necessary. The test area thus defined corresponds to 5% to 13% of the total area where we applied the cliff delineation methods and is distributed across the entirety of the study glaciers to exclude bias due to particular conditions (Fig. 3.S2, S3, S4).

The results of each cliff mapping method are compared to the manual results for the full test area, for both cliff and pond outputs. Each pixel within the buffer zones is then categorized as true positive, true negative, false positive or false negative as part of the confusion matrix for both pond and cliff coverages, in order to quantify our results (Fig. 3.8D). The best threshold parameters are determined by optimizing the Dice coefficient defined as:

(Eq. 3.12)
$$Dice = \frac{2TP}{2TP + FP + FN}$$

Where TP is the number of true positive pixels, FP the number of false positive pixels and FN the number of false negative pixels. As such, the Dice coefficient penalizes both missing cliff pixels and debris pixels falsely detected as cliff, and is not biased by TN, the number of true negative pixels (Buri et al., 2016a; Dice, 1945; Rittger et al., 2013). This contrasts with metrics such as the accuracy (Eq. 3.13) which produces a value with direct meaning (the portion of correctly mapped pixels), but which can lose meaning for mapping low-density features. As the cliff or pond area is generally small compared to the debris area in the buffer zones (less than 10% of area), the number of true negative pixels is usually high, and results in high accuracy values regardless of the false negative and positive values:

(Eq. 3.13)
$$Accuracy = \frac{TN + TP}{TN + TP + FP + FN}$$

Manually mapping cliffs in the Sentinel-2 images is difficult and highly uncertain due to the coarse spatial resolution of the sensor, so we instead degrade the validation datasets derived from the corresponding Pléiades scenes. The Pléiades and Sentinel-2 images are first co-registered using a normalized cross-correlation approach with ImGRAFT (Messerli and Grinsted, 2015) by taking the average displacement value to translate the Sentinel-2 image. We then degrade the Pléiades validation dataset to the Sentinel-2 resolution of 10 meters, and reclassify as cliffs or ponds the pixels that contain more than 50% of the original cliff or pond coverage.
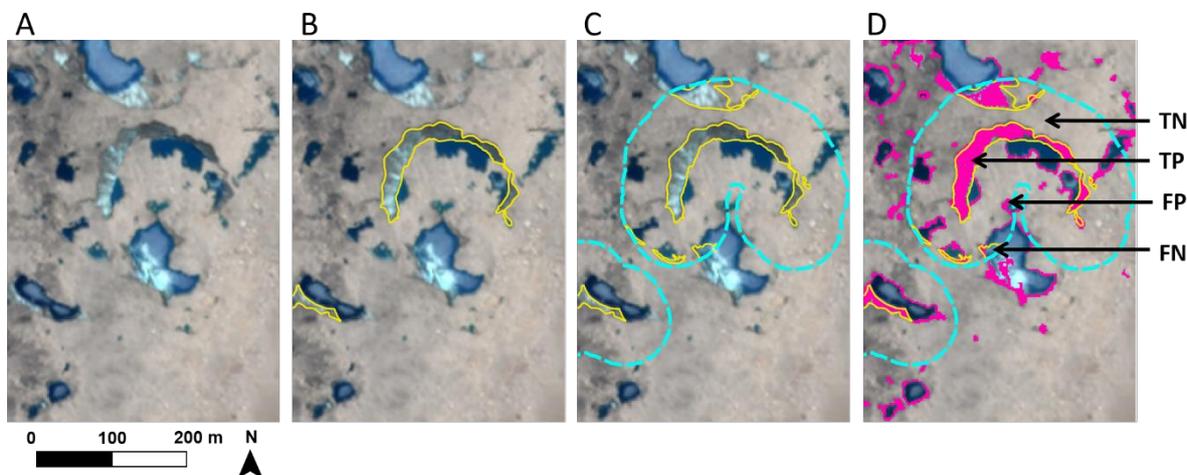
***Figure 3.8**. Producing the cliff validation dataset and evaluating results, showing the original Pléiades Khumbu 2016 false color composite image (A), manual delineation of high-confidence cliffs (B), the 'test area' as a 50 m buffer around the cliff and manual delineation of the remaining cliffs within that area (C), and comparison of results (pixels colored in pink) with the validation dataset (yellow outlines) by counting true positives, true negatives, false positives and false negatives (D).*

3.5.4. Application of other existing methods

We compare our SC, LSU and LSU-s approaches with other existing methods by applying these to the Langtang and Satopanth Pléiades 2 m multi-spectral images or DEMs when required, using the same parameters as in the original studies as much as possible. No DEM is available for the Khumbu scene so we do not test the slope-based methods for this scene. We test: 1) a fully automated **adaptive slope threshold (AST)** approach that also extends the narrowing ends of cliffs (Herreid and Pellicciotti, 2018), 2) a semi-automated **simple slope threshold (SST)** approach (Reid and Brock, 2014), 3) a semi-automated **adaptive binary threshold (ABT)** approach (Anderson et al., 2019b), and 4) an **OBIA segmentation combined with a manual delineation (OBIA-m)** (Kraaijenbrink et al., 2016b; Mölg et al., 2019, 2020). For the automated AST, we use the same set of initial parameters as applied on Canwell and Ngozumpa glaciers (Herreid and Pellicciotti, 2018). Due to computational limitations we run this approach using DEMs bilinearly re-sampled to 5 m resolution, as in the original study. For the semi-automated SST and ABT approaches (Anderson et al., 2019b; Reid and Brock, 2014), we recalibrate the parameters for each image as for our own methods. For the ABT, we emulate the original implementation by defining the brightness as the mean value of the four bands, and we consider as cliff the pixels for which the difference between brightness and mean brightness across a certain window is lower than a certain threshold (Anderson et al., 2019b):

(Eq. 3.14) $$Cliffs = (Brightness - mean\,brightness) < T_{offset}$$

We optimize the window size along with the brightness threshold. As a result, the ABT approach we test here also has less parameters than in the original study (Anderson et al., 2019b). For the OBIA-m approach (Kraaijenbrink et al., 2016b) we use the open-source software SAGA GIS to segment the multi-spectral image (Conrad et al., 2015). We do not reproduce the classification step detailed in the original study (Kraaijenbrink et al., 2016b), but rather use a manual delineation applied to the results of the segmentation step (Mölg et al., 2020, 2019). Results of each method are assessed against the same validation datasets that we use for all three scenes. We also take into account the results provided in the different studies and express them in terms of Dice coefficient to make them comparable.

3.6.   Results

3.6.1. Spectral Curvature

Using the NDWI and Curvature, we obtain maximum values of the Dice coefficient between 0.85 and 0.9 for ponds for the three scenes (Fig. 3.9A) and between 0.50 and 0.69 for cliffs (Fig. 3.9B) for the Pléiades image. For Sentinel-2, the maximum Dice coefficient is also high for ponds, between 0.78 and 0.89, but lower for cliffs, between 0.44 and 0.45 (Fig. 3.9D-E). The peaks in Dice coefficients are obtained for very similar threshold values in each image, and more broadly speaking, there are consistent ranges of values for which the Dice coefficient is close to its maximum value in all three images for both cliffs and ponds of both the Pléiades and the Sentinel-2 images. For cliffs in the Pléiades

images, this happens for filtered Curvature between -0.04 and -0.02. There is a slight shift in NDWI for Khumbu (Fig. 3.9A, D), where there is a lot more dark, wetted debris, which tends to also have higher NDWI values (Fig. 3.5). For this image, the range of values maximizing the Dice for cliffs is also shifted to slightly higher values and the maximum Dice is lower than in the other images (Fig. 3.9B). Overall, the areas mapped based on Sentinel-2 data are in good agreement with those based on Pléiades but the cliffs do not stand out as clearly (Fig. 3.9C, F).

3.6.2. LSU

Applying LSU to the Pléiades images, we obtain maximum Dice coefficients ranging between 0.60 and 0.88 for ponds and between 0.12 and 0.49 for cliffs (Fig. 3.9G-H). For Sentinel-2, the maximum Dice ranges between 0.55 and 0.62 for ponds, and between 0.16 and 0.49 for cliffs. Furthermore, the range of optimal NDWI and curvature values changes from one image to the other. We obtain low Dice values for Khumbu ponds, while for Langtang and Satopanth, very low optimal threshold values show that all pixels with any water content are categorized as ponds (Fig. 3.9G). Thus, for Satopanth and Langtang all the cliffs are mapped as ponds and cannot be characterized properly by an ice threshold (Fig. 3.9H). For the Khumbu image, the thinly debris-covered cliffs are mapped as debris and only the bare ice patches are categorized as cliffs (Fig. 3.9I). Similar results are observed for the Sentinel-2 images, although with some improvement in the Dice values for the cliffs (Fig. 3.9J-L).

3.6.3. LSU-s

For the LSU-s approach we obtain Dice coefficients ranging from 0.61 to 0.83 for ponds (Fig. 3.9M) and from 0.38 to 0.53 for cliffs (Fig. 3.9N) using the Pléiades images. For Sentinel-2, the maximum Dice coefficient is between 0.58 and 0.75 for ponds, and between 0.51 and 0.52 for cliffs. As with the SC results, there are ranges of values that maximize the Dice for each of the images, especially for Sentinel-2. For the cliffs, the main control on the results comes from the lower scale threshold. As long as the upper scale threshold is around 0.20, the change in Dice values is relatively small except for Khumbu where bright cliffs are prevalent (Fig. 3.9N, Q). The Khumbu Dice curve for cliffs is flatter for low values of lower scale threshold, highlighting that 'dark' cliffs have very low scale values in this image. The ponds are mapped after the cliffs here, and NDWI mapping results are slightly different from the ones obtained with the SC approach with a decrease of the maximum dice coefficients by 0.1 to 0.3 (Fig. 3.9A, D, M, P).
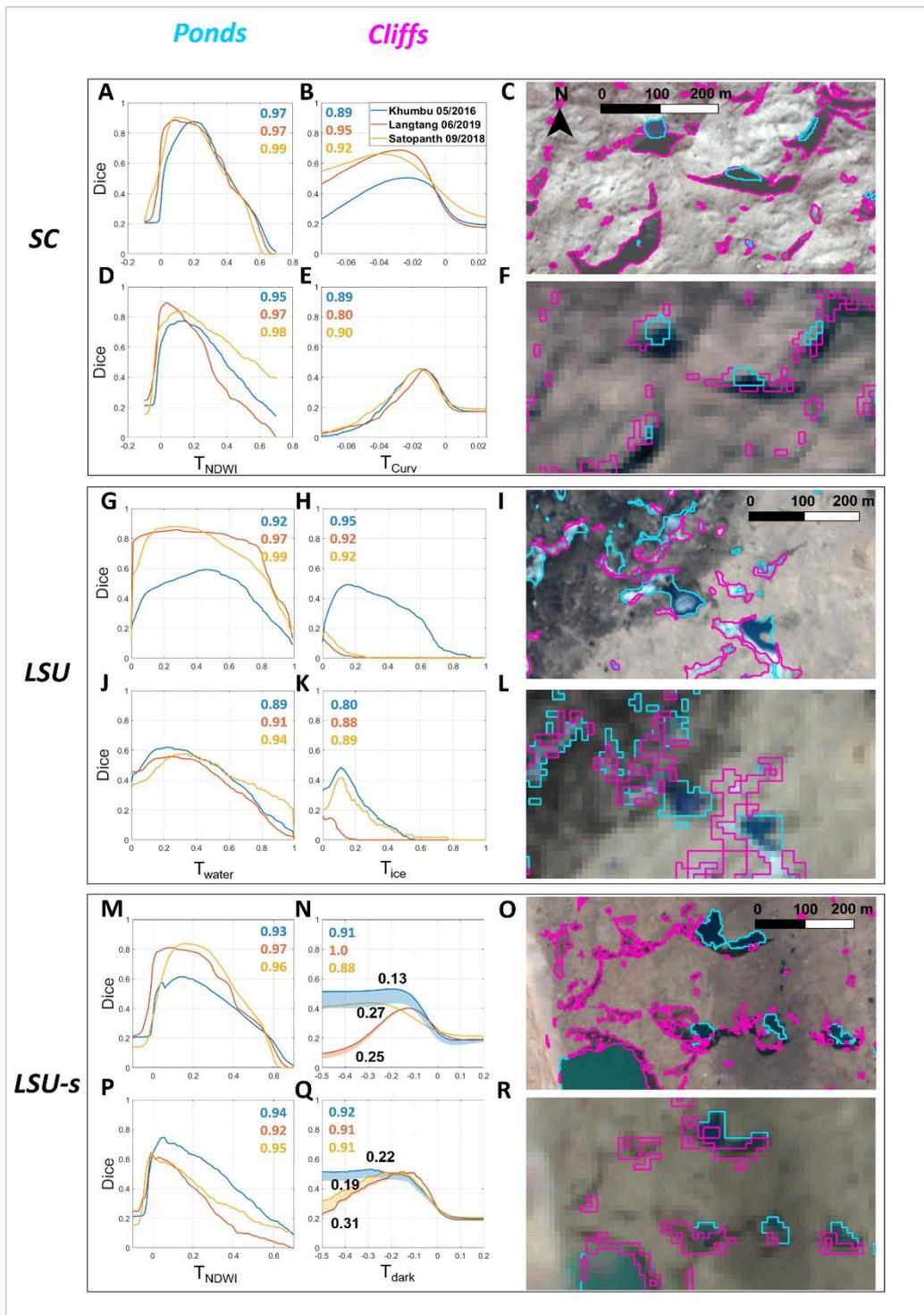
Figure 3.9. *SC, LSU and LSU-s results for the Pléiades and Sentinel-2 scenes showing the Dice coefficients obtained for ponds (left panels) and cliffs (middle panels) for different threshold values, as well as examples of cliff (pink) and pond (light blue) outlines plotted over the same areas of the Pléiades and Sentinel-2 false color composites (right panels). For SC, LSU and LSU-s methods the outline examples are extracted respectively from the Satopanth, Khumbu and Langtang scenes. For each method, the three upper panels correspond to the results obtained with the Pléiades images and the three lower panels are the results obtained with the Sentinel-2 scenes.*

3.6.4. Comparison of methods

The highest Dice coefficients are obtained for cliffs and ponds mapped with the SC approach applied to the Pléiades scene (Fig. 3.9, 10, Table 3.1). These values are high relative to other published approaches, but some noise remains and there are non-negligible false positive patches in the debris area compared to the manual delineation (Fig. 3.9C, 10B). The LSU method performs very poorly for both Pléiades and Sentinel-2 (Fig. 3.9I, 10C, G), but the LSU-s method has the best results for Sentinel-2 (Fig. 3.9P-R, 10H) with a relatively low number of false positives.
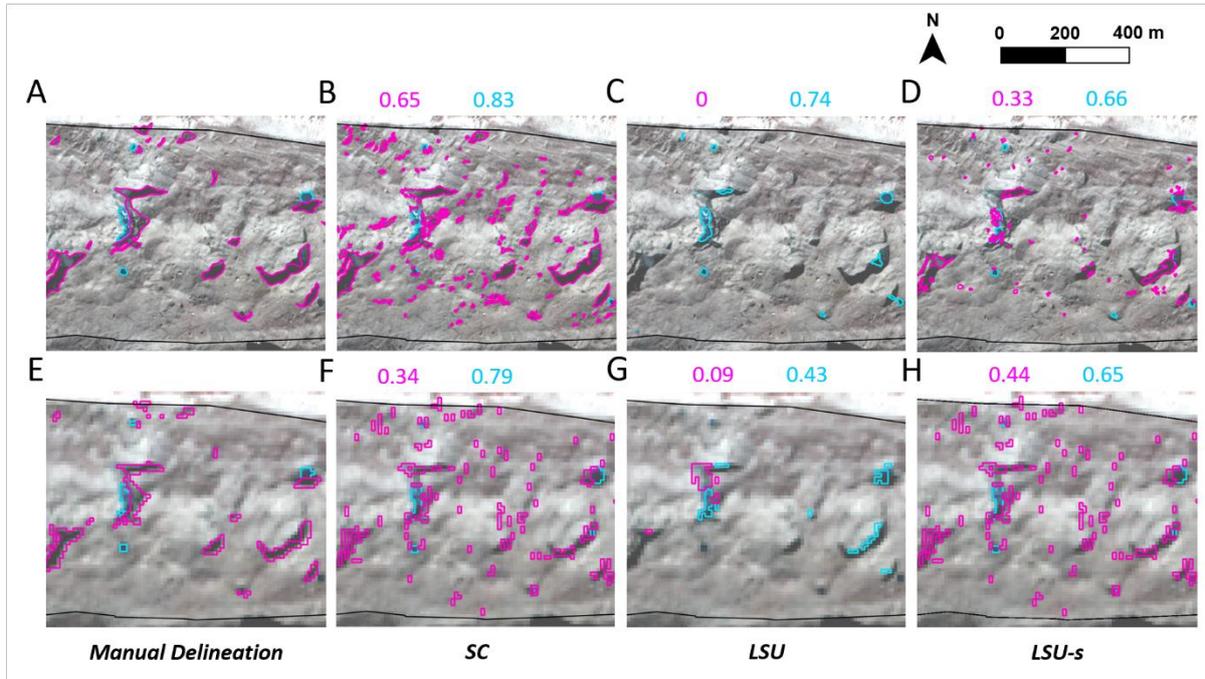
Figure 3.10. *Comparison of the three new methods with a manual delineation of cliffs and ponds on a portion of Bhagirati Kharak glacier (Satopanth 09/2018 scene). The upper panels are for the Pléiades image and the lower ones for the Sentinel-2 image with the false color composite as background. The values in pink (resp. light blue) correspond to the Dice coefficient of the cliffs (resp. ponds) relative to the manually delineated outlines in this small domain. The backgrounds correspond to the Pléiades and Sentinel-2 false color composites.*

We apply the other existing methods to Langtang and Satopanth Pléiades scenes, and to the Khumbu Pléiades scene for the ABT approach (Table 3.1). For the images tested, the OBIA-m gives the same results as the manual delineation, but is faster due to the initial automated segmentation of the orthoimage in objects with similar spectral characteristics. The optimized Dice coefficients of the SST are similar from one scene to the other (Table 3.1), but are not obtained for the same slope threshold values (Fig. 3.S5). The optimized Dice coefficients of the ABT vary between 0.24 and 0.64 depending on the scenes (Table 3.1, Fig. 3.S6). These results can be improved when delineating the ponds first with the NDWI (Table 3.1). The ponds are also not mapped by the slope-based approaches but this has a limited effect on the classification (Fig. 3.11, S3). The AST approach has a dice coefficient ranging from 0.40 to 0.55 obtained with the same initial parameters as in the original study (Herreid and Pelicciotti, 2018).

Table 3.1. *Evaluation of different mapping methods for cliffs. In color are the methods tested in this study, including those requiring manual delineation (red), and the automated and semi-automated ones*

(purple). For the three methods developed in this study, we chose the same threshold values for all three Pléiades scenes. Transferability is a qualitative assessment characterizing the ability of the methods to produce consistently good performance from scene to scene.

Original studies	Name	Data required	Original resolution (m)	Original Dice coefficient	Resolution for this study (m)	Dice Langtang	Dice Satopanth	Dice Khumbu	Transferability
Reid and Brock, 2014	*SST*	DEM	1	Not given	2	0.43	0.51	NA	High
Herreid and Pellicciotti, 2018	*AST*	DEM	5	0.52 and 0.40	5	0.49	0.55	NA	High
Kraaijenbrink et al., 2016	*OBIA*	Multispectral image. DEM for classification.	0.5	0.94	Not tested	Not tested	Not tested	Not tested	Not tested
Mölg et al., 2020, 2019	*OBIA-m*	Orthoimage	0.5 – 1	NA	2	NA	NA	High	High
Anderson et al., 2019	*ABT*	Multispectral image	0.5	0.65	2	0.64 *0.70**	0.49 *0.51**	0.24 *0.25**	Low
This study	*SC*	Multispectral image	NA	NA	2	0.69	0.65	0.50	High
This study	*LSU*	Multispectral image	NA	NA	2	0.02	0.04	0.50	Very low
This study	*LSU-s*	Multispectral image	NA	NA	2	0.38	0.40	0.52	High

* Values in italics correspond to Dice coefficient of cliffs after delineating the ponds using the NDWI
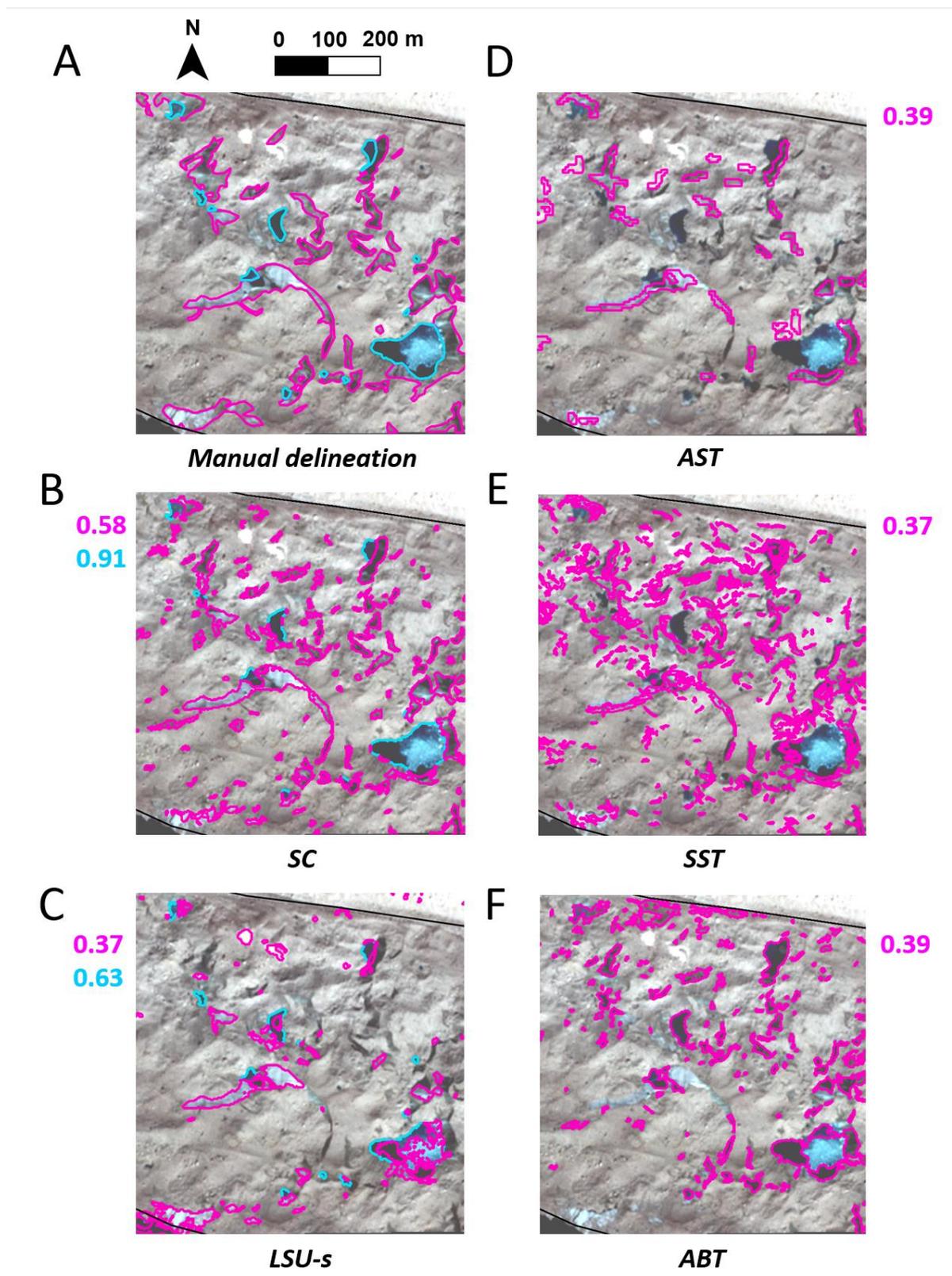
Figure 3.11. *Comparison of the manual delineation (A), SC (B), LSU-s (C), AST (D), SST (E) and ABT (F) approaches for a section of Bhagirati Kharak glacier (Pléiades Satopanth 09/2018 scene). The values in pink (resp. light blue) correspond to the Dice coefficient of the cliffs (resp. ponds) relative to the manually delineated outlines in this small domain. The background corresponds to the Pléiades false color composite.*

3.6.5. Cliff and pond coverage at each site

We report the count, total projected area and density (total feature projected area as a percentage of area) of cliffs and ponds obtained by applying the SC approach to the Pléiades and the LSU-s to the Sentinel-2 scenes as these are the best performing methods for the corresponding sensors (Table 3.2). The cliff density observed in the Pléiades scenes is the same for Khumbu and Satopanth (9.2%), but lower for Langtang (3.3%). The cliff density is higher than the pond density in all scenes, respectively 1.9, 3.7 and 13.1 times higher than the pond density on Langtang, Khumbu and Satopanth. The pond density is between 1.7 and 2.5% for Khumbu and Langtang, but only 0.7% for Satopanth.

There are 1.2 to 7.2 times fewer features detected with the LSU-s applied to the Sentinel-2 images compared to the SC applied to the Pléiades images, with this difference being higher for cliffs (Table 3.2). The pond density is higher for Sentinel-2 than for Pléiades, but for cliffs, this is only the case on Langtang glacier (Table 3.2). There are a high number of cliffs smaller than 100 m^2 outlined using the Pléiades imagery, accounting for 11 to 22% of the total area of the outlined cliffs in one image (Fig. 3.12), so the area per feature is higher for the Sentinel-2 outlines.

Table 3.2. Cliffs and ponds metrics obtained from the SC approach applied to the Pléiades images, and from the LSU-s approach applied to the Sentinel-2 images. The density corresponds to the total cliff projected area divided by the total debris-covered area.

Glacier	**Khumbu 05/2016**		**Langtang 06/2019**		**Satopanth and Bhagirati Kharak 09/2018**	
Sensor	**Pléiades**	**Sentinel-2**	**Pléiades**	**Sentinel-2**	**Pléiades**	**Sentinel-2**
Cliff metrics						
Number	1973	348	1858	383	2435	337
Planimetric area (m²)	526,000	222,600	273,600	388,500	524,100	205,500
Density (%)	9.2	3.9	3.3	4.7	9.2	3.6
Pond metrics						
Number	463	274	354	266	94	77
Planimetric area (m²)	142,800	173,900	144,600	211,300	37,000	51,600
Density (%)	2.5	3.0	1.7	2.5	0.7	0.9
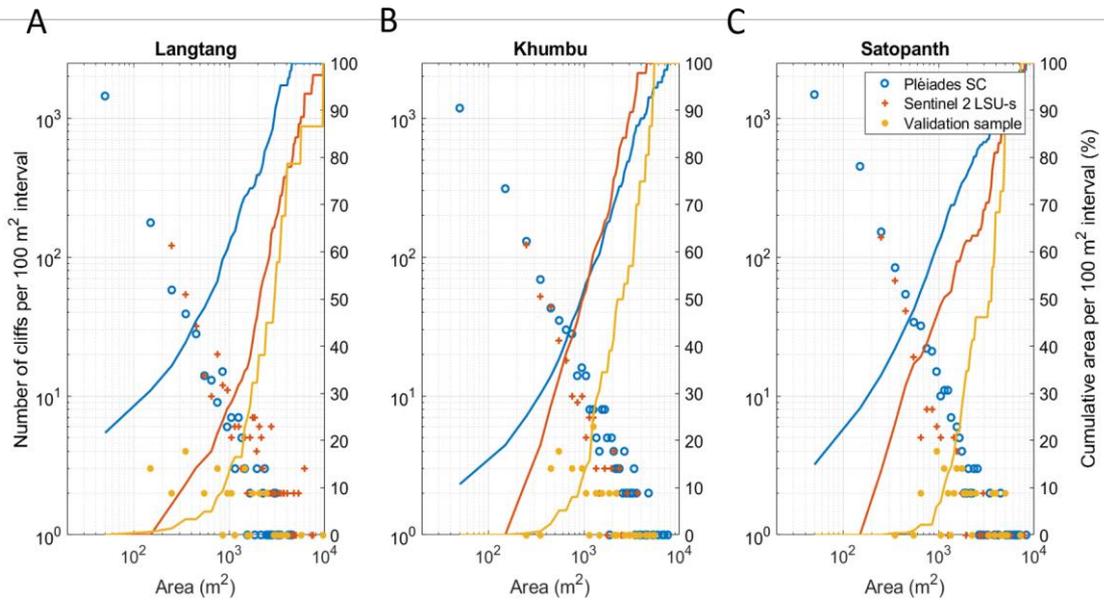
Figure 3.12. *Number (markers) and cumulative area (lines) of cliffs per 100 m² planimetric area intervals in each image for the SC applied to the Pléiades image, the LSU-s applied to the Sentinel-2 image, and the manually delineated validation dataset.*

3.7. Discussion

3.7.1. Evaluation of methods

Here we assess our new methods along with other published approaches in terms of their performance, transferability and ease of implementation.

3.7.1.1. Comparison with past studies

Our results for both Khumbu and Langtang using the SC method with Pléiades data are consistent with previous reported cliff and pond density (planimetric area of cliffs or ponds divided by the total area of the debris-covered zone where the delineation was applied) values using manually delineated outlines. Pond density on Khumbu in May 2009 was 2.9%, which is consistent with the 2.5% value that we find in our Khumbu pre-monsoon scene, in the upper portion of the glacier (Watson et al., 2017a). For Langtang, the pond coverage peaks around 2% in June (Miles et al., 2017c; Steiner et al., 2019), also consistent with our 1.7% density. We find a cliff density of 3.3% on Langtang, which agrees with previously reported values of 3.4% (+/- 0.9%) (Steiner et al., 2019). Previous studies have reported a 4% cliff density on Khumbu (Watson et al., 2017a), but it was calculated based on a digitization of cliffs as lines with no consideration of cliff area, this number is therefore not comparable with the 9.2% cliff density that we find. The pond density values obtained with the Sentinel-2 images are within the range of previously reported values for Khumbu and Langtang, and slightly higher than previously reported for the Langtang cliffs.

104

Our three new methods map ice cliffs simultaneously with ponds, which are detected with high accuracy across scenes and methods (Fig. 3.9), and which we briefly discuss here. Ponds are best mapped on both Pléiades and Sentinel-2 images (Dice coefficients higher than 0.85 and 0.75 respectively) using a NDWI threshold. As such, using a 10 m instead of a 2 m resolution image has relatively little impact on the pond classification accuracy, although the pond density is 25 to 30% higher with Sentinel-2 than with Pléiades in our results, highlighting a possible overestimation of the pond density with Sentinel-2 likely due to mixed marginal pond pixels (Table 3.2, Fig. 3.9A, D, M, P). The suitability of Sentinel-2 images for mapping ponds was identified by Watson et al., 2018 and is promising for extensive and repeated mapping of ponds. The range of threshold values maximizing the Dice (0.05-0.2) is consistent from image to image and sensor to sensor, and a value of 0.1 is the best compromise to delineate ponds automatically in all images. It is worth noting that images with large extents of dark, wetted debris exhibit higher NDWI and Curvature values (Fig. 3.5), as in the Khumbu scene. This results in a shift of the optimal threshold value from 0.05 to 0.2 to avoid mapping parts of the debris as ponds (Fig. 3.9A, D).

Considering our primary objective of mapping cliffs, we obtain satisfactory results for cliffs using the SC, with a Dice higher than 0.45 for the Sentinel-2 and higher than 0.5 for the Pléiades images. Performance is higher (Dice >0.6) for the Pléiades images when the extent of dark wetted debris is lower (Fig. 3.9B). Wetted debris patches can indeed be erroneously identified as cliffs due to their increased spectral curvature values. We obtain poor results for mapping cliffs using the LSU approach for both Pléiades and Sentinel-2. In this case, unless there is bright bare ice, the cliffs are identified as water or debris, which is the result of the mixed signals of wetted debris on an ice face. Cliffs with bright bare ice are more frequent on Khumbu, where we obtain relatively better results (Fig. 3.9H, I, K, L), while in the Langtang and Satopanth scenes almost all cliffs are categorized as ponds in the first step (Fig. 3.9G, H, J, K). We also found higher reflectance values for bare ice in the Khumbu scene than in the Langtang scene (Fig. 3.S1B), which indicates that the ice end-member we used is not representative enough to map the Langtang and Satopanth cliffs. This could come from changes in englacial debris concentration, and differences in orientation, density or foliation and these variations in the bare ice spectra from glacier to glacier and from scene to scene make the LSU approach difficult to apply in general. The LSU-s does not depend on the bare ice spectrum and uses the additional information from the Sentinel-2 re-sampled 20 m bands to maximize the Dice coefficient around 0.5 for each of the three scenes, making it the best method to map cliffs with this sensor (Fig. 3.9Q). In some cases of extensive darker debris patches (such as on Khumbu and locally on Satopanth), the scale filtering may not be sufficient to outline all the cliffs from the Sentinel-2 image, resulting in an underestimation of the total cliff area and density (Table 3.2). The LSU-s method does not perform as well for Pléiades as for Sentinel-2, especially in the Langtang and Satopanth scenes (Fig. 3.9N), for which there are false positive results for locally darker debris patches that are spectrally similar to thinly debris-covered cliffs (Fig. 3.9O).

We obtain varying results from the other cliff mapping approaches. A SST approach can produce a reasonably accurate cliff distribution with Dice coefficients between 0.43 and 0.51 for Langtang and Satopanth, but requires recalibration for each scene since the optimal slope threshold varies from 29° for Langtang to 40° for Miage (Fig. 3.S5, Reid and Brock, 2014). This recalibration can be avoided by using an automated method such as AST with its original parameters (Herreid and Pellicciotti, 2018), which also produces slightly higher Dice coefficients between 0.40 and 0.55 (Table 3.1, Fig. 3.11, S7). The dependence of this method on the DEM spatial resolution is partially compensated by extending

the cliff ends, where the cliff is narrowest and the slope susceptible to be saturated (Herreid and Pellicciotti, 2018). The ABT (Anderson et al., 2019b) requires particular conditions to produce reasonable results (Table 3.1, Fig. 3.11F). We optimized the brightness threshold and the window size of this method for the three Pléiades scenes and get a Dice of 0.64 for Langtang and 0.49 for Satopanth, but for Khumbu the Dice is lower than 0.25 (Table 3.1, Fig. 3.11F, Fig. 3.S6). This approach works relatively well for Langtang since the cliffs are generally much darker than the surrounding debris, but performance suffers in the Khumbu scene and parts of the Satopanth scene because 1) the debris can be as dark as the wetted cliff surfaces and 2) many cliffs have very bright bare ice patches (Fig. 3.11, (Anderson et al., 2019b). A second brightness threshold would be necessary to identify these cliffs. This method also only maps cliffs without taking the ponds into account, which results in most of the ponds being also mapped as cliffs due to their similar brightness values (Fig. 3.11, 3.S7). The ABT therefore benefits from pond mapping with NDWI prior to its application (Table 3.1), producing Dice coefficient values nearly as high as our SC approach for the Langtang scene.

3.7.1.3. *Transferability of methods*

We define transferability as the capability of a method to produce consistently good performance for different sites or input data. Transferability is therefore important to enable widespread use of a method. We assess each method's transferability by examining its performance across three scenes with different climatic and geomorphological settings.

We consider the SC approach to be transferable for Pleiades data as the Dice is maximized for the same range of curvature thresholds (-0.04 to -0.02). Based on the optimized Dice coefficients, a curvature value of -0.03 is a good compromise to map cliffs in all scenes (Fig. 3.9B). Similarly the LSU-s appears to be transferable for Sentinel-2 data, as an upper filtered scale threshold of 0.2 (log scale) and a lower filtered scale threshold of -0.2 (log scale) maximize the Dice coefficient of mapped cliffs around 0.5 in all three Sentinel-2 scenes while a NDWI threshold of 0.1 maximizes the Dice coefficient of ponds. Both slope-based approaches are also transferable, with Dice coefficients between 0.40 and 0.55 for all the scenes where they were applied, including on an Alaskan glacier for the AST (Herreid and Pellicciotti, 2018). This is not the case for the ABT (Anderson et al., 2019), which does not work when the debris is as dark or darker than the cliffs.

Our assessment of transferability encompasses climatic and geomorphological settings of Nepal and Indian Himalaya, including images taken in the pre-monsoon, monsoon and post-monsoon season. We expect that the approaches classified as transferable in this study should also be transferable to other glaciers in other mountain ranges, but accounting for variable lithology may require some adjustment to the LSU-s as well as to the SC approach, and the transferability beyond the Himalaya needs to be evaluated. Furthermore, application of any cliff mapping method is limited to cloud- and snow-free debris-covered areas, which need to be accurately outlined prior to the mapping. This was done manually in this study since we focused on a limited number of glaciers, but is an important prerequisite to be considered when trying to map cliffs at the regional scale in an automated way. For this purpose, the debris-covered area of a glacier can be mapped automatically using glacier outlines and a band ratio (Herreid et al., 2015; Kraaijenbrink et al., 2017), which has led to the recent release of global maps of supraglacial debris-cover extents (Herreid and Pellicciotti, 2020a; Scherler et al., 2018). Snow-covered areas can be mapped automatically using an adaptive normalized difference snow index (NDSI) (e.g. Girona-Mata et al., 2019; Rastner et al., 2019) and automated approaches exist to mask cloud-covered areas along with zones with deep shadows (Chen et al., 2013; Miles et al., 2017c; Zhu et al., 2015).

Manual delineation of cliffs over the entirety of a glacier is very time-consuming. For one or a few glaciers, applying the OBIA-m approach is a worthwhile improvement as it gives results equivalent to a full manual delineation while being several times faster. Indeed, once the segmentation has been applied, the operator only needs to select the clusters comprising cliffs and ponds and adjust the outlines (Table 3.1, Mölg et al., 2020, 2019).

For a larger domain, using a (semi-)automated and transferable approach can be advantageous as in theory no recalibration needs to be conducted. The AST approach detects cliffs iteratively using a set of pre-calibrated parameters and is as such entirely automated. However it is computationally expensive even for one glacier regardless of its setting (Herreid and Pellicciotti, 2018); we could only run it for 5 m resolution degraded DEMs (Table 3.S3). This method uses the abundance of cliffs to optimize the slope threshold so it also requires, contrary to the other approaches, very accurate outlines of the debris-covered area, otherwise it identifies steep surrounding topography as large cliffs, which can impact the slope threshold identifying ice cliffs (Herreid and Pellicciotti, 2018). The SC and LSU-s approaches are both transferable at the scale of the Himalaya, semi-automated and computationally much faster than the AST. The SC approach is the faster of the two, as it does not require the spectra of each pixel to be decomposed (Table 3.S3). The SST and ABT are also computationally efficient approaches (Table 3.S3) but less transferable than the SC or the LSU-s. When applying the SST and ABT approaches to glaciers with different surface characteristics, or the SC and LSU-s outside of the Himalaya, recalibrating the parameters of the method is necessary. This implies that for each scene a dataset of 20-30 cliffs and ponds needs to be manually outlined. This is feasible when dealing with a few satellite images, but becomes difficult when dealing with many glaciers with very different surface characteristics. Furthermore, this requires fine spatial resolution and high-quality spectral data for which manual delineation is possible.

3.7.2. Definition of ice cliffs

The different mapping methods have each been developed to target a specific definition of ice cliffs. While the slope-based approaches assume that the main characteristic of a cliff is its steepness (Herreid and Pellicciotti, 2018; Reid and Brock, 2014), the multi-spectral approaches, including the new approaches developed in this study and Anderson et al. (2019b), assume that surface reflectance characterizes cliffs and map them based on their spectral signature, without taking into account the slope. Other approaches such as manual delineation may use a combination of slope and spectral signal criteria, for example mapping first with the spectral information and refining the outlines by discriminating ice cliffs and shallow-sloping ice patches (Kraaijenbrink et al., 2016b; Steiner et al., 2019; Watson et al., 2017a). These variations in the definition used may lead to mismatch between the resulting datasets, even though they should broadly agree, as the surface exposure of ice within the debris-covered area implies that the debris has been displaced from this zone, which requires the presence of a slope, sometimes combined with the action of water (Moore, 2018).

Both spectral and slope-based delineation methods outline zones that do not look like cliffs and that an operator would classify as false positive objects, but that contain the spectral signature or high slope exhibited by cliffs, and sometimes both (Fig. 3.11). The semi-automated approaches applied to the Pléiades and, to a lesser extent, to the Sentinel-2 images, identify many small ice patches that would be impossible for an operator to map in a consistent way. These features considerably increase the number of mapped features, and slightly increase the total cliff density (Fig. 3.11, 12, Table 3.2). They are small

enough that they are often not represented by the slopes calculated from the DEMs, even if they are steeper than the debris. Depending on the spatial resolution, cleaning the results of the semi-automated approaches with a size threshold may be tempting to produce cliff outlines closer to what an operator sees, but their spectral signature does suggest that some ice is exposed or thinly debris-covered at these locations. Thus, these findings highlight a potential bias of the manual delineation, which only works for large features that have an identifiable shape and can cast a shadow, thus having a 'cliff' appearance. This is also true for the OBIA-m approach, for which it is difficult to apply an initial multi-scale segmentation to get the outlines of both big cliffs and small ice patches directly. Moreover, these small areas of shallow-sloping ice have seldom been counted as ice cliffs in previous studies (Anderson et al., 2019b), nor have they been accounted for when modeling the melt of debris-covered glaciers, but may account for substantial mass loss, as if they are partially or thinly debris-covered, they are susceptible to act as areas of enhanced melt (Evatt et al., 2015; Fyffe et al., 2020b; Ostrem, 1959; Reid and Brock, 2010). Thus, it seems important from a melt-modeling perspective to investigate the distribution and density of these small areas of shallow-sloping ice. However, their limited size and slope most probably prevents them from surviving due to debris redistribution, unless they develop into an actual cliff.

It is apparent that there is no broadly agreed definition of ice cliffs that can be used to tailor a method to their detection, and this seems an important step towards large-scale classification efforts. A plausible definition of an ice cliff could be a feature within an otherwise debris-covered area containing ice in its spectral and/or thermal signature (Herreid and Pellicciotti, 2018), but large and steep enough to survive over at least one melt season. However, the presence of the smaller areas of exposed ice detected in this study opens a new perspective. These patches should be investigated to understand their nature and distribution, their evolution (can they act as seeds for larger cliffs, or are they ephemeral features), and their contribution to glacier melt.

3.7.3. Future applications

A point to bear in mind when mapping steep features like ice cliffs from satellite imagery is that the final planimetric area will be impacted by possible shadowing and steep cliffs being concealed from the satellite view angle. Shadowing leads to an overestimation of the cliff planimetric area for all approaches based on the multi-spectral images. The pixels in the shadow are indeed categorized as ice cliff due to the low brightness and scaling factor values for the ABT and the LSU-s. The SC also maps shadows as cliffs due to its high sensitivity to small shifts in reflectance between the different band values. However, shadowing only affects steep north-facing cliffs (in the Northern Hemisphere), resulting in a limited impact on the cliff distribution at the glacier scale. All approaches are also equally affected by 1) the satellite viewing angle that results in cliffs with overhangs or steeper than the satellite viewing angle being concealed, 2) the spatial resolution of the image that prevents small steep features from being mapped. It is therefore key to use images with high satellite and sun elevation angles. In this study these angles where higher than 70° and 55° respectively for all images.

This being said, the transferability and efficiency of the semi-automated SC and LSU-s approaches opens up the possibility to systematically map ice cliffs on debris-covered glaciers at other sites, including in other mountain ranges, to study the distribution and evolution of ice cliffs across scales larger than an individual glacier or catchment. Although our confidence in the results of these approaches is already high, they could still be improved by combining spectral and slope-based approaches. This could be particularly important to discriminate between ice cliffs and seasonal snow patches, which were not a problem for our three scenes. Combining the spectral approaches with the

OBIA segmentation could also be something to explore, but would require the development of a multi-scale segmentation to account for cliffs of all shapes and sizes. Finally, adding a second brightness threshold to the ABT to account for bare ice portions of ice cliffs would be a useful improvement for this method. LSU-s enables the mapping of cliffs at the large scale using freely available Sentinel-2 data to study the variations of ice cliff coverage from glacier to glacier, region to region and potentially over time. Due to the coarser spatial resolution of the images, the Sentinel-2 cliff outlines from the LSU-s approach can be interpreted as a first-order map of the larger cliffs. Indeed, the Sentinel-2 LSU-s approach only maps the larger features and the resulting outlines are relatively crude (Table 3.2, Fig. 3.9R, 10, 12). In the case of extensive dark debris patches like on Khumbu, and to a lesser extent on Satopanth, the filtering of the *scale* may in some places not be strong enough for cliffs to contrast with their background, resulting in a high number of false negatives and an underestimation of the cliff density with regards to the outlines from SC applied to the Pléiades (Table 3.2). However, the larger cliffs are mapped and provide a close estimate of the total planimetric cliff area for the glacier. This is therefore a promising approach to assess ice cliff distribution across Himalayan debris-covered glaciers, given the availability of Sentinel-2 imagery covering large areas with high repeat frequency.

On the other hand, using fine spatial resolution imagery with the SC approach gives a highly detailed map of the ponds, ice cliffs, and smaller ice patches across the debris-covered area of a glacier. Supraglacial cliffs and ponds have significant implications for the glacier mass balance, and the effect of smaller bare ice patches is probably also important. There are already existing independent melt models of supraglacial ponds and cliffs (Buri et al., 2016a, 2016b; Miles et al., 2018, 2016) and the accurate mapping of all these features is a first and decisive step to quantify their impact on melt at the scale of a glacier or a catchment using a glacier melt model integrating these features.

3.8. Conclusion

This study has explored the potential of three new semi-automated, objective approaches to enable accurate mapping of cliffs and ponds from multi-spectral images within one glacier and from glacier to glacier. We also assessed their performance when applied to both fine spatial resolution, commercial (Pléiades, 2 m resolution, 4 bands) and freely-available, coarser spatial resolution images with more spectral information (Sentinel-2, re-sampled to 10 m resolution, 10 bands). Our main goal was to develop a method that can be applied across scales, and evaluate its potential in relation to existing approaches. The transferability of the new methods is assessed using three scenes with different climatic settings, elevations, debris types, cliff and pond characteristics, in Central and Eastern Himalaya.

We find that the Spectral Curvature (SC) approach, which uses Spectral Curvature to map cliffs after having removed ponds using NDWI, outperforms all other methods for the fine spatial resolution Pléiades data. This approach is transferable, semi-automated, computationally efficient, and is the best performing for each of the three scenes. The Linear Spectral Unmixing with scale (LSU-s) approach, an adapted linear spectral unmixing method, consistently produces the best performance for Sentinel-2 images by taking advantage of their additional spectral information. It is transferable and computationally efficient, making it the most appropriate method to map cliffs with this type of sensor. The two methods classify cliffs that occupy between 3 and 9 % of total planimetric area depending on the site and scene. We thus propose both as a way forward for either mapping repeat cliffs inventories at the scale of select glaciers to study processes of cliffs formation and evolution (SC approach); or to establish large scale inventories of cliffs features across distinct regions (LSU-s), to enable novel

analyses of much larger cliffs populations than tested to date, and quantify their characteristics, distribution and patterns over large scales.

Other existing methods all have potential for distinct applications, but seem less suitable for the two goals above. The only other automated method that is also transferable despite lower performances than the SC approach, the AST, is very slow from a computational standpoint. When seeking to identify cliffs for glaciers with consistent surface characteristics, the semi-automated SST and ABT approaches may be considered, even though they do not score as high or as not as transferable as the SC approach for the Pléiades scenes. The ABT may fail for glaciers with cliffs as bright as or brighter than the surrounding debris, but otherwise these methods generally perform well and are computationally very efficient. All of these methods are faster and more objective than a time-consuming manual delineation, even if an initial OBIA segmentation is used. None of the other existing approaches can be applied to the coarser Sentinel-2 data: the slope-based approaches require elevation data and are therefore not applicable to the Sentinel-2 images, while the coarse resolution of this sensor prevents the application of the other semi-automated or manual approaches to map cliffs.

Our results interestingly highlight a high number of smaller, sometimes shallow-sloping ice patches, which had not been previously accounted for in the assessment of ice cliffs and their contribution to melt. These smaller features reveal a bias in the manual delineation of cliffs towards identifying large features, and reflect the need for a clear definition of 'ice cliffs'. Although representing a small fraction of the total planimetric cliff area, these small ice patches could have non-negligible impacts on the melt of debris-covered glaciers.

3.9.   Acknowledgements

3.10. Declaration of competing interests

The authors declare that they have no known competing financial interests or personal relationships that could have appeared to influence the work reported in this paper.

3.11. Supplementary material

Table 3.S1. *Characteristics of the six images used in this study*

Area Name	Sensor	Acquisition date	Elevation range (m)
Langtang	Pléiades-1A	14/06/2019	4500 - 5600
	Sentinel-2B	17/06/2019	
Satopanth	Pléiades-1A	29/09/2018	3800-4600
	Sentinel-2A	29/09/2018	
Khumbu	Pléiades-1B	16/05/2016	4900 - 5400
	Sentinel-2A	23/05/2016	

Table 3.S2. *Characteristics of the sensor bands used in this study.*

Sensor	Bands	Spatial resolution (m)	Central wavelength (nm)	Bandwidth (nm)
Sentinel-2B*	B2	10	492.4	66
	B3	10	559.8	36
	B4	10	664.6	31
	B5	20	704.1	15
	B6	20	740.5	15
	B7	20	782.8	20
	B8	10	832.8	106
	B8A	20	864.7	21
	B11	20	1613.7	91
	B12	20	2202.4	175
	B1	2	490	120
	B2	2	550	120

Pléiades-1A**	B3	2	660	120
	B4	2	850	200

*Band characteristics are very similar for Sentinel-2A, and differ by a few nm at most

**Band characteristics are very similar for Pléiades-1B, and differ by a few nm at most
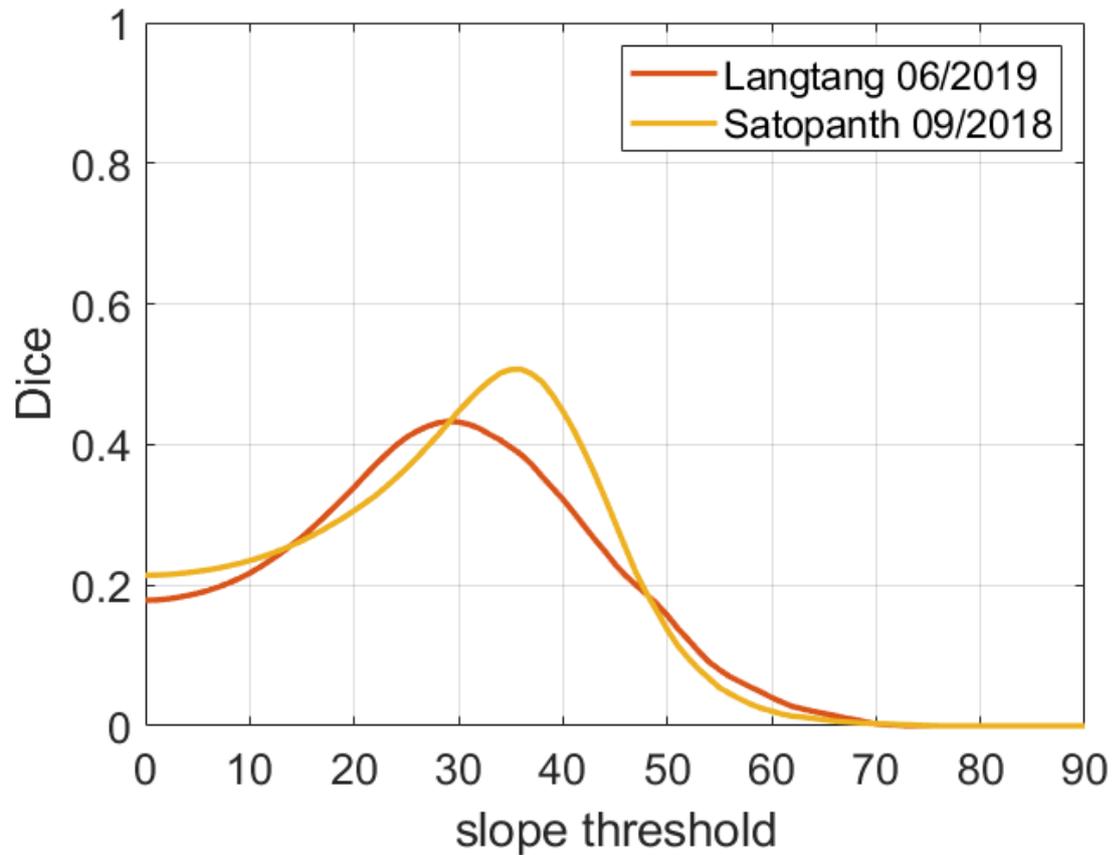
Figure 3.S1. Dice coefficients of cliff delineation obtained for different slope thresholds for the Pléiades Langtang and Satopanth scenes.
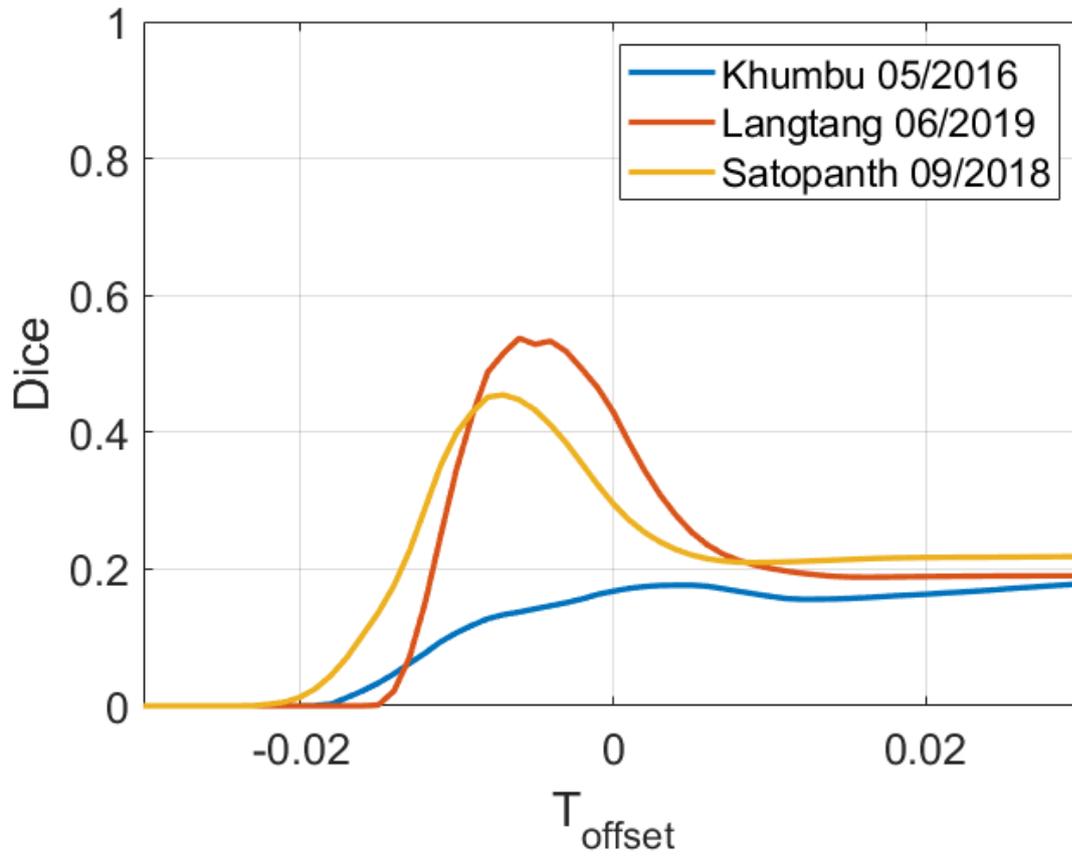
Figure 3.S2. *Dice coefficients of cliff delineation obtained for different offset from mean thresholds using the ABT approach for the Pléiades Langtang, Satopanth and Khumbu scenes.*
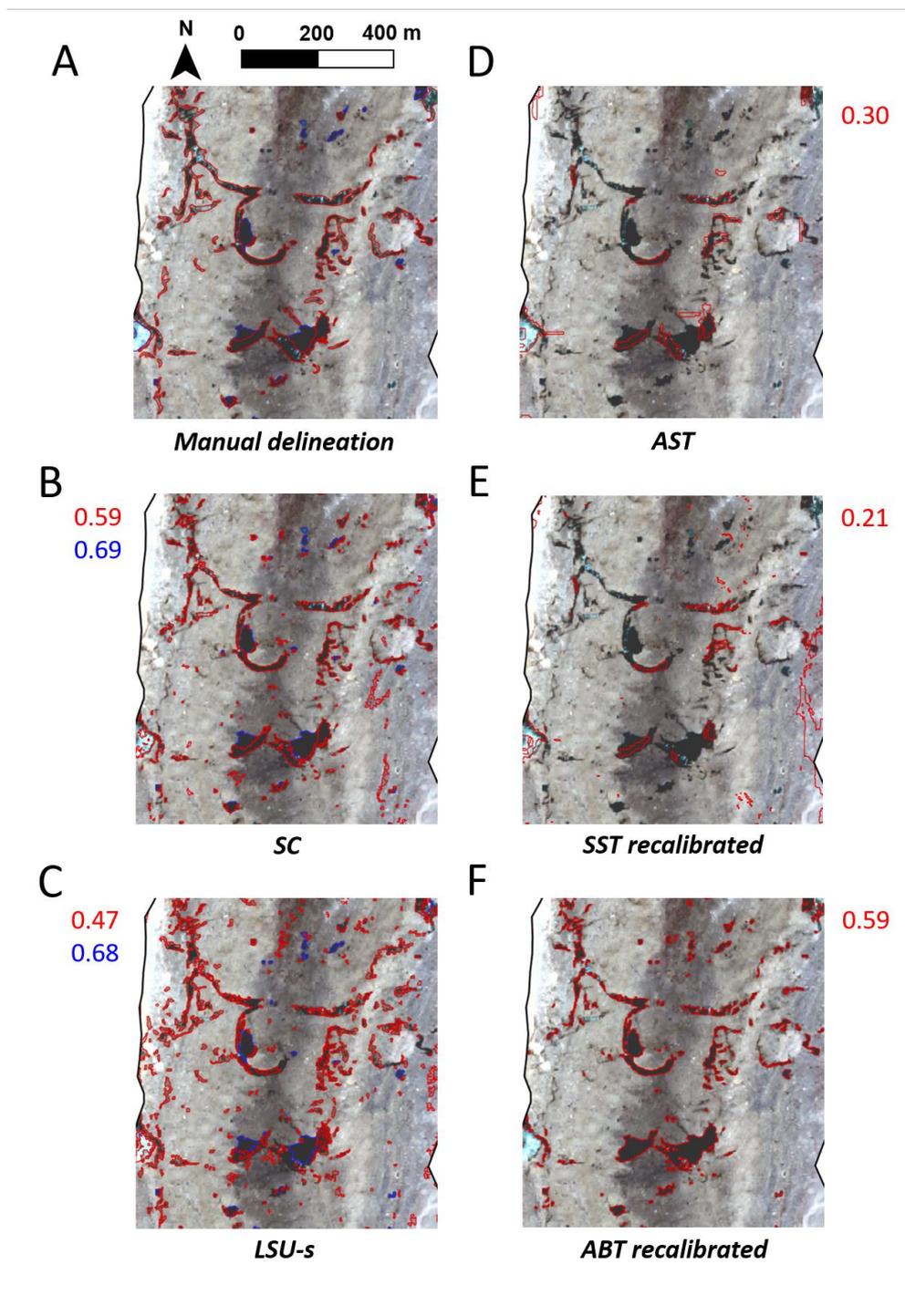
Figure 3.S3. *Comparison of the manual delineation (A), the SC (B), LSU-s (C), AST (D), SST (E) and ABT (F) approaches for a section of Langtang glacier (Pléiades 06/2019 scene). The values in red (resp. blue) correspond to the Dice coefficient of the cliffs (resp. ponds) relative to the manually delineated outlines in this small domain. The background corresponds to the Pléiades false color composite.*

Table 3.S3. *Efficiency of methods for the Satopanth Pléiades scene (9.3 km^2 domain, 2 m spatial resolution, except for AST, for which the DEM was re-sampled to 5 m). All the runs were conducted on a Windows 64-bit Operating System, with 20 Intel(R) Core(TM) i9-7900X CPUs @ 3.30 GHz. The*

total times do not include the stereo processing and atmospheric corrections of the satellite data, or the definition of the domain across which the delineation is applied.

Method	Inputs (other than DEM and/or multi-spectral image)	Total CPU time (seconds)	Parallel processing	Total delineation time (hours)
Manual	-	NA	NA	24
OBIA-m	-	NA	NA	8
SST	Optimization dataset	170	No	4
AST	-	300000	No	83
ABT	Optimization dataset	180	No	4
SC	-	180	No	0.05
LSU	-	7100	Yes (10 CPUs)	0.2
LSU-s	-	6900	Yes (10 CPUs)	0.2

Chapter 4: Interannual Dynamics of Ice Cliff Populations on Debris-Covered Glaciers from Remote Sensing Observations and Stochastic Modeling

[1] High Mountain Glaciers and Hydrology (HIMAL), Swiss Federal Institute for Forest, Snow and Landscape Research WSL, 8903, Birmensdorf, Switzerland

[2] Institute of Environmental Engineering, ETH Zurich, 8093 Zurich, Switzerland

[3] Department of Geography, Northumbria University, Newcastle, NE1 7RU, UK

Author contribution

MK, ESM and FP designed the study. ESM, PB and MM helped with the validation of the cliff outlines. PM advised and helped with the development of the stochastic birth-death model. SF helped with the handling of the ERA5-Land reanalysis data. MK completed all the analysis and composed the manuscript. FP supervised the study. All authors aided in the reviewing and editing of the manuscript.

Key points

- The proportion of ice cliffs on debris-covered glaciers can change by up to 20% from one year to the next

- There is no direct influence of climate, hydrology or glacier dynamics on cliff variability due to the complexity and interdependence of glacier surface processes

- The long-term variability of the cliff population is constrained unless it is modified by an extreme climatic and/or glacier change

4.1. Abstract

Ice cliffs are common on debris-covered glaciers and have relatively high melt rates due to their direct exposure to incoming radiation. Previous studies have shown that their number and relative area can change considerably from year to year, but this variability has not been explored, in part because available cliff observations are irregular. Here, we systematically mapped and tracked ice cliffs across four debris-covered glaciers in High Mountain Asia for every late ablation season from 2009 to 2019 using high-resolution multi-spectral satellite imagery. We then quantified the processes occurring at the feature scale to train a stochastic birth-death model to represent the cliff population dynamics. Our results show that while the cliff relative area can change by up to 20% from year to year, the natural long-term variability is constrained, thus defining a glacier-specific cliff carrying capacity. In a subsequent step, the inclusion of external drivers related to climate, glacier dynamics and hydrology highlights the influence of these variables on the cliff population dynamics, which is usually not a direct one due to the complexity and interdependence of the processes taking place at the glacier surface. In some extreme cases (here, a glacier surge), these external drivers may lead to a reorganization of the cliffs at the glacier surface and a change in the natural variability. These results have implications for the melt of debris-covered glaciers, in addition to showing the high rate of changes at their surface and highlighting some of the links between cliff population and glacier state.

4.2. Plain Language Summary

A large portion of High Mountain Asia's glaciers is covered by a layer of rock debris that reduces their melt. This melt reduction is compensated to some extent by the presence of ice cliffs that cover up to 12% of these glaciers and melt several times faster than the surrounding debris-covered ice. This enhanced contribution to melt needs to be taken account in glacier melt models as it has implication for downstream water resources. However, due to the difficulty to map ice cliffs from satellite images, we have little knowledge about their actual distribution and most importantly, on how quickly their population and therefore relative area changes in time at the scale of one glacier, let alone what drives this variability. Here, we systematically mapped ice cliffs on a yearly basis over a period of 10 years for four Asian glaciers to disentangle these questions. We found that the cliff area of a glacier could commonly change by 20% in one year, and in some cases up to 80%. We also found that a number of climatic and glaciological variables influenced to some extent this variability but none stood out clearly due to the complexity of the debris-covered glacier system.

4.3. Introduction

Debris-covered glaciers are widespread in all mountain ranges around the globe (Herreid and Pellicciotti, 2020a; Scherler et al., 2018) and especially in High Mountain Asia (HMA), where half of the glaciers larger than 2 km^2 have more than 5% of their total area covered by a layer of rock debris (Herreid and Pellicciotti, 2020a) varying in thickness from centimeter to meter scale. These glaciers are often characterized by undulating, hummocky topography (Bartlett et al., 2020) and their surface is punctuated by supraglacial ponds, streams and ice cliffs. Ice cliffs have been observed in all the main mountain ranges of the planet (Anderson et al., 2021a; Benn et al., 2001; Chinn and Dillon, 1987; Herreid and Pellicciotti, 2018; Inoue and Yoshida, 1980; Johnson, 1992; Mölg et al., 2019; Moore, 2018; Ogilvie, 1904; Reid and Brock, 2014; Röhl, 2006; Sakai et al., 1998; Shahgedanova et al., 2005)

and have been observed to account for 1 to 12% of the total debris-covered area (Anderson et al., 2021; Brun et al., 2018; Kneib et al., 2020; Reid & Brock, 2014; Sakai et al., 1998). They consist of steep, bare or very thinly debris-covered ice faces within the debris-covered part of the glacier and are often associated with supraglacial streams or ponds (Mölg et al., 2019; Steiner et al., 2019). Cliffs appear when the surface slope is too steep for the debris to remain on it (Moore, 2018). Therefore, ice cliff formation has been suggested to be triggered by several possible mechanisms, including the collapse of englacial conduits (Benn et al., 2012; Immerzeel et al., 2014; Reid and Brock, 2014; Sakai and Takeuchi, 2000; Watson et al., 2017b, 2017a; Westoby et al., 2020); slope oversteepening, for example from differential melt under the debris (Sakai et al., 1998; Sharp, 1949; Westoby et al., 2020); crevasse opening (Reid and Brock, 2014); undercutting by supraglacial ponds or streams (Moore, 2018; Nicholson et al., 2018) and melt enhancement at pond margins (Miles, Steiner, et al., 2017; Miles, Willis, et al., 2017; Röhl, 2006, 2008; Sakai & Takeuchi, 2000) that may sometimes lead to accelerated steepening from calving (Benn et al., 2012; Immerzeel et al., 2014; Röhl, 2008, 2006).

Contrary to the surrounding debris-covered ice, ice cliffs are directly exposed to incoming radiation and therefore act as melt 'hotspots' (Buri et al., 2016a; Juen et al., 2014; Sakai et al., 1998). In spite of the small area they occupy, ice cliffs and ponds are responsible for a significant contribution to glacier ablation, and ice cliff melt is estimated to be 3 to 8 times higher than debris-covered ice melt (Brun et al., 2018; Buri et al., 2021; Immerzeel et al., 2014; King et al., 2020; Mölg et al., 2019; Pellicciotti et al., 2015; Reid & Brock, 2014; Sakai et al., 1998; Thompson et al., 2016). By promoting the backwasting of steep slopes due to enhanced ablation, ice cliffs and ponds influence the morphology of debris-covered glaciers (Mölg et al., 2020; Watson et al., 2017a) and play a role in their long-term evolution by increasing their sensitivity to warming (Ferguson and Vieli, 2020). This could, at least partially, explain regional observations of enhanced mass loss of debris-covered glaciers (Gardelle et al., 2013; Kääb et al., 2012; Ragettli et al., 2016a), in spite of the overall melt-reducing effect of debris cover (Ostrem, 1959). Despite their important role in controlling the long-term evolution of debris-covered glaciers, cliffs and ponds are seldom represented in glacier melt models or glacio-hydrological models. The few models that have tried to account for ice cliffs and ponds use a fixed or linearly-derived melt enhancement factor (Hagg et al., 2018; Kraaijenbrink et al., 2017), or arbitrarily reduce the debris thickness (Ferguson and Vieli, 2020; Ragettli et al., 2015). In these models, a fixed cliff area is usually set, which is either the same as the pond area (Kraaijenbrink et al., 2017) or correlated to it (Ragettli et al., 2015). To our knowledge, only two models used cliff outlines manually derived from high-resolution satellite imagery (Buri et al., 2021; Hagg et al., 2018) and only one study modeled the energy-balance of each individual cliff at the glacier scale to quantify their contribution to melt (Buri et al., 2021). This poor representation comes from the difficulty of mapping ice cliffs from remote sensing imagery (Herreid & Pellicciotti, 2018; Kneib et al., 2020), resulting in a very limited knowledge about their distribution, especially over time, as well as their birth and decay mechanisms. While most of the work on ice cliffs has focused on a detailed analysis of a few of these features for an individual site at a single point in time (Anderson et al., 2021; Brun et al., 2016; Buri, Pellicciotti, et al., 2016; Reid & Brock, 2014; Sakai et al., 2002; Steiner et al., 2015; Watson, Quincey, Smith, et al., 2017; Westoby et al., 2020), two studies have looked at ice cliff distribution and evolution over several years for the multiple glaciers of a large catchment (Steiner et al., 2019; Watson et al., 2017a). These two studies offer major advances in understanding cliff dynamics at the glacier scale, showing that there is a high interannual variability in the cliff population. However, they largely ignored the controls or underlying processes of this variability. In both cases the data used was irregularly spaced in time and still relatively sparse, with at most one image every second year.

As a result, our understanding of the life cycle of ice cliffs, its drivers and its implications for the dynamics of the cliff population of a whole glacier is limited. Ponds and cliffs are often found close to one another, and it has been hypothesized that ponds contribute to the sustainability of cliffs due to their marginal melt effects, although cliffs can also survive for years without being connected to a pond (Brun et al., 2016; Miles et al., 2016; Steiner et al., 2019; Watson, Quincey, Carrivick, et al., 2017). Conversely, streams and cliffs may be associated, and it has been suggested that streams meandering across the debris-covered surface can lead to significant melt (Gulley et al., 2009) and to the formation of supraglacial valleys, or cryo-valleys, on the sides of which ice cliffs can form (Mölg et al., 2020; C. S. Watson et al., 2016). The development of such valleys has only been studied at one site and the length of time over which they evolve is not clear (Mölg et al., 2020). Beyond the supraglacial hydrology, incoming shortwave radiation is the main contributor to the melt of ice cliffs and therefore influences their preferential orientation and survival (Buri and Pellicciotti, 2018). In addition, climatic variability is expected to have an influence on ice cliffs by influencing glacier melt and thus the presence, volume or discharge of streams and ponds, but also by promoting ice cliff melt and backwasting (Buri et al., 2016a, 2016b; Reid and Brock, 2014; Sakai et al., 1998; Steiner et al., 2015). Surface meltwater and precipitation also determine the debris water content and therefore the debris layers' stability, which has implications for the formation and growth of the cliffs (Moore, 2018). Finally, crevasse opening has been pointed out as one of the possible events triggering the formation of a cliff (Reid and Brock, 2014), which would imply that glacier flow also influences cliff dynamics. However, it is difficult to assess the importance of these individual drivers and their contributions to the cliff dynamics at the glacier scale.

The aim of this study is therefore to *understand and model the interannual ice cliff dynamics and how they influence the variability of the cliff population at the glacier scale*. Specifically, we aim to 1) quantify the interannual variability of ice cliffs on a feature-by-feature and population basis; 2) attribute the observed interannual changes to individual types of cliff change; 3) characterize the stochastic behavior of cliff populations at the glacier scale and develop a model that represents it; and 4) assess the influence of external drivers on the interannual cliff variability.

4.4. Sites and data

4.4.1. Site description

In order to study the interannual variability of ice cliffs and its drivers at the glacier scale, we selected sites in different climatic settings and with different glacier characteristics (velocity, mass balance) but similar size and debris cover stage. Additionally, there needed to be a continuous and relatively long time series of satellite images to map ice cliffs over large portions of the glacier. Upon inspection of the Planet Labs RapidEye, we therefore identified four sites with sufficient suitable data.

We derived the long-term evolution of ice cliffs for four debris-covered glaciers located in the Karakoram (Urdok Glacier, Pakistan), Garhwal Himalaya (Satopanth and Bhagirath Kharak Glaciers, India) and Nepal Himalaya (Langtang Glacier) (Fig. 4.1). The glaciers' ablation areas were between 66% and 72% debris-covered, which corresponds to an advanced stage of debris-cover (Herreid & Pellicciotti, 2020b, Table 4.1). For Satopanth the debris is very thick (> 1 m) across much of the debris-covered area (Shah et al., 2019), and this is also thought to be the case on Langtang based on field observations from 2019. To our knowledge, no debris thickness measurements are available for Urdok or Bhagirath Kharak. Previous studies have shown that for Satopanth, Bhagirath Kharak and Langtang, ponds accounted for 0.6 to 2% of the debris-covered area and cliffs between 3.3 and 9.2 % (Kneib et

al., 2020; Miles, Willis, et al., 2017; Steiner et al., 2019, Table 4.1). On Langtang Glacier, it has been observed that cliffs and ponds tend to have a smaller relative area, defined as the ratio between the cliffs or ponds planimetric area and the area of the glacier over which they were mapped, in the dry post-monsoon than during the wet monsoon season (Miles, Willis, et al., 2017; Steiner et al., 2019). This is consistent with observations made at other HMA glaciers (C. S. Watson et al., 2016).

These four glaciers exhibit long debris-covered tongues (Table 4.1) and the terminus positions of Satopanth, Bhagirath Kharak and Langtang have not changed considerably in the past several decades (Nainwal et al., 2016; Wijngaard et al., 2019). These three glaciers show however negative mass balances of -0.5 to -0.3 (+/- 0.4) m w.e.yr^{-1} (Table 4.1), have relatively low average velocities along the centerline of their debris-covered area (Table 4.1), and their mass imbalance therefore translates into stagnating tongues with significant downwasting (Anderson and Anderson, 2016; Ferguson and Vieli, 2020; Rowan et al., 2015). Urdok stands out from these three with its smaller negative mass balance (Table 4.1), its relatively high velocities (23.0 m.yr^{-1} for 2009-2018 on average) and evidence of a previous surge in the 1990s (Bhambri et al., 2017). Urdok is therefore much more dynamic and in a healthier state than the three other glaciers, despite displaying an extensive debris-covered area.
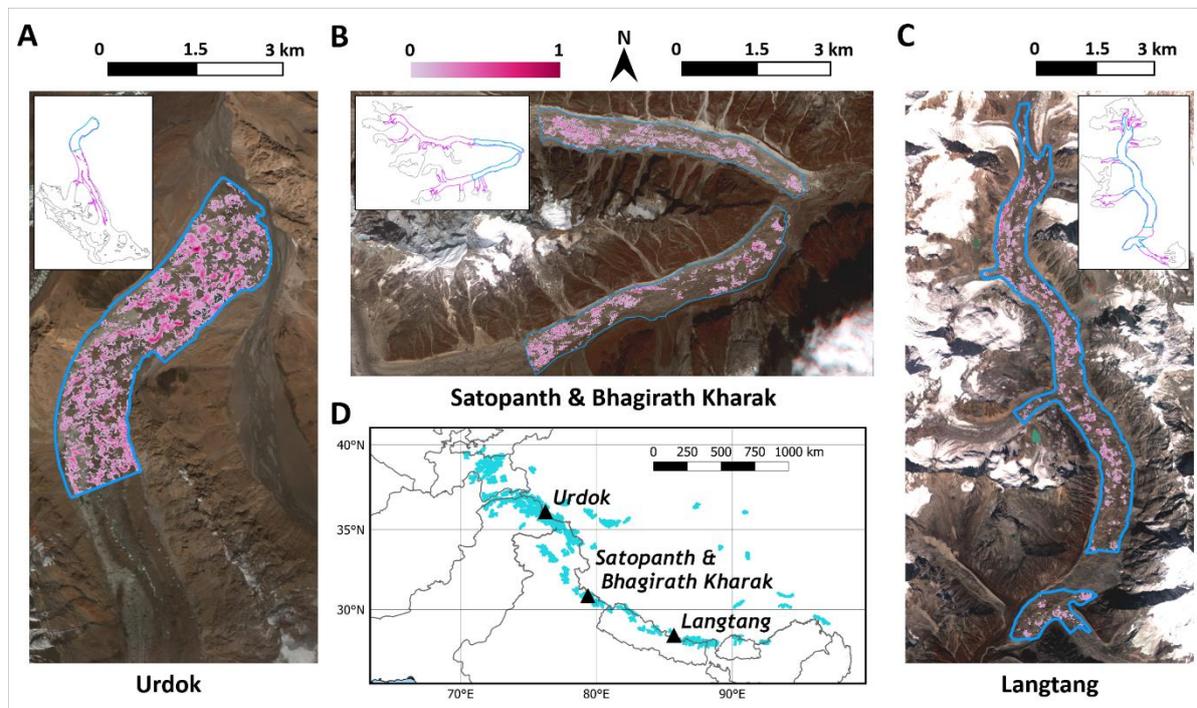
Figure 4.1: *Maps of the four study glaciers and their general location in HMA. Background image is the 2015 RapidEye scene for each site (color composite of bands 4, 2 and 1). The blue outlines correspond to the area of the glacier where the cliffs were mapped (AOI) and the pink colors correspond to the cliff density maps, where transparent color stands for no occurrence of cliffs while 1 corresponds to the presence of cliffs in all the images of the time series (2009-2019 for Urdok and Langtang, 2010-2019 for Satopanth and Bhagirath Kharak). The insets in (A), (B) and (C) show the AOIs (blue), debris-covered areas from Herreid & Pellicciotti, 2020b (purple) and RGI 6.0 glacier outlines (black) of each site.*

Table 4.1: *Glacier characteristics. Glacier mass balance was obtained by integrating elevation difference data from Brun et al., 2017a over the entirety of the glaciers and using a value of 850 +/- 60 kg.m^{-3} for ice density (Brun et al., 2017a; Huss, 2013).*

Glacier	References	Urdok	Satopanth	Bhagirath Kharak	Langtang
Length (km)	RGI Consortium, 2017	27	15	20	19
Debris cover (% total glacier area)	Herreid & Pellicciotti, 2020b	22	60	41	49
Stage (debris-covered portion of ablation area)	Herreid & Pellicciotti, 2020b	0.66	0.68	0.72	0.71
Evidence/records of surging (years)	Bhambri et al., 2017	Yes (1993-1997)	No	No	No
Mean 2009-2018 velocity along centerline in the debris-covered part (m.yr^{-1})	Gardner et al., 2018	23.0	14.7	14.7	4.1
Previously reported cliff density (%)	Steiner et al., 2019	NA	NA	NA	3.4 (+/− 0.9)
	Kneib et al., 2020	NA	9.2	9.2	3.3
Previously reported pond density (%)	Miles, Willis, et al., 2017	NA	NA	NA	0.6-2
	Kneib et al., 2020	NA	0.7	0.7	1.7
Glacier mass balance (m w.e.yr^{-1})	Brun et al., 2017a	-0.1 (+/− 0.3)	-0.5 (+/− 0.3)	-0.3 (+/− 0.3)	-0.5 (+/− 0.3)

4.4.2. Remote sensing data

We derived time series of ice cliffs and ponds at our four sites from RapidEye satellite images taken at a yearly interval from 2009 to 2019 (Table 4.S1). The RapidEye images acquired from Planet Labs (Planet Team, 2017) are already atmospherically corrected. They have five spectral bands in the visible and near infrared, with a spatial resolution of 5 m. We selected images that were all taken during the post-monsoon period (end of August to December, Table 4.S1), when stable and dry conditions maximize the chances of acquiring cloud-free images. No RapidEye images were found in 2009 or 2019 for Satopanth and Bhagirath Kharak or in 2019 for Urdok. For the missing 2019 images, we used PlanetScope images instead (Planet Team, 2017), resampled from 3 m to 5 m spatial resolution using a nearest neighbor interpolation. Images were selected at a yearly interval in order to ensure similar atmospheric conditions and remove the influence of the seasonal variations of cliffs and ponds (Miles, Willis, et al., 2017; Steiner et al., 2019; Watson et al., 2016). Therefore, we assumed that our observations would be the results of continuous changes from one year to the next. Images with snow and shadows from the surrounding topography were avoided as much as possible, but this was not always feasible and we could therefore not delineate ponds and cliffs across the whole debris-covered

area but had to limit the delineation to an Area of Interest (AOI) for each glacier, defined as the area where the mapping was possible over the full time series (Fig. 4.1). Furthermore, we did not apply the mapping over avalanche cones, including, for Langtang Glacier, those originating from the large avalanches triggered after the 2015 Gorkha earthquake in Nepal (Kargel et al., 2016). The final AOIs correspond to 43%, 23%, 40% and 63% of the total debris-covered areas (from Herreid & Pellicciotti, 2020b) of Urdok, Satopanth, Bhagirath Kharak and Langtang, respectively (Fig. 4.1).

4.4.3. Glacier velocity and climate data

To look at the controls of cliff dynamics we accessed the annual velocities for the years 2009 to 2018 from the NASA MEaSUREs - ITS_LIVE project (Dehecq et al., 2019; Gardner et al., 2018), resampled from 240 to 120 m resolution using the cubic spline interpolation method. For the debris-covered part of our study glaciers, the reported uncertainty maps from ITS_LIVE displayed very low values (< 1 m.yr^{-1}) and were thus considered negligible in everything that follows.

We used monthly air temperature and precipitation reanalysis data from the ERA5-LAND product (Muñoz Sabater, 2019), available in a 0.1°×0.1° grid. These time series covered our full study period. For each of the study glaciers we used the ERA5-Land data from the grid cell covering the center of the debris-covered area.

4.5. Methods

4.5.1. Image pre-processing

RapidEye images have an expected positional accuracy of less than 10 m according to the product specifications (Planet Team, 2017). Additionally, for each site, the orthoimages were all co-registered to the initial 2009 image (2010 for Satopanth and Bhagirath Kharak) using the ImGRAFT normalized cross correlation algorithm (Messerli and Grinsted, 2015) applied to near-glacier stable terrain, to ensure the best possible relative positioning.

4.5.2. Mapping

Ice cliffs were mapped manually by one operator in all multi-spectral images. The mapping was conducted independently for each image. We used shape and color information, as well as local changes in surface motion between two consecutive images as indicators of cliff location (Fig. 4.S1). Three automated mapping methods, the Adaptive Binary Threshold, Spectral Curvature and Linear Spectral Unmixing with scale (Anderson et al., 2021; Kneib et al., 2020), were tested to map the cliffs but the results were not conclusive due to the varying illumination conditions and variable off-nadir viewing angles resulting in increased shading for some of the scenes compared to the Pléiades and Sentinel-2 sensors for which the methods above were developed (Kneib et al., 2020; Watson et al., 2018). The ponds were mapped using a fixed Normalized Difference Water Index (NDWI) threshold of 0.1 (Huggel et al., 2002; Kneib et al., 2020; McFeeters, 1996; Watson et al., 2018), and the outlines were improved manually for ice-covered ponds, which were always a minority.

The data used for the delineation of cliffs is of varying illumination and shading, which can lead to difficulties in identifying features (Kneib et al., 2020; Steiner et al., 2019). We estimated the uncertainty

in the cliff and pond relative area obtained from our delineation by comparing our outlines with the consensus outlines produced by three independent operators for six domains of similar sizes ranging between 0.3 and 0.9 km^2 (two domains on Urdok and Langtang, one on Satopanth and one on Bhagirath Kharak) for the 2011 and 2016 images (Fig. 4.S2). For each pixel of the original image, we determined the fraction that was covered by cliff and pond areas as outlined by the three independent operators. We summed the three resulting fraction maps and defined the consensus outlines as the pixels with final values higher than 1.5. The final uncertainties for the cliff mapping were then taken as the mean of the absolute residual values, which were equal to 28% and 41% for the number of cliffs and ponds, respectively, and to 33% and 37% for their respective relative area (Fig. 4.S2).

As we are interested in the ice cliff variability, the precision is more important here than the accuracy, meaning that it is more critical to map individual cliff change in time right, rather than counting accurately all the cliffs and ponds in the images. Indeed, we needed to make sure that the observed trends were meaningful. For this, we compared the cliffs and ponds number and relative area obtained by the four independent operators (Operator 4 having mapped the cliffs and ponds in all images) to make sure that there was a good agreement in the resulting changes (Fig. 4.S3). The changes derived by Operator 4 from 2011 to 2016 in the validation domains agreed with the ones derived by at least two other operators in 10 cases out of 12 (Fig. 4.S3).

4.5.3. Tracking of cliffs

Once all the cliffs had been outlined in the images, we automatically tracked the evolution of each individual cliff from one image to the next, using a new algorithm developed ad hoc to directly compare the characteristics of the cliffs in consecutive images (Fig. 4.2). For two consecutive images, image 1 and image 2, we accounted for glacier surface velocity using the annual ITS_LIVE data (Dehecq et al., 2019; Gardner et al., 2018) to shift the position of the cliffs in image 1 in order to compensate for glacier motion (Fig. 4.2A). We then compared the cliff outlines of image 2 with the shifted cliff outlines of image 1. If the distance between the cliffs was less than 20 m in a year (Fig. 4.2B) and the aspect difference less than 30° in a year, modulus(180°) (Fig. 4.2D), we considered the cliffs to be the same, with one year difference. The 20 m.yr^{-1} threshold is conservative relative to observed cliff backwasting rates that are usually less than 15 m.yr^{-1} (Brun et al., 2016, 2018; Buri, Miles, et al., 2016; Han et al., 2010; Mölg et al., 2019; Reid & Brock, 2014; Steiner et al., 2015; Watson, Quincey, Carrivick, et al., 2017) and therefore also accounts for co-registration and surface velocity uncertainties. We did not have any Digital Elevation Model (DEM) for the RapidEye images, so the cliff aspect was estimated by fitting a circle to the cliffs' vertices using a quasi-Newton optimization method (Umbach & Jones, 2000, Fig. 4.2C). We approximated the aspect of each pixel as the direction of the vector starting at the center of the pixel and finishing at the center of the circle. We calculated the aspect of the cliff as the circular mean aspect of its pixels (Fig. 4.2C). Therefore, for the aspect difference, it was necessary to take modulus(180°) to account for straight cliffs that can see their mean aspect change by +/- 180° from one year to the next. For cliffs with a standard deviation of the aspect greater than 45°, we only compared the aspect of the pixels less than 20 m away to identify nearby circular cliffs as independent from one another. These tracking parameters (Table 4.S2) were calibrated against manual tracking of cliffs between the 2009 and 2010 Langtang scenes and validated for a randomly selected year at each of the three other sites. With these parameters, the automated and manual tracking agreed for 96.4% of the cliffs in the initial image for Langtang, and 90.2%, 91.7% and 90.0% for Urdok, Satopanth and Bhagirath Kharak respectively.

Based on the tracking results, we could determine the evolution of each cliff in time, but also the number of cliffs that appeared (birth events) or disappeared (death events) every year. We also quantified the split events, when one cliff splits into two cliffs or more (Fig. 4.2E), and merge events, when two or more cliffs merge into one (Fig. 4.2F). Cliffs were also observed to split and merge at the same time, resulting in a mix event. The most common event on the other hand was a cliff remaining a single cliff but changing shape and/or size, which we describe here as a persist event (Fig. 4.2E-F).
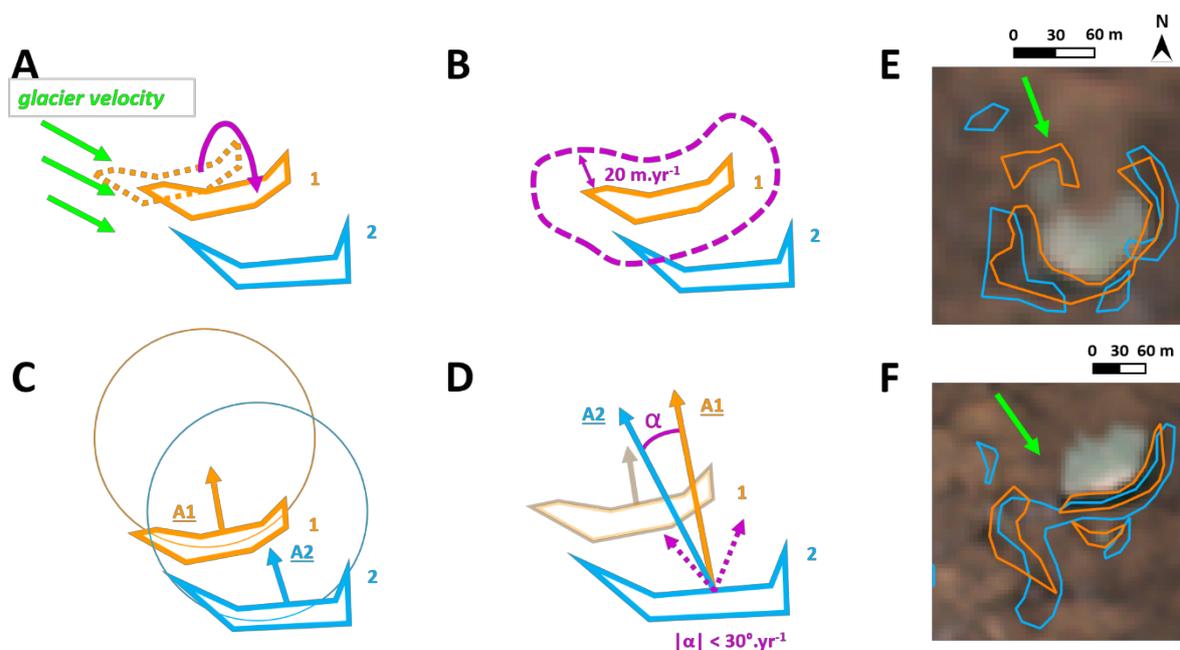
Figure 4.2: Tracking methodology. In orange are the cliff outlines in year 1 and in blue the cliff outlines in year 2. Panels (A-D) represent the different steps of the tracking with idealized outlines. (A) Correction for glacier velocity. (B) Distance check. (C) Aspect retrieval from fitted circles. (D) Mean aspect comparison. Panels (E-F) represent real cliff outlines from 2015 (orange) and 2016 (blue) on Langtang. (E) Split and persist events. (F) Merge, birth and persist events. Background image in (E) and (F) is the RapidEye 2015 scene (color composite of bands 4, 2 and 1). The green arrows represent the glacier flow direction.

4.6. Observational evidence of cliff dynamics

4.6.1. General dynamics of cliffs and ponds

The cliff relative area and the cliff number change considerably from one year to the next (Fig 4.3). These two variables are mostly uncorrelated, except for Langtang and to some extent for Satopanth. The number of ice cliffs remains centered around 328 for Urdok (Fig. 4.3A) and 116 for Satopanth (Fig. 4.3B), while it shows a small decrease for Bhagirath Kharak from an average of 106 to 84 cliffs between the first and second half of the study period (Fig. 4.3C) and a small increase for Langtang, from 177 to 221 (Fig. 4.3D). Although the number of cliffs remains relatively constant, Urdok experiences a large increase in cliff relative area between the years 2012 and 2015 from 3.2% to 14.0%. The cliff relative area on Urdok is also generally higher than the cliff relative area of the other three glaciers. The cliff

124

relative area changes every year on Satopanth, Bhagirath Kharak and Langtang centering around 3.6%, 3.9% and 3.0%, respectively, with a slight decrease for Satopanth from 3.9% to 3.3% and a slight increase for Langtang from 2.7% to 3.2% on average between the first and second half of the study period.

For all four glaciers, the cliff relative area is higher than the pond area by a factor ranging between 2.4 for Langtang and 7.3 for Bhagirath Kharak over the whole time series. For each glacier, the pond relative area and number appear to be uncorrelated with the cliff area and number, except for Satopanth where both pond and cliff relative area exhibit a decreasing trend. The pond relative area is much higher for Urdok (average value of 3.2%) than for the other glaciers, for which the average pond relative area is between 0.6% and 1.3%. The pond relative area on Urdok also has very strong variations and can more than double in a single year (Fig. 4.3E). The number of ponds is not correlated with the pond relative area except for Bhagirath Kharak. The number of ponds also remains relatively constant over time, except for Urdok, where there are also strong variations at the beginning of the study period.
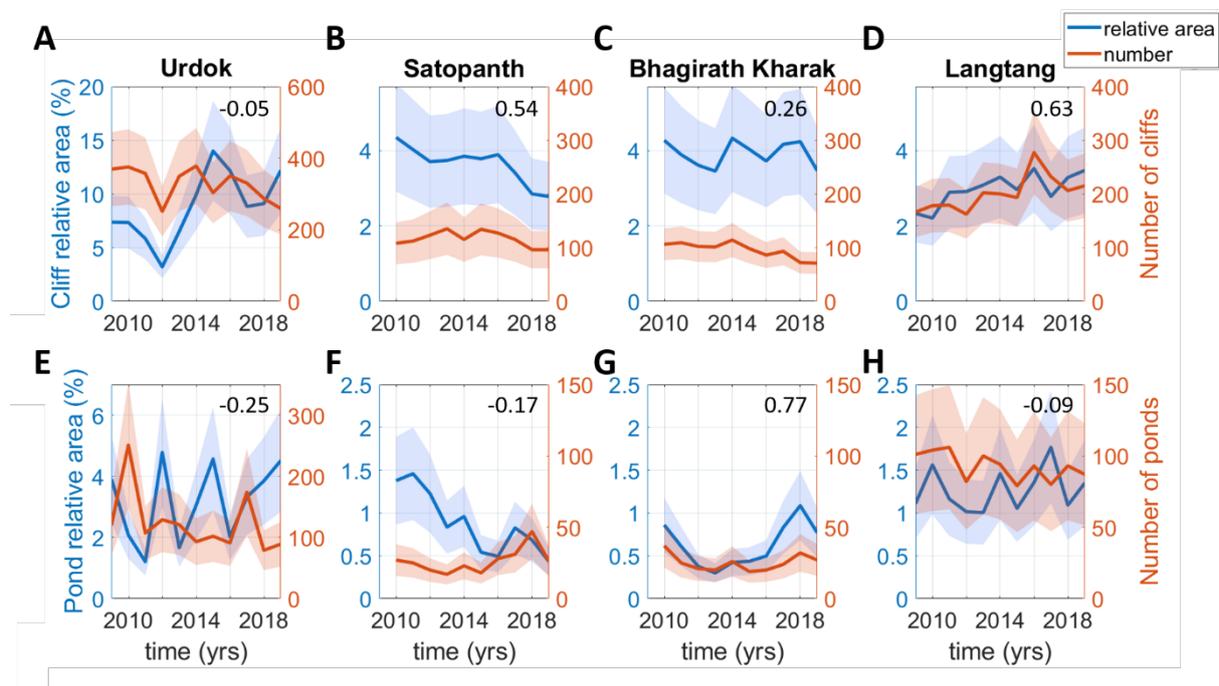
Figure 4.3*: Time series of cliffs and ponds number and relative area. The y-axis scales are different for Urdok and the three other glaciers. The shaded areas correspond to the uncertainty range calculated in the methods. The numbers in the upper right hand corner of the plots are the Pearson's correlation coefficients between the relative area and number time series.*

4.6.2. Contributions to the cliff dynamics

The tracking of the individual cliffs allowed us to count the birth, death, split, merge and persist events over time (Fig. 4.4, S4). By taking into account the cliff area before and after each event, we also derived the net and total area change related to each event for the whole cliff population (Fig. 4.4, S4). This enabled us to directly derive the contributions of different events to the changes in cliff number and area.
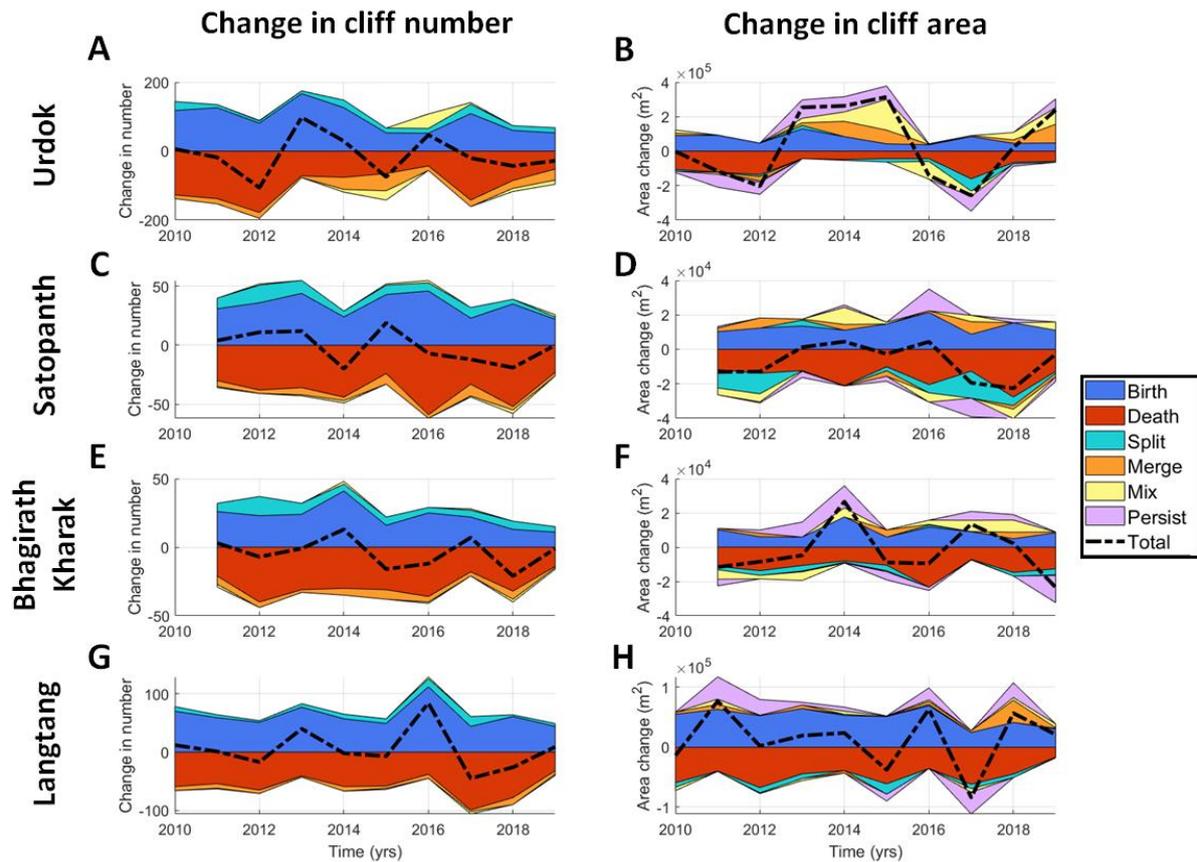
Figure 4.4: *Net contribution of different events to the general evolution of ice cliffs. The left panels show the change in cliff number and the right panels show the change in cliff area. For comparison, the mean cliff number (area) is 328 (6.8×10^5 m^2), 116 (1.5×10^5 m^2), 95 (1.2×10^5 m^2) and 201 (3.3×10^5 m^2) for Urdok, Satopanth, Bhagirath Kharak and Langtang, respectively. Note that the color envelopes are not overlapping but stacked on top of one another.*

For all four glaciers, the change in cliff number is centered around zero and the standard deviation varies between 10 and 20% of the total cliff number. For the four glaciers, the change in number is driven by the birth and death events. Split and merge events contribute respectively positively and negatively to the change in number, mix events can cause changes in both directions (Fig. 4.4A), and persist events do not contribute to the change in number but can contribute to the change in area. Split, merge and mix events only contribute to less than 10% of the change in number, except from 2014 to 2016 for Urdok where they contribute up to 40% of the change. In most cases, except for some years in Urdok and Bhagirath Kharak, an increase in cliff number is followed by an increase in death events. This is consistent with what we observe when comparing the number of death events and the total cliff number one year before (Fig. 4.S5), which shows that death events tend to compensate for a higher-than-average number of cliffs.

Changes in cliff area are mostly positive for Urdok, and negative for Satopanth, thus highlighting an increase and a decrease in cliff area, respectively. These changes are centered around zero for Bhagirath Karak and Langtang (Fig. 4.4). Their standard deviation varies from 7% of the cliff relative area for Satopanth to 45% for Urdok. For all glaciers, there is a significant contribution of birth and death events to changes in cliff relative area, and peaks in cliff relative area change usually correspond to peaks in birth events and/or lower death rates (Fig. 4.4). These peaks in the contribution of birth events to cliff area are amplified by the contribution of split, merge, mix and persist events, which usually contribute

126

in the same direction, either positively or negatively (Fig. 4.4). Of all these events, the persist events are usually predominant, even in terms of net contribution, but the mix or split events can also contribute considerably in some years, especially at Urdok and Satopanth.

4.6.3. Cliff size and pond influence

For the four study sites, we find that the cliff size follows a lognormal distribution (Fig. 4.S6). This lognormal distribution spans two orders of magnitude, from 100 m^2, which corresponds to four RapidEye pixels and can therefore be considered as the cliff detectability threshold, to ~10 000 m^2 (400 pixels), and even to more than 20 000 m^2 (800 pixels) for some cliffs in Urdok (Fig. 4.S6). The size of new cliffs or dying cliffs also follows a lognormal distribution with a similar standard deviation to the persisting cliffs, but they are generally smaller, with the mean of the lognormal distribution around 400-500 m^2 for Urdok and Langtang, 200-300 m^2 for Satopanth and Bhagirath Kharak, while it is between 500 and 800 m^2 for the persisting cliffs (Fig. 4.S6). As a result, the cliffs that are about to die, or that are less than one year old, tend to be smaller than other cliffs.

The size of splitting, merging and mixing cliffs also follows a lognormal distribution (Fig. 4.S7). The size distribution of merging cliffs is very similar to that of the persisting cliffs, which means that any cliff can be involved in a merge event, while the cliffs resulting from a merge event are larger than the norm. This is the contrary for split events, in which the cliffs that split are generally larger than normal but the cliffs resulting from split events follow the same size distribution as the total population (Fig. 4.S7). For the mix events the size distribution of cliffs before and after is more or less the same and similar to that of the total cliff population with some variations due to the small number of events relative to the persist events.

For split, merge, mix and persist events, the relationship between the sum of cliff sizes before (S_i) and after the event (S_f), is given by the area ratio α:

(Eq. 4.1)
$$\alpha = \frac{S_f}{S_i}$$

Our results show a large spread of α, which usually follows a lognormal distribution centered around 1, and range from 0.1 to 10 for the most extreme area changes (Fig. 4.S8). For persist events, this area ratio is dependent on the cliff initial size, with a tendency for smaller cliffs to increase in size while the larger cliffs tend to decrease in size (Fig. 4.S8). Such a trend is difficult to observe for other events, which occur less often than persist events.

Ultimately, the presence of ponds also has an influence on the birth and death events. For Urdok, Satopanth and Bhagirath Kharak, 10 to 35% of all the cliffs have an attached pond, and for Langtang this value varies between ~30% and ~50% (Fig. 4.S9). At all sites, the proportion of new or dying cliffs with an attached pond (less than 10 m away) is consistently lower than for the whole population, and can be as low as 10-12% for Langtang and Urdok, 0-2% for Satopanth and Bhagirath Kharak (Fig. 4.S9). Urdok is the site where the difference is less visible.

4.7. Stochastic modeling of cliff dynamics

Based on our observations from the tracking of ice cliffs we implemented a stochastic birth-death model to represent the cliff population dynamics and the interannual changes in cliff number and area for each glacier. We implemented two models, one that is purely stochastic and all events occur at random, for

which we considered the cliff populations to be closed systems with no influence from external drivers, and the second where we included the influence of air temperature, precipitation, pond area, and surface velocity on the birth and death rates and area ratios of persist events. In this second model, we kept the mix, split and merge events as stochastic events since they represent a minority of events and the influence of the external drivers was unclear.

4.7.1. Stochastic birth-death model

The purpose of a purely stochastic model is to describe the natural internal variability of a system given by randomly occurring events in time. A birth-death model is a basic type of model commonly used in ecology or epidemiology to study the demography of a population and to provide information on the probability distributions of the number and characteristics of individuals (Bailey, 1968; Kendall, 1948). Such models have also been used in the simulation of the birth and death of rainfall cells (e.g. Paschalis et al., 2013). Birth-death models characterize the evolution of a population following the underlying equation:

(Eq. 4.2) $$\frac{dP}{dt} = B(t) - D(t)$$

Where P(t) is the number of individuals (cliffs) in a given year, B(t) and D(t) are respectively the birth and death rate in cliffs/year. In the case of ice cliffs, we include merge, split and mix events, and the governing equation for the stochastic cliff population dynamics becomes:

(Eq. 4.3) $$\frac{dP}{dt} = B(t) - D(t) + S(t) - M(t) + Mi(t)$$

Where S(t), M(t) and Mi(t) are the split, merge and mix rates in cliffs/year, respectively. Mi(t) can be positive or negative while the other terms are all positive. All the terms are described by their probability density functions (mean and variance) estimated from data. There is a linear dependency between the death rate and the population size (Fig. 4.S5):

(Eq. 4.4) $$D(t + dt) = a\,P(t) + b + \xi$$

Where a and b are estimated from the death rates related to the total population and ξ is a stochastic noise term (Supplementary Material).

Equation (4.3) is solved in a time-stepping manner with $dt = 1\ year$, by drawing the terms B, S, M, Mi, ξ from their respective distributions, starting at time zero with a given initial cliff population. Each individual cliff in the population is assigned to undergo a death, mix, merge, split or persist event based on the probability of individual events in every year, its size and the size distribution of dying, mixing, merging, splitting and persisting cliffs (Supplementary Information, Model Description: 3. Cliff selection). The cliffs are tracked individually in the model and their size is updated at each time-step based on the area ratio distribution of the merge, split, mix or persist event that they undergo. New cliffs are attributed an initial size which is drawn randomly from the size distribution of new cliffs, and dying cliffs are removed from the cliff population. The implementation of the model is described in detail in the Supplementary Information (Model Description, Fig. 4.S10, Table 4.S3, S4).

Since the processes controlling the size changes of the cliffs are also stochastic for each event, the cliff area *A(t)* can be written following a similar equation as Eq. 4.3:

(Eq. 4.5) $$\frac{dA}{dt} = B_A(t) - D_A(t) + S_A(t) + M_A(t) + Mi_A(t) + Pe_A(t)$$

Where B_A, D_A, S_A, M_A, Mi_A, Pe_A are the changes in size from the birth, death, split, merge, mix and persist events which can be positive or negative, except for B_A and D_A which are always positive.

Note that if we combine (Eq. 4.3) and (Eq. 4.4) in a steady state case ($\frac{dP}{dt} = 0$ and $\frac{dA}{dt} = 0$), the mean changes from the different events compensate each other and force the mean population $\bar{P}$ to a given value that is independent of the initial conditions:

(Eq. 4.6) $$\bar{B} - (a\,\bar{P} + b) + \bar{S} - \bar{M} + \overline{Mi} = 0$$

Similarly for the cliff relative area (Eq. 4.5).

In this first version of the model, the probability distributions of the different terms of Eq. 4.3 and 4.5 are fixed in time and in this case $P(t)$ will converge in time to its steady-state value $\bar{P}$. However, these probability distributions can also be time-dependent with individual annual rates a function of external driving forces.

4.7.2. Influence of external drivers

In the second version of the model, we take into account external drivers and their influence on the cliff population dynamics. These external drivers are the monthly air temperature and precipitation from ERA5-Land (Muñoz Sabater, 2019) averaged over the summer months (June to September), the average annual glacier velocity and change in velocity over the centerline of the debris-covered part and the AOI from the ITS_LIVE velocity data (Dehecq et al., 2019), and the total pond area and change in pond area (Table 4.S5-S8). We relate cliff population dynamics and external drivers using a stepwise multivariate regression for the birth rate, relative death rate (defined as the ratio of death events and total number of cliffs at the previous time-step) and the parameters of the size-dependent mean area ratio of persist events (Supplementary Information, Stochastic model description, Table 4.S5-S8). For each of these regressions we use a linear model with an intercept and a linear term for each predictor. The predictors are added using stepwise regression if adding them increases the adjusted correlation coefficient Adj-R^2 value by more than 0.1, which guarantees that the new terms improve the model more than they would be expected by chance (Miles, 2014). This multivariate regression is applied to the whole time series from 2009 (2010 for Satopanth and Bhagirath Kharak) to 2018, since we only had velocity data until that year. We then account for the external drivers in the model by rewriting the birth rate, relative death and area ratio parameters at each time step $Param_j(t)$ as a function of the eight external drivers D_i using the coefficients $a_{i,j}$ and RMSE from the multivariate regression:

(Eq. 4.6) $$Param_j(t) = a_{0,j} + \sum_{i=1}^{8} \delta_{i,j} a_{i,j} D_i + \lambda_j(t)$$

Where $\lambda_j(t)$ is a stochastic term drawn at each time-step from a discrete normal distribution of mean zero and standard deviation equal to the RMSE of the multivariate regression. $\delta_{i,j}$ is equal to zero or one depending on the inclusion or exclusion of the external driver in the multivariate regression (Table 4.S5-S8).

4.7.3. Modeling results

We apply the stochastic birth-death model (without external drivers, section 4.7.1) to the cliff population of the four sites for the duration of the observation time series (Fig. 4.5). The model parameters are estimated from the entire study period, and we run the model 200 times for the period

2009-2019 starting from observed initial conditions in 2009 to quantify the probability distribution of cliff number and area over time. The model converges rapidly and there are no significant changes in mean or standard deviation after more than 200 simulations (Fig. 4.S11). The mean cliff number and area both converge to steady states within the first 10 years of the simulations (Fig. 4.5), and the standard deviation range and maximum spread are also stable in time after this point (Fig. 4.S12). The results obtained by calculating the parameters over the full time series are similar to those obtained when calculating the parameters over the first 5 years, even though the fit is less good, especially for the last years at Satopanth and Bhagirath Kharak (Fig. 4.S13), and are independent of the initial conditions (Fig. 4.S14). All the observations are within the modelled range of values except for year 2012 for the cliff relative area in Urdok (Fig. 4.5). This variability range is characterized by a standard deviation that is between 12 and 20% of the mean value after 10 years for both cliff relative area and number. This means that the observed variability in cliff properties (number and area) in time can be explained by a model in which cliff forming and destruction processes are completely random.
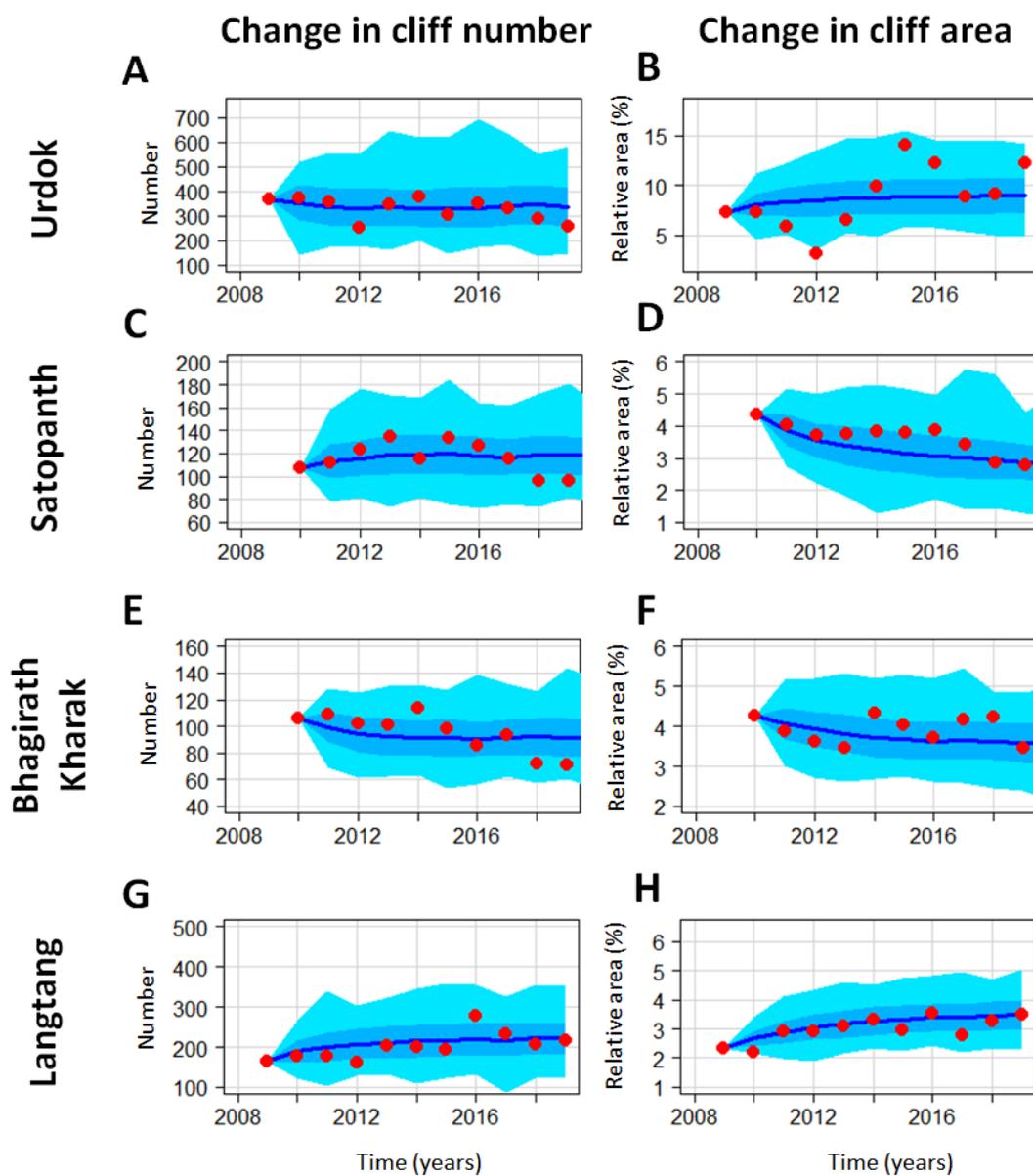
Figure 4.5*: Outputs from the stochastic model for the number of cliffs and their relative area. The model was run 200 times from 2009 (2010 for Satopanth and Bhagirath Kharak) to 2019. Parameters*

were estimated over the full time series. The red dots correspond to the observations from the mapping. The dark blue line corresponds to the average values of the 200 simulation runs. The mid blue area represents the standard deviation of the runs and the light blue area the maximum and minimum values.

The stepwise multivariate regression applied to the four glaciers shows that the most significant drivers for the birth rates are the total pond area and the change in pond area (Table 4.S5). They are the first predictors selected in the stepwise multivariate regression for Urdok, Satopanth and Bhagirath Kharak. For Langtang the air temperature is more significant but the multivariate regression at this site is not statistically significant according to its high P-value (Table 4.S5). Similarly, the glacier velocity and velocity change in the AOI or across the whole debris-covered area are the most significant drivers for the relative death rate and area ratio for the sites where the multivariate regression is statistically significant (Table 4.S6-S8). All the tested drivers contribute significantly to a few model parameters at different sites except for precipitation that has no significant contribution (Table 4.S5-S8).

When applying the model accounting for external drivers, we find that the mean cliff number and relative area do not converge but rather follow similar annual variations to the observations (Fig. 4.6). The variability range is smaller than for the purely stochastic model but all the observations fall within the model minimum and maximum values and most of them are within the standard deviation bounds. For Urdok however the abrupt increase in cliff relative area between 2012 and 2015 is still not captured well while the cliff relative area is underestimated on average for Bhagirath Kharak (Fig. 4.6B, F). This means that external driving variables in the stochastic model are able to reduce uncertainties, better match interannual variability in observations, and in some cases identify situations where the random model fails.
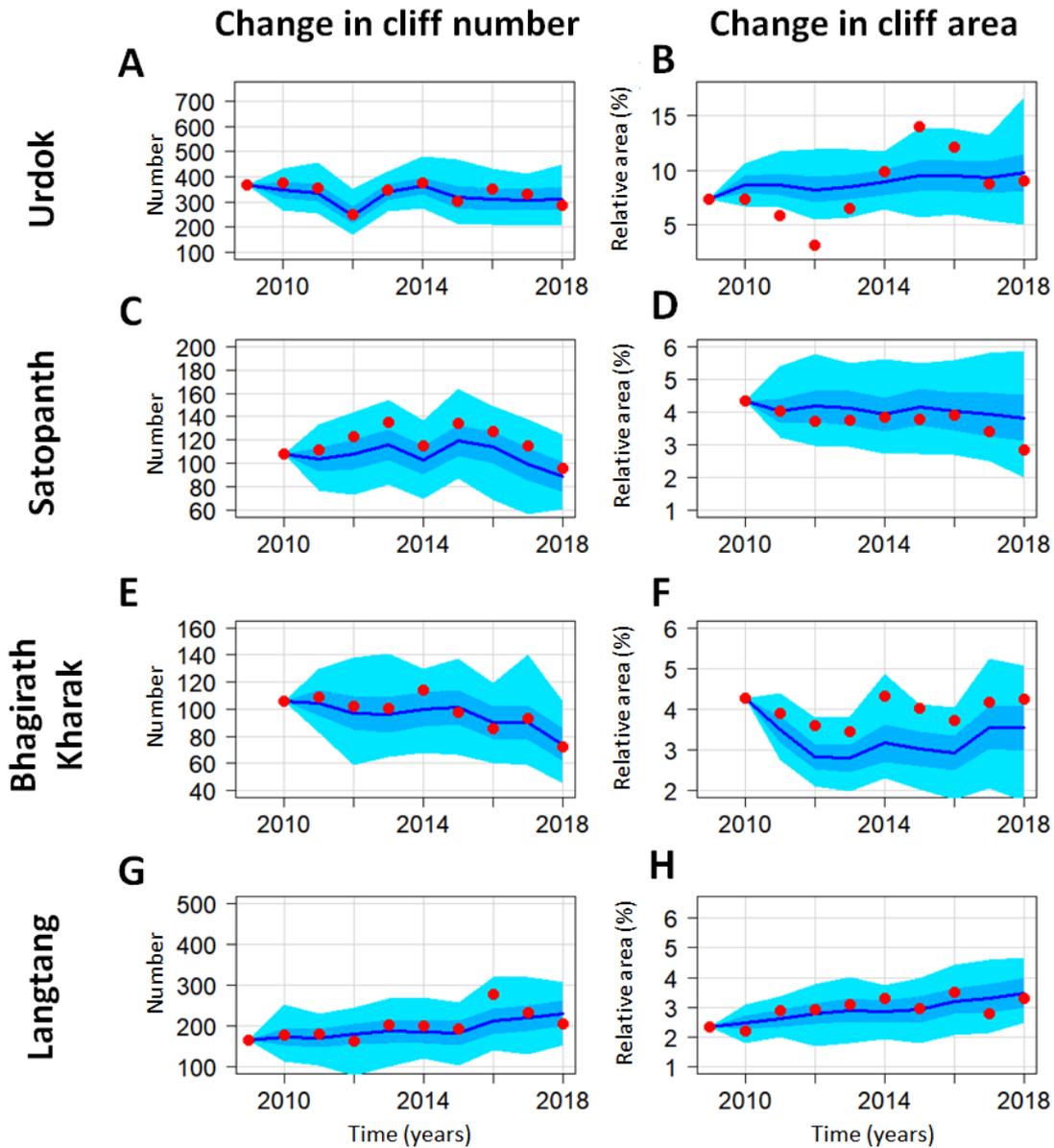
Figure 4.6: Outputs from the stochastic model with external drivers for the number of cliffs and their relative area. The model was run 200 times from 2009 (2010 for Satopanth and Bhagirath Kharak) to 2019. Parameters were estimated over the full time series. The red dots correspond to the observations from the mapping. The dark blue line corresponds to the average values of the 200 simulation runs. The mid blue area represents the standard deviation of the runs and the light blue area the maximum and minimum values. The y-axis scales are the same as for Figure 4.5.

4.8. Discussion

4.8.1. Mapping and tracking limitations

For the cliff mapping we used RapidEye data from Planet Labs (Planet Team, 2017) because of their high spatial resolution (5 m) and relatively long time series (more than a decade of images freely available with an academic license). These are however georectified images without a contemporaneous DEM, so no mapping approach based on slope (Herreid and Pellicciotti, 2018; Reid and Brock, 2014)

could be used in a multi-temporal sense. We tested different multi-spectral approaches, namely the adaptive brightness threshold, the spectral curvature and linear spectral unmixing with scale (Anderson et al., 2021; Kneib et al., 2020), but the results were not satisfying and consistent enough for this sensor, due to the varying illumination conditions and increased shading for some of the scenes compared to the Pléiades and Sentinel-2 sensors for which the methods above were developed (Kneib et al., 2020; Watson et al., 2018). Despite the important effort required and the possible operator bias (Herreid and Pellicciotti, 2018), we thus favored the use of manual delineation of cliffs for this study. For ponds, we used an NDWI threshold since this approach had already been validated for pond mapping with RapidEye data (Watson et al., 2018). Some manual improvement was still necessary for ice-covered ponds but the time investment was minimal compared to the manual delineation of all the cliffs. In the future, the use of an automated approach for cliffs using high-resolution sensors with a high overpass rate to minimize shading such as PlanetLabs will likely enable the study of longer time series and on a seasonal time scale.

The main uncertainties from the cliff mapping come from the operator bias (Fig. 4.S2) and the change in illumination and shadowing from image to image, especially because we did not have access to any high-resolution slope data, which can help discriminate some cliffs (Herreid and Pellicciotti, 2018; Steiner et al., 2019). For the same reason, we could not calculate the cliff slope and aspect and only used ice cliff planimetric area to calculate the cliff relative area. The manual mapping was greatly improved by comparing sequential images. Disruptions in glacier surface motion were thus anticipated to be caused by backwasting cliffs or draining or filling ponds, which helped to constrain the mapping. Accounting for these disruptions in glacier surface motion was performed manually in this study but is a promising method to map cliffs and derive their backwasting rates in an automated way (Altena and Kääb, 2020). Furthermore, comparing the outlines with those derived by independent operators for six different domains across six different images enabled us to constrain the uncertainties from the mapping (Fig. 4.S2). Ultimately, reducing the uncertainties from the mapping requires automated approaches and higher resolution images (Kneib et al., 2020; Salerno et al., 2012). Cliffs and ponds can be mapped at resolutions coarser than 5 meters but this results in higher uncertainties and increases the detectability threshold to only map the larger features (Herreid & Pellicciotti, 2018; Kneib et al., 2020; Miles, Steiner, et al., 2017; Watson et al., 2018). This is especially true for ice cliffs, which have a more elongated shape and can be very steep, thus in general, the finer the spatial resolution, the better (Brun et al., 2018; Immerzeel et al., 2014; Kraaijenbrink et al., 2016).

The tracking disagreements between the manually and automatically tracked cliffs were 10% at most and occurred mostly for cases of small cliffs, for which the aspect was difficult to determine, or cliffs with a sharp aspect discontinuity (e.g. Fig. 4.2F). In such cases, it was difficult to tell which of the manual or automated tracking was correct, and since there were less than 10% of disagreements, we considered the uncertainties from the tracking to be negligible compared to the mapping uncertainties. Having an accurate DEM for each image would have reduced the tracking error considerably by eliminating the cases described above (Steiner et al., 2019). Furthermore, the mean aspect of cliffs can change considerably from one year to the next, so we do not recommend the application of this tracking algorithm for intervals longer than a year.

For this study, which focused on the cliff number and relative area variability, the precision and consistency of the mapping was actually more important than the accuracy of the outlines. The agreement between the four independent operators in the trends of cliff area and number that they derived independently between 2011 and 2016 for six validation domains (Fig. 4.S3) shows that while there were disagreements in the actual values, the trends were mostly similar. Therefore, we would

133

expect that if another operator were trying to reproduce the same experiment, the absolute numbers may disagree with the ones from this study, but the variability and general patterns and therefore the results would be the same.

We also note that the AOISs of the four studied glaciers did not cover the full extent of the debris-covered areas due to snow, shadows and avalanching (Fig. 4.1), and were mostly limited to the lower portions of the glaciers, where we expect thicker debris and more stagnant ice (Anderson and Anderson, 2018). This could potentially bias these observations towards particular cliff-types influenced more by ponds than supraglacial streams, and less by ice dynamics. Similarly, the differences in relative coverage of the AOIs on the different glaciers could influence some of the relative changes observed, which needs to be taken into account in the interpretation of the results.

4.8.2. Life cycle of ice cliffs

The systematic mapping of ice cliffs and ponds at annual intervals in the post-monsoon season and for the same AOI highlights the high variability of these features from one year to the next (Fig. 4.3). This has implications for the melt of debris-covered glaciers, while from a process understanding standpoint it informs about the rates of changes of the glacier surface. This interannual variability had been investigated before (Steiner et al., 2019; Watson et al., 2016; 2017; Miles et al., 2017) but never in such a consistent way. Our results show that the cliff relative area can change regularly by typically 20% from one year to the next, and the pond relative area by more than 40%. In this regard, Urdok is a special site that exhibits even larger variations (up to 100% changes in cliff relative area and 300% changes in pond relative area). As cliffs and ponds are major contributors to the mass balance of debris-covered glaciers and enhance melt by a factor of 3 to 8 relative to the surrounding debris-covered ice (Brun et al., 2018; Buri et al., 2021; Immerzeel et al., 2014; Juen et al., 2014; King et al., 2020; Miles et al., 2018; Mölg et al., 2019; Reid & Brock, 2014; Thompson et al., 2016), these results highlight the need to take into account the variability of these features in glacier melt models.

Interannual ice cliff variability is extreme at the feature scale, with typically 15 to 30%, and in some years up to 50%, of new cliffs forming every year (Fig. 4.4). The dynamics vary from cliff to cliff, with some cliffs observed in only a single year (usually the smallest ones), and others persisting for the whole study period. The evolution of a cliff is partly constrained by the presence or absence of a pond (Fig. 4.S8). The fact that at all sites the proportion of pond-associated cliffs is greater for persisting cliffs than for dying or new cliffs implies that association with a pond is indeed a key factor promoting cliff longevity (Brun et al., 2016; Buri, Miles, et al., 2016; Miles et al., 2016; Watson, Quincey, Carrivick, et al., 2017). Ponds encourage cliff persistence, and pond drainage can be a precursor to cliff death. Fluctuations in the ponded area have a significant influence on the birth rate of the Urdok and Satopanth cliffs and the relative death rates of the Urdok cliffs (Table 4.S5-S6). The negative relationship between the cliff birth rate and pond area for Urdok and Bhagirath Kharak (Table 4.S5) could indicate that draining ponds wash away the debris, leading to cliff birth. However, despite this control for individual cliffs, there is no clear relationship between cliff and pond relative area at the scale of an individual glacier (Fig. 4.3) because the ponds only affect less than 50% of the cliff population (Fig. 4.S9). Therefore, at the glacier scale, the pond influence is muted by other factors and their contribution to cliff persistence is not always significant. Cliffs and ponds also evolve on different time-scales, with ponds having much stronger seasonal variations than cliffs (Miles, Willis, et al., 2017).

The size of the cliff also plays a role in its evolution. We found that cliffs tend to follow a lognormal distribution with regards to their size, which is consistent with what has been found on Khumbu glacier

(Watson et al., 2017a). Some studies using semi-automated mapping found that the number of cliffs or ponds on a glacier increases exponentially as size decreases (Kneib et al., 2020; Miles, Willis, et al., 2017), which could mean that there is an observational bias for mapping only the large features relative to the sensor resolution (Salerno et al., 2012), but this would need to be confirmed by very high resolution mapping from field observations and UAV flights. New cliffs and dying cliffs are in general smaller than the other cliffs, even if there are exceptions. Interestingly, we also found that the area ratio of persist events decreases with the initial cliff size (Fig. 4.S7). However, these observations are likely biased by the fact that we cannot detect ice cliffs smaller than a few pixels (< 100-200 m^2), which means that what we count here as birth or death events may just be persist events, but involving features that have passed beyond the satellite images' limit of detectability. The area ratio of persist events is centered around 1 but there are cases where the cliff size is multiplied or reduced by a factor up to 10, which can happen when the cliff expands laterally on the nearby slopes. This expansion or reduction probably depends on the stability of the debris on an ice slope, which is linked to the slope angle but also to the debris water content and the presence of a pond or stream at the base of the slope (Moore, 2018).

Merge, split or mix events also contribute to the interannual variability of the cliff population, especially for the change in cliff relative area. Their contribution to cliff area change follows the same general pattern as the contribution of persist events (Fig. 4.4), which means that while these events are mostly stochastic and, for merge and mix events, dependent on the local cliff concentration, at the glacier scale their contribution to the cliff area change has the same drivers as the persist events.

All these events contribute to increasing the interannual variability of the cliff population, except for death events, which to some extent compensate for strong variations in cliff number and as a result, relative area. Indeed, at all sites an increase in the number of cliffs usually results in an increase in the number of death events the year after. Such feedback is the basis of most birth-death models in a closed system with limited resources (Bailey, 1968; Kendall, 1948).

4.8.3. Controls on ice cliff variability

Determining the controls of the variability of the cliff population is important to understand the observed patterns and relate this to processes happening at the glacier surface, but also in a broader sense to understand whether these variations are purely stochastic or on the contrary are representative of a particular glacier state or evolution. The stochastic model runs provide new insights into the natural internal variability of the cliff population at the glacier scale based on the observed variability of the system. This gives a first approximation of the system bounds in the long term, assuming that the glacier surface does not undergo major changes. Our stochastic model outputs a distribution of cliffs that depends on the initial conditions for the first few years but rapidly converges to a steady state that depends on the parameters of the different events and that has an internal variability that is proportional to its mean value. We estimated the parameters over a period of 10 years (Fig. 4.5) and 5 years (Fig. 4.S13) and obtained similar results despite a less good fit in the second half of the time series when the parameters were estimated over the first five years, which shows that the variability of the cliff populations only changed marginally over our observation period. Assuming that the general climatic and glaciological conditions encountered persist, the results of the model inform us on the long-term variability of the cliff populations of these four glaciers (Fig. 4.S12).

The stochastic assumption enables us to calculate the internal variability of the system but does not tell us if this variability can be influenced by external drivers. Adding the influence of external drivers in the model reduces the variability and improves the fit with the observations, which shows that these

external drivers do have an influence on the variability of the system. The results from the multivariate regression help explain some of the observed variability and link it with climate, glacier velocity or pond evolution. None of the tested variables stands out as a principal driver and all contribute to some extent to the observed changes. They are, however, all related to the melt at the surface of the glacier, since climate variables influence melt and this melt will increase the amount of water circulating at the surface of the glacier via ponds and streams, while enhancing basal sliding and therefore glacier velocity (Kraaijenbrink et al., 2016; Yang et al., 2020).

Urdok is an interesting study site as its cliff population undergoes extreme variations, and shows a major increase in cliff relative area between years 2012 and 2015 that the internal variability fails to explain. This change results from an increase in cliff size from merge, mix and persist events (Fig. 4.4) and coincides with a strong increase in the average velocity of the debris-covered area (Fig. 4.7) that could be indicative of a surge event. The fact that this increase in cliff relative area is driven by merge and mix events is a sign that there is a large reorganization of the cliffs at the scale of the glacier, while at the same time they increase in size. The comparison of cliff outlines between 2012 and 2015 shows that the cliffs expand laterally in the direction of their principal axis along sinuous paths across the glacier surface (Fig. 4.7D-G). This can be interpreted as the rapid development of large 'cryo-valleys' at the surface of the glacier, as these cliffs develop and expand on either side of supraglacial streams, thus reshaping the surface of the glacier within the span of a few years. Similar mechanisms have been described on Zmutt glacier (Mölg et al., 2020) but over the course of several decades and without the occurrence of a glacier surge. Rather, the development of cryo-valleys at Zmutt seems to have occurred as the glacier stagnated, leading to persistent configurations of the glacier's drainage network (Mölg et al., 2020), whereas in the case of Urdok, the cryo-valley development coincides with an up-glacier (but not local) increase in velocity, suggesting reorganization of drainage networks driving water to the glacier's surface above the study area, which is supported by the erratic interannual fluctuations of pond area observations during this period (Fig. 4.3). Understanding the mechanism of Urdok Glacier's increase in velocity is outside the scope of the present study and an opportunity for further investigation, but the example shows clearly that cliff and pond populations can undergo considerable changes due to external drivers.

Our stochastic model lets us quantify the possible range of the number and relative area of ice cliffs and our observations fall within the model bounds in all cases except for Urdok. There, the glacier is undergoing a major change which results in the complete rearrangement of the cliffs at its surface. We interpret the variability bounds given by the model as a physical constraint on the system. These bounds define the cliff carrying capacity of a glacier. Indeed, the number and relative area of cliffs is constrained by the availability of steep slopes, which is in turn constrained by the number of hummocks and cryo-valleys (Bartlett et al., 2020; King et al., 2020; Mölg et al., 2020). The size of the hummocks is constrained by the glacier size (Bartlett et al., 2020), which gives an upper bound to the cliff relative area. However, the development of cryo-valleys enables cliffs to arrange themselves in a very different and denser way than on a purely hummocky surface, and this transition is clearly visible in the case of Urdok (Fig. 4.7). The exact reasons for this transition are unclear but are probably linked to the surge event highlighted by the change in velocity of the debris-covered area, which impacts the glacier hydrological system (Chudley & Willis, 2019; Gulley et al., 2009; Miles, Willis, et al., 2017; Quincey et al., 2015). Indeed, the data for Urdok suggests that a surge front migrated through the upper part of the glacier (above the AOI) with little impact on the velocity or strain rates in the AOI but resulted in the routing of more water at the surface of the AOI, thus leading to the development of cryo-valleys. Therefore, the ice cliff population is expected to evolve within the bounds given by the stochastic model parameters, but this steady state can be modified by intense changes in surface topography resulting

from major glaciological or climatic changes. As a result, we expect that the state and distribution of ice cliffs on a glacier could inform us to some extent about its dynamic state and climatic drivers.
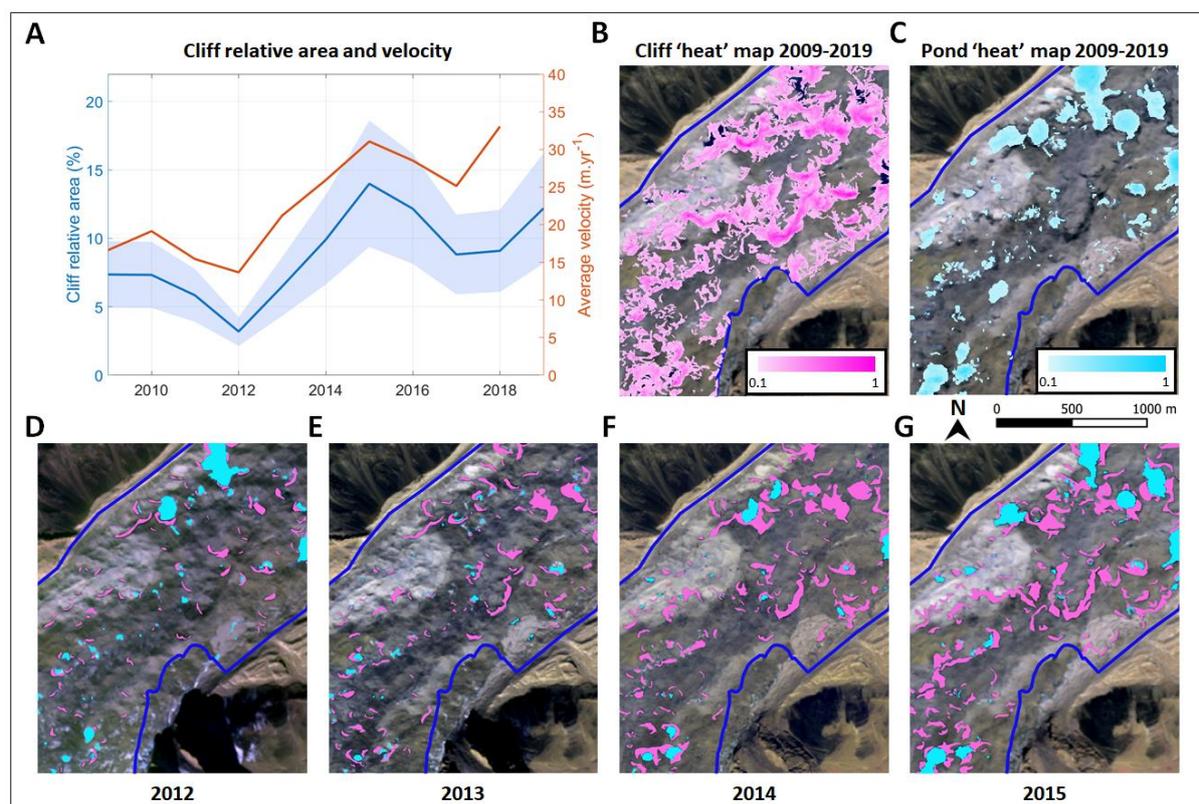
Figure 4.7*: Development of cryo-valleys between 2012 and 2015 on Urdok glacier. (A) cliff relative area and average surface velocity along the centerline of the debris-covered area over time. (B-C) Cliff and pond density maps of the lower portion of Urdok, where 0 corresponds to no cliff or pond occurrence over the whole time series and 1 corresponds to the occurrence of cliffs or ponds in all images. Background image is the 2015 RapidEye scene (color composite of bands 5, 4 and 2). (D-G) Maps of cliffs (pink) and ponds (blue) on the same portion of Urdok for the 2012 to 2015 RapidEye images. Background images are the corresponding RapidEye scenes (color composite of bands 5, 4 and 2).*

The fact that none of the tested variables stands out as a main driver of the cliff variability highlights the complexity underlying ice cliff evolution, due to a number of competing and interlinked processes happening at the glacier surface (Fig. 4.8). Indeed, changes in glacier velocity or climate may translate differently at the local scale depending on the local hydrology, debris thickness and topography. At this local slope scale, the cliff area change, including formation or decay, is ruled by debris mobilization, which depends on local slope characteristics (Moore, 2018). These include the slope angle, the debris water content along with the state of the base of the slope and the possibility for sliding debris to be removed (Moore, 2018), but also on the surrounding topography which may constrain the cliff's lateral expansion. A number of processes that are interdependent and difficult to quantify at larger scales may modify these slope characteristics. For example, the development of a supraglacial stream or pond from sub-debris melt and in-debris flow routing (Fyffe et al., 2019; Miles, Steiner, et al., 2017; Westoby et al., 2020) has the combined effect of increasing the melt at the base of the slope and removing the debris sliding down it (Benn et al., 2001; Miles et al., 2016; Moore, 2018). The development of supraglacial streams is therefore beneficial to an increase in cliff relative area along cryo-valleys (Mölg et al., 2019) as long as the incision rate does not exceed the sub-debris melt rate (e.g. Reid & Brock, 2010), which

would lead the stream to form an englacial conduit via a cut-and-closure mechanism (Gulley et al., 2009; Jarosch and Gudmundsson, 2012). Such a stream could however be interrupted by the opening of a crevasse, which depends on the glacier strain rates, while at the same time such crevasses could initiate ice cliff formation via an increase of the slope angle and the removal of debris (Reid and Brock, 2014). Crevasses may also affect flow routing and therefore the draining or filling of ponds (Miles, Willis, et al., 2017; Watson et al., 2016), with consequences on melt or slope availability for cliffs (Miles et al., 2016). These processes are all influenced by external variables such as climate and glacier dynamics, but also depend on the local topography (Fig. 4.8). When looking at the cliff population of a glacier in the long term, the stochastic approach ignores these processes that are conceptually understood or at least hypothesized, but difficult to measure. However, in some cases like for Urdok Glacier, they may trigger major changes in the cliff relative area, which calls for a need to quantify these processes more accurately to better understand the drivers of cliff evolution.

Figure 4.8: *(A) Processes influencing ice cliff area change from the local slope to the glacier scale. The glacier surface processes are all attributed a different color. (B-C) Evolution of a cliff-pond system on Langtang Glacier and a cryo-valley cliff on Urdok Glacier from 2009 to 2019. The pink outlines correspond to the different states of the cliffs that first appeared in the images in 2011 for Langtang and 2009 for Urdok. The associated ponds are represented in blue. The colored dots at the base of each map represent the most likely glacier surface processes at play at this location in the previous 2 years.*

4.8.4. Outlooks

The significant variability of ice cliffs that we observed shows that cliff population dynamics need to be taken into account for distributed glacier melt models operating at multi-year timescales. Indeed, for example on Langtang, an increase in cliff relative area of 20% could translate into 4% of additional volume loss of the debris-covered area (Buri et al., 2021). The stochastic cliff birth-death models are

computationally efficient tools to represent this variability and an interesting next step would be to analyse backwasting rates in combination with the different events we described here. This would likely require high resolution DEMs for the cliff time series or at least solid assumptions for cliff slope. For this purpose, and despite available cliff energy-balance models (Buri et al., 2016b; Juen et al., 2014), a better understanding of the relationship between the different steps of the cliff life cycle, debris redistribution and action of supraglacial streams and ponds, especially during the melt season, would be very valuable. It has been suggested that cliffs could increase in size during the monsoon season (Steiner et al., 2019) due to debris mobilization from precipitation and melt, but such a seasonality has not been clearly observed; a more detailed analysis of what happens to cliffs sub-seasonally, and especially during the monsoon, and the implications for cliff-associated melt would thus be highly relevant. A better understanding of these processes would also help improve the stochastic model that is, at present, highly empirical and glacier specific. Quantifying various surface processes, understanding their spatial and temporal scales, and linking them with climatic variables and glacier dynamics will likely enable a more robust representation of ice cliff variability.

This study also shows that there can be very different ice cliff population dynamics for different glaciers, which depend at least partially on the mechanisms that drive cliff birth and organization. However, this variability is difficult to constrain due to the lack of large-scale observations of ice cliffs. The emergence of semi-automated approaches to map these features from remote sensing data (Anderson et al., 2021; Herreid & Pellicciotti, 2018; Kneib et al., 2020) should enable this large-scale mapping and as a result a better understanding of cliffs' broad spatial variability. Finally, the cliff tracking approach and dataset along with the model developed here offer an opportunity to further investigate the causes of individual and bulk cliff behavior and thus better understand the local drivers of cliff birth and death and the possible influence of the local topography, surface hydrology, geomorphology or glacier motion.

4.9. Conclusions

In this study, we combined systematic mapping of ice cliffs at yearly intervals with a method to track individual cliffs in order to quantify and characterize the cliff population variability of four HMA glaciers. Our results show that the cliff relative area can commonly change by 20% and up to 80% from one year to the next at the surface of a glacier. Due to the melt enhancement effect of the cliffs, this variability will have large implications for the melt of debris-covered glaciers and should therefore be accounted for in glacier and glacio-hydrological models, at least in a stochastic way in a first step to include this additional uncertainty from natural cliff variability in the melt rates.

This interannual variability is driven by a combination of contributions from different events occurring at the cliff scale and that rule the cliff life cycle. Birth and death events dominate the variability in the number of ice cliffs. Death events constrain the number of ice cliffs, thus defining the cliff carrying capacity of a glacier while birth events are stochastic, with some dependence on the pond interannual variability. These ponds promote cliff persistence but affect less than 50% of the population and thus are not the main driver of the cliff population's interannual variability. The changes in cliff relative area are also driven by the net contributions of persist events in addition to net contributions from split, merge or mix events that vary consistently.

These events can be represented in a stochastic birth-death model to constrain the long-term natural variability of the number and area of cliffs. Some of the changes are however not entirely stochastic and our results show that they can be influenced by climate, supraglacial ponds and/or surface velocity, in spite of the complexity of all the interdependent processes occurring at the glacier surface. As a result,

major climatic or glaciological changes, such as we have seen in the case of a surge, may lead to a reorganization of ice cliffs at the glacier surface and a change in the natural variability of the system.

4.10. Open Research

All the cliff and pond outlines generated for this study are available on Zenodo (10.5281/zenodo.4632840) along with the different codes used, including the ones used for the tracking and the modeling (Kneib et al., 2021). Other datasets used for this research are elevation changes (Brun et al., 2017), surface velocity data from ITS_LIVE (Dehecq et al., 2019; Gardner et al., 2018), climate data from ERA5-Land (Muñoz Sabater, 2019) and debris-covered glacier outlines (Herreid and Pellicciotti, 2020b).

4.11. Acknowledgements

4.12. Supplementary material

Table 4.S1: *Multi-spectral satellite data used to map cliffs and ponds.*

Site	Year	Sensor	Date of acquisition
Langtang	2009	RapidEye	03/11/2009
	2010	RapidEye	26/10/2010
	2011	RapidEye	16/12/2011
	2012	RapidEye	08/11/2012
	2013	RapidEye	11/10/2013
	2014	RapidEye	11/10/2014
	2015	RapidEye	25/10/2015
	2016	RapidEye	21/10/2016
	2017	RapidEye	12/11/2017
	2018	RapidEye	20/10/2018
	2019	RapidEye	14/10/2019
Urdok	2009	RapidEye	26/09/2009
	2010	RapidEye	20/11/2010
	2011	RapidEye	29/09/2011
	2012	RapidEye	27/10/2012
	2013	RapidEye	29/09/2013
	2014	RapidEye	18/08/2014
	2015	RapidEye	09/08/2015
	2016	RapidEye	30/12/2016
	2017	RapidEye	24/09/2017
	2018	RapidEye	12/09/2018

	2019	PlanetScope	04/09/2019
Satopanth & Bhagirath Kharak	2010	RapidEye	17/10/2010
	2011	RapidEye	21/09/2011
	2012	RapidEye	23/09/2012
	2013	RapidEye	20/09/2013
	2014	RapidEye	06/10/2014
	2015	RapidEye	16/09/2015
	2016	RapidEye	23/10/2016
	2017	RapidEye	02/10/2017
	2018	RapidEye	30/10/2018
	2019	PlanetScope	10/10/2019
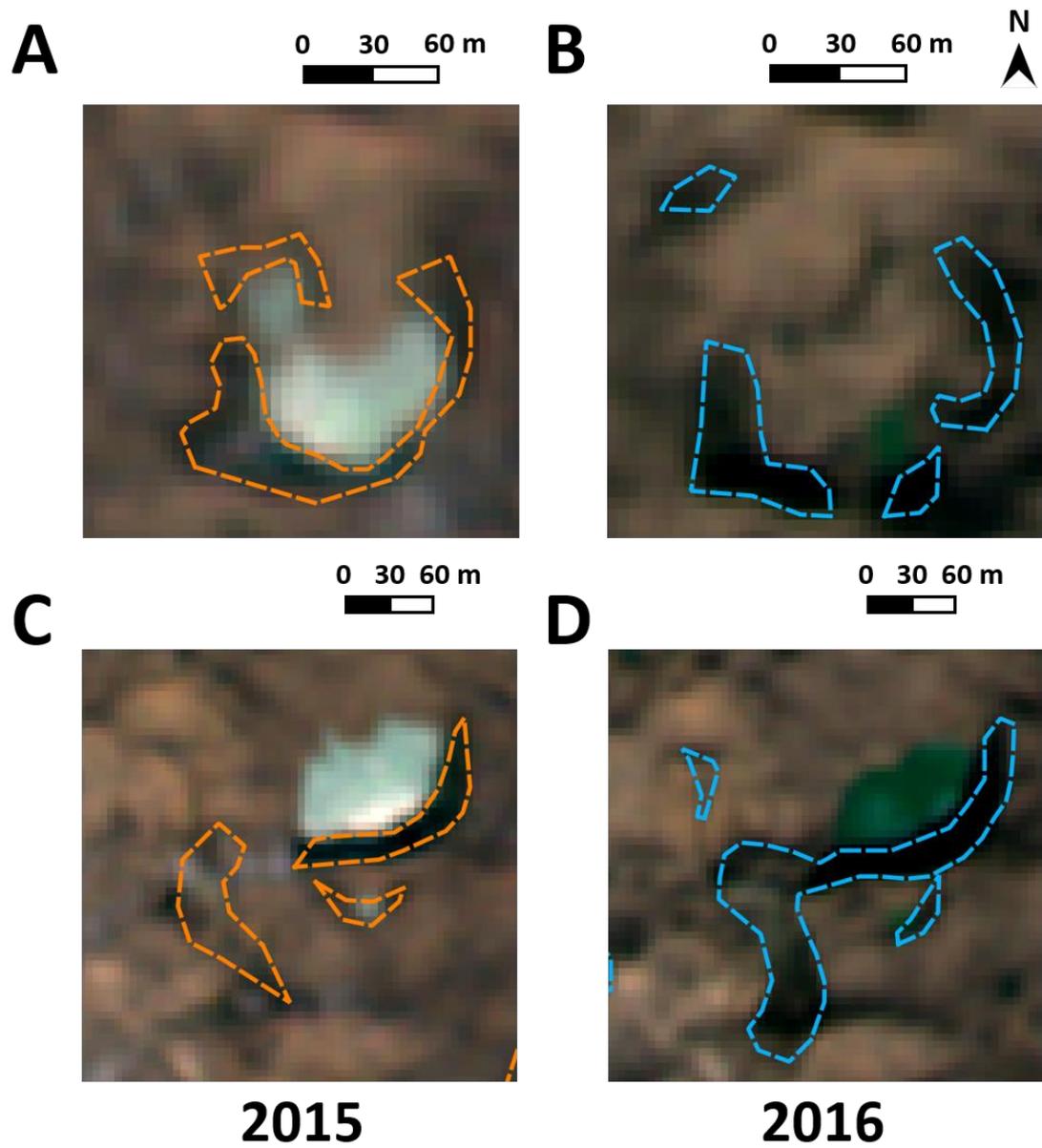
Figure 4.S1: *Mapping of ice cliffs at two locations (upper and lower panels) on Langtang Glacier from the 2015 and 2016 RapidEye images. In orange are the cliff outlines in 2015 and in blue the outlines in 2016. Background images are the RapidEye 2015 and 2016 scenes (color composite of bands 4, 2 and 1).*
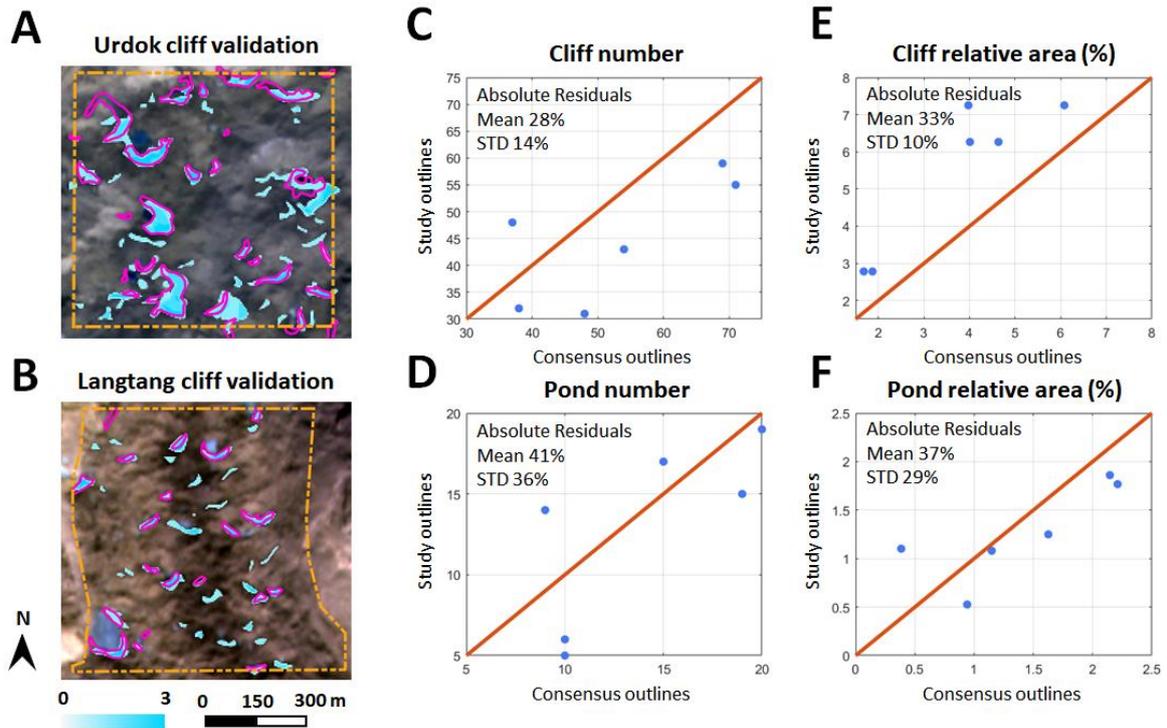
Figure 4.S2*: Mapping uncertainties. Panels (A) and (B) show two of the six domains where the cliffs and ponds were validated (orange dashed lines), one on Urdok and the other on Langtang. The pink outlines correspond to the 2011 cliff outlines used in this study and the blue patches are the sum of the non-binary rasterization of outlines from the three independent operators from the same year. The background images are the 2011 RapidEye images (color composites of bands 5, 4 and 2). Panels (C) to (F) represent the cliff and pond relative area and number of this study versus those of the consensus outlines (blue dots), in comparison with the 1:1 line (red). Each dot corresponds to the values from the two domains in each image used for validation.*

144
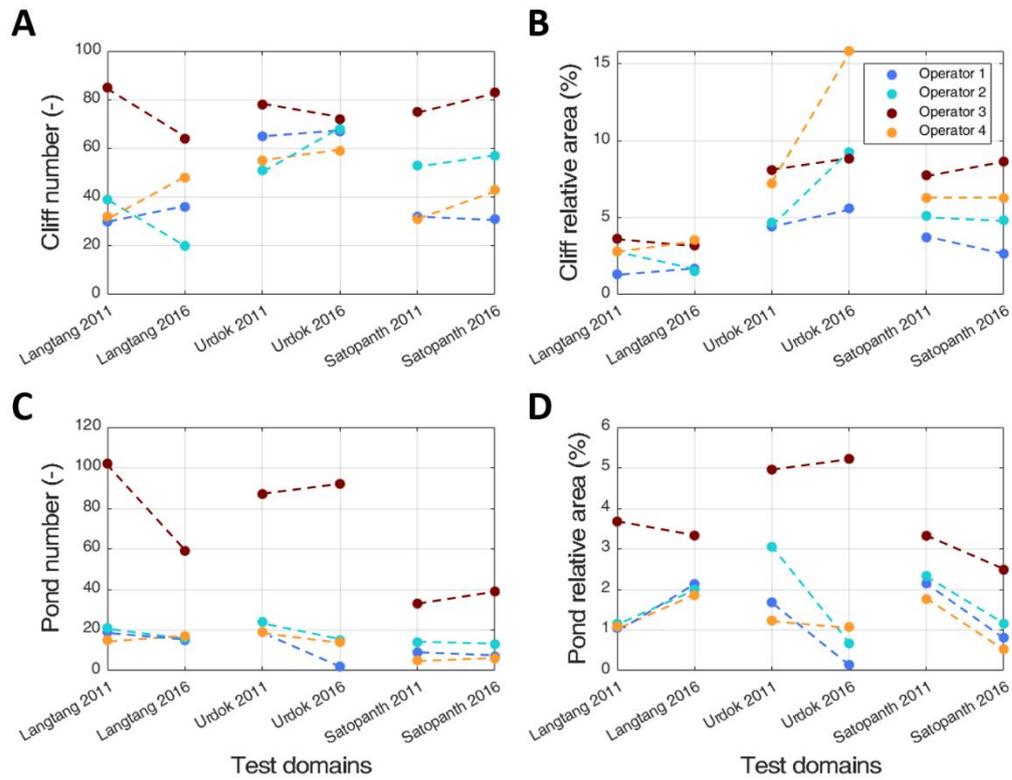
Figure 4.S3*: Comparison of the cliffs and ponds number and relative area mapped by the four independent operators in the six validation domains in 2011 and 2016. The different colors correspond to the four operators and the dashed lines represent the trends between 2011 and 2016. Operator 4 was responsible for the cliff and pond delineation in all images outside of the validation period.*

Table 4.S2. *Parameters of the tracking algorithm.*

Tracking parameters	Values
Maximum distance (between cliffs)	20 m.yr^{-1}
Maximum aspect difference	30°.yr^{-1} mod 180 °
Aspect standard deviation threshold over which only the closest pixels are considered	45°
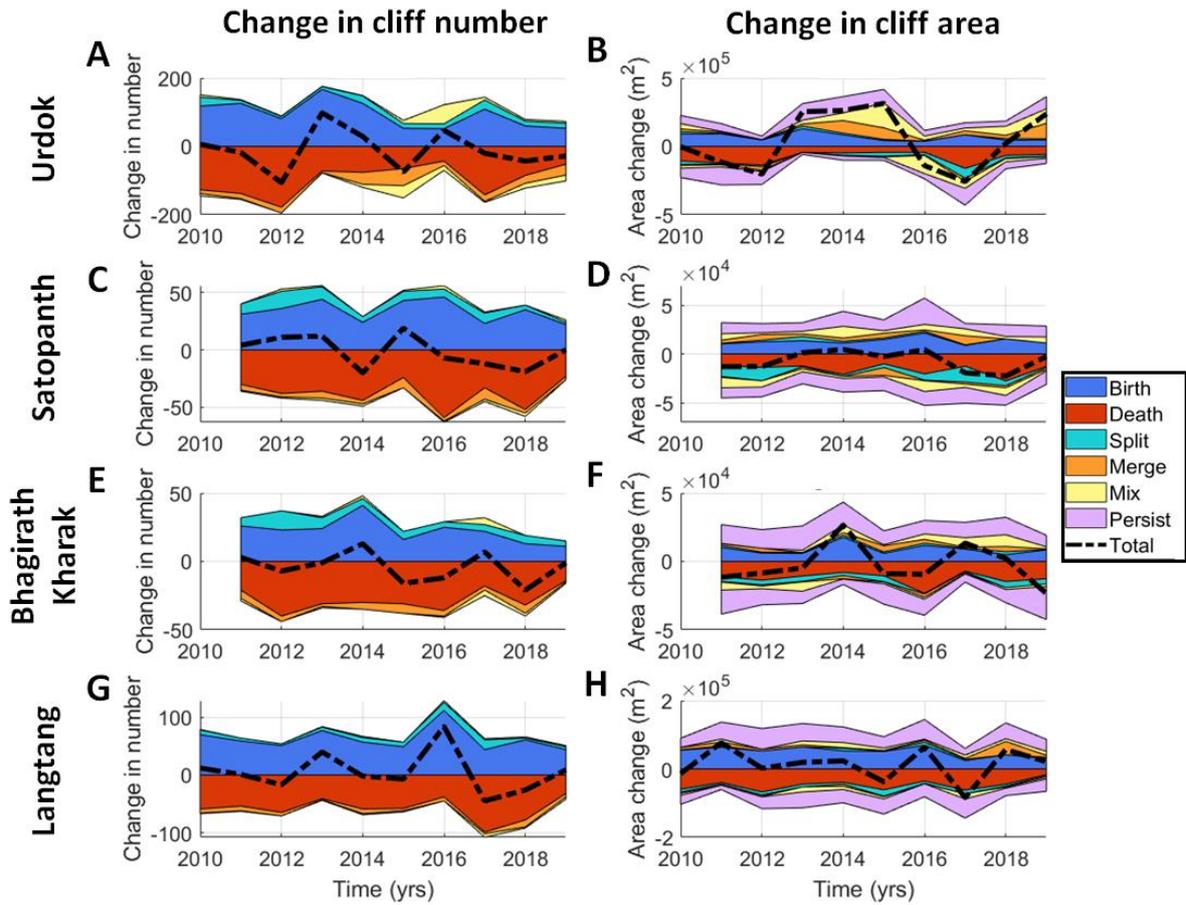
Figure 4.S4: *Total contribution of different events to the general evolution of ice cliffs. The left panels show the change in cliff number and the right panels show the change in cliff area. For comparison, the mean cliff number (area) is 328 (6.8×10⁵ m²), 116 (1.5×10⁵ m²), 95 (1.2×10⁵ m²) and 201 (3.3×10⁵ m²) for Urdok, Satopanth, Bhagirath Kharak and Langtang, respectively. Note that the color envelopes are not overlapping but stacked on top of one another.*

146
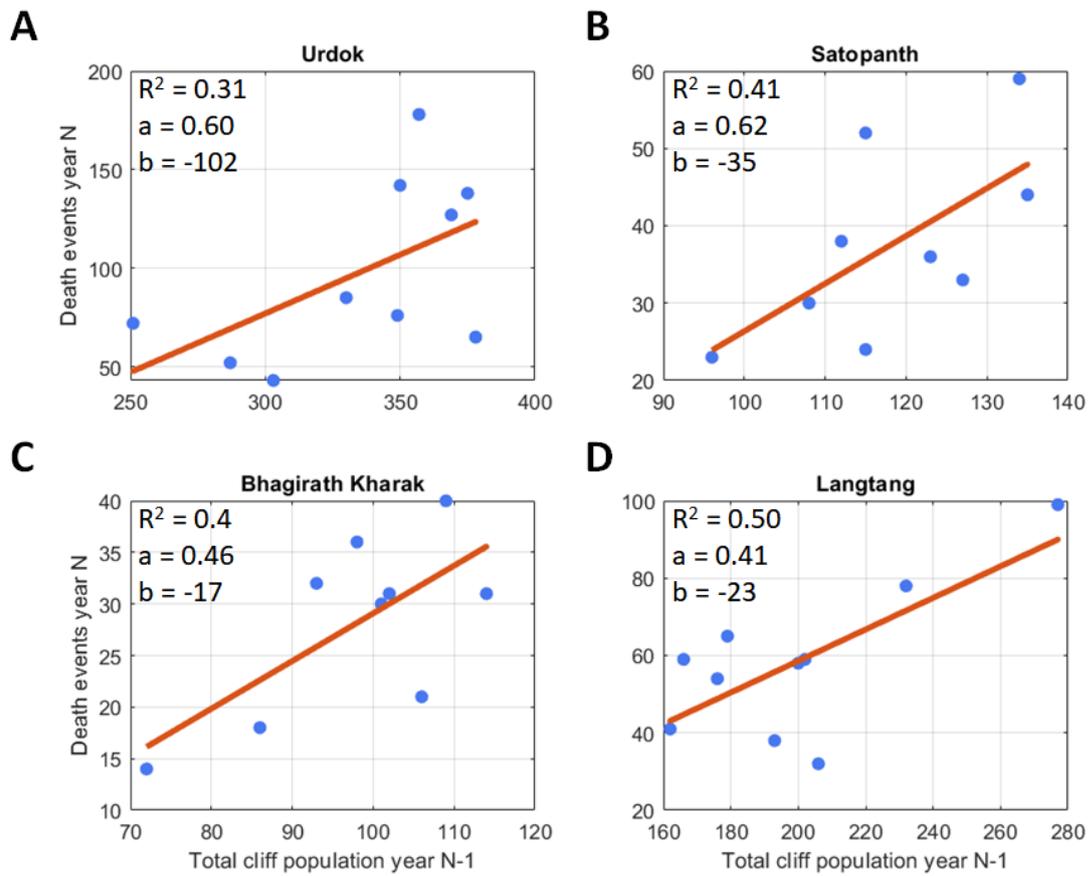
Figure 4.S5: Number of death events plotted against the total number of cliffs the year before at all sites. The red line corresponds to the linear regression between the two datasets of slope a, intercept b, and coefficient of determination R^2.
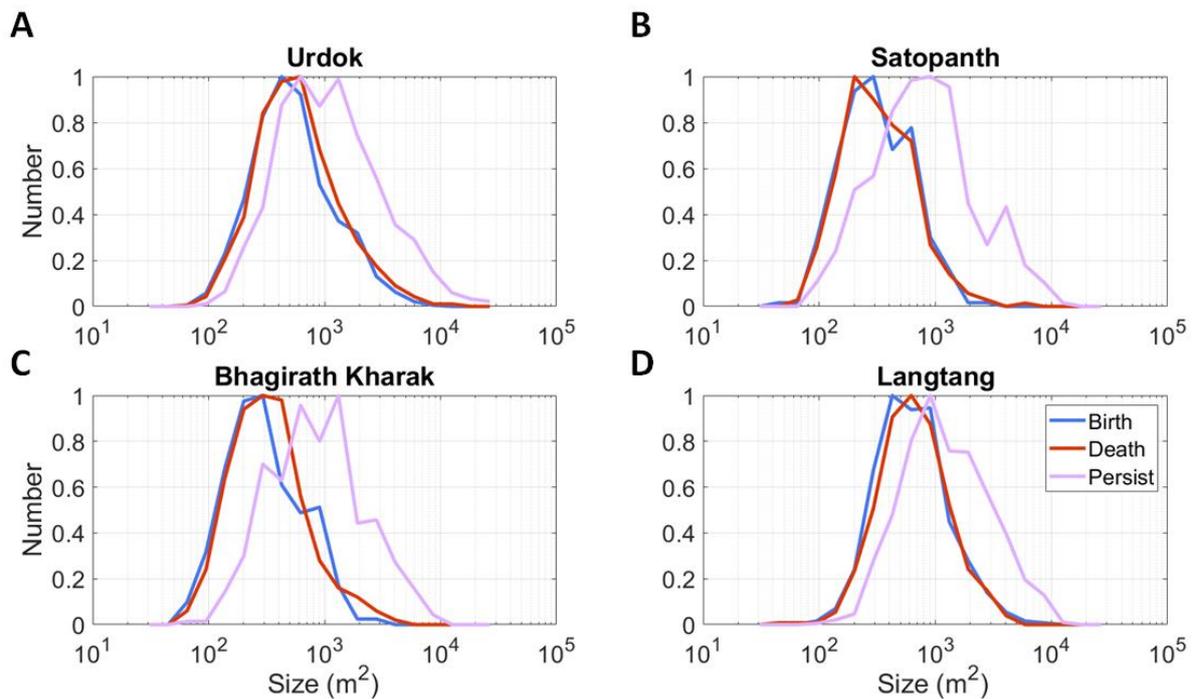
Figure 4.S6: *Size distribution of new cliffs, dying cliffs (cliffs gone the next year) and persisting cliffs at each site and calculated over the whole time series.*
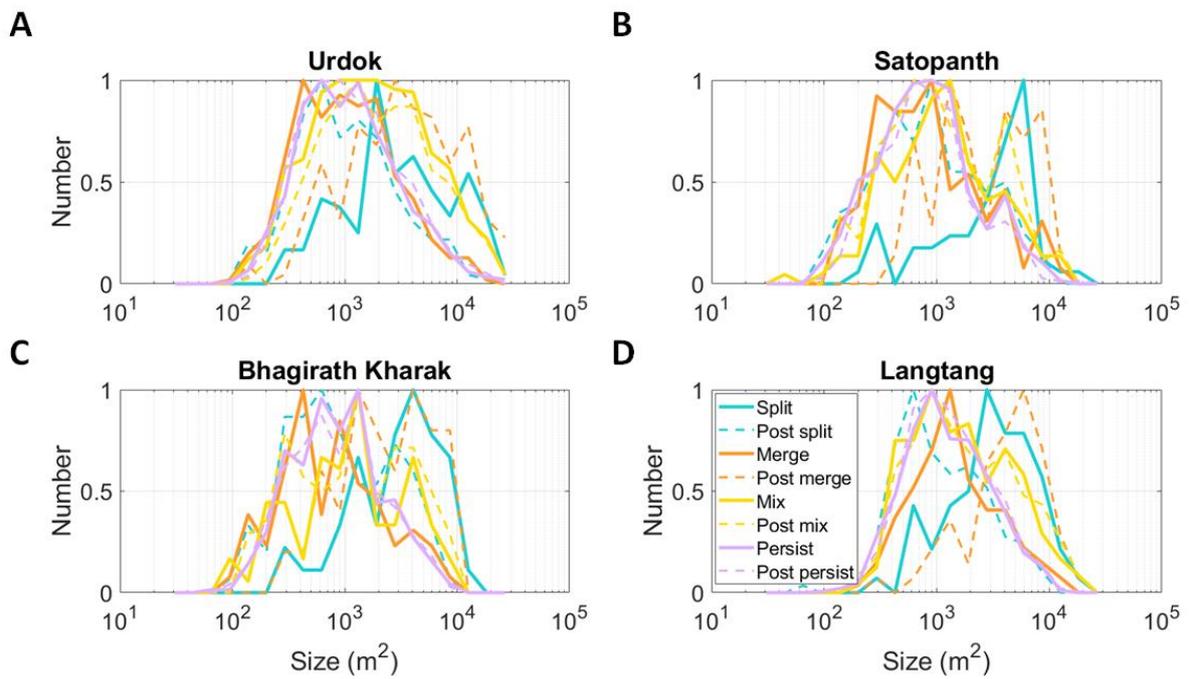
Figure 4.S7: *Size distribution of cliffs just before (continuous lines) and just after (dashed lines) a split, merge, mix or persist event at each site and calculated over the whole time series.*
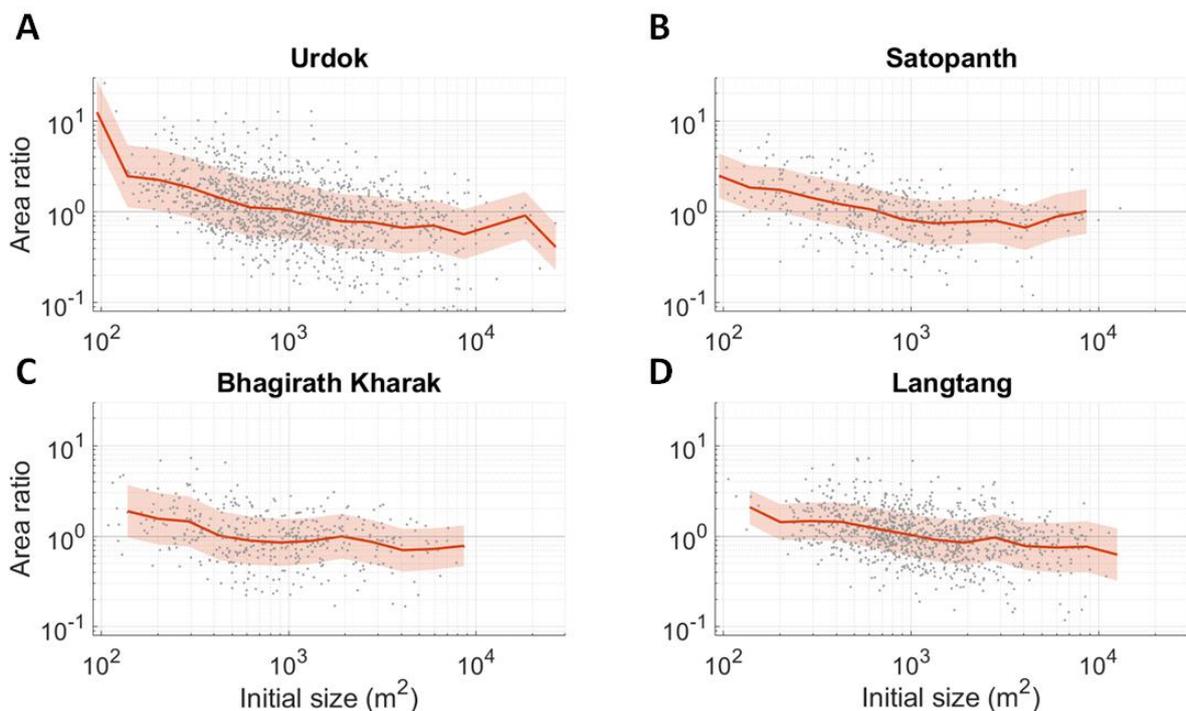
Figure 4.S8: *Area ratio of persisting cliffs as a function of the initial size. The grey points correspond to all the persist events of the time series. The data was binned in 19 bins of equal size in the log scale, from 25 m^2 to 32000 m^2. The red lines are the mean area ratio values for these bins and the standard deviation is represented by the light red area.*
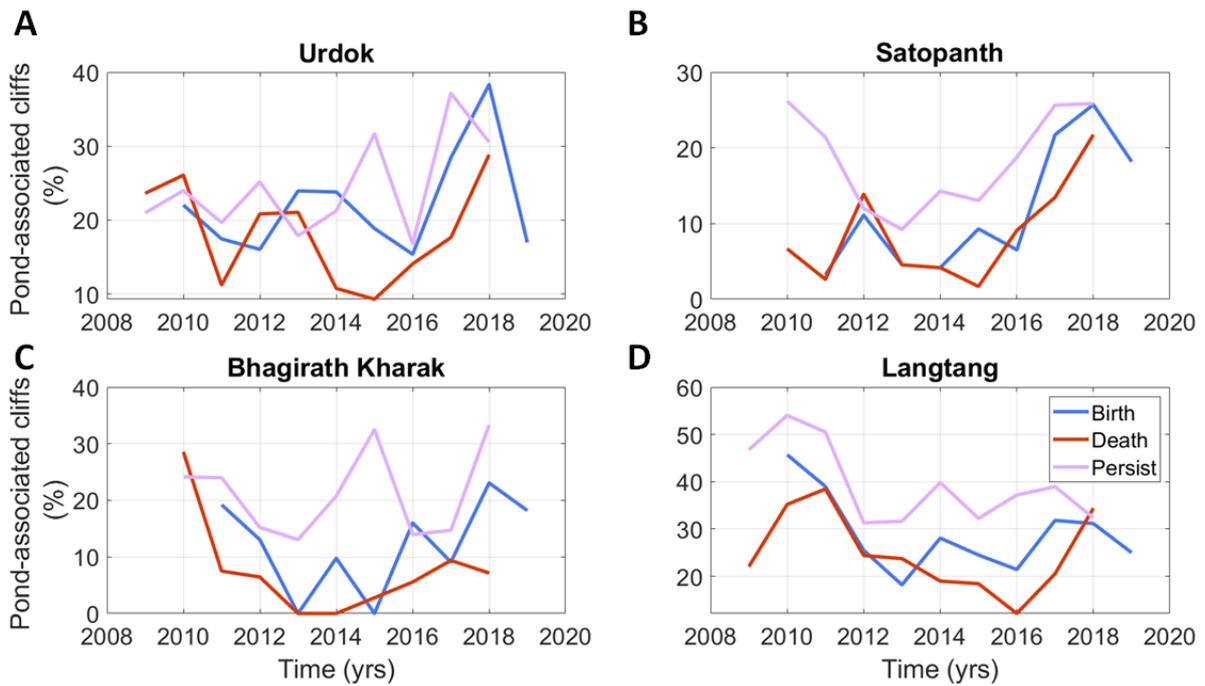
Figure 4.S9: *Proportion of cliffs less than 10 m away from a pond in the new cliffs, dying cliffs and persistent cliffs populations, over time and at each site.*

4.12.1. Stochastic model description

This stochastic model represents the evolution of each individual cliff of a given population based on different parameters describing the occurrence and characteristics of birth, death, merge, split, mix and persist events (Fig. 4.S10). The model takes as input an initial number of cliffs, each with its own size. At each time step, the cliffs undergo death, split, merge, mix, persist or birth events and their number and sizes change. The only constraint on the cliff sizes calculated from the model is that they are within the minimum and maximum sizes, respectively equal to 100 m² (four RapidEye pixels) and the maximum observed cliff size during the period over which parameters are estimated. At each time step, these events are represented following the same procedure (Fig. 4.S10):

4.12.1.1. Rates of events

The number of birth, split, merge and mix events are drawn randomly at each time step from the discrete normal distributions of the yearly number of birth, split, merge and mix events, which are estimated from the data. The number of death events is obtained from the linear regression between death events and cliff population the year before (Eq. 4.4, Fig. 4.S5) and the stochastic term ξ is given by the normal distribution of the residuals of the linear regression.

149

Death, split, persist and birth events only involve one cliff, but merge and mix events involve two or more cliffs. This number of cliffs per event (initial cliff ratio) is calculated for each merge and mix event based on discrete normal distributions estimated from the data.

4.12.1.3.   *Cliff selection*

The dying cliffs are selected based on the parametrized lognormal distribution of the size of dying cliffs (Fig. 4.S6). For each death event, a number is generated from the lognormal distribution and the cliff with the size closest to this number is selected for this event and removed from the population of cliffs. A similar process is applied to select the cliffs that are to undergo a split or mix event out of the cliffs that have not already been selected to undergo a death event. The cliffs that are to undergo a merge event are randomly selected from the remaining cliffs. All the cliffs that remain undergo a persist event. The size of the new cliffs generated by the birth events are directly generated from the size distribution of new cliffs (Fig. 4.S4).

4.12.1.4.   *Area ratio*

The cliffs undergoing a death event are removed from the population and the size of the new cliffs is generated in the 'Cliff selection' step. For each merge, split, mix and persist event, the final size (sum of final cliff sizes) is calculated from the initial size (sum of initial cliff sizes) and the area ratio (Eq. 4.S1). The area ratio is generated from a lognormal distribution that is dependent on the size of the initial cliffs. The parameters of this size-dependent lognormal distribution, the area ratio mean $\bar{\alpha}$ and variance $Var(\alpha)$ follow a log-linear relationship with the cliff initial sizes (Fig. 4.S6):

(Eq. 4.S1) $$log(\bar{\alpha}) = c_{Mean} \times log(S_i) + d_{Mean}$$

(Eq. 4.S2) $$log(Var(\alpha)) = c_{Var} \times log(S_i) + d_{Var}$$

Where S_i is the cliff initial size, c_{Mean}, c_{Var}, d_{Mean} and d_{Var} are the parameters of the linear regression. The linear regressions are calculated after binning of the data based on their initial size in 19 bins of equal length in the log scale (Fig. 4.S6). In the stochastic model, c_{Mean} and d_{Mean} are fixed, and in a second step, they are expressed as a function of the external drivers based on the results from the multivariate regression.

4.12.1.5.   *Number of final cliffs/event*

Split and mix events result in two or more cliffs. The final size of these events, calculated from the initial size and the area ratio, has to be split between the resulting two or more final cliffs. The number of final cliffs per event (final cliff ratio) is calculated for each individual event from the discrete normal distribution of final cliff ratio. The final size is then randomly distributed between the final cliffs.

This process is repeated for the duration of the modeled period. Since the model is stochastic, each model runs result in a different time series, so the model needs to be run several times to generate a variability range (Fig. 4.S9).
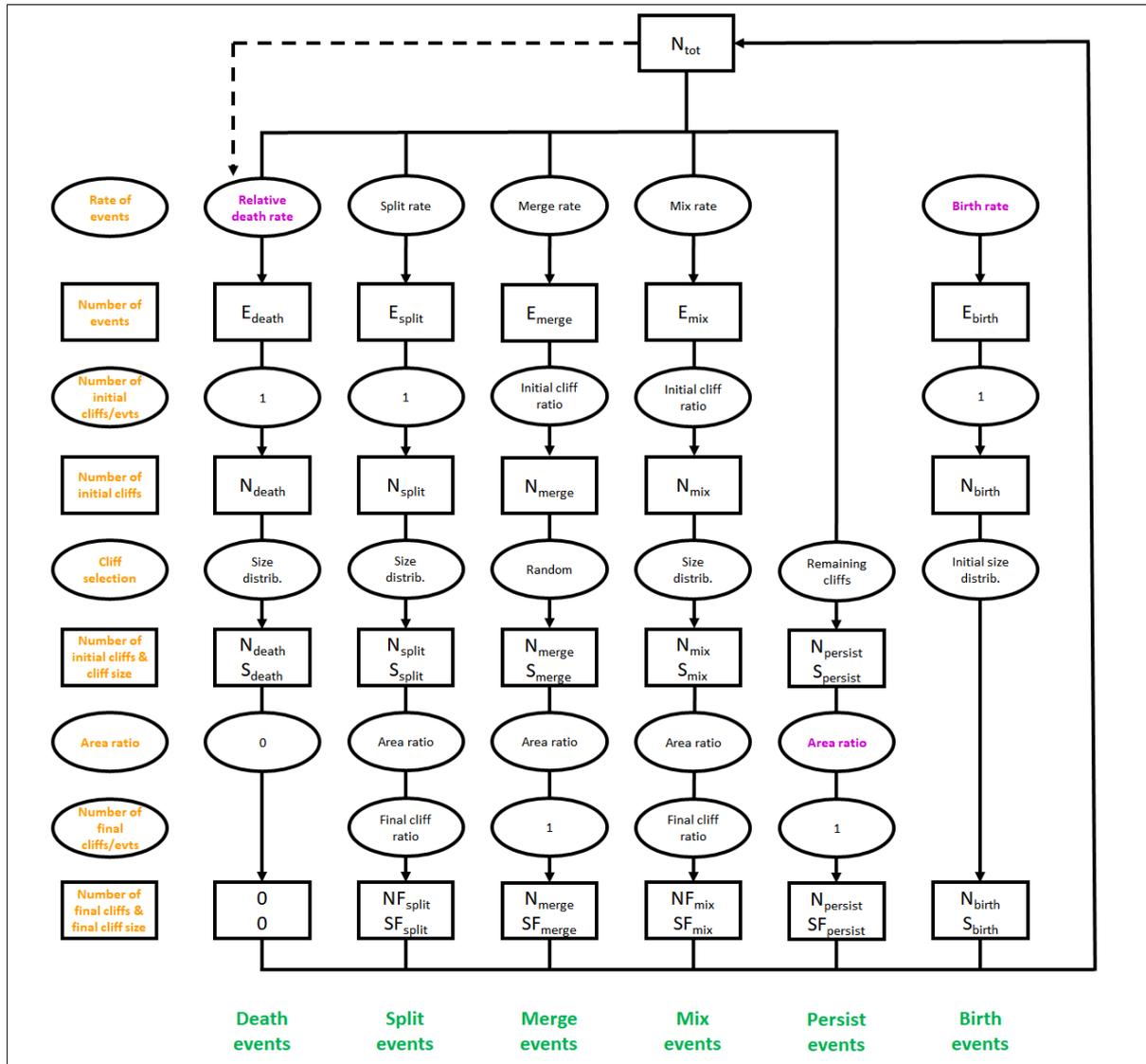
Figure 4.S10*: Stochastic birth-death model flowchart. Rectangular boxes describe the state of the system at each step, while the oval boxes describe an action item based on one or more parameters. The orange text describes the general action or state. The purple text corresponds to steps where we add the influence of external drivers in the second version of the model.*

Table 4.S3*. Stochastic model parameters. The parameters were estimated for each glacier over the first five years or the full time series depending on the model runs. a, b and ξ correspond to the parameters in Eq. 4.3.*

Parameters	Probability density function	Model step
	Cliff size limits	
Maximum size	One value (area of largest observed cliff)	All
Minimum size	One value (100 m^2)	All
	Death events	
a	One value	Rate of events
b	One value	Rate of events
ξ	Discrete normal distribution (Mean, Variance)	Rate of events
Size of dying cliff	Lognormal distribution (Mean, Variance)	Cliff selection
	Split events	
Number of split events	Discrete normal distribution (Mean, Variance)	Rate of events
Size of splitting cliff	Lognormal distribution (Mean, Variance)	Cliff selection
Area ratio	Initial size dependent lognormal distribution (Mean, Variance as in Eq. 4.S1 and 4.S2)	Area ratio
Final cliff ratio	Discrete normal distribution (Mean, Variance)	Number of final cliffs/events
	Merge events	
Number of merge events	Discrete normal distribution (Mean, Variance)	Rate of events
Initial cliff ratio	Discrete normal distribution (Mean, Variance)	Number of initial cliffs/event
Area ratio	Initial size dependent lognormal distribution (Mean, Variance as in Eq. 4.S1 and 4.S2)	Area ratio
	Mix events	
Number of mix events	Discrete normal distribution (Mean, Variance)	Rate of events

Initial cliff ratio	Discrete normal distribution (Mean, Variance)	Number of initial cliffs/event
Size of initial cliff	Lognormal distribution (Mean, Variance)	Cliff selection
Area ratio	Initial size dependent lognormal distribution (Mean, Variance as in Eq. 4.S1 and 4.S2)	Area ratio
Final cliff ratio	Discrete normal distribution (Mean, Variance)	Number of final cliffs/events
	Persist events	
Area ratio	Initial size dependent lognormal distribution (Mean, Variance as in Eq. 4.S1 and 4.S2)	Area ratio
	Birth events	
Number of birth events	Discrete normal distribution (Mean, Variance)	Rate of events
Size of new cliffs	Lognormal distribution (Mean, Variance)	Cliff selection

Table 4.S4. *Stochastic model parameter values for each of the four study glaciers. The parameters are the same as the ones described in Table 4.S3. The parameters shown in this table were estimated for each glacier over the full time series.*

Parameters	Values			
	Langtang	Urdok	Satopanth	Bhagirath Kharak
	Cliff size limits			

Maximum size (m²)		8844	21919	13036	7866
Minimum size (m²)		100	100	100	100
Death events					
a		0.29	0.55	0.49	0.29
b		4	-69	-24	0
ξ	Mean, Variance	-0.02, 0.16	-0.07, 0.33	-0.03, 0.20	-0.04, 0.25
Size of dying cliff	Mean, Variance	6.58, 0.66	6.29, 0.77	5.71, 0.72	5.63, 0.67
Split events					
Number of split events	Mean, Variance	5.6, 1.8	12.4, 7.0	8.0, 3.0	6.0, 1.6
Size of splitting cliff	Mean, Variance	8.3, 0.75	7.5, 0.96	7.8, 1.09	7.8, 0.99
Area ratio	c_{Mean}	-0.71	-0.54	-0.38	-0.38
	d_{Mean}	5.78	4.29	2.81	2.98
	c_{Var}	-0.29	0.12	-0.09	-0.13
	d_{Var}	2.87	-0.27	1.18	1.28
Final cliff ratio	Mean, Variance	2.07, 0.15	2.14, 0.11	2.21, 0.14	2.28, 0.33
Merge events					
Number of merge events	Mean, Variance	5.8, 2.2	14, 8.0	4.6, 2.1	3.8, 1.5
Initial cliff ratio	Mean, Variance	2.06, 0.08	2.14, 0.15	2.13, 0.22	2.25, 0.19
Area ratio	c_{Mean}	-0.08	-0.18	-0.09	-0.21
	d_{Mean}	0.74	1.37	0.90	1.67
	c_{Var}	-0.21	0.29	0.08	-0.01
	d_{Var}	2.26	-1.35	-0.38	0.61
Mix events					

Number of mix events	Mean, Variance	5.2, 2.9	12.4, 6.6	6.6, 1.1	4.4, 1.5
Initial cliff ratio	Mean, Variance	2.36, 0.30	2.43, 0.38	2.33, 0.11	2.38, 0.30
Size of initial cliffs	Mean, Variance	7.5, 0.94	7.0, 1.08	6.9, 1.14	7.0, 1.12
Area ratio	c_{Mean}	0.38	0.44	0.06	-0.14
	d_{Mean}	-3.3	-3.9	-0.4	1.4
	c_{Var}	-0.13	0.05	-0.08	-0.05
	d_{Var}	1.6	0.15	1.08	0.72
Final cliff ratio	Mean, Variance	2.33, 0.33	2.35, 0.21	2.29, 0.26	2.40, 0.49
Persist events					
Area ratio	c_{Mean}	-0.27	-0.30	-0.24	-0.16
	d_{Mean}	2.0	2.2	1.7	1.1
	c_{Var}	0.058	-0.018	-0.031	-0.024
	d_{Var}	0.14	0.85	0.73	0.77
Birth events					
Number of birth events	Mean, Variance	62.8, 10.5	123.6, 30.6	35.6, 8.4	26.0, 9.2
Size of new cliffs	Mean, Variance	6.57, 0.68	6.22, 0.79	5.58, 0.71	5.58, 0.72

Table 4.S5. *Multivariate regression results for the number of birth events. In green are the sites for which the multivariate regression is statistically significant (P value ≤ 0.05). Empty cells show that the corresponding predictors were not included in the multivariate regression of birth rate. The cells colored in orange show that the corresponding predictor was chosen in the first step of the stepwise multivariate regression.*

Birth rate (num.yr^{-1})	Intercept (num.yr^{-1})	Predictor coefficients								R^2	P-value	RMSE	Adj-R^2
		Air Temp.	Precip. (mm)	Total pond area	Pond area change	Vel. DCG (m.yr^{-1})	Vel. AOI (m.yr^{-1})	Acc. DCG (m.yr^{-2})	Acc. AOI (m.yr^{-2})				

		(°C)		(m²)	(m².yr⁻¹)								
Langtang	-32	64								0.34	0.10	18	0.24
Urdok	416			-4.0e-4		-2.1	-59		27	0.97	0.003	10	0.93
Satopanth	33				-6.8e-4					0.66	0.01	5.6	0.61
Bhagirath Kharak	32			-5.0e-4						0.23	0.23	7.9	0.11

Table 4.S6. Multivariate regression results for the relative death rate. In green are the sites for which the multivariate regression is statistically significant (P value ≤ 0.05). Empty cells show that the corresponding predictors were not included in the multivariate regression of relative death rate. The cells colored in orange show that the corresponding predictor was chosen in the first step of the stepwise multivariate regression.

Relative death rate (yr⁻¹)	Intercept (yr⁻¹)	Predictor coefficients								R^2	P-value	RMSE	Adj-R^2
		Air Temp (°C)	Precip. (mm)	Total pond area (m²)	Pond area change (m².yr⁻¹)	Vel. DCG (m.yr⁻¹)	Vel. AOI (m.yr⁻¹)	Acc. DCG (m.yr⁻²)	Acc. AOI (m.yr⁻²)				
Langtang	0.31									-	-	0.055	-
Urdok	0.61				2.5e-7	-1.3e-2				0.74	0.02	0.068	0.65
Satopanth	1.92						-0.11	7.6e-2		0.52	0.16	0.070	0.33
Bhagirath Kharak	0.30								-3.1e-2	0.75	0.01	0.036	0.71

Table 4.S7. *Multivariate regression results for the mean area fraction slope of the persist events. In green are the sites for which the multivariate regression is statistically significant (P value ≤ 0.05). Empty cells show that the corresponding predictors were not included in the multivariate regression of the mean area fraction slope. The cells colored in orange show that the corresponding predictor was chosen in the first step of the stepwise multivariate regression.*

Slope of mean area fraction c_{Mean} (-)	Intercept (-)	Predictor coefficients								R^2	P-value	RMSE	Adj-R^2
		Air Temp. (°C)	Precip. (mm)	Total pond area (m²)	Pond area change (m².yr⁻¹)	Vel. DCG (m.yr⁻¹)	Vel. AOI (m.yr⁻¹)	Acc. DCG (m.yr⁻²)	Acc. AOI (m.yr⁻²)				
Langtang	0.25						-0.08	0.11		0.71	0.03	0.072	0.61
Urdok	0.59	0.13		7.5e-7						0.60	0.07	0.100	0.46
Satopanth	-9.5e-2								-0.11	0.75	0.01	0.050	0.71
Bhagirath Kharak	0.19	-0.10			7.4e-6			-4.0e-2		0.75	0.01	0.036	0.71

Table 4.S8. *Multivariate regression results for the mean area fraction intercept of the persist events. In green are the sites for which the multivariate regression is statistically significant (P value ≤ 0.05). Empty cells show that the corresponding predictors were not included in the multivariate regression of the mean area fraction intercept. The cells colored in orange show that the corresponding predictor was chosen in the first step of the stepwise multivariate regression.*

Intercept of mean area fraction d_{Mean} (-)	Intercept (-)	Predictor coefficients								R^2	P-value	RMSE	Adj-R^2
		Air Temp (°C)	Precip. (mm)	Total pond area (m²)	Pond area change (m².yr⁻¹)	Vel. DCG (m.yr⁻¹)	Vel. AOI (m.yr⁻¹)	Acc. DCG (m.yr⁻²)	Acc. AOI (m.yr⁻²)				
Langtang	-1.6						0.55	-0.78		0.70	0.03	0.51	0.60
Urdok	-4.7	-1.0		-4.9e-6						0.60	0.07	0.73	0.46
Satopanth	0.68								0.76	0.75	0.01	0.37	0.70
Bhagirath Kharak	-1.8	0.82						0.33		0.71	0.05	0.53	0.59
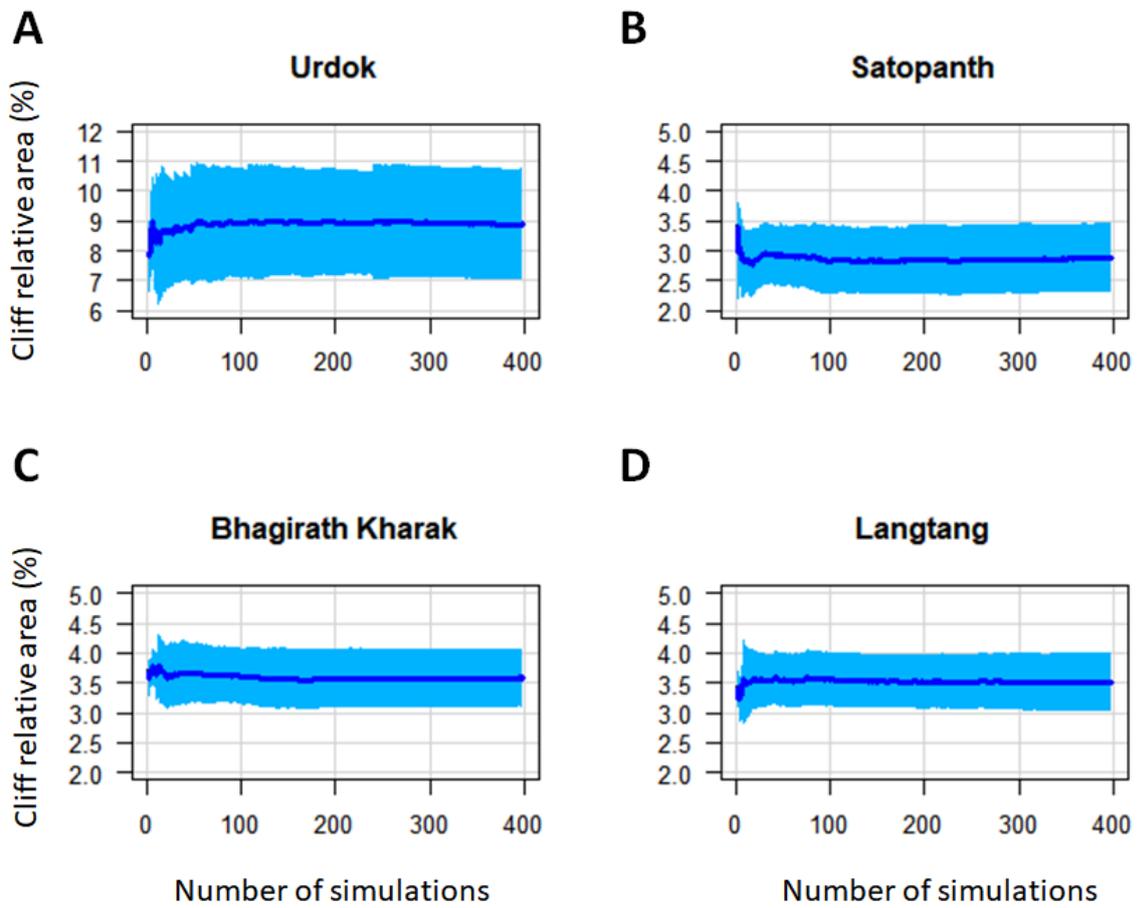
Figure 4.S11: Mean (blue line) and standard deviation (mid blue area) of the modeled cliff relative area after 10 years as a function of the number of simulations.
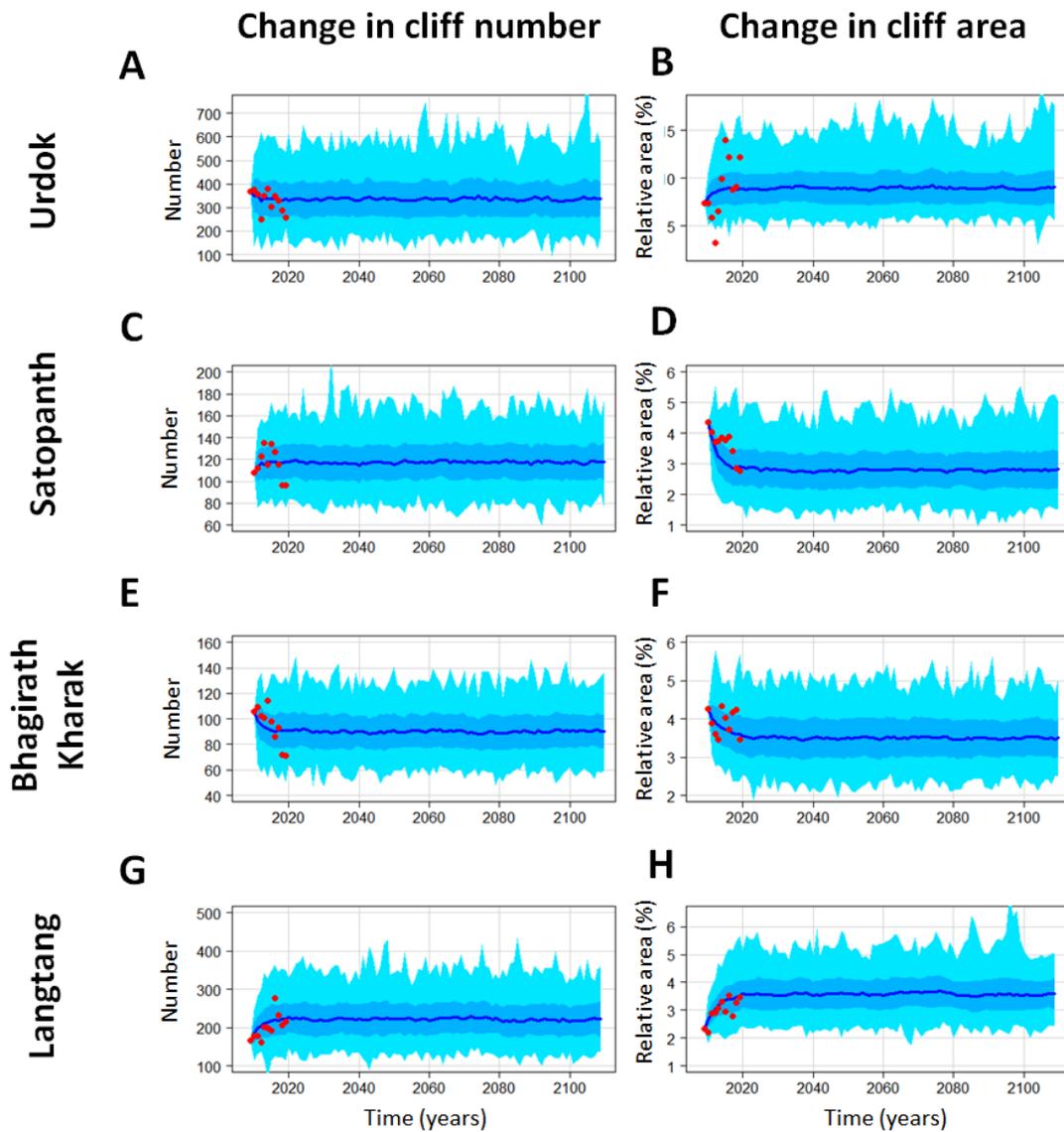
Figure 4.S12: *Outputs from the stochastic model for the number of cliffs and their relative area. The model was run 200 times from 2009 (2010 for Satopanth and Bhagirath Kharak) to 2120. Parameters were estimated over the full time series. The red dots correspond to the observations from the mapping. The dark blue line corresponds to the average values of the 200 simulation runs. The mid blue area represents the standard deviation of the runs and the light blue area the maximum and minimum values.*
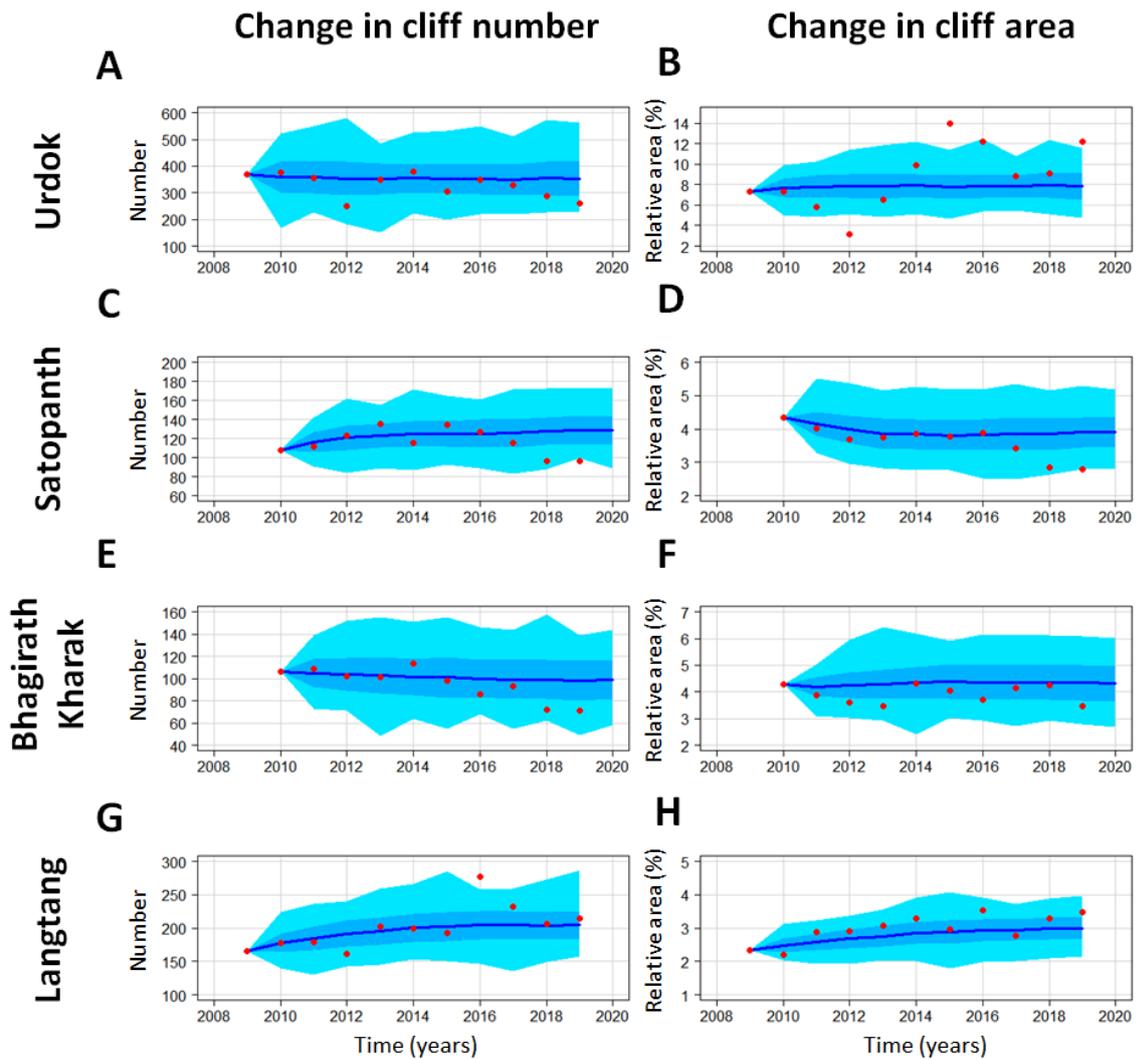
Figure 4.S13*: Outputs from the stochastic model for the number of cliffs and their relative area. The model was run 200 times from 2009 (2010 for Satopanth and Bhagirath Kharak) to 2019. Parameters were estimated over the first 5 years of the time series. The red dots correspond to the observations from the mapping. The dark blue line corresponds to the average values of the 200 simulation runs. The mid blue area represents the standard deviation of the runs and the light blue area the maximum and minimum values.*

160
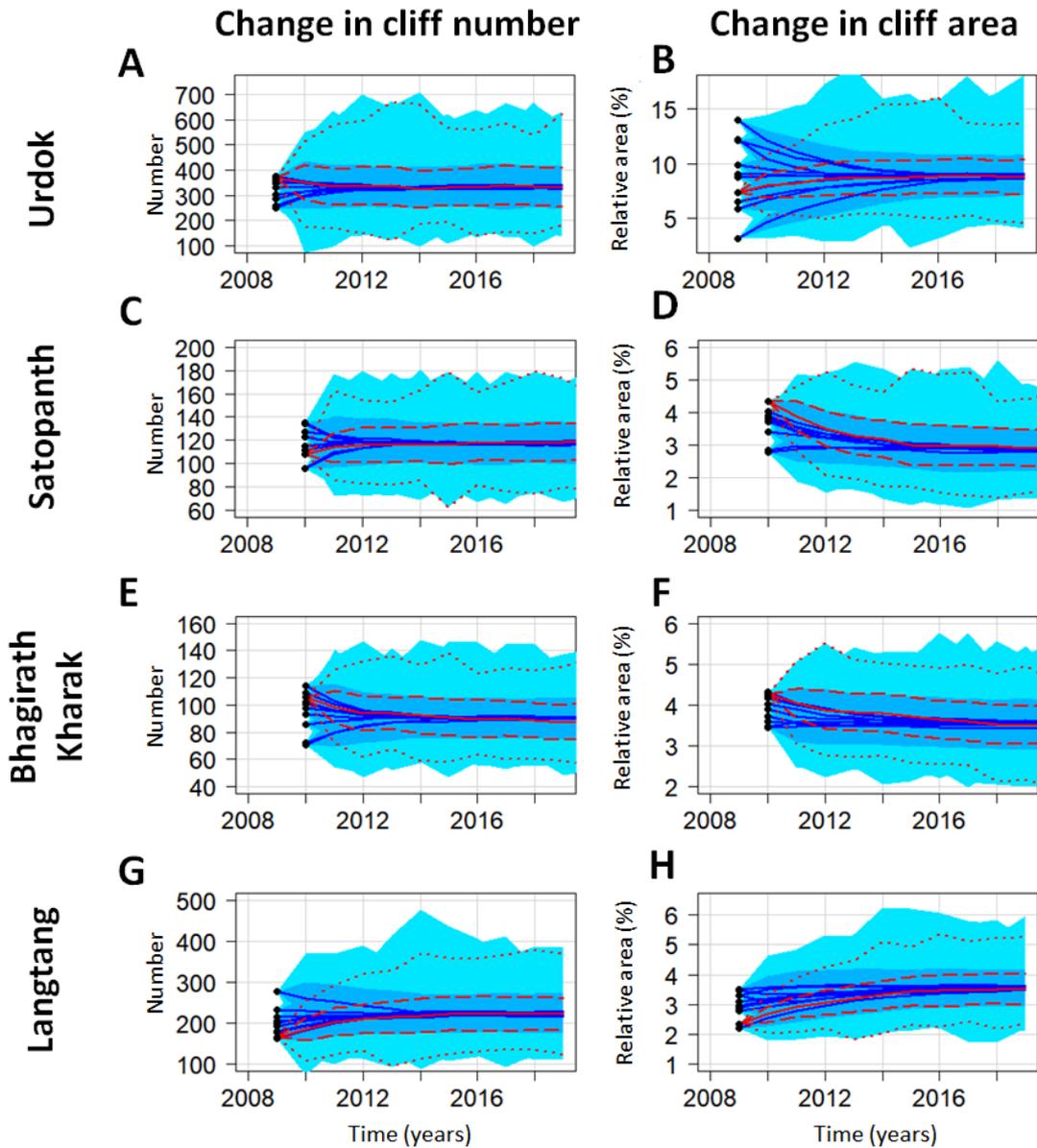
Figure 4.S14*: Outputs from the stochastic model for the number of cliffs and their relative area for different initial conditions (black dots), corresponding to each year of the time series. The model was run 200 times from 2009 (2010 for Satopanth and Bhagirath Kharak) to 2019 for each initial condition. Parameters were estimated over the first 10 years of the time series. The dark blue lines correspond to the average values of the 200 simulation runs. The mid blue areas represent the standard deviation of the runs and the light blue areas the maximum and minimum values. The red lines correspond to the average (solid), standard deviation (long dashes) and extreme extents (dots) for the 2009 initial conditions*

Chapter 5: Controls on ice cliff formation, distribution and characteristics on debris-covered glaciers

To be submitted by 15/12/2022 in *Geophysical Research Letters*, authored by Marin Kneib[1,2], Catriona Fyffe[1,3], Evan S. Miles[1], Shayna Lindemann[1], Thomas E. Shaw[1], Pascal Buri[1], Michael McCarthy[1], Boris Ouvry[4], Yota Sato[5], Philip D.A Kraaijenbrink[6], Zhao Chuanxi[7,8], Peter Molnar[2], Andreas Vieli[4], Francesca Pellicciotti[1,3]

[1] High Mountain Glaciers and Hydrology (HIMAL), Swiss Federal Institute for Forest, Snow and Landscape Research WSL, 8903, Birmensdorf, Switzerland

[2] Institute of Environmental Engineering, ETH Zurich, 8093 Zurich, Switzerland

[3] Department of Geography, Northumbria University, Newcastle, NE1 7RU, UK

[4] Department of Geography, University of Zurich, 8057 Zurich, Switzerland

[5] Graduate School of Environmental Studies, Nagoya University, Nagoya, Japan

[6] Utrecht University, Department of Physical Geography, PO Box 80115, 3508 TC, Utrecht, The Netherlands.

[7] College of Earth and Environmental Sciences, Lanzhou University, Lanzhou 730000, China

[8] State Key Laboratory of Tibetan Plateau Earth System, Environment and Resources (TPESER), Institute of Tibetan Plateau Research, Chinese Academy of Sciences, China

Author contribution

MK, CF, ESM and FP designed the study. CF, TS, BO, AV, YS, PDAK, ZC and YW provided multi-temporal UAV data and helped interpreting the formation mechanisms. TS provided the ERA5-Land reanalysis data. MM provided the debris thickness data. SL mapped and categorized the cliff formation events with multi-temporal UAV data under the supervision of MK, CF and FP. PM, ESM, CF and FP helped shape the statistical analysis of the controls. MK validated the newly-formed cliff outlines and mechanisms, completed all the analysis of the cliff distribution patterns and composed the manuscript. FP supervised the study. All authors aided in the reviewing and editing of the manuscript.

Key points

- We derived an unprecedented dataset of 37537 ice cliffs and their characteristics across 86 debris-covered glaciers in High Mountain Asia
- We find that 38.9% of the cliffs are stream-influenced, 19.5% pond-influenced and 19.7% are crevasses
- Ice cliff distribution and characteristics can be predicted by velocity, indicating both the dynamics and state of evolution of debris-covered glaciers

5.1. Abstract

Ice cliff distribution plays a major role in determining the melt of debris-covered glaciers but its controls are largely unknown. We assembled a dataset of 37537 ice cliffs and determined their characteristics across 86 debris-covered glaciers within High Mountain Asia (HMA). We complemented this dataset with the analysis of 202 cliff formation events from multi-temporal UAV observations for a subset of glaciers. We find that 38.9% of the cliffs are stream-influenced, 19.5% pond-influenced and 19.7% are crevasses. Surface velocity is the main predictor of cliff distribution at both local and glacier scale, indicating its dependance on the dynamic state and hence evolution stage of debris-covered glacier tongues. Supraglacial ponds contribute to maintaining cliffs in areas of thicker debris, but this is only possible if water accumulates at the surface. Overall, total cliff density decreases exponentially with debris thickness as soon as debris gets thicker than 10 cm.

5.2. Plain language summary

Debris-covered glaciers are common throughout the world's mountain ranges and are characterised by the presence of steep ice cliffs among the debris-covered ice. It is well-known that the cliffs are responsible for a large portion of the melt of these glaciers but the way they form, and as a result the controls on their development and distribution across glaciers remains poorly understood. Novel mapping approaches combined with high-resolution satellite and drone products enabled us to disentangle some of these controls and to show that the ice cliffs are generally formed and maintained by the surface hydrology (ponds or streams) or by the opening of crevasses. As a result, they depend both at the local and glacier scale on the dynamic state of the glaciers as well as the evolution stage of their debris cover. This provides a pathway to better represent their contribution to glacier melt in predictive glacier models.

5.3. Introduction

Debris-covered glaciers are found in all mountain ranges (Scherler et al., 2018), and supraglacial debris extents and thickness are expected to increase in a warming climate (Compagno et al., 2022; Herreid and Pellicciotti, 2020a; Stokes et al., 2007). However, despite considerable advances in the past two decades, projecting the mass balances of these glaciers remains challenging (Anderson et al., 2021a; Gardelle et al., 2013; Kääb et al., 2012; Pellicciotti et al., 2015; Rounce et al., 2021). This is partly due to the presence of supraglacial features such as ice cliffs and ponds, which melt up to 20 times faster than the surrounding debris-covered ice, therefore compensating the debris insulating effect to some extent (Anderson et al., 2021a, 2021b; Brun et al., 2018; Buri et al., 2021; Miles et al., 2018b, 2022; Reid and Brock, 2014; Sakai et al., 1998, 2002). Ice cliffs have been shown to contribute 17+/-4% of the melt of the debris-covered ice in a large catchment of High Mountain Asia (HMA) (Buri et al., 2021), and this contribution is particularly important at high elevation where sub-debris melt is limited by low air temperature, as well as close to the glacier terminus, where the debris is thicker (Buri et al., 2021; Miles et al., 2022).

While models are now able to accurately simulate the energy and mass balance contribution of ice cliffs (Sakai et al., 1998; Han et al., 2010; Reid and Brock, 2014; Steiner et al., 2015; Buri et al., 2016a; Kneib et al., 2022), the application of such models at large spatial scales is limited by uncertainty in ice cliff distribution. Indeed, estimates of ice cliff density vary widely from glacier to glacier, between 1 and 15% of the debris-covered area (Anderson et al., 2021a; Brun et al., 2018; Falaschi et al., 2021; Immerzeel et al., 2014; Juen et al., 2014; Kneib et al., 2020; M. Kneib et al., 2021; Loriaux and Ruiz, 2021; Mishra et al., 2021; Mölg et al., 2019; Reid and Brock, 2014; Sakai et al., 1998, 2002; Sato et al., 2021; Steiner et al., 2019; Thompson et al., 2016; Watson et al., 2017a). It has been shown that ice cliff

distribution can vary by up to ~20% from year to year, but remains relatively constrained, unless major changes in the glacier dynamics occur (M. Kneib et al., 2021; Steiner et al., 2019; Watson et al., 2017a). The distribution of ice cliffs has important implications for the mass balance of debris-covered glaciers (Buri et al., 2021; Pellicciotti et al., 2015) and their long-term evolution (Ferguson and Vieli, 2021; Racoviteanu et al., 2022). Deriving ice cliff distributions is challenging because ice cliffs are difficult to map, due to their small size, steep slope and varying spectral characteristics (Anderson et al., 2021a; Herreid and Pellicciotti, 2018; M. Kneib et al., 2021). The inconsistent mapping of cliffs makes it difficult to understand the underlying controls on cliff distribution and as a result to extrapolate these distribution patterns and physical characteristics (slope, aspect) of ice cliffs to larger spatial scales.

Locally, ice cliff evolution happens at the interface between hydrological and debris processes (Buri et al., 2016b; Kneib et al., 2022; Reid and Brock, 2014; Watson et al., 2017b; Westoby et al., 2020). The survival of ice cliffs is inherently linked to the stability of debris on ice, which depends on the slope, but also on the debris thickness and water content, as well as the debris buttressing at the base of a slope (Moore, 2018). The local slope can change in relatively short time scales with differential melt caused by heterogeneous debris thicknesses (Moore, 2021; Nicholson et al., 2018; Sharp, 1949), which results in the surface of debris-covered glaciers being particularly hummocky where the debris gets thicker than 20-30 cm (Bartlett et al., 2020; King et al., 2020; Mölg et al., 2020). Supraglacial ponds and streams contribute to slope destabilisation and debris evacuation by removing debris and enhancing melt at the base of the debris-covered slopes, which leads to undercuts. This is expected to be one of the main triggers for ice cliff formation (Miles et al. 2017a, 2017b; Mölg et al., 2019; Röhl 2006, 2008; Sakai and Takeuchi 2000), but also an important aspect for the survival of the cliffs (Anderson et al., 2021a; Benn et al., 2012, 2001; Brun et al., 2016; Kneib et al., 2022; Sato et al., 2021; Watson et al., 2017b). Other cliff formation mechanisms could include crevasse opening (Reid and Brock, 2014; Steiner et al., 2019) or the collapse of englacial conduits (Benn et al., 2012; Gulley and Benn, 2007; Gulley et al., 2009; Immerzeel et al., 2014; Miles et al., 2018a, 2020; Ragettli et al., 2016a; Reid and Brock, 2014; Sakai and Takeuchi, 2000), but these hypotheses have never been tested in a quantitative way.

Remote sensing studies of ice cliffs have shown that these features have average slopes higher than 30°, and are largely oriented north (Anderson et al., 2021a; Herreid and Pellicciotti, 2018; Kraaijenbrink et al., 2016b; Reid and Brock, 2014; Steiner et al., 2019; Watson et al., 2017a, 2017b). This is due to stronger shortwave-radiation gradients at the surface of south-facing cliffs (in the Northern Hemisphere), leading to their flattening and reburial (Buri and Pellicciotti, 2018; Sakai et al., 2002). Studies of the distribution of ice cliffs over small groups of glaciers have highlighted the strong link between ponds and cliffs, with more than 40% of the ponds being linked to a cliff in the two HMA catchments of Nepal where this was tested (Steiner et al., 2019; Watson et al., 2017a). This could hint at a preferential location of ice cliffs where the pond density is high, i.e. where the glacier longitudinal gradient and surface velocities are lower, therefore promoting the stagnation of surface water in depressions (Ferguson and Vieli, 2021; Quincey et al., 2007; Quincey and Glasser, 2009; Racoviteanu et al., 2021; Reynolds, 2000; Sakai and Fujita, 2010; Salerno et al., 2012; Steiner et al., 2019). This, however, does not seem to be the main control, and ice cliffs have also been shown to develop at the confluence of glacial tributaries and in locations of high compressive strain rates, where debris could be more heterogeneous (Anderson et al., 2021b; Benn et al., 2012; Kraaijenbrink et al., 2016b; Steiner et al., 2019). Furthermore, debris thickness also seems to have a negative feedback on cliff formation and therefore distribution, especially in the absence of ponds (Anderson et al., 2021a; Watson et al., 2017a).

In this study, we derive for the first time the distribution of ice cliffs on a large sample of HMA glaciers and determine the key controls on the distribution and characteristics of ice cliffs on debris-covered glaciers. For this purpose we 1) map ice cliffs across 86 glaciers in HMA, 2) determine their physical characteristics, 3) attribute their distribution to local and glacier-wide controlling factors. We take advantage of a recently developed semi-automated method (Kneib et al., 2020) to map cliffs from high-resolution multi-spectral satellite images and a number of large-scale remote sensing products to classify ice cliffs and ponds and determine the controls of their distribution. The findings are further corroborated by complementary observations from high-resolution, multi-temporal Unoccupied Aerial Vehicle (UAV) data at five of the studied glaciers (Section 5.8.1).

5.4. Data and methods

5.4.1. Characterization of glacier surface

We used 14 Pléiades stereo-images acquired between 2017 and 2021 to derive 2m-resolution multi-spectral images and Digital Elevation Models (DEMs) covering 86 debris-covered glaciers across HMA (Berthier et al., 2014; Shean et al., 2016; Fig. 1; Table S2), 70 of which had more than 65% of their debris-covered area that could be classified after removal of clouds, shadows and fresh-snow (Table S3). The DEMs were used to derive surface slope and aspect, as well as the glacier 'hummockiness', which we defined as the percentage of area for which the Statistical Measure of Relief (SMR) calculated over a 8 m window was greater than 50 m (King et al., 2020). The multi-spectral images were used to manually update the glacier and debris outlines of the RGI 6.0 (Pfeffer et al., 2014; Scherler et al., 2018; Table S3). Glacier longitudinal gradient was computed using the 30m resolution AW3D DEM (Tadono et al., 2014; Dehecq et al., 2019) and combined with glacier ice thicknesses (Farinotti et al., 2019) to estimate driving stress over a distance of two ice thicknesses. Distributed glacier velocity, compressive and tensile strain rates were obtained from the global 50m resolution composite by Millan et al. (2022). We additionally used the distributed debris thickness dataset of McCarthy et al. (2022) for all glaciers larger than 2 km2 (64 glaciers, 47 of which have more than 65% of their debris-covered area that could be classified). All these datasets were aggregated 1) in 500 m distance bins along the glacier flowlines (Kienholz et al., 2014; King et al., 2020) and 2) for each glacier. Data gaps within the bins were filled using a nearest neighbour interpolation.

Multi-temporal UAV data with a monitoring period longer than 2 years and with at least 3 high-resolution (<1 m) DEMs and orthoimages were available at five of the studied glaciers. This complementary data was used to identify ice cliff formation events and derive the characteristics of newly formed ice cliffs (Section 5.8.1).

5.4.2. Ice cliff, pond and stream delineation

Ice cliffs and ponds were derived automatically in each Pléiades scene following the Spectral Curvature method (Kneib et al., 2020). Ponds were also mapped using a Normalized Difference Water Index (NDWI) threshold of 0.1 (Kneib et al., 2020; McFeeters et al., 1998; Watson et al., 2018). For some of the scenes this resulted in a high number of false positive cliff identifications due to local shadows or changing geology, which were filtered out manually by a single operator (Kneib et al., 2021, Fig. 5.S7, 5.S8). No consideration of slope was included in this delineation of ice cliffs; they were mapped solely based on spectral characteristics (Anderson et al., 2021a; Kneib et al., 2020). The ice cliffs are then implicitly defined here as exposed ice in an otherwise debris-covered domain, therefore likely to undergo 'enhanced' melt locally. Some of these features were clearly identifiable as crevasses due to

their elongated, straight or slightly curved shapes and these zones were outlined manually in the images. Past studies have only examined high-relief (several m) ice cliffs, but here our interest is in all exposed ice in the debris-covered area, so we include smaller features common for thin-debris areas, as well as crevasses, which similarly enhance surface ablation (Colgan et al., 2016).

We accounted for pond seasonality by automatically mapping areas with a NDWI value greater than 0.1 in all 10 m resolution Sentinel-2 images of the previous melt season (May-November), after filtering clouds and shaded areas (Kneib et al., 2020; McFeeters et al., 1998; Watson et al., 2018). We retained as ponds (at least temporary ones) the areas for which more than three cloudless Sentinel-2 images were available and where the NDWI was greater than 0.1 more than 33% of the time. The processing was carried out in Google Earth Engine for the period 2019-2021, and older images were processed using the MAJA atmospheric correction processor (Hagolle et al., 2015). False positives (streams, proglacial lakes, zones affected by shadows or with very thin debris) were removed manually. The resulting pond density values are consistent with the ones from the Pléiades images (Fig. 5.S9) and additionally account for strong seasonal variability at some of the sites (Miles et al., 2017c; Watson et al., 2016). The final pond outlines were defined as the union between the Pléiades and Sentinel-2 outlines, enabling us to identify the areas influenced by ponds, whether or not a pond was present at the time of the Pleiades acquisition.

Using the Pléiades DEMs, we mapped supraglacial channels (which we use as a proxy for supraglacial streams in all that follows) across all the glaciers using the TopoToolbox flow routing algorithm (Schwanghart and Scherler, 2014), after filling the DEM sinks shallower than 5m and removing the crevassed areas. These 'streams' were defined as the pixels with an upstream area higher than 10000 m2 and were used to calculate the stream sinuosity (Anderson et al., 2021b; Mölg et al., 2020).

The minimum cliff and pond detection size is given by the resolution of the Pléiades data (2m). The uncertainties in the mapping of cliffs and ponds were assessed by eroding and dilating the mapped features by 0.5 pixels (1 m for cliffs, 5 m for ponds), and taking the upper (+42% for cliffs, +77% for ponds) and lower (-38% and -49%) area bounds as uncertainty values (Brun et al., 2018; Fig. 5.S10). The Pléiades outlines were validated at one of the glaciers with near-contemporaneous outlines obtained from a 1m-resolution UAV orthoimage (Fig. 5.S11).

166
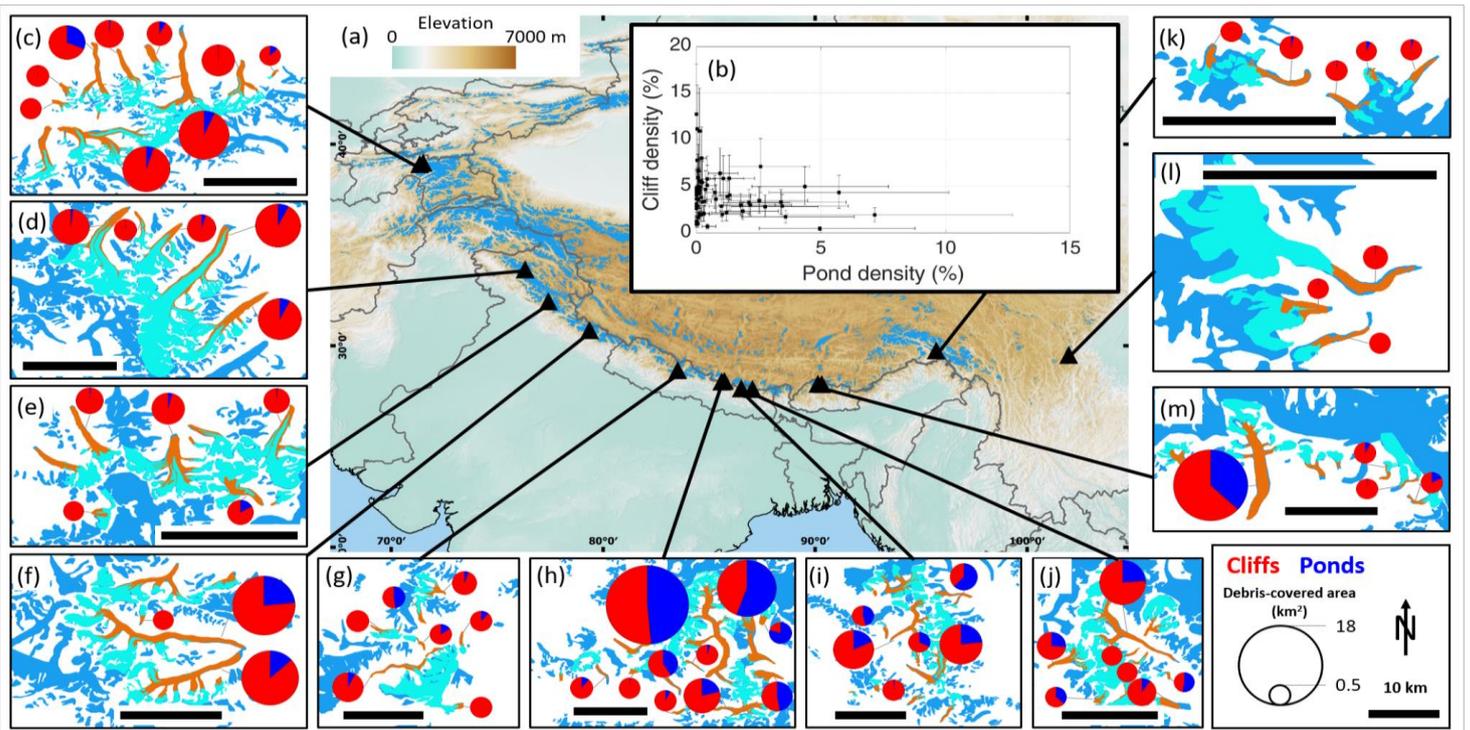
Figure 5.1: *(a) Map of HMA with each triangle representing one of the 14 Pléiades scenes (some scenes are very close to each other) and the boxes to the side (c-m) showing a zoomed view of the glaciers in these areas. The background in the GTOPO 30 arc seconds (~1 km) DEM, and the glacierised areas are indicated in blue. The inset boxes show the glacier RGI 6.0 outlines in dark blue, the glaciers visible in the Pléiades images in turquoise and their debris-covered areas in brown. The pie charts are scaled to the absolute size of the debris-covered areas and show the relative proportion of ponds (dark blue) and cliffs (red) for each glacier for which more than 65% of their debris-covered area could be classified. (b) Cliff and pond density of each of these glaciers. The bars show the uncertainties.*

5.5. Results

5.5.1. Influence of supraglacial hydrology on ice cliff distribution

The majority of cliffs are preferentially located in the vicinity of ponds and streams, as their density strongly decreases with distance from these hydrological features (Fig. 5.2a, b). In particular, a large majority of the ponds are in close proximity to cliffs, and for half of the glaciers, more than 85% of the ponds influence at least one neighbouring cliff (Fig. 5.2d). This is further confirmed by field observations (Fig. 5.2e-g) and multi-temporal UAV observations showing that the influence of streams or ponds is responsible for more than 79.2% of the newly-formed cliff area while another 16.7% is caused by crevasse opening (Fig. 5.S2). This leads us to define a 40m-buffer around ponds and streams within which we classify the cliff pixels as pond-influenced or stream-influenced, with a priority given to the ponds (Fig. 5.2). In addition to stream- and pond-influenced cliffs, crevasses represent 19.7% of the cliff area across all glaciers (Fig. 5.2) and are mostly located in the upper extents of the debris-covered areas. Crevasses also appear lower down glacier, at shear margins, and in the vicinity of proglacial lakes or lateral streams entering the glacier (Fig. 5.S6). The remaining cliffs are qualified as undefined. The stream mapping parameters have little influence on this classification, while the choice of the stream and pond buffer mainly modifies the relative proportion of undefined cliffs (Fig. 5.2h,

5.S12). Ultimately, the pond-influenced cliffs represent 19.5% of the total cliff area, the stream-influenced cliffs 38.9% and the undefined cliffs 21.9% (Fig. 5.2c).

The slope and density of ice cliffs vary between the three categories, while this is less the case for aspect and size (Fig. 5.S13). Crevasses are usually more densely distributed (15.2% of buffer area), followed by the pond-influenced (6.7%), stream-influenced cliffs (4.3%) and undefined cliffs (2.1% of remaining area, Fig. 5.S13a). Despite a variety of glacier aspects (Table S3), there is a clear preferential cliff aspect distribution in the NNW direction for all categories (Fig. 5.S13d), while the newly formed cliffs do not appear to have a preferential aspect (Sato et al., 2021; Fig. 5.S4).
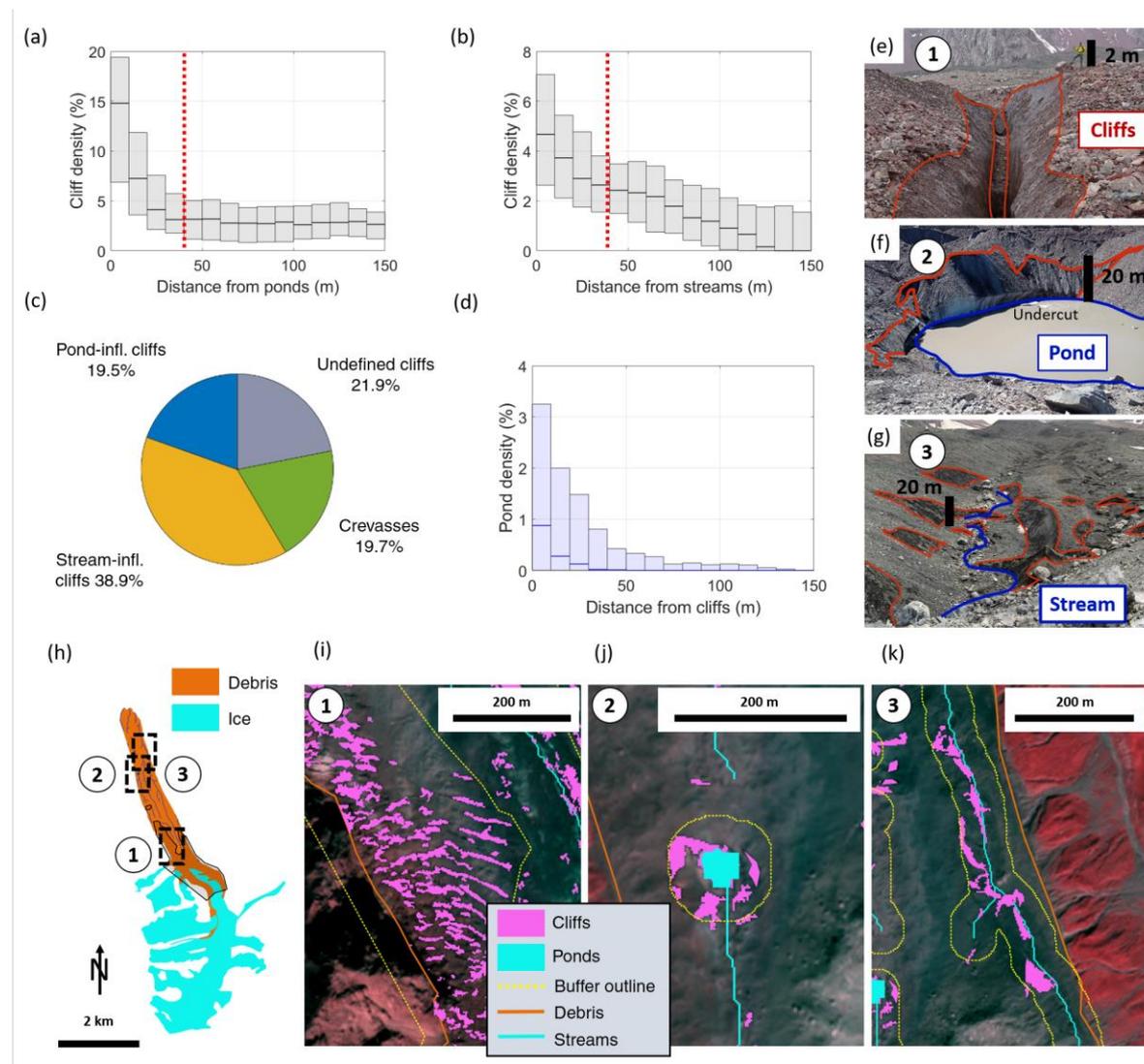
Figure 5.2: *Cliff density for all glaciers as a function of (a) distance from ponds after removal of the crevasses and (b) distance from streams, after removal of the pond-influenced cliffs. The box plots indicate the median, 25th and 75th percentiles of the cliff density within each 10m bin for each glacier. The red dotted lines show the 40m buffers. (c) Area proportion of undefined, pond- and stream-influenced cliffs and crevasses across all debris-covered glaciers. (d) Pond density for all glaciers as a function of distance from cliffs. (h) Example of classification of ice cliffs from Kyzylsu Glacier, Tajikistan: 1/ crevassed-areas, 2/ pond-influenced cliffs and 3/ stream-influenced cliffs, with the pictures (e-g) and Pléiades view (i-k) of the corresponding zones. Image credit: Marin Kneib and Evan*

5.5.2. Controls on ice cliff distribution

The variables associated with ice cliff distribution vary depending on the category of ice cliff that is considered (Fig. 5.4, 5.S15). Stream-influenced and undefined cliffs follow a similar distribution for all predictors (Fig. 5.S15), which could indicate that a majority of the undefined cliffs were formerly stream-influenced and backwasted away from the channels. One associated variable that stands out for these cliffs is debris thickness, as 80% of stream-influenced cliffs are located in areas with debris estimated to be thinner than 33 cm, while 45% of the pond-influenced cliffs are located in areas with thicker debris (Fig. 5.S15). This results in the total cliff density decreasing exponentially ($Y = 5.8e^{-\frac{X}{2}}$, $R^2 = 0.73$) as soon as the debris gets thicker than 10 cm (Fig. 5.3a, 5.S16). On the other hand, crevasses and pond-influenced cliffs have a clearly contrasting response to the different controls investigated. Indeed, 80% of the crevasses are located in areas with surface velocities higher than the 13 m.yr^{-1} threshold or in areas with debris thinner than 20 cm (Fig. 5.S15). Pond-influenced cliffs clearly depend on pond density, and are thus preferentially located in non-dynamic areas with lower longitudinal gradient and velocity and with thicker debris (Fig. 5.4, 5.S15, 5.S17).
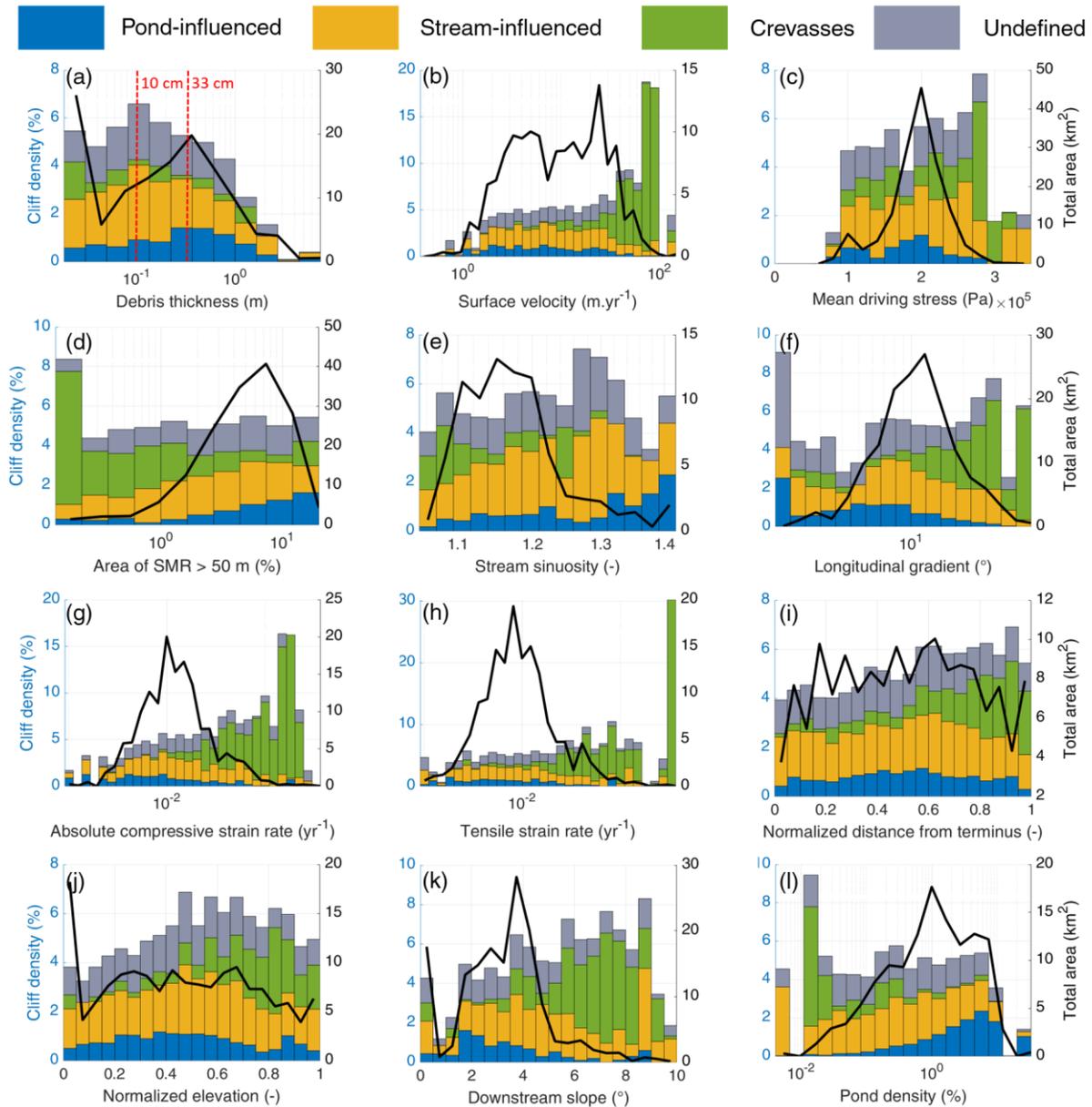
Figure 5.3: *Mean cliff density split by cliff category for all bins of all glaciers where more than 65% of the debris-covered area could be classified as a function of (a) debris thickness, (b) surface velocity, (c) mean driving stress, (d) 'hummockiness', (e) stream sinuosity, (f) longitudinal gradient, (g) absolute compressive strain rate, (h) tensile strain rate, (i) normalized distance from terminus, (j) normalized elevation above terminus, (k) downstream slope*

When aggregating the metrics per glacier, a clear relationship between mean surface velocity across the debris-covered area and ice cliff density becomes apparent (Fig. 5.4, 5.S18). The influence of climatic variables seems instead to be limited (Fig. 5.S19). Ice cliff density decreases with decreasing velocity, up to a point where the trajectory seems to bifurcate. The debris-covered tongues with the highest cliff density and fastest velocity have a larger proportion of crevasses, generally located in the upper reaches of the debris-covered area (state 1, Fig. 5.4), where the ice is still dynamic. At slower velocities (<10 m.yr^{-1}), two trajectories are apparent: 1) glaciers with a large proportion (> ⅓) of pond-influenced cliffs and higher cliff densities (state 3a, Fig 5.4), and 2) glaciers with a majority of stream-influenced cliffs, which tend to have lower cliff densities (state 3b, Fig. 5.4). The majority of

the glaciers are found at an intermediary stage between these three end-members, with a decreasing proportion of crevasses and an increasing proportion of stream- and pond-influenced cliffs as velocity decreases (state 2, Fig. 5.4).
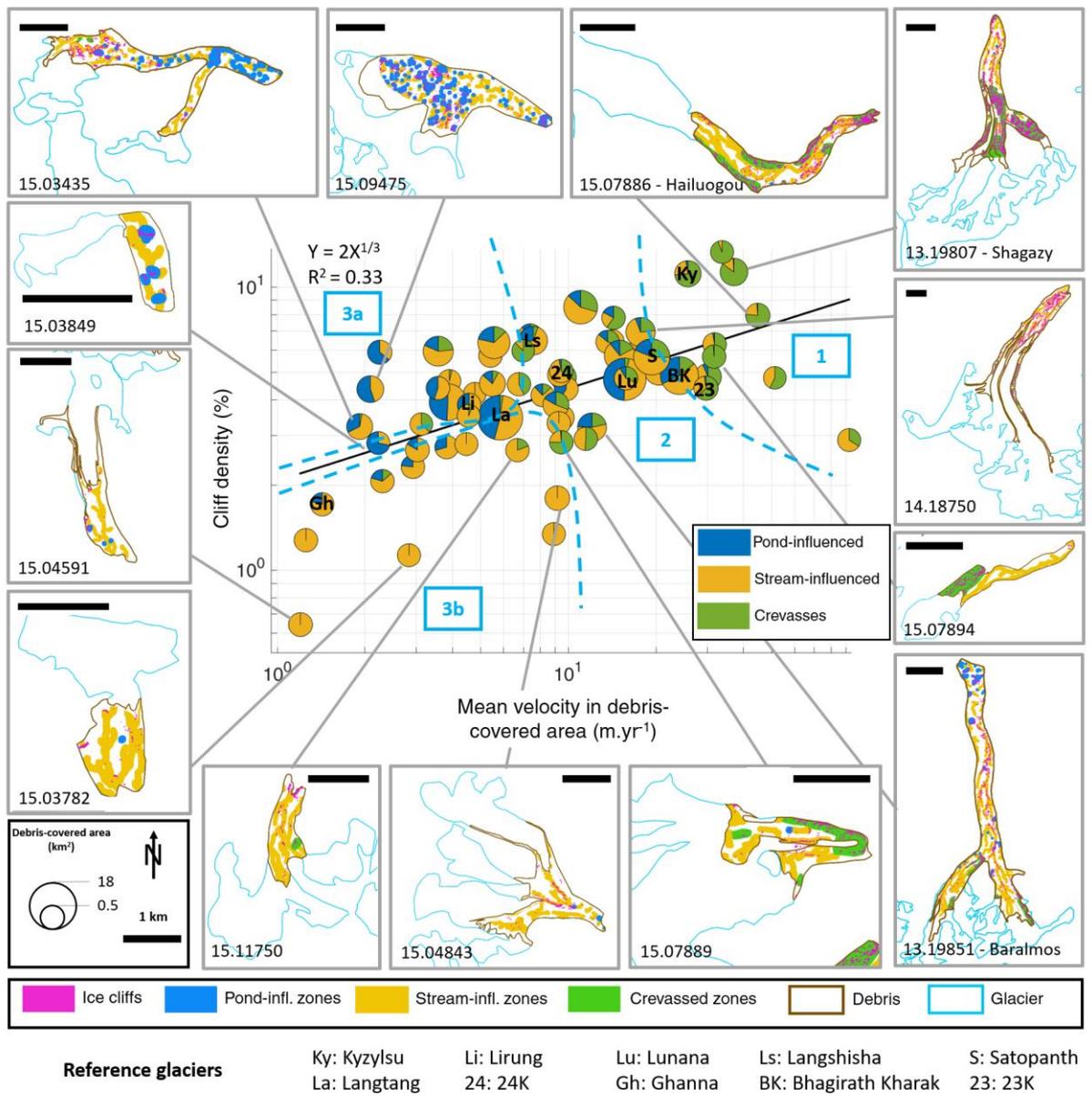
Figure 5.4: *Glacier-wide cliff density as a function of mean velocity in the debris-covered area for all glaciers where more than 65% of the debris-covered area could be classified. The proportion of undefined cliffs was not represented for readability. The boxes to the side show example maps of some of the glaciers with their surface classifications. Some additional reference glaciers are indicated in the main plot in black. The expression and R^2 of the black linear regression are indicated in the upper left corner. In light blue are shown four glacier clusters.*

5.6. Discussion and conclusions

5.6.1. Ice cliff evolution

We have identified the presence of supraglacial streams and ponds, along with the opening of crevasses, to be one of the main mechanisms responsible for ice cliff formation and development (Reid and Brock, 2014). Newly-formed ice cliffs tend to be smaller in size and do not appear to have any preferential aspect (Fig. 5.S5; Fig. 5.S4; Kneib et al., 2021). They grow and are maintained by the presence of crevasses in areas of high strain rates, ponds or streams (through debris destabilisation and thermo erosional incision), and our observations especially highlight the important role of ponds in maintaining ice cliffs in zones of thick debris (Fig. 5.3a). They also maintain the slope of the cliffs steeper than the streams, as they are more likely to stay in contact with them (Mölg et al., 2020). However, the cliffs tend to get reburied when they backwaste away from these supraglacial features (Fig. 5.2a, b), especially when they are south-facing (in the Northern Hemisphere). This results in the total population of ice cliffs being preferentially oriented in a north-west to north direction for our study sites (Buri and Pellicciotti, 2018), showing a strong control of solar radiation on the long term survival and shapes of ice cliffs.

5.6.2. Linking ice cliff distribution and glacier state

The main controls on ice cliff density at the glacier scale are debris thickness and surface velocity, although controls on the cliff distribution also vary with the cliff category (Fig. 5.4). Cliff density decreases exponentially with debris thickness exceeding 10 cm, and this relationship would even be enhanced if the debris thickness estimates accounted for the presence of cliffs and ponds (McCarthy et al., 2021; Rounce et al., 2021). Similarly, and this is especially the case when accounting for crevasses, surface velocity has a positive feedback on cliff density (Fig. 5.4, 5.5; Anderson et al., 2021a). The ice cliffs therefore depend on the dynamics and the state of the glacier. A dynamic debris-covered glacier (mean surface velocity higher than 10 m.yr^{-1}) is usually characterised by thin debris, crevasses comprising the majority of exposed ice, and few stream-influenced cliffs. Glacier slow-down results in the up-glacier migration and eventual disappearance of crevasses, the extension of stream-influenced cliffs and possibly the appearance of pond-influenced cliffs. Ponds can indeed maintain cliffs in more stagnant zones of thicker debris, also characterised by low longitudinal gradients and driving stress as well as increased hummock prevalence (Steiner et al., 2019; Watson et al., 2017a). This however requires the accumulation of water in surface depressions, which occurs for larger glaciers with lower longitudinal gradients (Fig. 5.5). Most HMA glaciers in this stage of evolution are located in the Central and Eastern Himalaya (Fig. 5.1; Benn et al., 2012; Racoviteanu et al., 2021; Watson et al., 2016, 2017a).
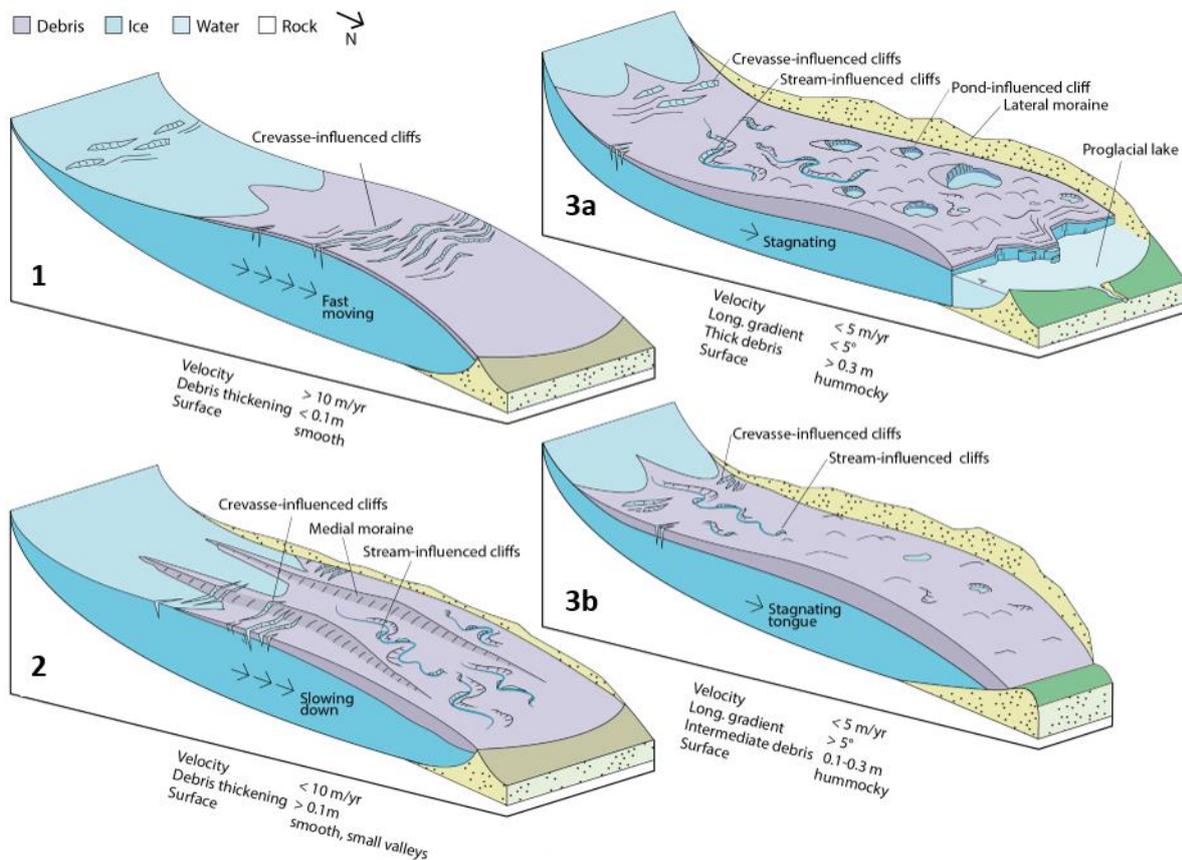
Figure 5.5: *The four glacier evolution states indicated in figure 5.5, with their ice cliff distributions. State 1 corresponds to a fast flowing glacier with thin debris and extensive crevassing. State 2 corresponds to more advanced debris cover, with thicker debris and lower velocities that enable the development of supraglacial valleys and stream-influenced cliffs in the non-crevassed areas. State 3a corresponds to large stagnating debris-covered tongues, characterised by large hummocks, thick debris and ponds forming in the surface depressions, maintaining cliffs in these zones of thick debris. State 3b is also a stagnating tongue with thick debris, but with high enough longitudinal gradient or low enough surface flow that prevent the formation of ponds and therefore the survival of cliffs. Figure credit: Martin Heynen.*

5.6.3. Implications for glacier mass balance

This study highlights the prevalence of exposed ice from crevassing in (but not limited to) the upper reaches of the debris-covered areas (Fig. 5.S6). These features would likely enhance melt even more than traditional stream- and pond-influenced cliffs due to greater surface roughness at their location increasing turbulent fluxes, and additional reflected shortwave contributions from the opposite crevasse walls (Pfeffer and Bretherton, 1987; Cathles et al., 2011; Colgan et al., 2016; Purdie et al., 2022). Time-lapse images actually show the upper walls of crevasses backwasting as traditional ice cliffs would (Fig. 5.S20). However, their melt enhancement relative to debris-covered ice remains to be investigated (Buri et al., 2016a). Furthermore, crevasses stay localised in space and their longer-term evolution and influence on shaping the debris-covered glacier surface remains unclear (Kirkbride and Deline, 2013).

Ice cliff density and characteristics depend on the state of evolution of the debris-covered glacier (Fig. 5.6), and can locally vary considerably due to atypical glacier dynamics or debris thicknesses (Fig. 5.5).

The findings and relationships detailed in this study outline a framework to estimate the distribution of ice cliffs on top of debris-covered glaciers based on their flow characteristics and debris thickness, without having to map the cliffs, and most importantly how this distribution will evolve with changing glacier dynamics. This represents a key advance to estimate the longer-term ice cliff contribution to the mass balance of debris-covered glaciers at the large scale, as the cliff density and characteristics can easily be combined with estimates of cliff enhancement factors (Miles et al., 2022).

5.7.   Open research

5.8.   Acknowledgements

5.9. Supplementary material

5.9.1. Ice cliff formation

5.9.1.1. Multi-temporal UAV data

Here we took advantage of multi-temporal Unsupervised Aerial Vehicle (UAV) surveys over portions of five of the studied glaciers: Trakarding, Langtang, Lirung, 23K and 24K Glaciers (Brun et al., 2016; Chuanxi et al., in prep; Immerzeel et al., 2014; Kraaijenbrink et al., in prep; Sato et al., 2021; Table 5.S1; Fig. 5.S1). The surveys were conducted over a period of 2-5 years, with a repeat time of at least one year (Table 5.S1). The resolution of the original DEMs and orthoimages varied between 0.1 and 0.2 m, and they were all co-registered using surrounding stable terrain (see details in Chuanxi et al., in prep; Kraaijenbrink et al., in prep; Sato et al., 2021). From 2016 we used all available cloudless Sentinel-2 images (10m resolution) of the survey domains taken during the melt season to identify seasonal ponds. These images were atmospherically-corrected using the MAJA processing workflow (Hagolle et al., 2015).

Table 5.S1: *Multi-temporal UAV datasets. The Trakarding data are from Sato et al. (2021), the 23K and 24K data are from Chuanxi et al. (in prep) and the Langtang and Lirung data are from Kraaijenbrink et al. (in prep) as well as from Immerzeel et al. (2014) and Brun et al. (2016).*

Glacier	UAV survey dates	Original DEM and ortho resolution (m)	Resampled DEM resolution (m)	Survey domain area (km²)	Survey domain (% total debris-covered area)
Trakarding (RGI-15.03448)	27/10/2017	0.2	1	2.9	43
	18/10/2018	0.2			
	18-19/10/2019	0.2			
23K (RGI-15.11752)	27/09/2018	0.08	1	0.51	38
	13/08/2019	0.07			
	12/10/2019	0.07			
	20/08/2020	0.08			
	22/10/2020	0.1			
24K (RGI-15.11758)	27/09/2018	0.09	1	0.59	64
	13/08/2019	0.07			
	12/10/2019	0.07			

	Date	Value			
	20/08/2020	0.13			
	22/10/2020	0.09			
Langtang (RGI-15.04121)	07/05/2014	0.1	1	1.5	8.2
	22/10/2015	0.1			
	04/05/2016	0.1			
	09/10/2016	0.1			
	26/04/2017	0.1			
	22/10/2017	0.1			
	22/04/2018	0.1			
Lirung (RGI-15.04045)	18/05/2013	0.1	1	0.47	0.49
	22/10/2013	0.1			
	01/05/2014	0.1			
	10/2014	0.25			
	18/10/2015	0.1			
	30/04/2016	0.1			
	06/10/2016	0.1			
	20/04/2017	0.1			
	19/10/2017	0.1			
	28/04/2018	0.1			
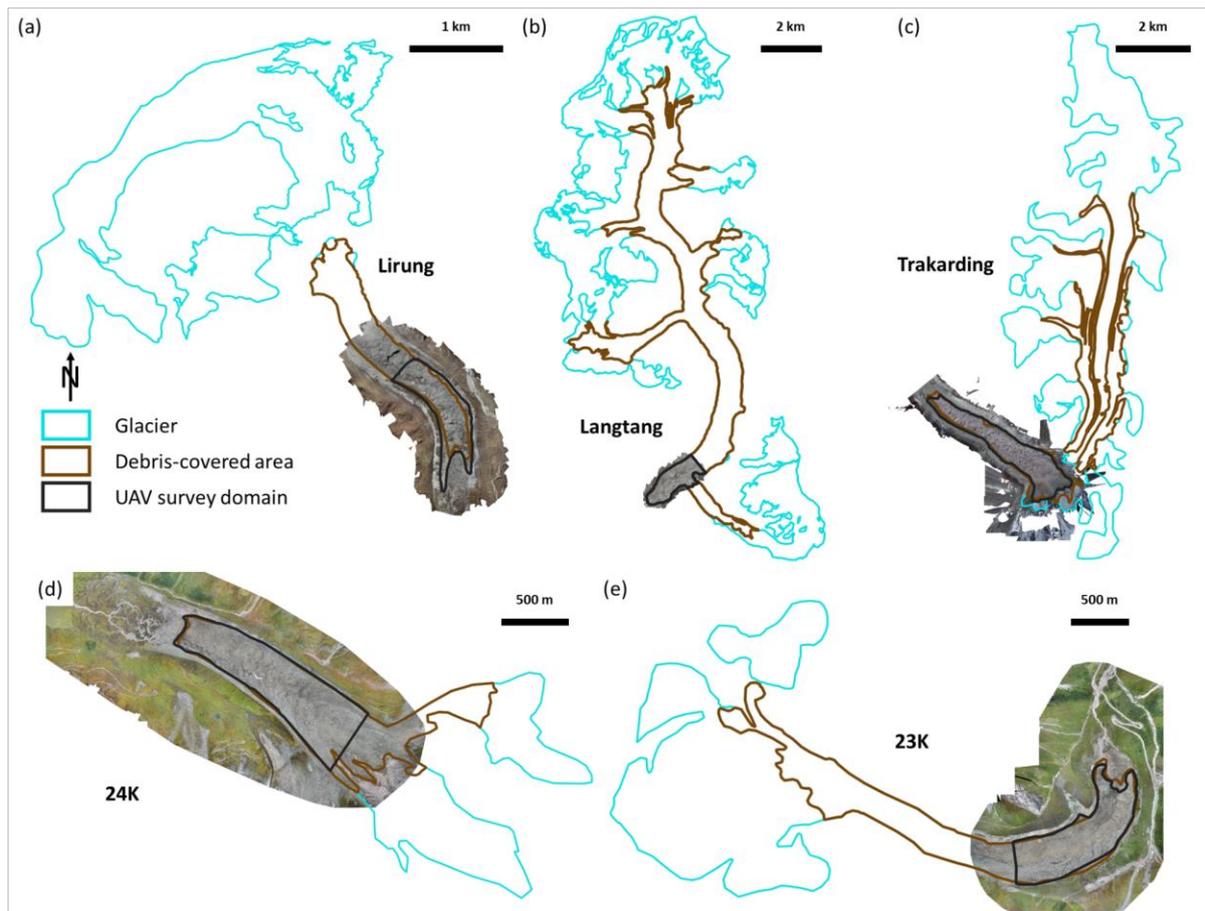
Figure 5.S1: *UAV survey domain for each glacier. Background images are the (a) Lirung 10/2017, (b) Langtang 04/2018, (c) Trakarding 10/2017, (d) 24K 09/2018 and (e) 23K 09/2018 UAV orthoimages. Glacier and debris outlines are the ones derived from the corresponding Pléiades images.*

5.9.1.2.   *Identification of newly-formed ice cliffs*

We manually identified newly-formed cliffs in the orthoimages as patches of bare ice that were not visible in previous images, irrespective of their slope. The outlines of these newly-formed cliffs were further derived manually. The DEMs were resampled to 1m to derive slope and aspect of all pixels, and to map supraglacial channels using a flow-routing algorithm following the same approach as for the Pléiades DEMs (Schwanghart and Scherler, 2014).

The mechanisms underlying the ice cliff formation were determined by a single operator based on 1/ the proximity to ponds (including seasonal ponds identified in the Sentinel-2 images), visible streams or supraglacial channels and 2/ the initial shape of the cliffs and the general organisation of the glacier surface at this location. This classification, as well as the ice cliff outlines, were then validated by a second independent operator.

5.9.1.3.   *Results*

We identified 202 newly-formed cliffs (38 for Langtang, 27 for Lirung, 57 for Trakarding, 38 for 23K and 42 for 24K) and classified the formation mechanisms as 'pond-influenced', 'stream-influenced', 'crevasses' or 'undefined' when the formation mechanism was not clear. Since the same classification

was used for newly-formed cliffs and the entire cliff population, we could directly compare the characteristics of the newly-formed cliff pixels with the values obtained from looking at the entire cliff population with the Pléiades data, specifically for the UAV survey domains (Fig. 5.S2, 5.S5).

The proportion of cliff categories was mostly consistent between newly-formed cliffs and the entire cliff population, except for Lirung where the triggering mechanism for most newly-formed cliffs could not be determined, and for Trakarding, where the proportion of pond-influenced new cliffs was greater (Fig. 5.S2). There were no consistent differences in the slope distribution of the newly-formed cliffs and the whole cliff population within these five domains. The slope of crevasses was consistently shallower, which was likely due to the DEM resolution being too coarse to represent their slope accurately. The slope distribution of the stream-influenced, pond-influenced and undefined cliffs was overall similar for the total cliff population, while the slope of the newly-formed pond-influenced cliffs tended to be steeper than for the other categories (Fig. 5.S3). The most striking differences were visible in the aspect distributions, where the full cliff population was generally oriented north-west to north, except for Lirung, while the newly-formed cliffs seemed to either be completely random (e.g. for Trakarding) or preferentially oriented in the general glacier flow direction (Fig. 5.S4). In terms of cliff size, the newly-formed cliffs were consistently smaller, and so for all categories (Fig. 5.S5).
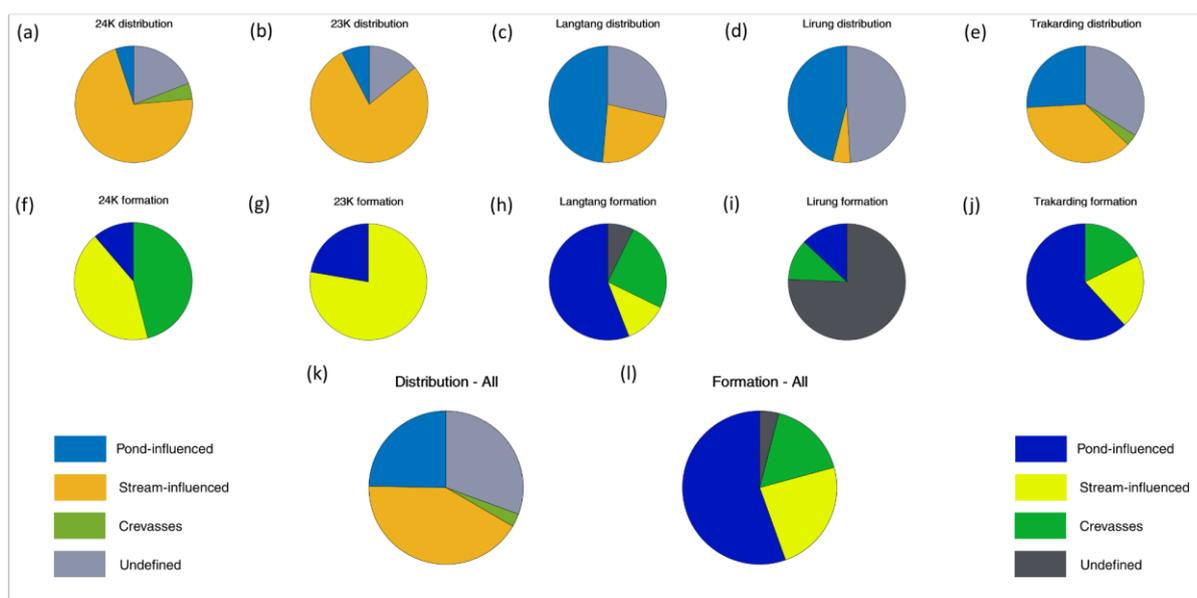
Figure 5.S2: *Area proportion of different ice cliff categories within the five UAV survey domains from the total cliff population derived from the Pléiades data (a-e) and from the newly-formed cliffs identified in the multi-temporal UAV data (f-j). (k-l) Combination of all five sites, weighted by the area of the survey domain and the duration of the UAV study period.*
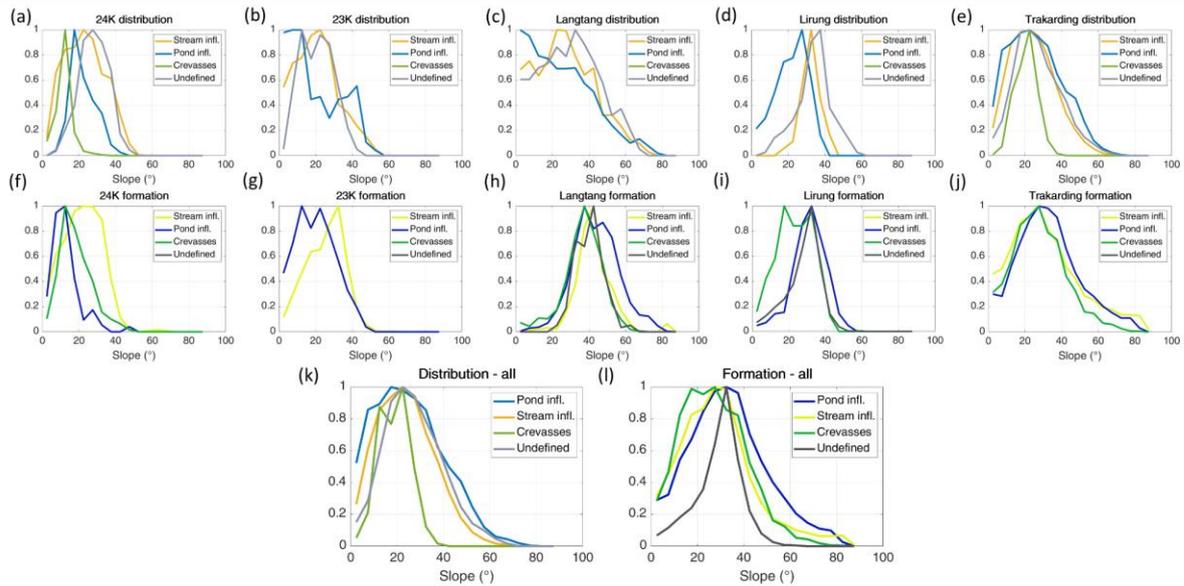
Figure 5.S3: *Slope distribution of the pixels of different ice cliff categories within the five UAV survey domains from the total cliff population derived from the Pléiades data (a-e) and from the newly-formed cliffs identified in the multi-temporal UAV data (f-j). (k-l) Combination of all five sites.*
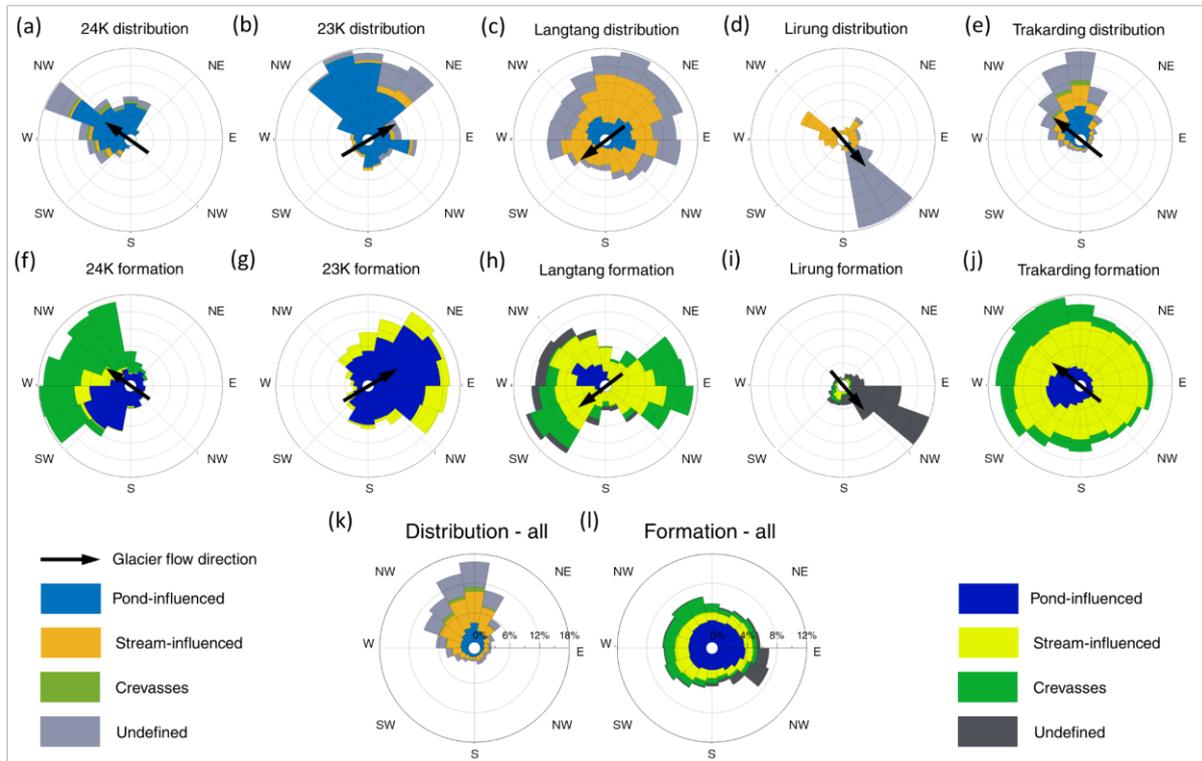
Figure 5.S4: *Aspect distribution of the pixels of different ice cliff categories within the five UAV survey domains from the total cliff population derived from the Pléiades data (a-e) and from the newly-formed cliffs identified in the multi-temporal UAV data (f-j). (k-l) Combination of all five sites.*

179
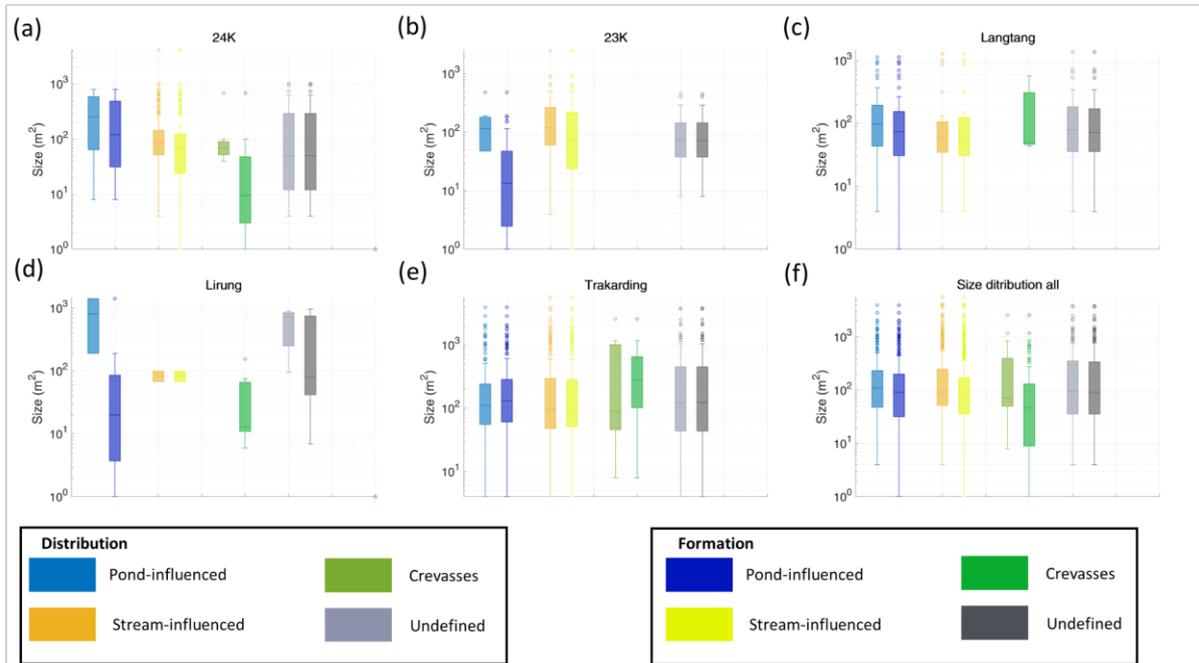
Figure 5.S5: *Size distribution of the cliffs of different ice cliff categories within the five UAV survey domains from the total cliff population derived from the Pléiades data and from the newly-formed cliffs identified in the multi-temporal UAV data (a-e). (f) Combination of all five sites.*

5.9.1.4.   Discussion

This focused study of the characteristics of newly-formed cliffs enabled us to link ice cliff formation with ice cliff distribution. Ice cliff formation mechanisms are indeed expected to have a strong influence on the distribution of ice cliffs across the glacier surface due to the high cliff birth and death rates (Kneib et al., 2021). The relatively long-term monitoring periods and the large number of sites covered here, with various glaciological and climatic characteristics (Fugger et al., 2022; Kneib et al., 2022; Sato et al., 2021), enabled us to identify a large number of ice cliff formation events and outline a number of interesting patterns. The main outcome was that as for ice cliff distribution, the formation mechanisms were driven by the glacier hydrology, including the proglacial or englacial hydrology for some of the crevasse-opening scenarios (Fig. 5.S6). Other interesting findings were that there was no preferential north-facing aspect for newly-formed cliffs, which was additional evidence for the faster reburial of south-facing cliffs (Buri and Pellicciotti, 2018). Additionally, newly-formed cliffs tended to be smaller in size, which confirmed the observations made at other sites with coarser resolution sensors (Kneib et al., 2021).

There remained limitations in the analysis of these patterns due to the relatively small area covered and the observational bias to the lower part of the debris-covered area of these glaciers. Additionally, despite the relatively high frequency of repeat surveys, the time intervals usually remained too long to precisely describe the formation mechanisms (Kneib et al., 2022). For instance, the 'pond-influenced' formations could have been due to pond drainage or filling, but this was not always clear due to too long time intervals between images so we kept the generic term. Similarly for 'stream-influenced' formations, the exact mechanism was not always clear and the presence of water in the channel could not always be verified from the images (based on field observations from the various sites we anyway expected the

water level in the streams to vary considerably seasonally), so a classification based on the presence of meanders in the surface DEMs was usually a strong argument to classify the newly-formed cliffs as stream-influenced. Crevasses were easily identifiable from their elongated, sometimes slightly curved shapes, but the triggering mechanism responsible for crevasse opening could not always be clearly identified (Reid and Brock, 2014; Steiner et al., 2019) and could vary from simple shear at the glacier lateral margins (for 24K especially) to the influence of proglacial lakes or streams entering the glacier laterally (for Trakarding especially, Fig. 5.S6). We did not see any evidence of englacial conduit collapse for the duration of the monitoring periods, although the development of concentric crevasses preluding some of these events on debris-covered glaciers have been described at several locations in the Swiss Alps (Egli et al., 2021; Mölg et al., 2019; Fig. 5.S6). Similarly, we did not have enough evidence to categorise formation events as being solely caused by slope steepening from differential melt, and for the large majority of events the hydrology or the glacier dynamics seemed to play a decisive role (Moore, 2018; Sharp, 1949). These formation events were actually most likely due to a combination of factors leading to slope steepening prior to the emergence of the new cliff, and the formation mechanisms that we identified most likely mainly reflected the 'triggering' event leading to debris removal and cliff formation.
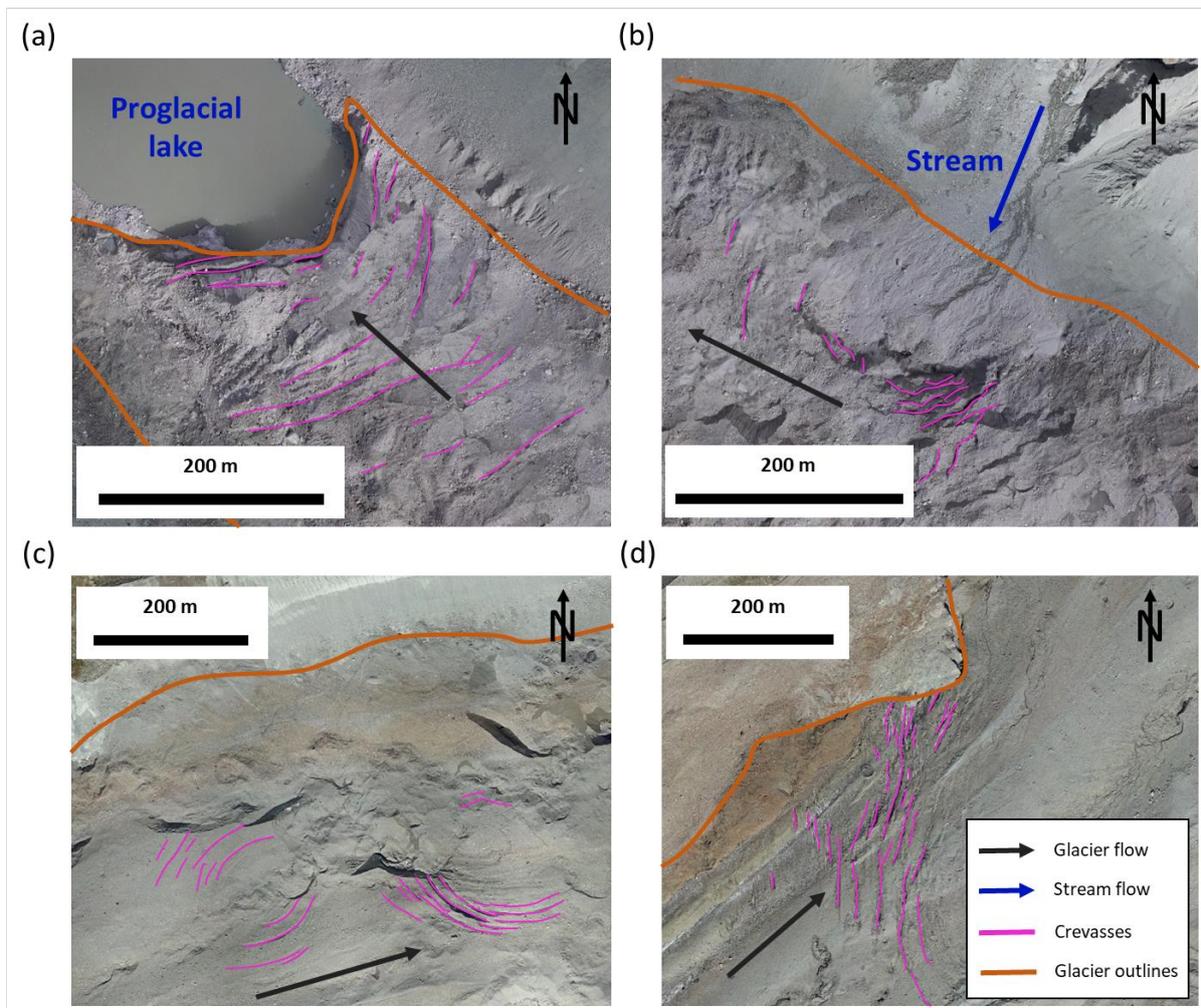
Figure 5.S6: *Crevasse patterns on (a-b) Trakarding Glacier, 10/2019 and (c-d) Zmutt Glacier, 09/2018. (a) Influence from a proglacial lake. (b) Stream entering the glacier from the side. (c) Circular*

crevasses symptomatic of englacial or subglacial conduit, likely preceding a conduit collapse. (d)
Simple shear situation at the glacier lateral margins.

5.9.2. Pléiades data

Table 5.S2: *Pléiades stereo-images used in this study.*

Acquisition name	Acquisition date	Location (coordinates of centre point)	Number of debris-covered glaciers in scene (>65% of debris-covered area mapped)	Source
24K	20/09/2021	29.77°N, 95.70°E	5	Royal Society
Baralmos	13/09/2021	39.03°N, 71.37°E	4	ERC RAVEN
Bhutan	08/11/2017	28.10°N, 90.27°E	4	PGO
Hailuogou	29/09/2021	29.56°N, 101.94°E	3	Royal Society
HP	12/09/2020	32.25°N, 77.43°E	5	PGO
Kyzylsu	19/09/2021	39.06°N, 71.50°E	5	ERC RAVEN
Ladakh	24/09/2020	33.76°N, 76.30°E	5	PGO
Langtang	14/06/2019	28.28°N, 85.73°E	8	ERC RAVEN
Lirung	13/10/2019	28.23°N, 85.54°E	3	ERC RAVEN
Lunana	07/11/2017	28.12°N, 90.15°E	1	PGO
Makalu	16/10/2018	27.85°N, 87.04°E	7	PGO
RS	15/10/2017	28.76°N, 83.52°E	8	PGO
Satopanth	18/09/2021	30.78°N, 79.35°E	5	ERC RAVEN

| Trambau | 01/12/2017 | 27.89°N, 86.51°E | | 7 | | PGO |

5.9.3. Methods to derive ice cliff distribution
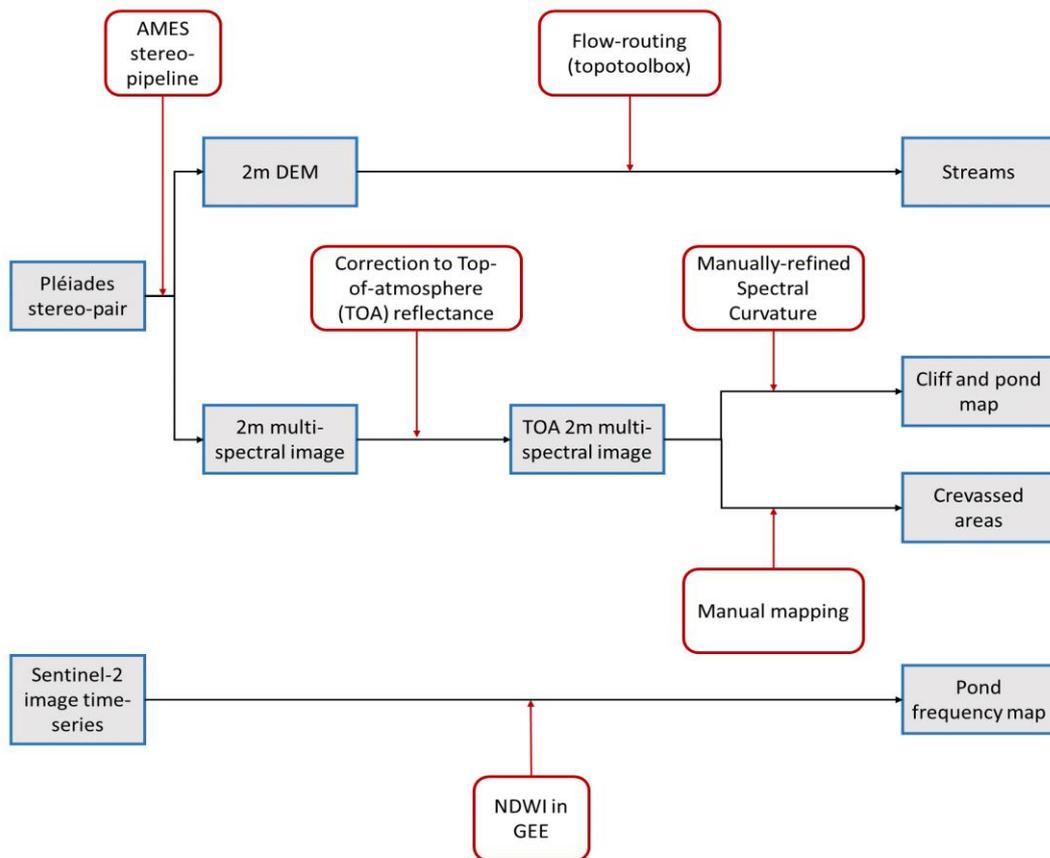
Figure 5.S7: *Processing steps of the Pléiades and Sentinel-2 images to obtain final cliff, pond, stream and crevasse maps.*
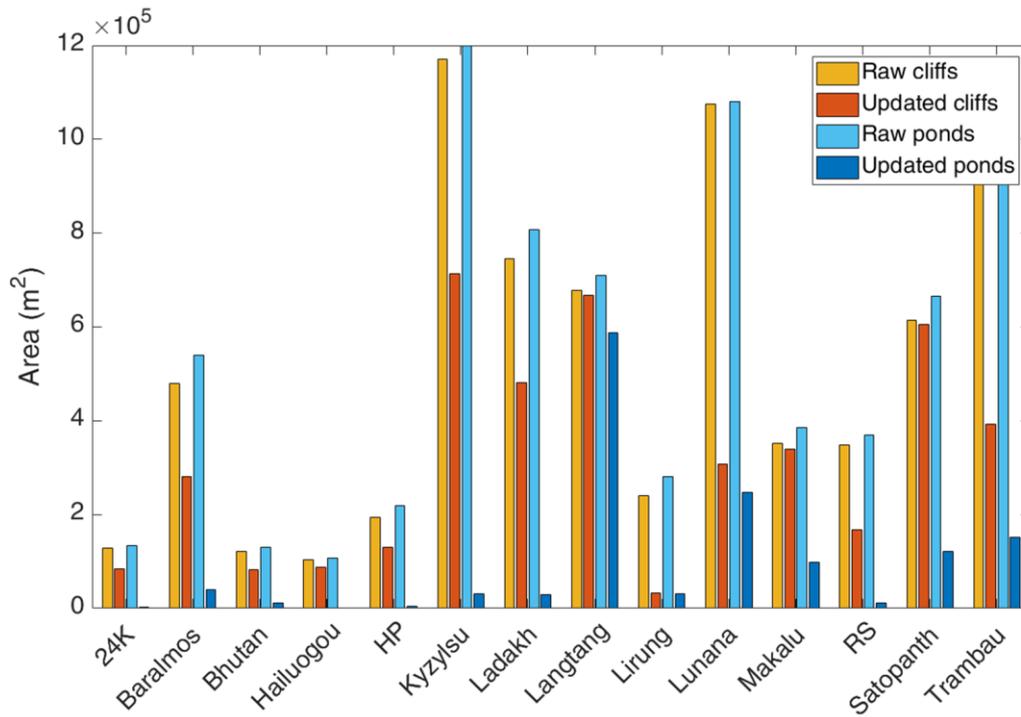
Figure 5.S8: *Cliff and pond area before and after manual trimming of automatically derived outlines for each scene.*
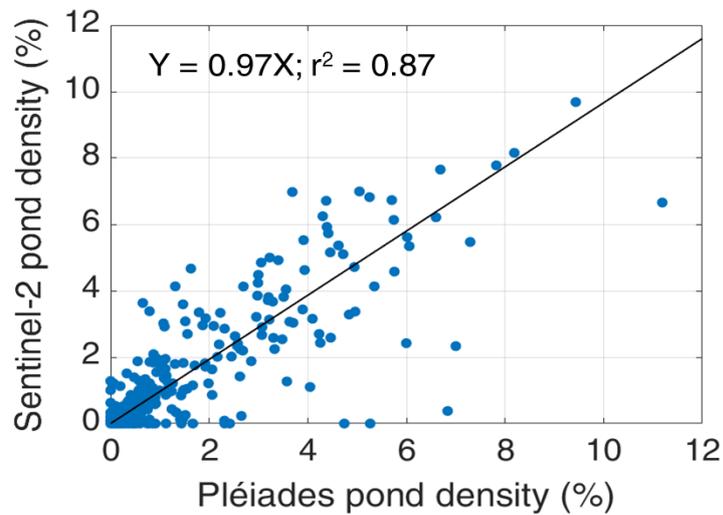
Figure 5.S9: *S2 pond density vs. Pléiades pond density for each bin.*
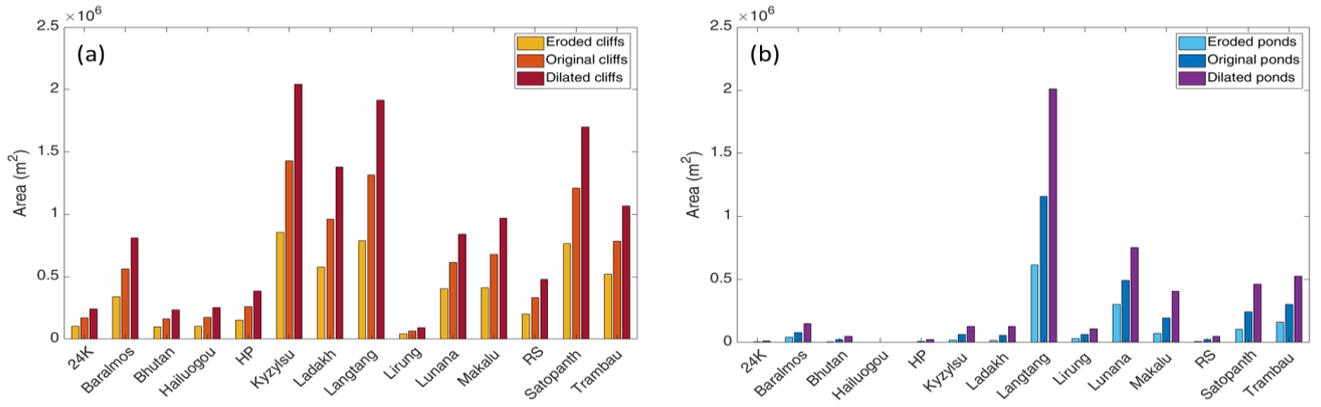
Figure 5.S10: *(a) Cliff and (b) pond original, dilated and eroded area for each scene.*
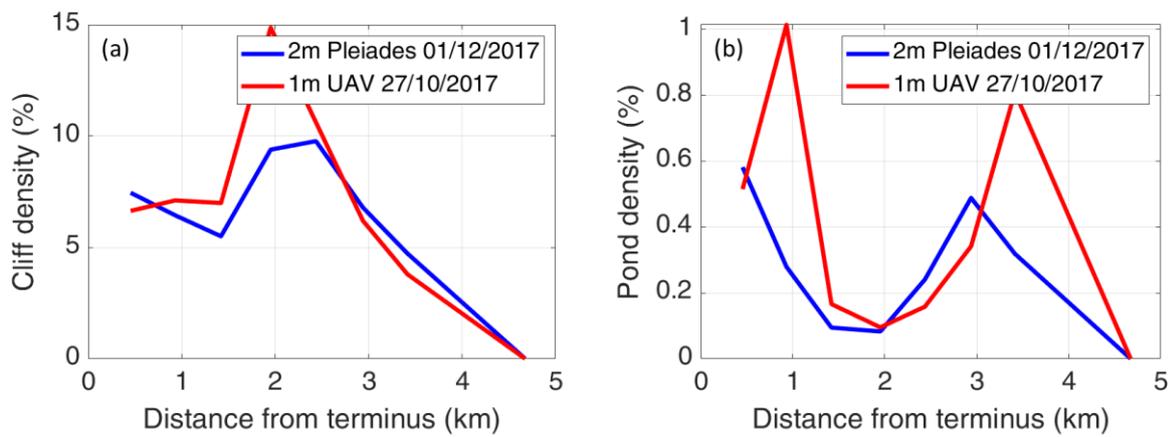
Figure 5.S11: *Cliff (a) and pond (b) density as a function of distance from the terminus calculated based on the Pléiades outlines from this study and those independently derived using a 1m UAV orthoimage.*
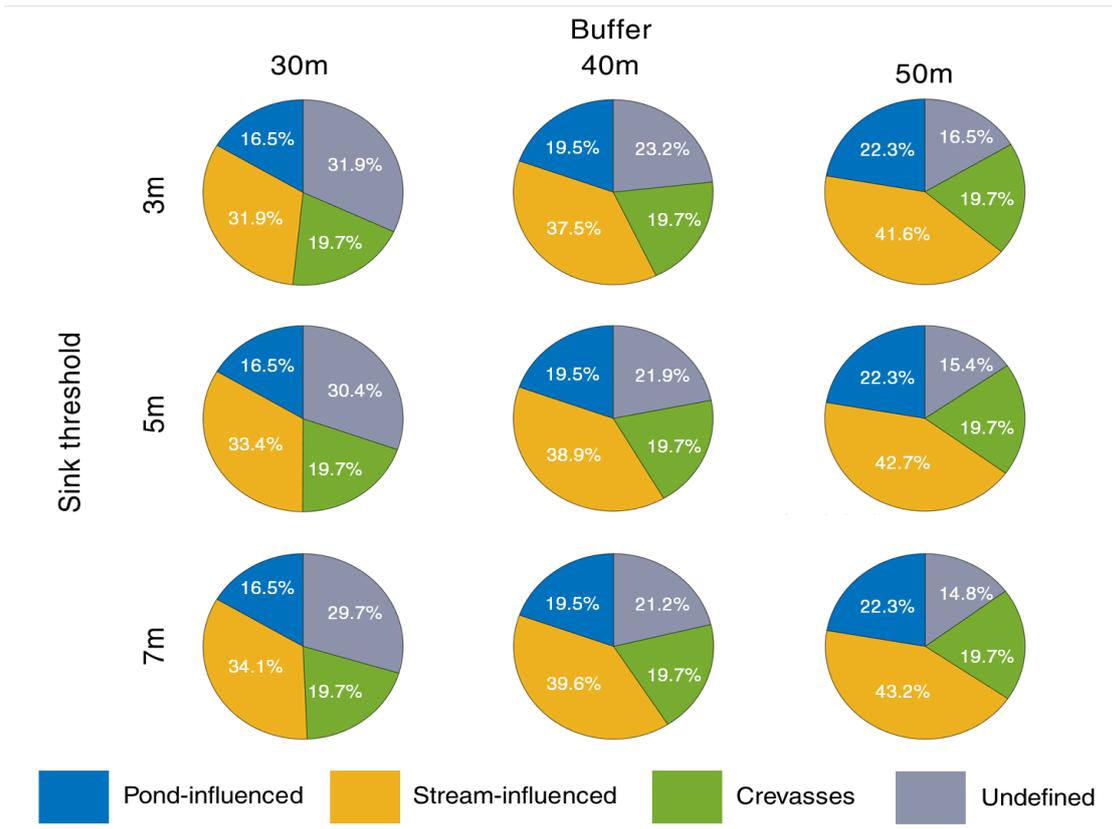
Figure 5.S12: *Area proportion of each cliff category depending on the DEM sink filling threshold for the mapping of the streams and the stream and pond buffer, for all cliff pixels.*
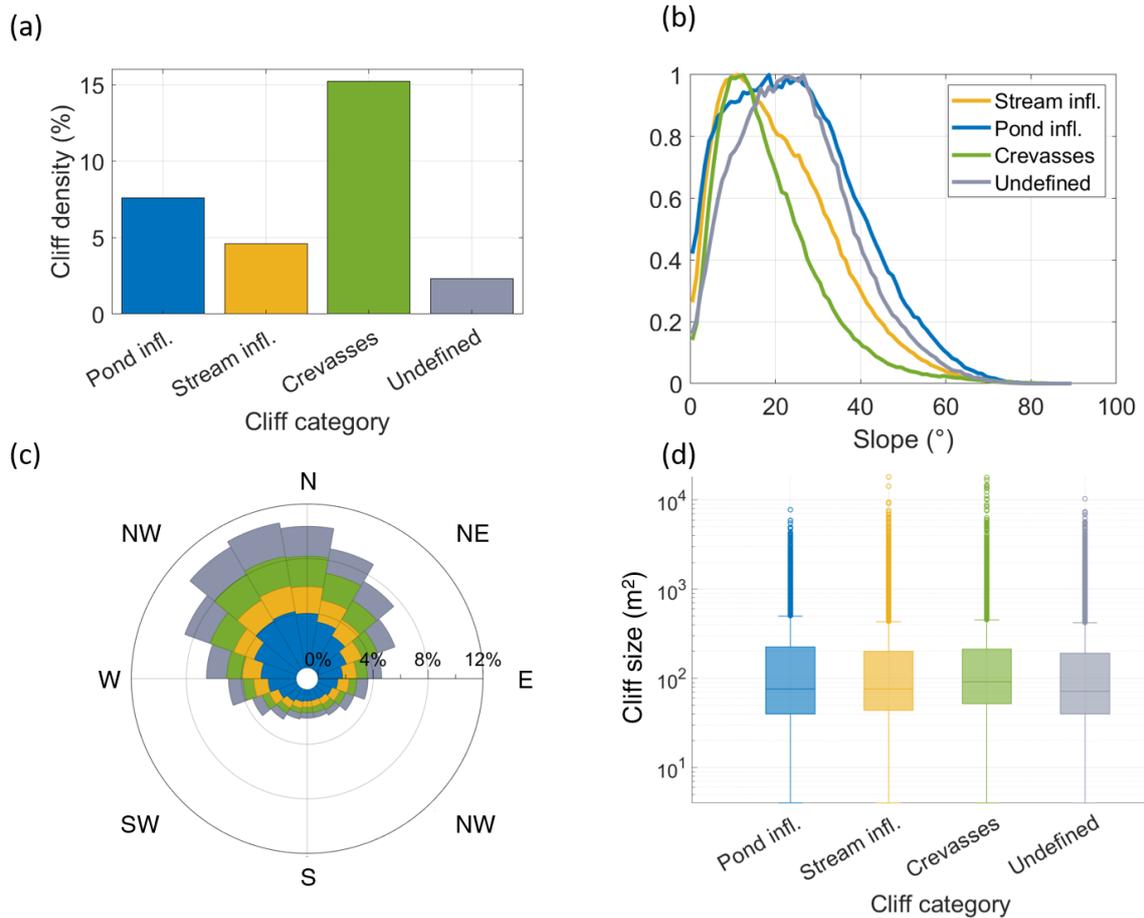
Figure 5.S13: *(a) Ice cliff density within buffer areas, (b) normalised slope distribution and (c) aspect distribution for all cliff pixels. (d) Size distribution of individual cliffs (defined as 8-connected objects in the cliff map) showing the median, 25th and 75th percentiles. The circles are considered as outliers.*
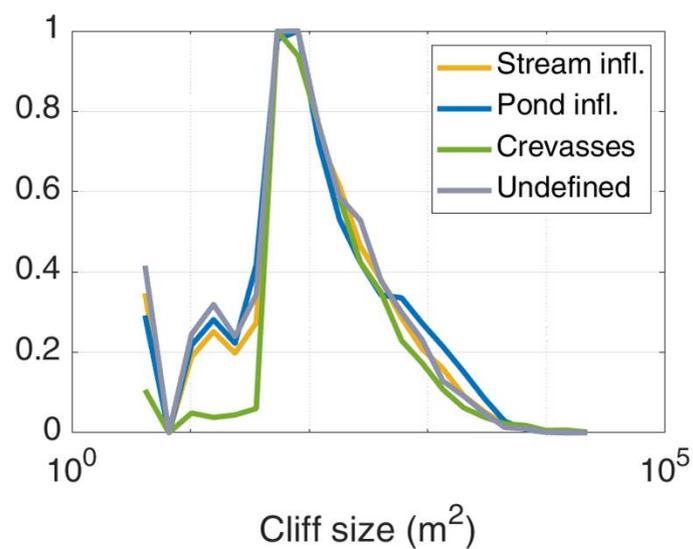
Figure 5.S14: *Normalised size distribution of the different cliff categories. The distributions are limited by the resolution of the Pléiades pixels (4 m², and the ability of the operator to identify ice cliffs less than ~25 pixels or 100 m² (Kneib et al., 2020).*

Table 5.S3: *Mean and standard deviation of the lognormal distribution of cliff size for the different cliff categories.*

Cliff category	Mean	Standard deviation
All	4.46	1.39
Pond-influenced	4.50	1.46
Stream-influenced	4.44	1.41
Crevasses	4.72	1.18
Undefined	4.34	1.42
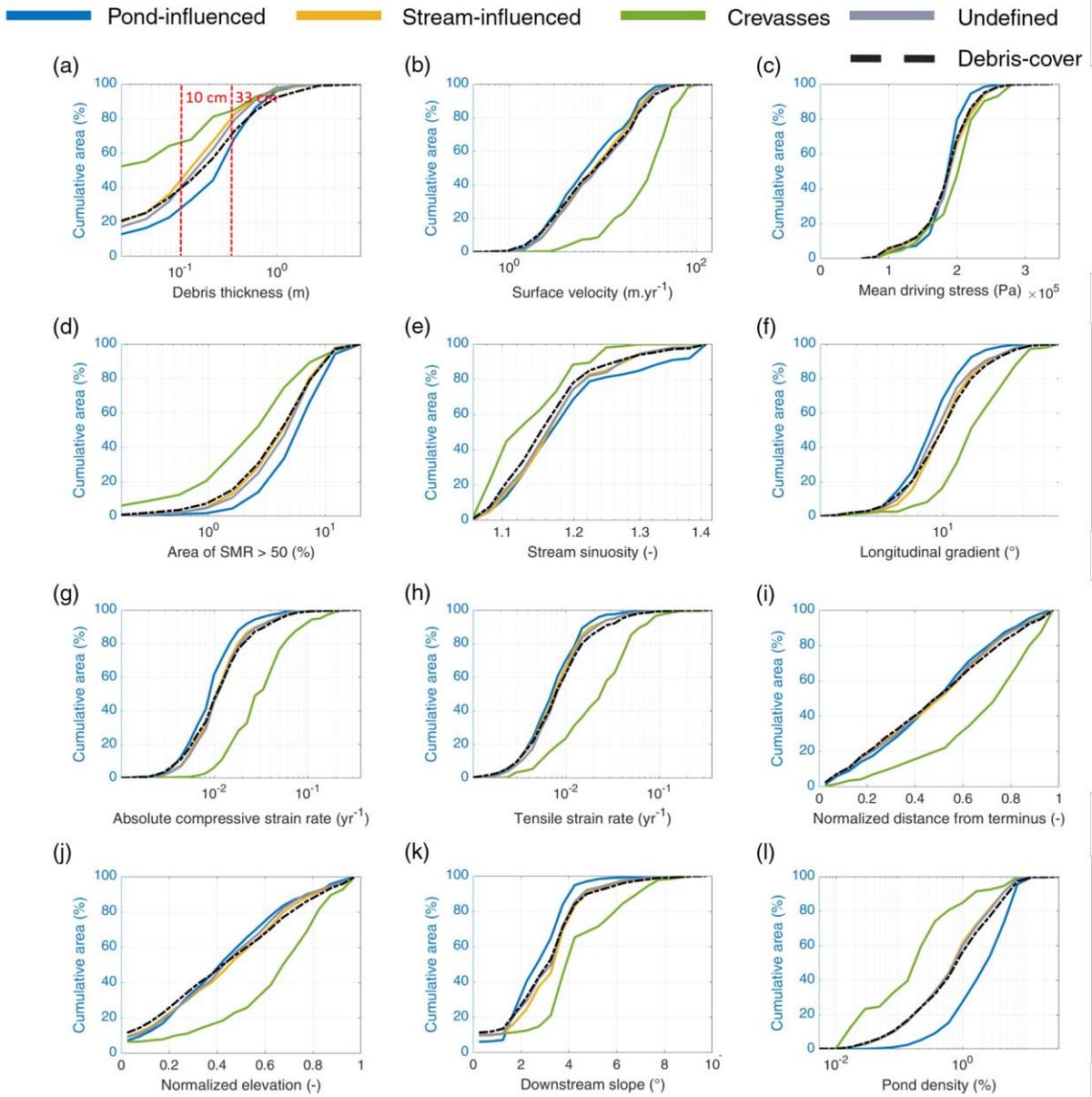
Figure 5.S15: *Cliff cumulative area in each category as a function of various metrics for all bins of all glaciers where more than 65% of the debris-covered area could be classified. The black line shows the cumulative area of all the bins.*
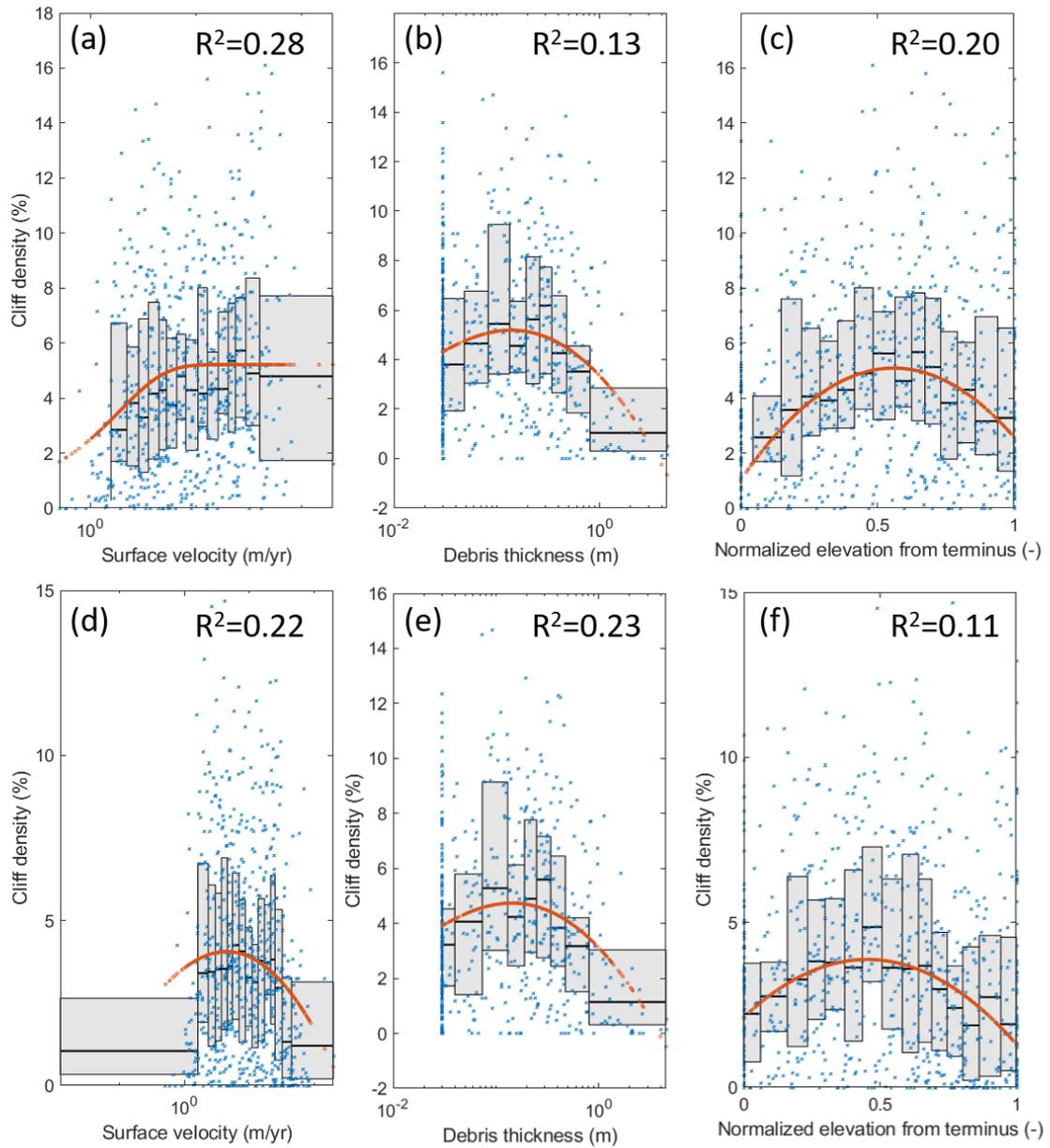
Figure 5.S16: *Cliff density with (a-c) and without crevasses (d-f) as a function of (a,d) surface velocity, (b,e) debris thickness and (c,f) normalized elevation from terminus for all bins of all glaciers for which more than 65% of the debris-covered area could be classified. The grey zones indicate the median and the interquartile range where each bin includes one tenth of the data. The red dots show a polynomial fit to the median values and the R^2 the results of this fit for the binned data.*
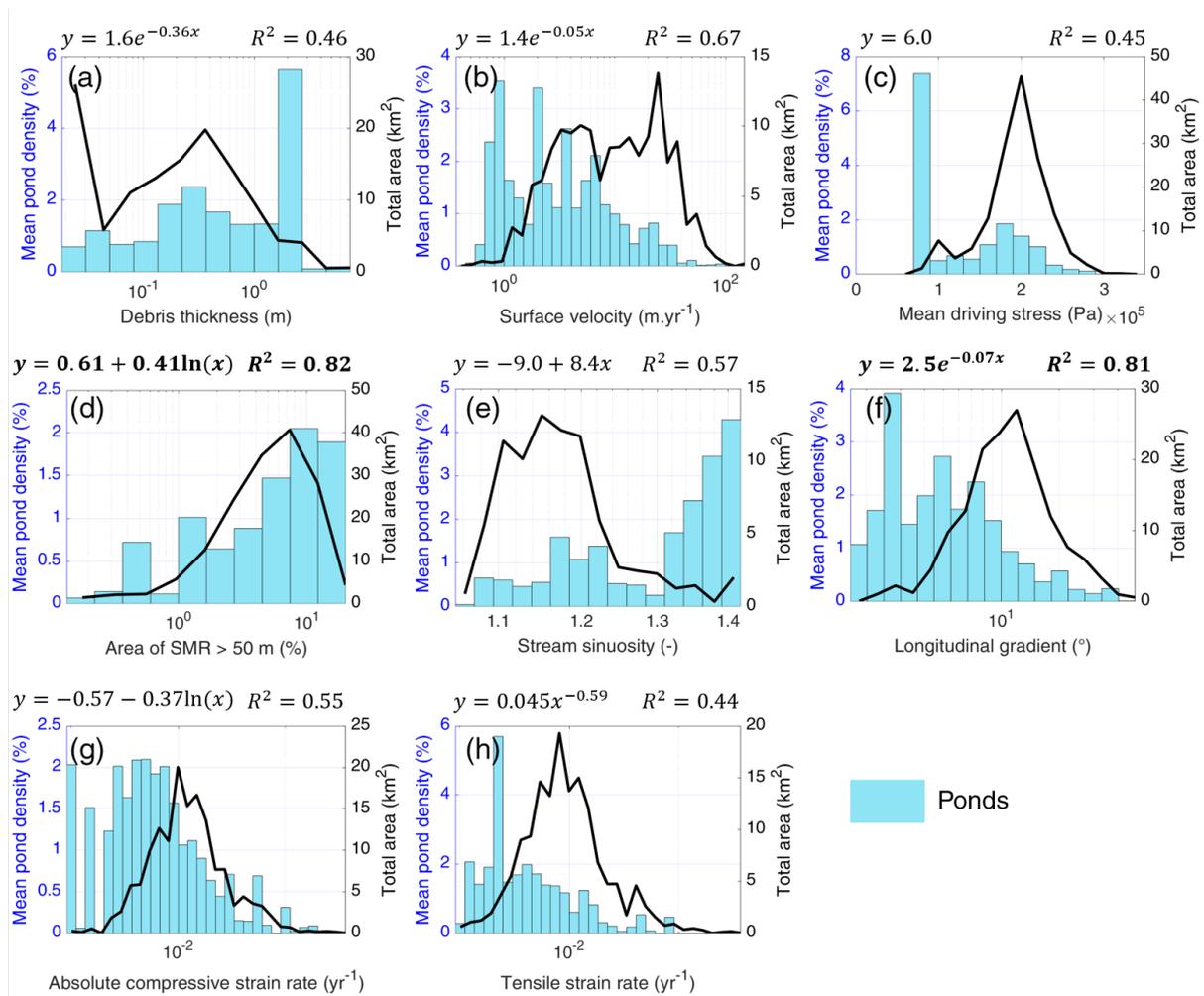
Figure 5.S17: *Mean pond density as a function of different variables for all bins of all glaciers where more than 65% of the debris-covered area could be classified: (a) debris thickness, (b) surface velocity, (c) mean driving stress, (d) 'hummockiness', (e) stream sinuosity, (f) longitudinal gradient, (g) absolute compressive strain rate and (h) tensile strain rate. The black line shows the area distribution of all the bins. The equations on top of the plot show the best linear relationships that could be found between the mean pond density (y) and the different variables (x), with their respective R^2 value, only accounting for the points with more than 10 observations. The relationships with an R^2 value higher than 0.8 are indicated in bold.*
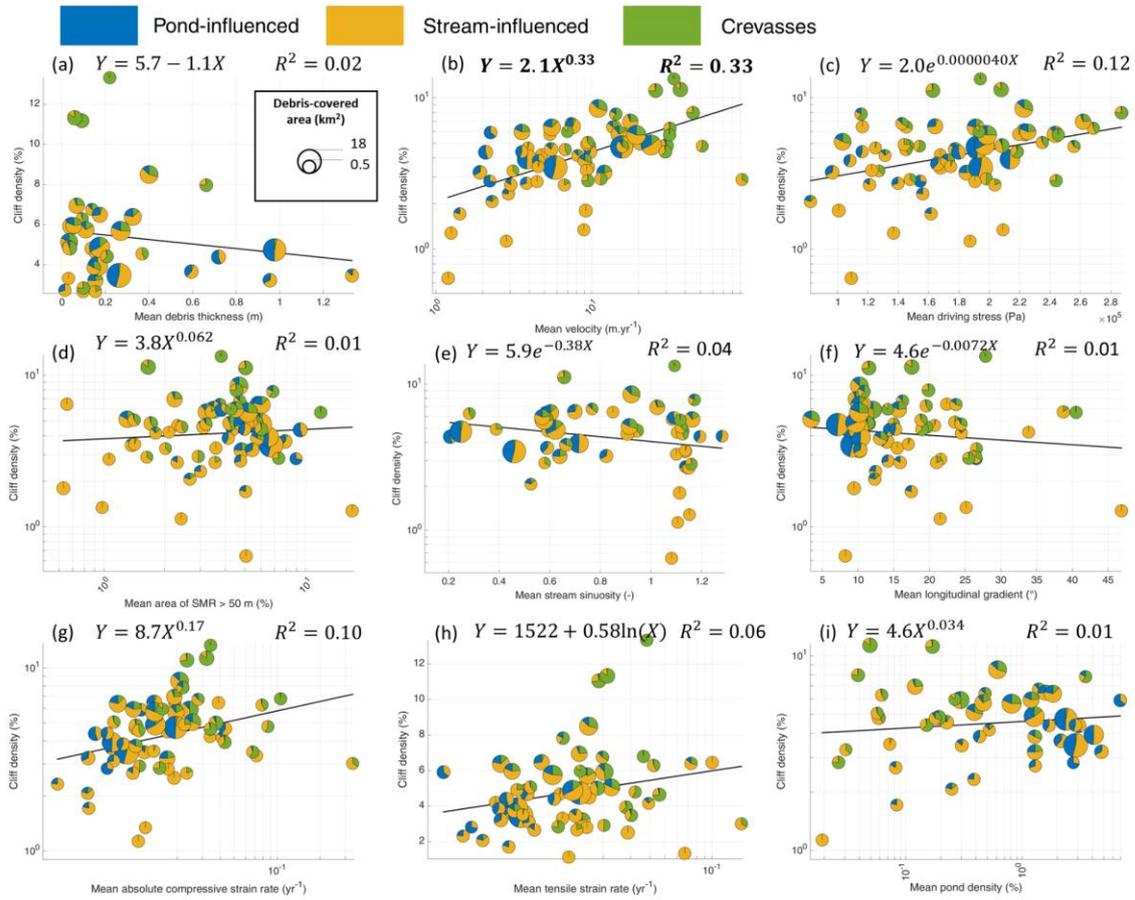
Figure 5.S18: *Cliff density for all glaciers where more than 65% of the debris-covered area could be classified, as a function of mean (a) debris thickness, (b) velocity, (c) driving stress, (d) hummockiness, (e) stream sinuosity, (f) longitudinal gradient, (g) compressive strain rate, (h) tensile strain rate, (i) pond density.*
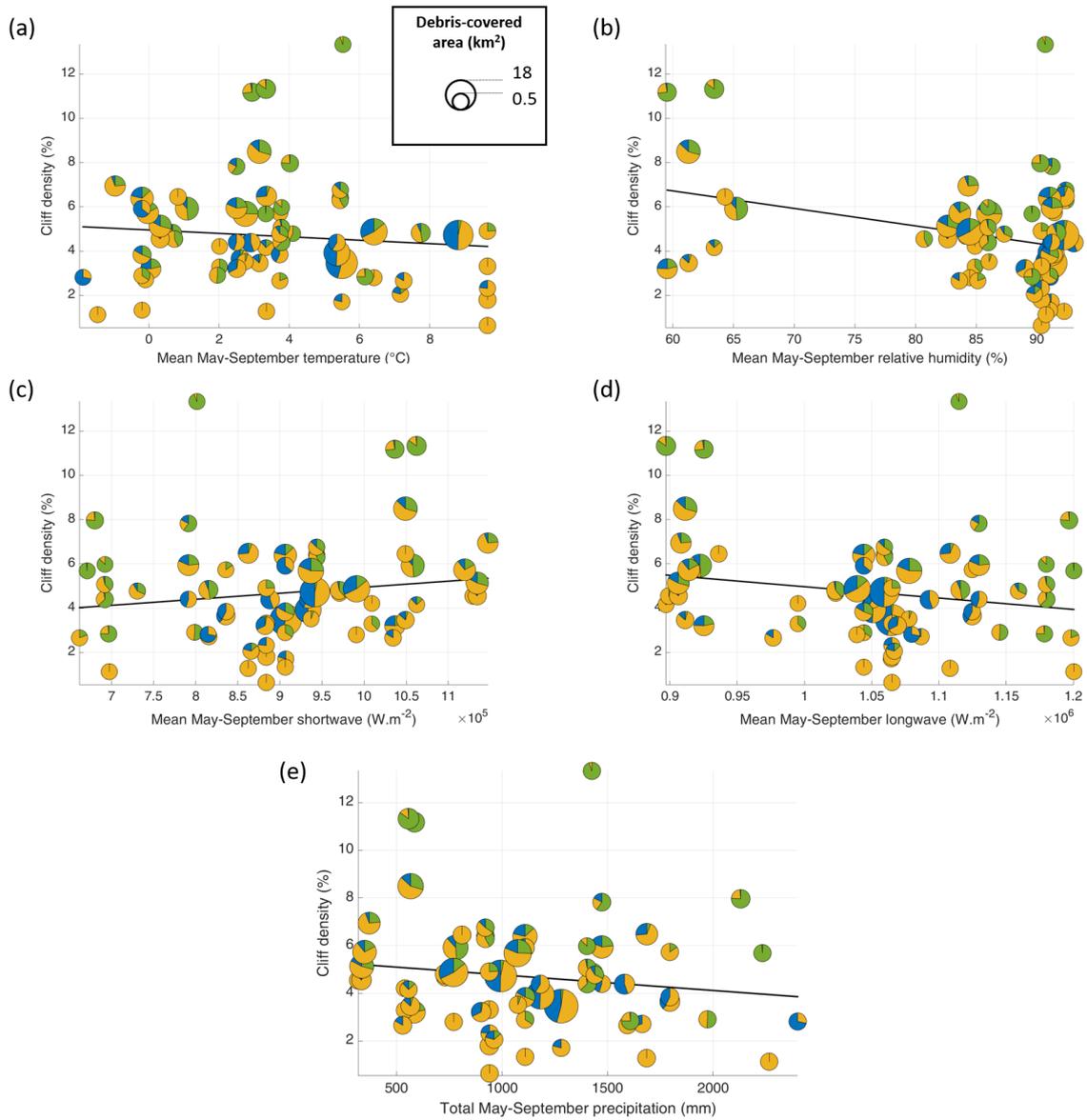
Figure 5.S19: *Cliff density for all glaciers where more than 65% of the debris-covered area could be classified, as a function of May-September (a) air temperature, (b) relative humidity, (c) incoming shortwave radiation and (d) incoming longwave radiation. The climatic variables are from ERA5-Land reanalysis data (Muñoz-Sabater et al., 2019), and the air temperature was lapsed to the mean elevation of the debris-covered area considering the mean above-debris lapse rates (-0.0088°C.m^{-1}) following Shaw et al. (2016). The proportion of undefined cliffs was not represented for better readability.*
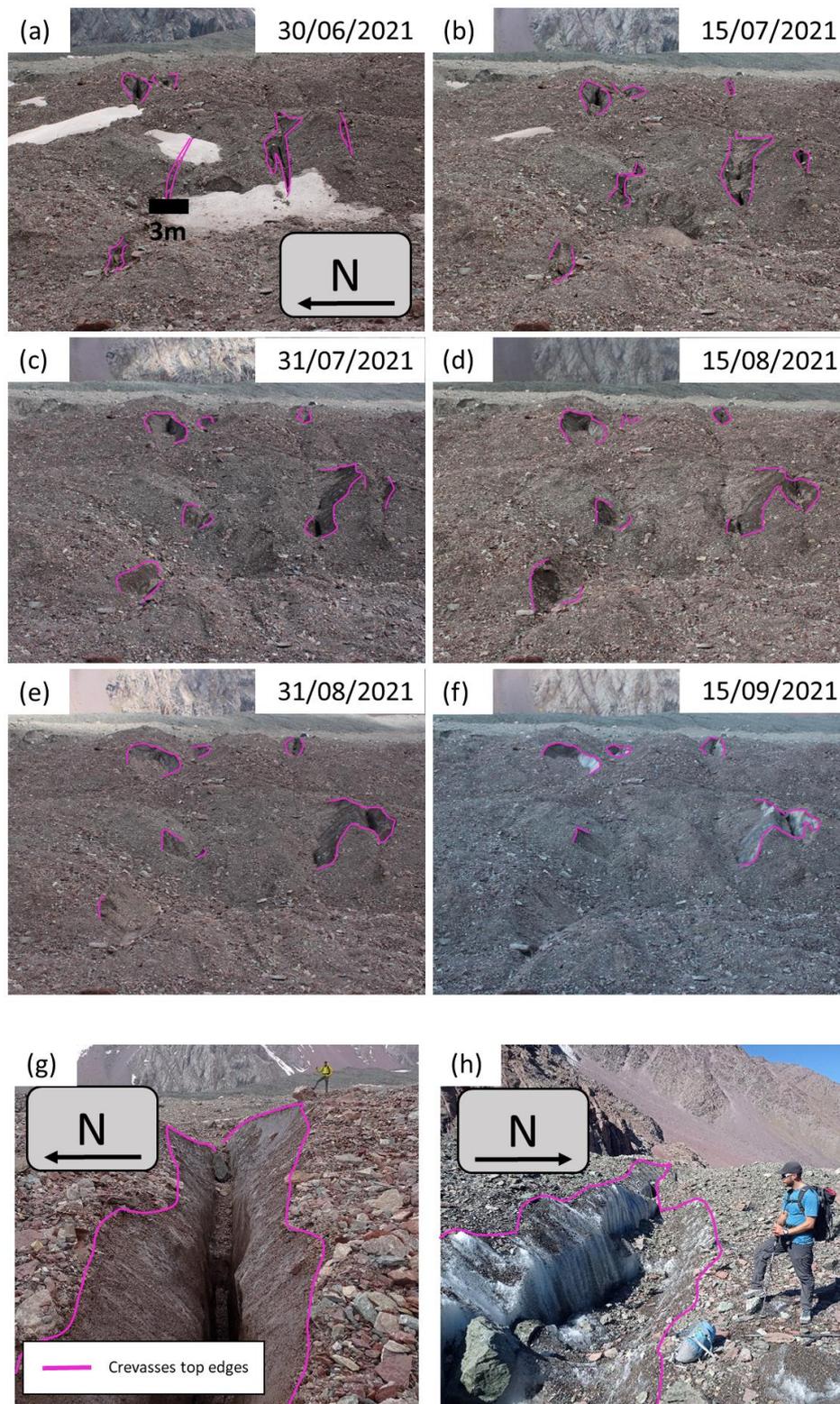
Figure 5.S20: *Crevasses on Kyzylsu Glacier (a-f) at bi-weekly time-steps during the 2021 melt season and (g-h) close-up views of other crevasses in September 2021 (image credit: Marin Kneib).*

Chapter 6: Conclusion

6.1. Key findings

This work goes from the very local study of a few cliffs at very high spatio-temporal (~0.2m DEMs, weekly observations) resolution to the analysis of the distribution and evolution of tens of thousands of ice cliffs spread out across HMA. The four parts of this dissertation have built on one another through a progression of scales and methodologies and are strongly interlinked.

6.1.1. Processes controlling the evolution and melt of ice cliffs at the local scale

In Chapter 2, the aim was to document for the first time the sub-seasonal variability of ice cliffs during the melt season and quantify how the cliff melt patterns were affected by debris redistribution, streams and ponds.

The weekly DEMs derived with time-lapse photogrammetry highlighted a **very high sub-seasonal variability in melt and area change**. The melt rates at the surface of the cliffs varied between 0 and 8 cm.day^{-1} and changed considerably over time as well as across the cliffs' surfaces. We also found that some of the cliffs' shapes and sizes changed dramatically during the melt season, with notably a cliff undergoing a 100% area increase within 2 months.

At both sites, the net shortwave radiation was driving the sub-seasonal variability of cliff melt. The air temperature was controlling the sign of the net longwave radiation and higher temperatures on 24K Glacier resulted in positive net longwave, which translated into 20% higher melt rates than on Langtang. **At the scale of a single cliff, the thickness of the thin debris layer deposited on top of the slope would either enhance melt by reducing albedo, reduce melt by 30-60% when it became thicker or patchier, or entirely cut melt when the cliff would become reburied**. Interestingly, thin debris accumulation on top of the cliff was partly controlled by precipitation events that would wash away the debris. Ultimately, the melt rates derived from weekly DEMs corrected for glacier flow highlighted the validity and transferability of the ice cliff energy-balance model.

The ice cliff area evolution on the other hand was also strongly dependent on debris redistribution. **This redistribution was controlled by the presence or drainage of supraglacial ponds on Langtang Glacier and the connectivity to the supraglacial streams on 24K Glacier**. These two glaciers indeed display distinct debris thicknesses and longitudinal gradients that favor water accumulation in surface depressions on Langtang and surface flow on 24K. Not accounting for this area change of the cliffs during the melt season led to total melt estimates being off by 5 to 80%.

These findings link the local cliff evolution with sub-debris melt and debris redistribution, and outline the importance of the supraglacial hydrology in shaping the surface of the debris-covered glaciers. They also indicate the strong spatio-temporal variability of cliff melt and cliff area change, which needs to be accounted for when assessing the cliff contribution to the melt of debris-covered glaciers.

6.1.2. Automated mapping of ice cliffs from high-resolution multi-spectral satellite images

Expanding our observations at the local cliff scale to the glacier and regional scale required the development of new remote sensing approaches to automatically map a large number of cliffs, over large regions, but also in time. Indeed, due to the small size, steep slopes and mixed spectral signature of ice cliffs, these features had only been mapped manually in previous remote sensing studies analyzing the glacier scale cliff distribution and evolution.

We focused our efforts on Pléiades and Sentinel-2 multi-spectral images and developed two mapping approaches, adapted to the spectral resolution of the sensors: a Spectral Curvature (SC) approach for Pleiades and a Linear Spectral Unmixing with scale (LSU-s) approach for Sentinel-2. The two new methods performed better than any other published method to date. The Dice values were higher than 0.5 for the Spectral Curvature applied to Pléiades images and higher than 0.4 for the LSU-s applied to Sentinel-2 images. **Both methods were transferable from glacier to glacier**, although the debris end-members for the LSU-s may need to be changed for debris with very different spectral signatures. **The Spectral Curvature approach applied to Pléiades data is well adapted to high precision mapping of cliffs on a few glaciers, while the Sentinel-2 LSU-s approach has the potential to be applied at the very large scale to derive large inventories of cliffs** to analyze their distribution and evolution patterns.

The application of these methods to three different sites in the Himalaya showed the cliff density to be between 3% and 9%, which was consistent with other cliff inventories. It also highlighted a large number of small cliffs which had been overlooked in previous studies and that would require to be studied in more detail to understand if they are actually cliffs and in this case how much they contribute to the melt of debris-covered glaciers.

Importantly, these automated mapping approaches paved the way to the objective mapping of ice cliffs at the large scale, which represents a key step to estimate the large-scale contribution of ice cliffs to glacier mass balance, as well as to understand the controls of ice cliff distribution and evolution.

6.1.3. Variability of ice cliffs on an interannual scale

In chapter 4, the aim was to quantify and understand the controls of the interannual evolution of cliff area and size at the surface of debris-covered glaciers. Previous remote sensing studies had indeed hinted that the cliff distribution could change considerably from year to year, but without being able to identify the reasons for these changes.

We analyzed the evolution of the cliff population of four glaciers of HMA: Urdok Glacier (Karakorum), Langtang Glacier (Central Nepal Himalaya), Satopanth and Bhagirath Kharak Glaciers (Garhwal Himalaya). All of them are extensively debris-covered, but located in different climatic regions and characterized by different glacier dynamics. We tracked the evolution of each individual ice cliffs over a period of 10 years and identified when they first appeared and when they died, including all the steps in between (splitting, merging, area change).

The systematic study at the four different glaciers highlighted the strong temporal variability of the population of ice cliffs, with the overall cliff density regularly changing by 20% from year to year and sometimes up to 80%. **The change in cliff number was dominated by the birth and death events, which both preferentially affected the smaller cliffs**. When considering the cliff population as a

whole, death events depended linearly on the total cliff population and thus acted as a regulator of the number of cliffs on the glacier. On the contrary, birth events seemed to be more stochastic. Other events included split, merge and mix events that had a limited impact on the number of ice cliffs and mostly influenced the cliff area. We used a stochastic model to represent the variability in ice cliff area and number, which enabled us show that each glacier was characterised by a cliff carrying capacity, i.e. that **unless the glacier was affected by major changes in glacier dynamics, the cliff population and area remained bounded in time**. The analysis of the controls of the cliffs' temporal variability did not show a strong consistency between the sites; the pond interannual variability seemed to partly control the cliff persistence but only affected ~50% of the cliffs. However, Urdok Glacier in the Karakorum did undergo a complete change in its cliff distribution and density within a few years when the upper part of the glacier underwent a surge, thus modifying its hydrological regime.

These results showed that the ice cliff population of a glacier evolves stochastically with time around a mean value. In case of considerable changes in glacier dynamics, this mean value can change considerably within a few years. These are useful findings to account for ice cliff evolution in projections of glacier mass balance. They also highlight the link between glacier dynamics, supraglacial hydrology and ice cliff evolution.

6.1.4. Controls of the distribution of ice cliffs

This chapter combined all the knowledge acquired in the previous steps and used it to interpret the ice cliff distribution across 86 glaciers in HMA. These cliffs were delineated based on the Spectral Curvature approach derived in chapter 3, and the mechanisms controlling their distribution were identified and validated based on the findings from chapters 2 and 4, as well as from the analysis of the formation of 202 cliffs using multi-temporal UAV data.

This large-scale study of ice cliff distribution, the first mapping effort of such a large population of cliffs, provided key relationships linking glacier state of evolution and dynamics with the type, density and characteristics (slope, aspect) of ice cliffs. A main outcome of this study was the **strong link between the supraglacial hydrology (streams and ponds) and ice cliffs**. The presence of streams and ponds was the main triggering factor for the formation of ice cliffs and the undercutting and debris removal contributed to the survival of the cliffs, which otherwise would get progressively reburied. This study also showed that close to 20% of the exposed ice on these debris-covered glaciers was actually due to crevasses, which had never been accounted for in previous studies, and could have important implications for the mass balance of these glaciers. Indeed, crevasses are likely to also enhance melt, but in a different way than 'traditional' ice cliffs do, due to their lower albedo values, the reflections on the opposite crevasse walls, and overall smaller height and debris-view factors.

Ultimately, we were able to **link ice cliff distribution and density with glacier dynamics and debris thickness**. Indeed, despite the important role of ponds in maintaining ice cliffs on thickly debris-covered, low-gradient, stagnating debris-covered glacier tongues, ice cliff density was found to decrease exponentially with increasing debris thickness as soon as debris got thicker than ~10 cm. Similarly, at the glacier scale the cliff density was positively correlated to the mean velocity in the debris-covered area. Based on these findings, we could describe how the population of ice cliffs changed as the glaciers slowed down and developed thicker and more extensive debris in their ablation area.

These are key results that present a novel understanding of the ice cliff distribution. They additionally provide the quantitative links between cliff density and characteristics and the glacier characteristics,

which, combined with estimates of cliff enhancement factors, can be used to project the large-scale contribution of ice cliffs to the mass balance of debris-covered glaciers.

6.2. Discussion and implications

Ultimately, this work successfully answered a few questions, but also raised many more, and the new understanding gained and methodological developments accomplished pave the way for promising future research on these topics.

6.2.1. Method development

This work includes some major methodological advances in terrestrial and satellite remote sensing for the study of ice cliffs, as well as a novel stochastic birth-death model to study the evolution of a population of cliffs.

6.2.1.1.   Time-lapse photogrammetry

The semi-automated production of accurate and well-aligned DEMs at very high spatio-temporal resolution using time-lapse photogrammetry was a major undertaking in terms of 1) equipment development, 2) field logistics to deploy twenty 15kg setups at three remote sites of HMA, 3) method development and 4) processing of large datasets. These efforts proved to be very worthwhile and the quality of the data enabled the validation of the distributed energy-balance model of ice cliffs and the identification of key processes related to the debris redistribution.

The processing of the image sets to DEMs is still not entirely automated, and requires the use of (pseudo-) ground control points to constrain the camera parameters and reduce the systematic errors for each DEM. However, once the workflow was in place, it took less than an hour per set of images to process DEMs with vertical errors lower than +/- 0.2m, 800 metres away from the camera array. Successful additional tests with cheaper and more portable setups on Zmutt Glacier, Switzerland, show that this method is promising for the monitoring of surface changes at high spatio-temporal resolution.

The applications of time-lapse photogrammetry are numerous in Earth Sciences (Armstrong et al., 2018; Filhol et al., 2019; Mallalieu et al., 2017). For ice cliffs, these high-temporal DEMs provide the means to advance the development of dynamic cliff models (Buri et al., 2016b) and to link the cliff, debris and hydrological processes for different glacier settings and cliff characteristics. We have for example been able to capture the changes occurring at crevassed locations on Kyzylsu Glacier with time-lapse photogrammetry, which would be a great way to explore the specific processes influencing this type of cliffs (Fig. 6.1)
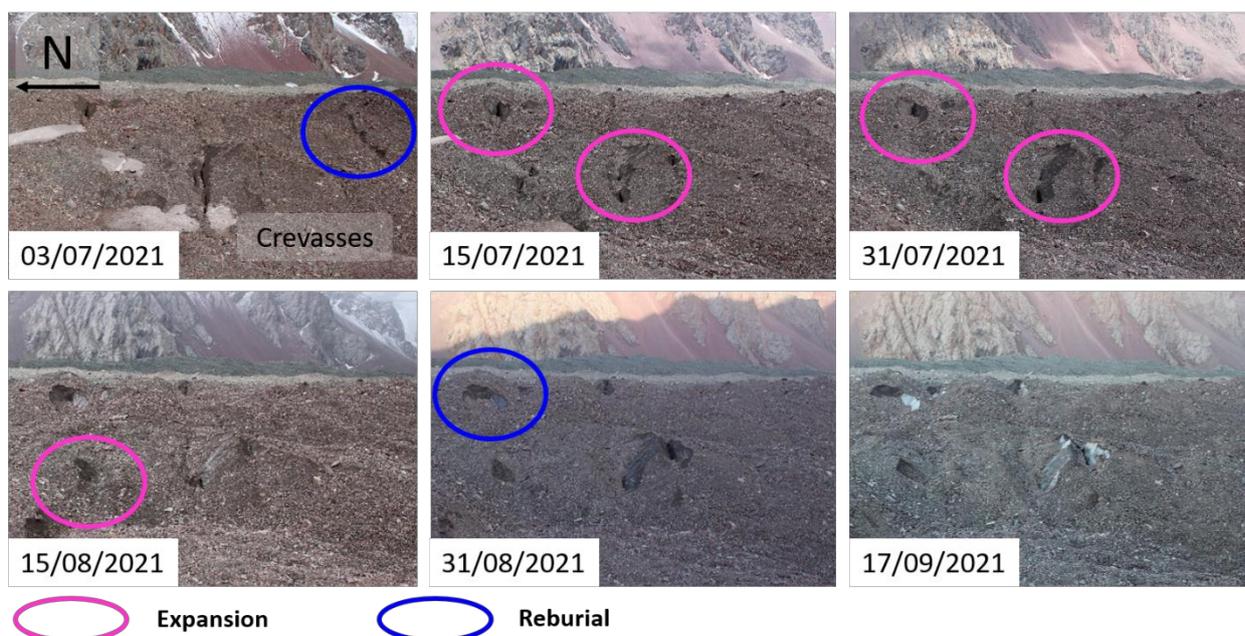
Figure 6.1: *Evolution of crevasses into cliffs on Kyzylsu Glacier, Tajikistan, between July and September 2021.*

6.2.1.2. *Mapping and tracking of ice cliffs*

The (semi-)automated mapping of ice cliffs was an important methodological step forward that has provided a novel tool for the scientific community and for this work in particular. Combined with the development of a novel algorithm to track ice cliffs automatically in time, it has enabled taking the study of ice cliffs to a whole new spatial and temporal scale compared to what had been achieved before, which was key to disentangle ice cliff distribution, formation and evolution patterns.

There remain some important limitations for these mapping approaches to be fully automated. The application of the Spectral Curvature method to 14 Pléiades scenes in chapter 5 showed that the method tended to overestimate the cliff density, sometimes considerably, for scenes with more extensive shadows or darker debris (Fig. 5.S8). Similarly, in 2020 I co-supervised a MSc thesis to automatically map ice cliffs at the large-scale using the LSU-s method applied to PlanetScope 3m-resolution multi-spectral images. However, this effort failed, likely due to the low spectral accuracy of the images (Walz, 2021). While the two approaches performed better than other methods based on slope or brightness (Anderson et al., 2021b; Herreid and Pellicciotti, 2018), they could be improved by combining the spectral information with other metrics such as shape and slope (Kraaijenbrink et al., 2016). This could possibly be done with deep learning, using the large-scale cliff datasets derived with high confidence in chapter 5 (Kraaijenbrink et al., 2018, 2016b; Wangchuk and Bolch, 2020; Xie et al., 2020).

Future large-scale application and developments of these mapping methods are promising to take this understanding even further. The community is still lacking a global map of supraglacial ice cliffs and ponds, although we have recently made progress in this direction by applying the LSU-s approach to all glaciers in HMA using adaptive debris spectral end-members in Google Earth Engine (Miles et al., in prep).

This work also strived to provide new perspectives on the representation of ice cliff evolution. The development of the cliff stochastic birth-death model enabled disentangling and constraining the long-term changes of the ice cliff population of various glaciers. This model implicitly accounted for the local processes affecting the evolution of individual cliffs and was adapted to also account for external variables.

The model needed however to be recalibrated for each individual glacier, which was difficult due to the large dataset required for this exercise (Fig. 4.S13). Most of the parameters related to the area ratios had similar values from glacier to glacier, which indicates that they would probably be transferable from site to site. A way forward would then be to normalise the number of different events by debris-covered area and link them with the characteristics of the glacier-wide cliff distribution (chapter 5), which was not possible in chapter 4 due to the lack of high-resolution DEMs.

This would likely be useful to account for cliff area variability when projecting the cliff distribution at the surface of debris-covered glaciers in the long-term (Ferguson and Vieli, 2021).

6.2.2. Contribution of ice cliffs to glacier mass balance

6.2.2.1.   A world of debris-covered glaciers

Debris-cover area (or stage) stems from the interplay of headwall erosion rates, that supply debris material onto the ice, and glacier dynamics that conveys the debris down to the terminus (McCarthy et al., 2021). When both contributions are constant the system is at an equilibrium and the debris cover area is stable. In our world however, glaciers are undergoing rapid changes due to climate warming and the direct implications are of a general glacier slowdown (Dehecq et al., 2019), while headwall erosion rates are not expected to decrease (Scherler, 2014). As a result debris-cover is expected to expand (Herreid and Pellicciotti, 2020), and this trend has been observed in a number of regions of the world (Bhambri et al., 2011; Deline, 2005; Kamp et al., 2011; Mölg et al., 2019; Thakuri et al., 2014; Xie et al., 2020, Fig. 6.2). While it is still unclear at which rates these changes in debris cover, but also debris thickness, occur, it is evident that debris cover on glaciers will increase in the coming decades.

This thesis has shown that ice cliffs are common features of debris-covered glaciers, that they evolve with the glacier dynamics, shape the surface of glaciers and influence their melt patterns. These results are however still limited to a short time period covering the last ~10 years, the only one for which the quality of remote sensing products from UAV or satellite is good enough to extract meaningful maps and melt patterns of ice cliffs. In this sense, there is a large potential for more long-term monitoring of ice cliffs and the tools developed within this thesis provide a good framework to do so in a consistent way. This monitoring of ice cliffs should be expanded in time to cover long-term changes in the population of ice cliffs (> 1 decade) and in space to look at the cliff evolution in other mountain ranges. Due to the small size of the cliffs and their interactions with debris and hydrology, high-resolution data (< 2 m) will be necessary along with complementary datasets of accurate debris thickness and conductivity, detailed stream networks and pond variability.
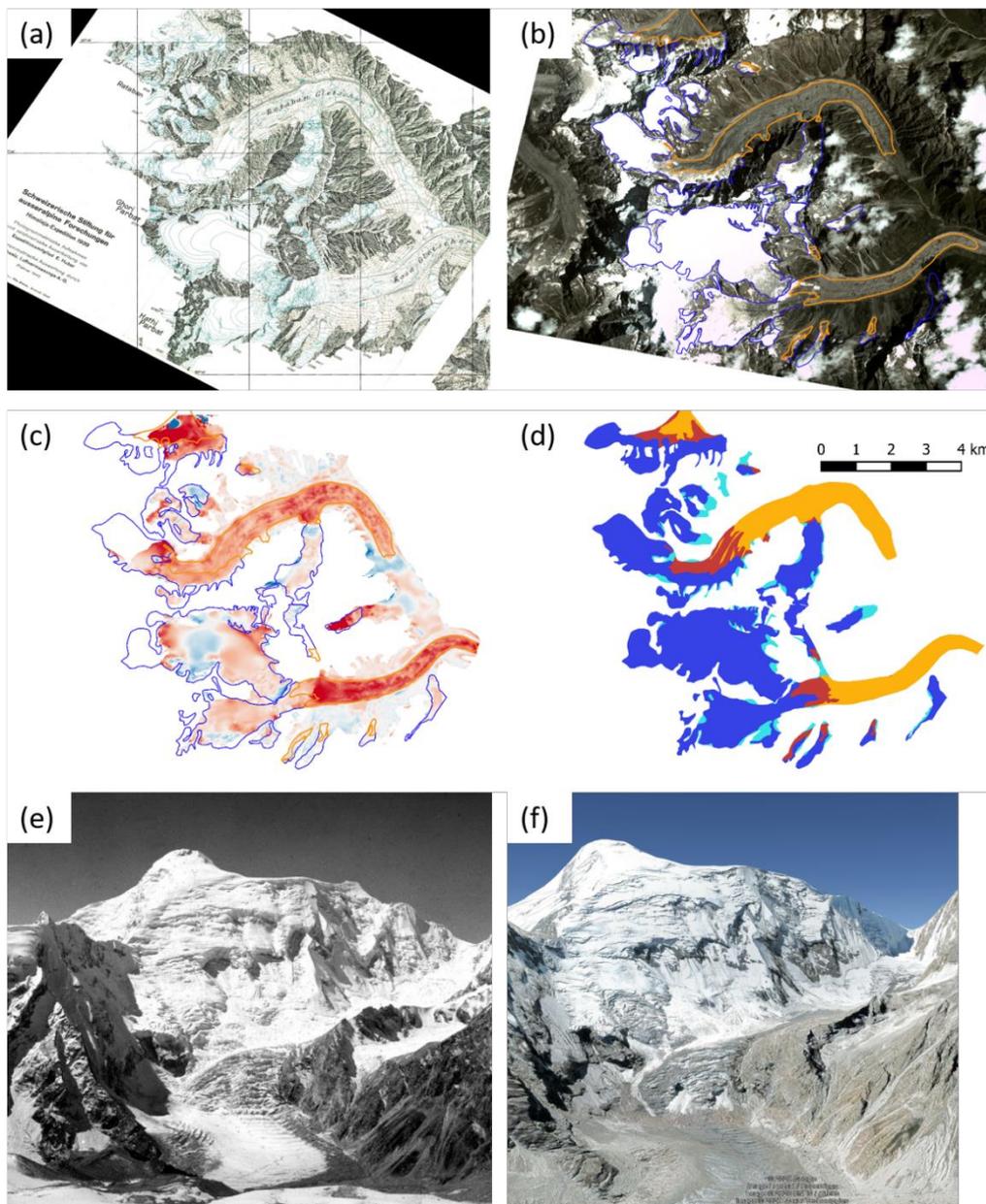
Figure 6.2: *Long-term glacier changes in the Garhwal Himalaya, India. (a) 1939 topographic map of Kosa and Rataban (Raj Bank) Glaciers. (b) 2021 Planet image of the same glaciers. (c) 1939-2017 thinning patterns at this site from the digitised 1939 topographic map and the 2017 HMA DEM of the zone (Shean et al., 2020). (d) changes in debris and glacier extents, with the 2021 glacier (dark blue), debris (red) and the 1939 glacier (light blue) and debris (orange) outlines. (e) 1939 image of the upper area of Bhagirath Kharak Glacier. (f) 2020 view of the same location from Google Earth. The 1939 images and maps were taken by the 1939 Swiss expedition to the Garhwal Himalaya, and I plan to use this invaluable dataset to study the long-term changes of these glaciers using complementary remote sensing and field data.*

6.2.2.2.   Representation of ice cliffs in glacier mass balance models

The melt contribution of ice cliffs to the mass balance of debris-covered glaciers is of importance (Anderson et al., 2021a, 2021b; Brun et al., 2018; Kääb et al., 2012; Pellicciotti et al., 2015), but has so far never been included explicitly in glacio-hydrological or glacier mass balance models, except in very

201

simplified ways (Ferguson and Vieli, 2021; Hagg et al., 2018; Kraaijenbrink et al., 2017). Other than these examples, glacier-wide ice cliff melt was always calculated independently from the overall glacier mass balance (Brun et al. 2018; Buri et al., 2021; Reid and Brock, 2014; Sakai et al., 1998). Therefore, despite considerable advances on the understanding of the melt patterns and dynamics of debris-covered glaciers, it is still unclear what causes their higher-than-expected thinning rates (Brun et al., 2019; Gardelle et al., 2013; Kääb et al., 2012; King et al., 2020).

The new generation of regional and global glacier models will include the effect of cliffs and ponds on glacier mass balance in an implicit way (Compagno et al., 2022). Indeed, these models are starting to use large scale debris thickness estimates produced at relatively coarse resolution (>50 m) from satellite thermal images or SMB products (McCarthy et al., 2021; Rounce et al., 2021). These products implicitly include the sub-pixel influence of supraglacial ponds and ice cliffs on the thermal or SMB data, which means that due to additional cliff and pond melt or lower surface temperatures, the debris thickness estimates are reduced in a non-linear way relative to the actual debris thicknesses measured directly in the field. Based on debris thickness estimations with and without masking out cliffs and ponds, Rounce et al., (2018) estimated that this mixed pixel effect could result in a reduction of debris thickness estimates by up to 0.8 m with their approach in the more thickly debris-covered parts of some of the glaciers in the Khumbu region. Considering the exponential decrease of the Ostrem curve, this mixed-pixel effect could still be relatively important for the melt of areas with thinner debris, including for some of the results presented in chapter 5. More importantly, 1) it is not clear how the sub-pixel effect of cliffs and ponds in thermal and SMB data scales with their actual melt contributions and 2) this implicit representation of the cliff and pond contribution is not representative of their temporal and spatial melt and area variability, especially when the debris thickness inversion is conducted with thermal imagery taken at one specific time step. This implicit contribution of cliffs and ponds to debris thickness estimates is likely not the best way forward to precisely account for the melt contribution of ice cliffs and is something that will need to be taken into account in future research (Kneib et al., 2021).

The difficulty in explicitly representing glacier-wide cliff (or pond) melt lies within the representation of the complex dynamics of these features (size- and terrain-dependent energy fluxes, aspect control, topographic shading, area and shape variability…) by models with grid sizes one or two orders of magnitude larger than the cliffs. However, these effects could also be parametrized with the help of robust cliff inventories and some projections of their evolution (Kneib et al., 2021; chapter 5). Three promising recent developments pave the way for this explicit representation of ice cliff melt in glaciological models:

- The application of the cliff dynamic model to all ice cliffs in the Langtang catchment using manual outlines enabled calculating the ice cliff contribution to melt at the scale of a whole HMA catchment (Buri et al., 2021).

- The development of robust cliff melt enhancement factors from the point-scale energy-balance modelling of cliff, pond, sub-debris and clean ice melt at 20 on-glacier AWS sites (Miles et al., 2022).

- The development of robust approaches to map cliffs at the large-scale (Anderson et al., 2021b; Herreid and Pellicciotti, 2018; Kneib et al., 2020), and the quantification of the links between glacier state and dynamics, and ice cliff density and characteristics (chapter 5).

6.2.3. Towards modeling an evolving debris-covered glacier surface

A striking aspect of this work was to witness how quickly these ice cliffs 'moved' and evolved. Repeat visits at the field sites were always full of surprises in terms of how much change had happened within the course of a few months only (Fig. 6.3). These changes result from the combination of sub-debris, cliff and pond melt, stream incision, debris transport, glacier dynamics represented by the opening of crevasses, and englacial conduits. Each single one of these elements has its importance in shaping the evolution of a debris-covered glacier, and in many ways, the combination of these influences contributes to the heterogeneous melt patterns.

Now that we have shown that our current understanding of the ice cliff energy balance is robust and transferable from site to site (chapter 2), the main uncertainties in the representation of cliff melt modelling at the local scale comes from the representation of the ice cliff evolution, and especially its interaction with debris. This was represented to some extent in the dynamic version of the cliff energy-balance model (Buri et al., 2016b), but using a very simple parametrization with only a slope threshold to define cliff versus debris-covered area, and prescribing constant debris thickness and sub-debris melt rate. The recent development of physically-based models to represent debris transport (Moore 2018, 2021; Mölg et al., 2020) offers a great opportunity to couple ice cliff backwasting with debris motion. Similarly, a more direct representation of the interaction between conduits, crevasses, streams, ponds and cliffs (incision at the base) would be highly relevant.

Such advances would still require to invest some work in developing a parametrization of debris motion on steeper slopes, to bridge the gap between representations of debris creep (Anderson, 2000; Mölg et al., 2019; Moore, 2021) and gravitational transport (Van Woerkom et al., 2019), so as to be able to redistribute unstable debris in a physical way (Moore, 2018). The use of multi-temporal UAV or terrestrial (from time-lapse cameras) DEMs and orthoimages of debris-covered slopes with various angles, lengths, aspects and in different climatic regimes would be a fairly easy way forward to quantify debris motion and therefore complement some initial observations conducted on Miage Glacier (Fyffe et al., 2020a; Westoby et al., 2020). This data already exists from the work conducted in chapters 2 and 5 of this thesis, and we have acquired complementary datasets on Kyzylsu and Zmutt Glaciers (Table 6.S1). Using cross-correlation techniques, it should be possible to disentangle glacier flow, ablation under debris and actual debris transport and develop a parametrization for this using data from a variety of sites. This would be key to model debris thickness at very high resolution and thus account for differential melt across the debris-covered surface.

Figure 6.3: *Changes on 24K Glacier between June (left) and October 2019 (right). (a-b) Lower supraglacial stream. (c-d) Lower pond. (e-f) Middle pond. Image credit: Marin Kneib.*

Additional work would also be necessary to represent specific processes at the cliff scale. This includes the study of specific types of cliffs, such as crevasses, which are quite common at the surface of debris-covered glaciers according to our findings from Chapter 5. Indeed, it is unclear how the cliff energy-balance model would perform in such a situation with two steep ice walls facing each other, and if it would be able to provide a good estimate of their melt contribution. Similarly, stream incision and its influence on cliff formation and development of supraglacial valleys could also benefit from advanced observations of the local processes occurring at the interface between cliffs and streams. Such effects are harder to model as the streams tend to undercut the cliffs, and are therefore often invisible from UAV surveys. I have been collaborating on this topic with members of the Glaciology group of the University of Zürich who are designing field experiments based on time-lapse cameras and laser scans to monitor stream undercutting on Zmutt Glacier, Switzerland, and on Satopanth Glacier during our upcoming field campaign in India planned for September 2022.

All these 'bricks' of understanding combined would enable one to represent the evolution of the debris-covered surface of a glacier with time, and address some fundamental questions related to the formation of supraglacial hummocks, the long-term evolution of supraglacial valleys, the respective influence of various debris sources (rock falls, moraine slumping, lateral moraines) on the surface topography and mass balance, or the long-term evolution of mass balance profiles across debris-covered glaciers.

6.3. Supplementary material: related work that I have been involved with during the course of this PhD thesis

6.3.1. Ice cliff contribution to melt on Trakarding Glacier

In the past year, I have been involved in the application of the cliff dynamic model to all the cliffs on Trakarding Glacier, another site in Nepal with different climatic and cliff distribution characteristics than Langtang (Sato et al., *in prep,* Fig. 6.S1). This study focuses on comparing the model results with the actual cliff evolution patterns, as characterised based on a glacier-wide remote sensing dataset from high-resolution UAV data (Sato et al., 2021). This will complement the observations made from this thesis at the feature scale and provide ways to move forward with regards to accounting for debris influence on ice cliff evolution and melt contribution.
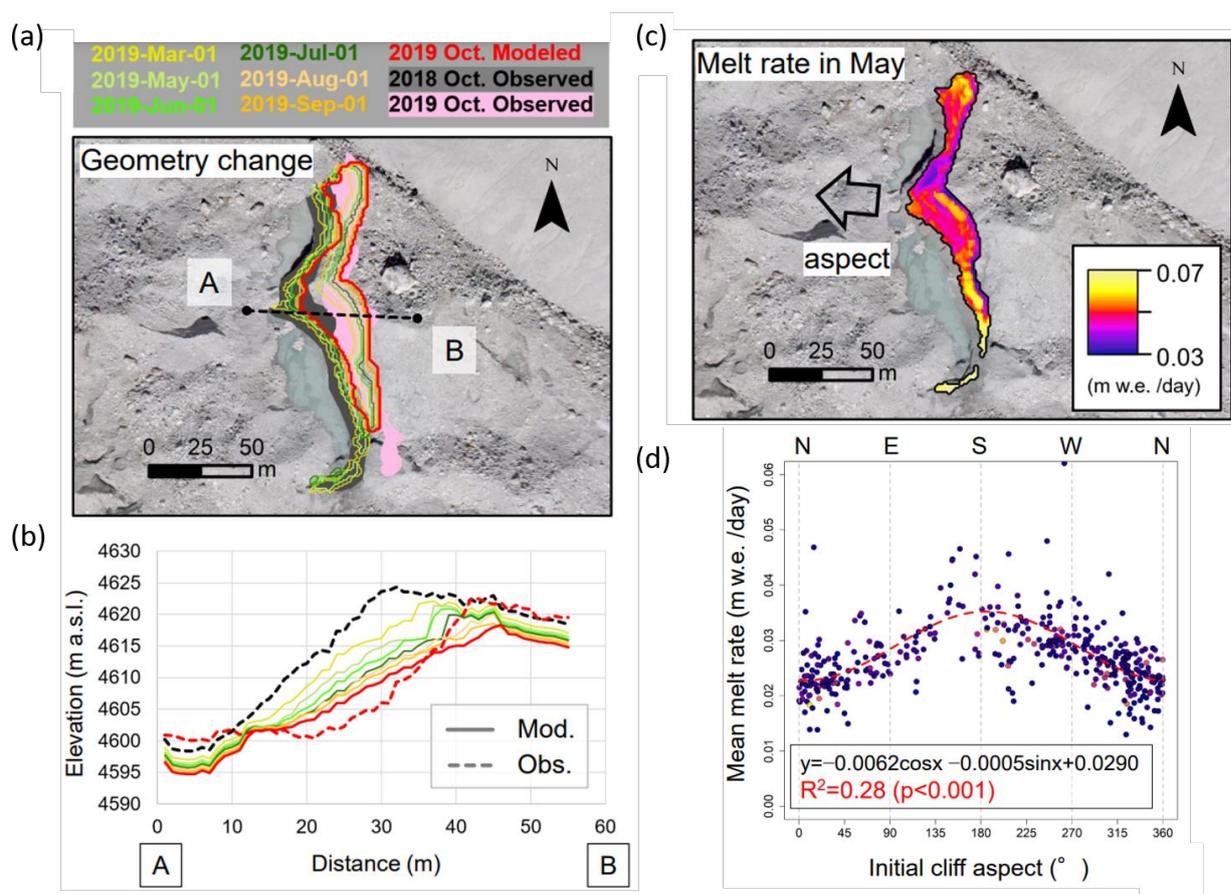
Figure 6.S1: *Modelled and observed outlines (a) and profile (b) of a random cliff on Trakarding Glacier from October 2018 to October 2019. (c) Mean melt rate in May for the same cliff. (d) Mean melt rate as a function of initial aspect for all simulated cliffs on Trakarding Glacier. Figure from Sato et al. (in prep), presented at EGU 2022.*

6.3.2. Solving the 'debris-cover anomaly'

6.3.2.1. At the glacier scale

Precise understanding of the respective contributions of emergence velocity, sub-debris, cliff and pond melt to glacier thinning and their variability from glacier to glacier is key to derive the relative influence of each term in specific glacier settings (Anderson et al., 2021a, b). Our HIMAL group has been

collaborating with researchers from the Institute of the Tibetan Plateau, China, and Northumbria University, UK, to disentangle the different contributions to glacier thinning for 23K and 24K Glaciers, two glaciers belonging to the same small catchment in Eastern Tibet, both debris-covered but with opposite thinning patterns (Chuanxi et al., *in prep*). This study leverages the high resolution DEMs and orthoimages from several high-resolution UAV surveys taken in 2019 and 2020. On 23K, thinning rates increase with elevation while they decrease for 24K Glacier. Solving for the emergence velocity, it was apparent that these different patterns were related to the different dynamic states of the glaciers, with 24K being much more dynamically active, probably related to an overall steeper longitudinal gradient (Fig. 6.S2). The SMB on the other hand seemed to be mainly controlled by debris thickness with the presence of supraglacial cliffs locally influencing the spatial variability (Fig. 6.S2). This therefore shows the importance of glacier dynamics when interpreting the thinning patterns of debris-covered glaciers, as they can vary considerably from glacier to glacier, along with the secondary control of ice cliffs on the mass balance patterns (Chuanxi et al., *in prep*).
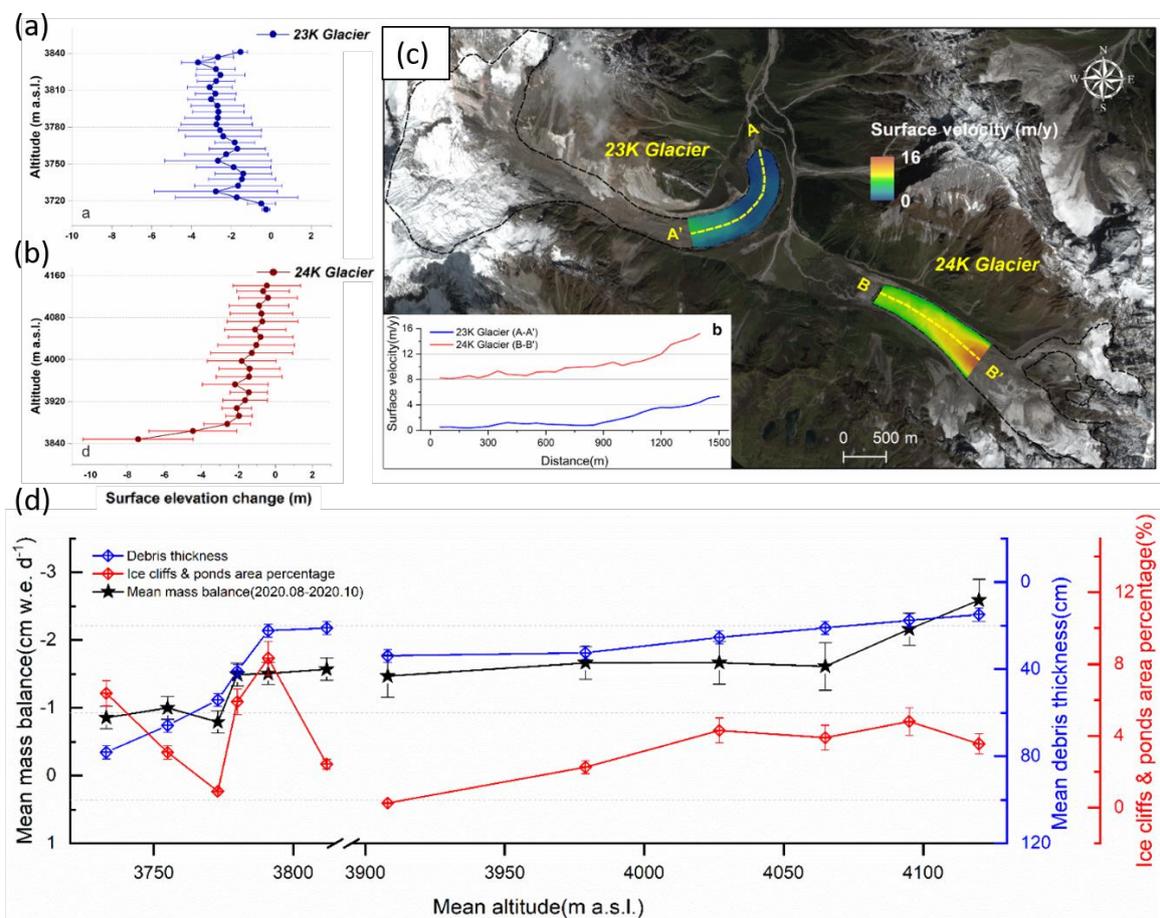
Figure 6.S2: *(a-b) Annual average glacier surface elevation changes within 5-m (23K)/15-m (24K) elevation bands with the corresponding standard deviations for August 2019-August 2020. (c) Spatial distribution of annual surface velocities (August 2019-August 2020) for the survey areas of the two glaciers. (d) Daily mean SMB and its uncertainties for the individual zones of the two glaciers during the ablation period, the mean debris thickness and its uncertainties and the mean percentage of the ice cliff and ponds area. Figure from Chuanxi et al. (in prep).*

The specificity of the different glaciers and their dependence on local topography, aspect, debris thickness and distribution patterns of supraglacial features makes it all the more challenging to disentangle the controls on the debris-cover anomaly at the subregional to regional scale (Brun et al., 2019). I have been involved recently in a study led by Evan Miles (HIMAL group) that aims to solve this debris-cover anomaly at the scale of HMA, by quantifying each of these components for each individual glacier (Miles et al., in prep). Using a recent specific mass balance and emergence velocity product (Miles et al., 2021) combined with an inventory of ice cliffs and ponds and an independent product of thin debris locations (i.e. where debris is thin enough to enhance melt relative to clean ice, Rounce et al., 2021) for all glaciers in HMA, we hope to quantify the contribution of each of these components at different scales to explain the anomalous thinning patterns described in the literature (Brun et al., 2019; Gardelle et al., 2013; Kääb et al., 2012). More specifically, the ice cliff and pond contribution is based on outlines derived from Sentinel-2 images in Google Earth Engine and on enhancement factors modelled at four sites in HMA (Miles et al., 2022). The preliminary results, based on an extrapolation of literature values for the cliff and pond distribution, show that while the debris-covered glaciers do undergo lower emergence velocity, this alone does not solve the anomaly. On the other hand, the effect of cliffs and ponds and the effect of thin debris are each sufficient to explain this anomaly (Fig. 6.S3).
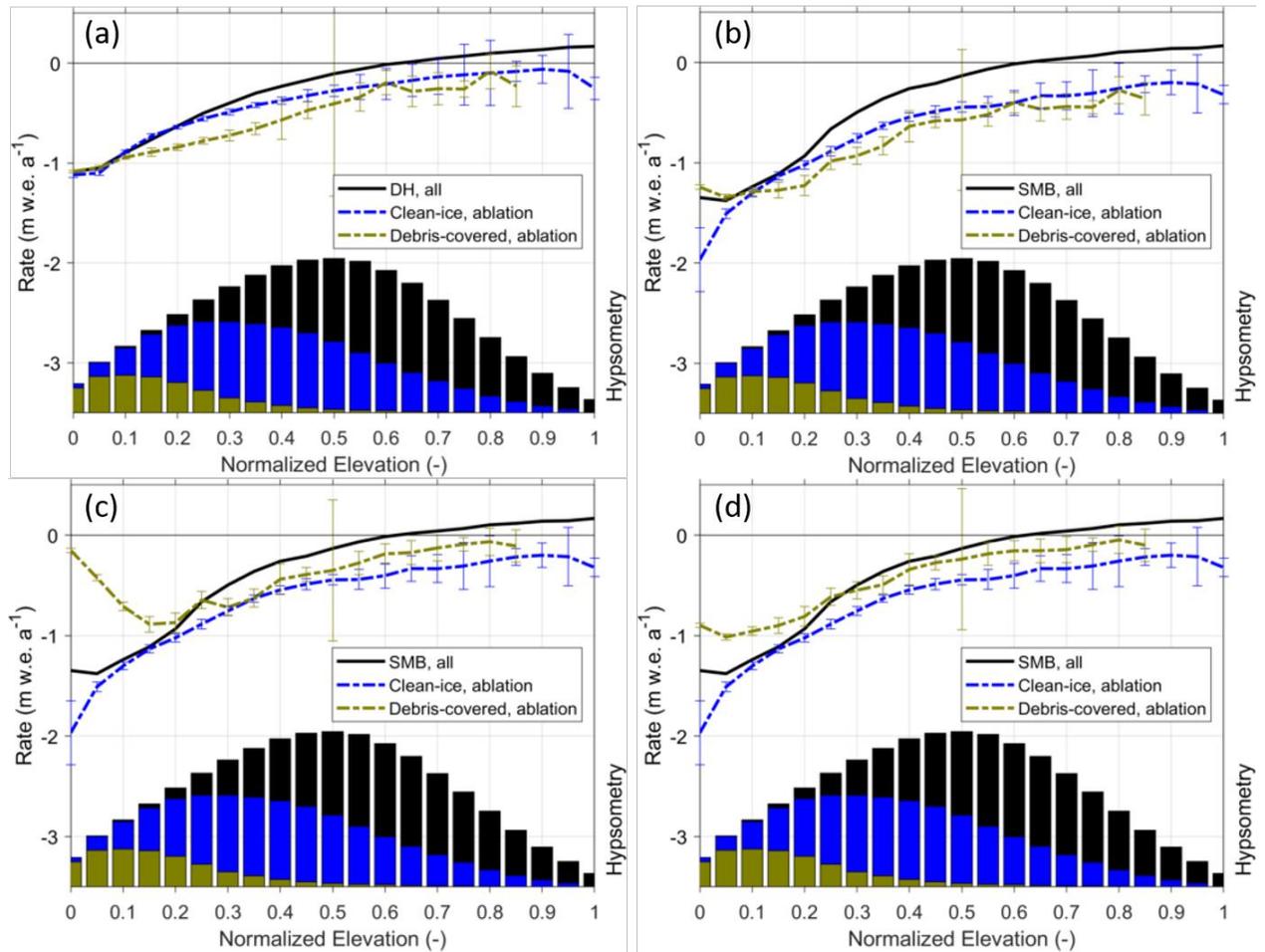
Figure 6.S3: *Thinning rates of debris-covered and debris-free glaciers as a function of normalised elevation (a) without any changes, (b) after removal of the emergence velocity component, (c) after*

removal of the cliff and pond melt and (d) after the removal of thin debris melt. Figure from Miles et al. (in prep) presented at EGU 2022.

6.3.3. Hydrology of debris-covered glaciers

This work aims at characterising the hydrological regime of debris-covered glaciers and how it differs from that of debris-free glaciers (Miles et al., 2020). A detailed study of the hydrological regime of the debris-covered Miage Glacier has already highlighted major elements which include the co-existence of efficient drainage from the debris-free part of the glaciers, and of non-efficient drainage from the thickly debris-covered area (Fyffe et al., 2019; Miles et al., 2020). Further work in which I was involved during this thesis aimed at exploring whether this influence of debris-cover was visible in the hydrographs of mountain streams distributed across Switzerland. While the main control on the hydrographs was related to the overall glacierized area in the catchments, debris cover still seemed to have an amplitude reduction effect in addition to maintaining longer lag-times further into the ablation season (Willi, 2021).

During the field campaigns of this thesis, a lot of work was also invested to test the validity of the results from Fyffe et al., (2019), at other sites (Fyffe et al., *in prep*, Table 6.S1). These included the installation of gauging stations at the glaciers' termini, repeated dye injections and the monitoring of the water level of supraglacial ponds (Fig. 6.S4). Such a database will be invaluable to improve the representation of the hydrology of debris-covered glaciers (Miles et al., 2020).
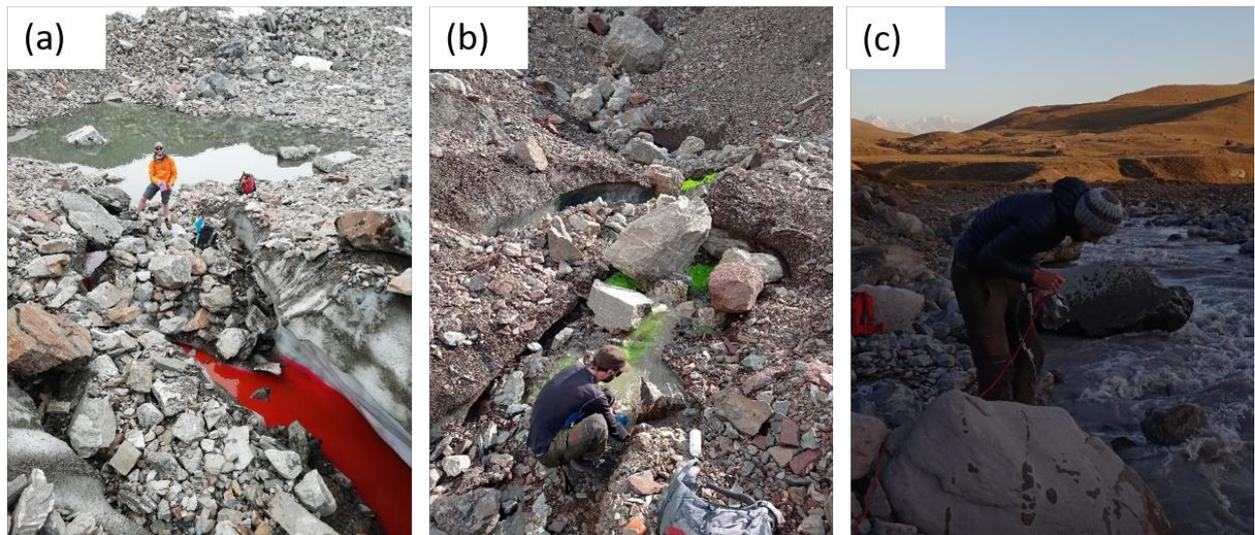
Figure 6.S4: *Dye tracing experiments on (a) 24K and (b) Kyzylsu Glaciers. (c) Discharge measurements in the proglacial stream of Kyzylsu Glacier. Image credit: Marin Kneib.*

Table 6.S1: *Field campaigns on debris-covered glaciers that I participated in as part of this PhD thesis, and measurements taken for complementary and future work.*

Where	When	Measurements taken		
		Glacier melt and dynamics	**Hydrology**	**Meteorology**

Langtang Glacier, Central Nepal	05/2019 and 11/2019	1. Time-lapse photogrammetry 2. UAV flights (incl. thermal) 3. Ablation stakes 4. Debris thickness 5. Firn core extraction	1. Gauging station in proglacial stream 2. Dye injections 3. Water level of supraglacial ponds	1. On-glacier AWS installation 2. Heat conductivity in debris 3. Temperature lapse-rates
24K Glacier, Eastern Tibet	06/2019 and 10/2019	1. Time-lapse photogrammetry 2. UAV flights (incl. thermal) 3. Ablation stakes 4. Debris thickness 5. Ice thickness (with GPR)	1. Gauging station in proglacial stream 2. Dye injections	1. On-glacier AWS checking 2. Heat conductivity in debris
Zmutt Glacier, Swiss Alps	3 visits between 06/2020 and 09/2020	1. Time-lapse photogrammetry 2. UAV flights		
Kyzylsu Glacier, Tajikistan	06/2021 and 09/2021	1. Time-lapse photogrammetry 2. UAV flights 3. Ablation stakes 4. Debris thickness 5. Moraine dating	1. Gauging station in proglacial stream 2. Dye injections 3. Water level of supraglacial ponds	1. On-glacier AWS installation 2. Heat conductivity in debris 3. Temperature lapse-rates 4. Snow measurements (snow stakes, pluviometer)
Satopanth Glacier, India	Planned for 09/2022	1. Long-term repeat photography 2. UAV flights 3. Debris thickness 4. Ablation stakes 5. Time-lapse photogrammetry	1. Gauging station in proglacial stream	

Chapter 7: Curriculum Vitae

Marin KNEIB – PhD student, HIMAL group, WSL, ETHZ

1.   Personal information

Date of birth	12 May 1995, Cambridge (UK)
Nationality	French
Address	Schützengraben 13, 8200 Schaffhausen
Phone number	(+33)6 52 65 94 10
E-mail	marin.kneib@wsl.ch
ORCID	0000-0002-2420-0475

2.   Education

Since 10/2018   PhD, ETH Zürich, WSL (Swiss federal institute for forest, snow and landscape).
09/2015 – 07/2018   Master in executive engineering, Mines ParisTech (Paris).
09/2014 – 07/2015   Bachelor in executive engineering, Mines ParisTech (Paris).
09/2012 – 07/2014   Preparatory school, Lycée du Parc (Lyon).
07/2012   French Scientific Baccalaureate, Lycée Lacordaire (Marseille).

3.   Employment history

Since 10/2018   PhD student (WSL, ETHZ), Zürich
01/2018 – 09/2018   Master project, (EPFL), Lausanne
03/2017 – 09/2017   Scientific assistant (ETHZ), Zürich
08/2016 – 02/2017   Project officer, French Development Agency (AFD), Nairobi, Kenya
09/2015 – 02/2016   Scientific assistant (Caltech), Pasadena, California

4.   Approved research projects

06/2022   CAIRN: Contribution of avalanches to glacier mass balance. PI, 108 kCHF (SNSF)
04/2021   HATHI: Historical archives to monitor long-term evolution of Himalayan debris-covered glaciers. PI, 12 kCHF (SPI).

5.   Supervision of junior researchers

02/2022 – 09/2022   Shayna Lindemann (Master thesis, ETH Zürich), co-superision with F. Pellicciotti and C. Fyffe.
01/2021 – 10/2021   Seraina Walz (Master thesis, University of Zürich), co-supervision with F. Pellicciotti and E. Miles.
02/2021 – 07/2021   Raphaël Willi (Master thesis, ETH Zürich), co-supervision with F. Pellicciotti and C. Fyffe.
01/2019 – 07/2019   Simone Jola (Internship, University of Lausanne), co-supervision with F. Pellicciotti and E. Miles.

6.   Teaching activities

06 & 09/2021   Training of young Tajik scientists on field monitoring of debris-covered glaciers.
09/2014 – 12/2018   Tutoring in Mathematics, Physics and Chemistry, high-school level.

7. Scientific outreach activities

2021/22	Supervision of glaciology-related experiments for an introduction to physics class (11-12 years old), Lyon, France.
05/2021	Participation in a radio broadcast on The Future of glaciers in High Asia, la RTS, Switzerland
08/2020	Oral presentation on the impact of climate change on glaciers (public event), Les Contamines, France.

8. Scientific reviewing

Since 01/2021	Reviewer for The Cryosphere, Journal of Glaciology, Frontiers in Earth Science, Geocarto International and GIScience & Remote Sensing

9. Prizes, awards

05/2020	Fieldwork grant of the Swiss Snow, Ice and Permafrost Society (600 CHF) to study the dynamics of ice cliffs on Zmutt Glacier, Switzerland.

10. Personal skills

Languages   French (native), English (fluent), German (Highly proficient), Spanish (Good)

Fieldwork

09/2022	India (expedition leader)
07 & 09/2021	Tajikistan, (responsible for the planning of the field campaigns)
06 & 10/2019	Tibet, (responsible for the planning and expedition leader of the 2nd field campaign)
05 & 11/2019	Nepal
07/2017	Northwest Greenland
Since 05/2017	Swiss and French Alps (leader of several multi-day field campaigns).

Computer skills

Programing	R, Matlab, Python
Software	QGIS, AMES Stereo Pipeline, Agisoft Metashape, Google Earth Engine

Mountaineering

Alpinist, climber, trail runner and ski mountaineer. Numerous expeditions throughout the world.

International culture   French, more than two years spent in the US, travels in High Mountain Asia, Canada, Madagascar, East Africa, Peru, Chile, Greenland, Eastern Europe.

Volunteering

06/2020 – 06/2022	Solinetz, Urdorf. Organizing social lunches for migrants.
10/2014 – 09/2016	Association Pichac Kuna, Paris. Protection of alpine ecosystems in Peru.
11/2014 – 07/2016	Association Rivotra, Paris. Raising awareness of Madagascan children on health, typhoons and protection of the environment.
09/2011 – 05/2013	Association Massabielle, Marseille. Tutoring at elementary school level in the suburbs of Marseille.
07/2004 – 07/2011	Scout.

09/2008 – 07/2009   Club des Chaperons Verts, Marseille. Raising awareness of primary school children to climate change.

11.   Publications in peer-reviewed scientific journals

First author publications (PhD)

1.   **Kneib M.,** Fyffe, C., Miles, E.S., Lindemann, S., Shaw, T., Buri, P., McCarthy, M., Ouvry, B., Sato, Y., Kraaijenbrink, P.D.A., Chuanxi, Z., Molnar, P., Vieli, A., Yang, W., Pellicciotti, F. (in prep.). Ice cliff distribution and characteristics on debris-covered glaciers.

2.   **Kneib, M.,** Miles, E.S., Buri, P., Fugger, S., McCarthy, M., Shaw, T., Chuanxi, Z., Truffer, M., Westoby, M., Yang, W., Pellicciotti, F. (submitted to The Cryosphere). Sub-seasonal variability of supraglacial ice cliff melt rates and associated processes from time-lapse photogrammetry. https://doi.org/10.5194/tc-2022-81

3.   **Kneib, M.,** Miles, E. S., Buri, P., Molnar, P., McCarthy, M., Fugger, S., & Pellicciotti, F. (2021). Interannual Dynamics of Ice Cliff Populations on Debris-Covered Glaciers from Remote Sensing Observations and Stochastic Modeling. Journal of Geophysical Research: Earth Surface. https://doi.org/10.1029/2021JF006179

4.   **Kneib,** M., Miles, E. S., Jola, S., Buri, P., Herreid, S., Bhattacharya, A., Watson, C. S., Bolch, T., Quincey, D., & Pellicciotti, F. (2020). Mapping ice cliffs on debris-covered glaciers using multispectral satellite images. Remote Sensing of Environment, 112201. https://doi.org/10.1016/j.rse.2020.112201

First author publications (prior PhD)

5.   **Kneib, M.,** Cauvy-Fraunié, S., Escoffier, N., Boix Canadell, M., Horgby, & Battin, T. J. (2020). Glacier retreat changes diurnal variation intensity and frequency of hydrologic variables in Alpine and Andean streams. Journal of Hydrology, 583. https://doi.org/10.1016/j.jhydrol.2020.124578

Co-authored publications (PhD)

6.   Shaw, T., Miles, E.S., Chen, D., Jouberton, A**., Kneib, M.,** Fugger, F., Ou, T., Lai, H.W., Fujita, K., Yang, W., Fatichi, S., Pellicciotti, F. (submitted to Environmental Research Letters). Multi-Decadal Monsoon Characteristics and Glacier Response in High Mountain Asia.

7.   McCarthy, M., Miles, E.S., **Kneib, M.,** Buri, P., Fugger, S., & Pellicciotti, F. (submitted to Communications in Earth and Environment). Supraglacial debris thickness and supply rate in High-Mountain Asia. https://eartharxiv.org/repository/view/2906/

8.   Menenti, M., Li, X., Jia, L., Yang, K., Pellicciotti, F., Mancini, M., Shi, J., Escorihuela, M.J., Zheng, C., Chen, Q., Lu, J., Zhou, J., Hu, G., Ren, S., Zhang, J., Liu, Q., Qiu, Y., Huang, C., Zhou, J., Han, X., Pan, X., Li, H., Wu, Y., Ding, B., Yang, W., Buri, P., McCarthy, M.J., Miles, E.S., Shaw, T.E., Ma, C., Zhou, Y., Corbari, C., Li, R., Zhao, T., Stefan, V., Gao, Q., Zhang, J., Xie, Q., Wang, N., Sun, Y., Mo, X., Jia, J., Jouberton, A.P., **Kneib, M.,** Fugger, S., Paciolla, N., & Paolini, G. (2021). Multi-Source Hydrological Data Products to Monitor High Asian River Basins and Regional Water Security. Remote Sensing, 13(24), 5122. https://doi.org/10.3390/rs13245122

9.   Ren, S., Miles, E. S., Jia, L., Menenti, **M., Kneib,** M., Buri, P., McCarthy, M., Shaw, T., Yang, W., & Pellicciotti, F. (2021). Anisotropy Parameterization Development and Evaluation for

Glacier Surface Albedo Retrieval from Satellite Observations. Remote Sensing, Vol. 13, Page 1714, 13(9), 1714. https://doi.org/10.3390/rs13091714

10.	Miles, E., McCarthy, M., Dehecq, A., **Kneib, M.,** Fugger, S., & Pellicciotti, F. (2021). Health and sustainability of glaciers in High Mountain Asia. Nature Communications 12:1, 12(1), 1–10. https://doi.org/10.1038/s41467-021-23073-4

Co-authored publications (prior PhD)

11.	Jouvet, G., Weidmann, Y., **Kneib, M.,** Detert, M., Seguinot, J., Sakakibara, D., & Sugiyama, S. (2018). Short-lived ice speed-up and plume water flow captured by a VTOL UAV give insights into subglacial hydrological system of Bowdoin Glacier. Remote Sensing of Environment, 217, 389–399. https://doi.org/10.1016/j.rse.2018.08.027

## 12.	Contributions to conferences (only first author contributions listed)

1.	**M. Kneib,** E.S. Miles, P. Buri, S. Fugger, M. McCarthy, T. Shaw, Z. Chuanxi, M. Truffer, M. Westoby, W. Yang, F. Pellicciotti, Sub-seasonal evolution of ice cliffs captured with time-lapse photogrammetry, 2022, WSL scientific symposium in memory of Koni Steffen, Davos, Switzerland, Poster.

2.	**M. Kneib,** E.S. Miles, P. Buri, S. Fugger, M. McCarthy, T. Shaw, Z. Chuanxi, M. Truffer, M. Westoby, W. Yang, F. Pellicciotti, Sub-seasonal evolution of ice cliffs captured with time-lapse photogrammetry, 2022, EGU General Assembly 2022, Vienna, Austria, Talk.

3.	**M. Kneib,** E.S. Miles, S. Jola, S. Walz, P. Buri, S. Herreid, A. Bhattacharya, C.S. Watson, T. Bolch, D. Quincey, F. Pellicciotti, Mapping Ice Cliff Distribution on Debris-Covered Glaciers in High Mountain Asia, 2021, Dragon 2021 Symposium, online, Talk.

4.	**M. Kneib,** E.S. Miles, P. Buri, P. Molnar, T.E. Shaw, M. McCarthy, S. Fugger, F. Pellicciotti, A stochastic birth and death model to represent the evolution of ice cliff population and their total contribution to melt at the glacier scale, 2020, AGU Fall Meeting, online, Talk.

5.	**M. Kneib,** P. Buri, E.S. Miles, F. Brun, P. Wagnon, F. Pellicciotti, Modeling elevation and aspect controls of ice-cliffs on debris-covered glaciers in High Mountain Asia, 2019, IUGG, Montréal, Canada, Poster.

6.	**M. Kneib,** M. Detert, M. Funk, G. Jouvet, Y. Weidmann, Monitoring the water flow of meltwater plumes at the front of Bowdoin Glacier, Northwest Greenland, by UAV photogrammetry and Particle Image Velocimetry, 2017, High Altitudes meet High Latitudes: Globalizing Polar Issues, Crans-Montana, Switzerland, Poster.

## 13.	Other artefacts with documented use

Datasets

1.	**Kneib, M.,** Miles, E. S., Buri, P., Molnar, P., McCarthy, M., Fugger, S., & Pellicciotti, F. (2021). Data and Scripts for Interannual Dynamics of Ice Cliff Populations on Debris-Covered Glaciers from Remote Sensing Observations and Stochastic Modeling (Version 1.0). Zenodo. https://doi.org/10.5281/zenodo.4632840

2.   Miles, E., McCarthy, M., Dehecq, A., **Kneib, M.,** Fugger, S., & Pellicciotti, F. (2020). Results for "Health and sustainability of glaciers in High Mountain Asia." https://doi.org/10.5281/ZENODO.4585622

3.   **Kneib, M.,** Miles, E. S., Jola, S., Buri, P., Herreid, S., Bhattacharya, A., Watson, C. S., Bolch, T., Quincey, D., & Pellicciotti, F. (2020). Data for "Mapping ice cliffs on debris-covered glaciers using multispectral satellite images." https://doi.org/10.5281/ZENODO.4897357

Software

1.   **Kneib, M.** (2021). Code for tracking of ice cliffs. Github. https://github.com/MarinKneib/CliffTracking

Bibliography

Altena, B., Kääb, A., 2020. Satellite remote sensing of ice cliff migration. EGUGA 5057.

Anderson, L.S., Anderson, R., Buri, P., Armstrong, W., 2019a. Debris cover and the thinning of Kennicott Glacier, Alaska, Part A:in situ mass balance measurements. Cryosph. Discuss. 1–28. https://doi.org/10.5194/tc-2019-174

Anderson, L.S., Anderson, R.S., 2018. Debris thickness patterns on debris-covered glaciers. Geomorphology 311, 1–12. https://doi.org/10.1016/j.geomorph.2018.03.014

Anderson, L.S., Anderson, R.S., 2016. Modeling debris-covered glaciers: response to steady debris deposition. Cryosph. 10, 1105–1124. https://doi.org/10.5194/tc-10-1105-2016

Anderson, L.S., Armstrong, W., Anderson, R., Buri, P., 2019b. Debris cover and the thinning of Kennicott Glacier, Alaska, Part B: ice cliff delineation and distributed melt estimates. Cryosph. Discuss. 1–29. https://doi.org/10.5194/tc-2019-177

Anderson, L.S., Armstrong, W.H., Anderson, R.S., Buri, P., 2021a. Debris cover and the thinning of Kennicott Glacier, Alaska: In situ measurements, automated ice cliff delineation and distributed melt estimates. Cryosphere 15, 265–282. https://doi.org/10.5194/tc-15-265-2021

Anderson, L.S., Armstrong, W.H., Anderson, R.S., Scherler, D., Petersen, E., 2021b. The Causes of Debris-Covered Glacier Thinning: Evidence for the Importance of Ice Dynamics From Kennicott Glacier, Alaska. Front. Earth Sci. 0, 723. https://doi.org/10.3389/FEART.2021.680995

Anderson, R.S., 2000. A model of ablation-dominated medial moraines and the generation of debris-mantled glacier snouts. J. Glaciol. 46, 459–469. https://doi.org/10.3189/172756500781833025

Armstrong, L., Lacelle, D., Fraser, R.H., Kokelj, S., Knudby, A., 2018. Thaw slump activity measured using stationary cameras in time-lapse and Structure-from-Motion photogrammetry. Arct. Sci. 4, 827–845. https://doi.org/10.1139/as-2018-0016

Ayala, A., Pellicciotti, F., MacDonell, S., McPhee, J., Vivero, S., Campos, C., Egli, P., 2016. Modelling the hydrological response of debris-free and debris-covered glaciers to present climatic conditions in the semiarid Andes of central Chile. Hydrol. Process. 30, 4036–4058. https://doi.org/10.1002/hyp.10971

Bailey, N.T., 1968. Stochastic birth, death and migration processes for spatially distributed populations. Biometrika 55, 189–198. https://doi.org/10.1093/biomet/55.1.189

Banerjee, A., 2017. Brief communication: Thinning of debris-covered and debris-free glaciers in a warming climate. Cryosphere 11, 133–138. https://doi.org/10.5194/tc-11-133-2017

Bartlett, O.T., Ng, F.S.L., Rowan, A. V., 2020. Morphology and evolution of supraglacial hummocks on debris-covered Himalayan glaciers. Earth Surf. Process. Landforms esp.5043. https://doi.org/10.1002/esp.5043

Bemis, S.P., Micklethwaite, S., Turner, D., James, M.R., Akciz, S., Thiele, S.T., Bangash, H.A., 2014. Ground-based and UAV-Based photogrammetry: A multi-scale, high-resolution mapping tool for structural geology and paleoseismology. J. Struct. Geol. 69, 163–178. https://doi.org/10.1016/j.jsg.2014.10.007

Benn, D.I., Bolch, T., Hands, K., Gulley, J., Luckman, A., Nicholson, L.I., Quincey, D., Thompson, S., Toumi, R., Wiseman, S., 2012. Response of debris-covered glaciers in the Mount Everest region to recent warming, and implications for outburst flood hazards. Earth-Science Rev. https://doi.org/10.1016/j.earscirev.2012.03.008

Benn, D.I., Lehmkuhl, F., 2000. Mass balance and equilibrium-line altitudes of glaciers in high-mountain environments. Quat. Int. 65–66, 15–29. https://doi.org/10.1016/S1040-

6182(99)00034-8

Benn, D.I., Thompson, S., Gulley, J., Mertes, J., Luckman, A., Nicholson, L., 2017. Structure and evolution of the drainage system of a Himalayan debris-covered glacier, and its relationship with patterns of mass loss. Cryosph. 11. https://doi.org/10.5194/tc-11-2247-2017

Benn, D.I., Wiseman, S., Hands, K.A., 2001. Growth and drainage of supraglacial lakes on debrismantled Ngozumpa Glacier, Khumbu Himal, Nepal. J. Glaciol. 47, 626–638. https://doi.org/10.3189/172756501781831729

Berthier, E., Vincent, C., Magnússon, E., Gunnlaugsson, Á.Þ., Pitte, P., Le Meur, E., Masiokas, M., Ruiz, L., Pálsson, F., Belart, J.M.C., Wagnon, P., 2014. Glacier topography and elevation changes derived from Pléiades sub-meter stereo images. Cryosph. 8, 2275–2291. https://doi.org/10.5194/tc-8-2275-2014

Beyer, R.A., Alexandrov, O., McMichael, S., 2018. The Ames Stereo Pipeline: NASA's Open Source Software for Deriving and Processing Terrain Data. Earth Sp. Sci. 5, 537–548. https://doi.org/10.1029/2018EA000409

Bhambri, R., Bolch, T., Chaujar, R.K., Kulshreshtha, S.C., 2011. Glacier changes in the Garhwal Himalaya, India, from 1968 to 2006 based on remote sensing. J. Glaciol. 57, 543–556. https://doi.org/10.3189/002214311796905604

Bhambri, R., Hewitt, K., Kawishwar, P., Pratap, B., 2017. Surge-type and surge-modified glaciers in the Karakoram. Sci. Rep. 7, 1–14. https://doi.org/10.1038/s41598-017-15473-8

Bliss, A., Hock, R., Radić, V., 2014. Global response of glacier runoff to twenty-first century climate change. J. Geophys. Res. Earth Surf. 119, 717–730. https://doi.org/10.1002/2013JF002931

Bolch, T., Buchroithner, M.F., Peters, J., Baessler, M., Bajracharya, S., 2008. Identification of glacier motion and potentially dangerous glacial lakes in the Mt. Everest region/Nepal using spaceborne imagery. Nat. Hazards Earth Syst. Sci. 8, 1329–1340. https://doi.org/10.5194/nhess-8-1329-2008

Bolch, T., Kulkarni, A., Kääb, A., Huggel, C., Paul, F., Cogley, J.G., Frey, H., Kargel, J.S., Fujita, K., Scheel, M., Bajracharya, S., Stoffel, M., 2012. The state and fate of himalayan glaciers. Science (80-.). https://doi.org/10.1126/science.1215828

Bolch, T., Pieczonka, T., Benn, D.I., 2011. Multi-decadal mass loss of glaciers in the Everest area (Nepal Himalaya) derived from stereo imagery. Cryosph. 5, 349–358. https://doi.org/10.5194/tc-5-349-2011

Bonekamp, P.N.J., van Heerwaarden, C.C., Steiner, J.F., Immerzeel, W.W., 2020. Using 3D turbulence-resolving simulations to understand the impact of surface properties on the energy balance of a debris-covered glacier. Cryosph. 14, 1611–1632. https://doi.org/10.5194/tc-14-1611-2020

Brun, F., Berthier, E., Wagnon, P., Kääb, A., Treichler, D., 2017. A spatially resolved estimate of High Mountain Asia glacier mass balances from 2000 to 2016. Nat. Geosci. https://doi.org/10.1038/ngeo2999

Brun, F, Berthier, E., Wagnon, P., Kääb, A., Treichler, D., 2017. Elevation changes of High Mountain Asia from 2000 to 2016, links to GeoTIFFs. PANGAEA. https://doi.org/https://doi.org/10.1594/PANGAEA.876545

Brun, F., Buri, P., Miles, E.S., Wagnon, P., Steiner, J., Berthier, E., Ragettli, S., Kraaijenbrink, P., Immerzeel, W.W., Pellicciotti, F., 2016. Quantifying volume loss from ice cliffs on debris-covered glaciers using high-resolution terrestrial and aerial photogrammetry. J. Glaciol. https://doi.org/10.1017/jog.2016.54

Brun, F., Wagnon, P., Berthier, E., Jomelli, V., Maharjan, S.B., Shrestha, F., Kraaijenbrink, P.D.A., 2019. Heterogeneous Influence of Glacier Morphology on the Mass Balance Variability in High

Mountain Asia. J. Geophys. Res. Earth Surf. 124, 1331–1345. https://doi.org/10.1029/2018JF004838

Brun, F., Wagnon, P., Berthier, E., Shea, J.M., Immerzeel, W.W., Kraaijenbrink, P.D.A., Vincent, C., Reverchon, C., Shrestha, D., Arnaud, Y., 2018. Ice cliff contribution to the tongue-wide ablation of Changri Nup Glacier, Nepal, central Himalaya. Cryosph. 12, 3439–3457. https://doi.org/10.5194/tc-12-3439-2018

Burger, F., Ayala, A., Farias, D., Thomas, |, Shaw, E., Macdonell, S., Brock, B., Mcphee, J., Pellicciotti, F., 2018. Interannual variability in glacier contribution to runoff from a high-elevation Andean catchment: understanding the role of debris cover in glacier hydrology. https://doi.org/10.1002/hyp.13354

Buri, P., Miles, E.S., Steiner, J.F., Immerzeel, W.W., Wagnon, P., Pellicciotti, F., 2016a. A physically based 3-D model of ice cliff evolution over debris-covered glaciers. J. Geophys. Res. Earth Surf. 121, 2471–2493. https://doi.org/10.1002/2016JF004039

Buri, P., Miles, E.S., Steiner, J.F., Immerzeel, W.W., Wagnon, P., Pellicciotti, F., 2016b. A physically based 3-D model of ice cliff evolution over debris-covered glaciers. J. Geophys. Res. Earth Surf. 121, 2471–2493. https://doi.org/10.1002/2016JF004039

Buri, P., Miles, E.S., Steiner, J.F., Ragettli, S., Pellicciotti, F., 2021. Supraglacial Ice Cliffs Can Substantially Increase the Mass Loss of Debris-Covered Glaciers. Geophys. Res. Lett. 48. https://doi.org/10.1029/2020GL092150

Buri, P., Pellicciotti, F., 2018. Aspect controls the survival of ice cliffs on debris-covered glaciers. Proc. Natl. Acad. Sci. 115, 4369–4374. https://doi.org/10.1073/pnas.1713892115

Buri, P., Pellicciotti, F., Steiner, J.F., Miles, E.S., Immerzeel, W.W., 2016c. A grid-based model of backwasting of supraglacial ice cliffs on debris-covered glaciers. Ann. Glaciol. 57, 199–211. https://doi.org/10.3189/2016AoG71A059

Casey, K.A., Kääb, A., Benn, D.I., 2012. Geochemical characterization of supraglacial debris via in situ and optical remote sensing methods: a case study in Khumbu Himalaya, Nepal. Cryosph. 6, 85–100. https://doi.org/10.5194/tc-6-85-2012

Cathles, L.M., Abbot, D.S., Bassis, J.N., MacAyeal, D.R., 2011. Modeling surface-roughness/solar-ablation feedback: application to small-scale surface channels and crevasses of the Greenland ice sheet. Ann. Glaciol. 52, 99–108. https://doi.org/10.3189/172756411799096268

Cauvy-Fraunié, S., Dangles, O., 2019. A global synthesis of biodiversity responses to glacier retreat. Nat. Ecol. Evol. 3, 1675–1685. https://doi.org/10.1038/s41559-019-1042-8

Chen, W., Fukui, H., Doko, T., Gu, X., 2013. Improvement of glacial lakes detection under shadow environment using ASTER data in Himalayas, Nepal. Chinese Geogr. Sci. 23, 216–226. https://doi.org/10.1007/s11769-012-0584-3

Chinn, T.J.H., Dillon, A., 1987. Observations on a Debris-Covered Polar Glacier "Whisky Glacier", James Ross Island, Antarctic Peninsula, Antarctica. J. Glaciol. 33, 300–310. https://doi.org/10.3189/s002214300000887x

Chudley, T.R., Willis, I.C., 2019. Glacier surges in the north-west West Kunlun Shan inferred from 1972 to 2017 Landsat imagery. J. Glaciol. 65, 1–12. https://doi.org/10.1017/jog.2018.94

Colgan, W., Rajaram, H., Abdalati, W., McCutchan, C., Mottram, R., Moussavi, M.S., Grigsby, S., 2016. Glacier crevasses: Observations, models, and mass balance implications. Rev. Geophys. https://doi.org/10.1002/2015RG000504

Compagno, L., Huss, M., Miles, E.S., McCarthy, M.J., Zekollari, H., Dehecq, A., Pellicciotti, F., Farinotti, D., 2022. Modelling supraglacial debris-cover evolution from the single-glacier to the regional scale: an application to High Mountain Asia. Cryosph. 16, 1697–1718.

https://doi.org/10.5194/tc-16-1697-2022

Conrad, O., Bechtel, B., Bock, M., Dietrich, H., Fischer, E., Gerlitz, L., Wehberg, J., Wichmann, V., Böhner, J., 2015. System for Automated Geoscientific Analyses (SAGA) v. 2.1.4. Geosci. Model Dev. 8, 1991–2007. https://doi.org/10.5194/gmd-8-1991-2015

Cuffey, C., Paterson, W.S.B., 2010. The Physics of Glaciers.

Dehecq, A., Gourmelen, N., Gardner, A.S., Brun, F., Goldberg, D., Nienow, P.W., Berthier, E., Vincent, C., Wagnon, P., Trouvé, E., 2019. Twenty-first century glacier slowdown driven by mass loss in High Mountain Asia. Nat. Geosci. 12, 22–27. https://doi.org/10.1038/s41561-018-0271-9

Deline, P., 2005. Change in surface debris cover on Mont Blanc massif glaciers after the "Little Ice Age" termination, The Holocene. https://doi.org/10.1191/0959683605hl809rr

Dice, L.R., 1945. Measures of the Amount of Ecologic Association Between Species. Ecology 26, 297–302. https://doi.org/10.2307/1932409

Egli, P.E., Belotti, B., Ouvry, B., Irving, J., Lane, S.N., 2021. Subglacial Channels, Climate Warming, and Increasing Frequency of Alpine Glacier Snout Collapse. Geophys. Res. Lett. 48. https://doi.org/10.1029/2021GL096031

Evatt, G.W., Abrahams, I.D., Heil, M., Mayer, C., Kingslake, J., Mitchell, S.L., Fowler, A.C., Clark, C.D., 2015. Glacial melt under a porous debris layer, in: Journal of Glaciology. International Glaciology Society, pp. 825–836. https://doi.org/10.3189/2015JoG14J235

Falaschi, D., Rivera, A., Lo Vecchio Repetto, A., Moragues, S., Villalba, R., Rastner, P., Zeller, J., Salcedo, A.P., 2021. Evolution of Surface Characteristics of Three Debris-Covered Glaciers in the Patagonian Andes From 1958 to 2020. Front. Earth Sci. 9. https://doi.org/10.3389/feart.2021.671854

Farinotti, D., Magnusson, J., Huss, M., Bauder, A., 2010. Snow accumulation distribution inferred from time-lapse photography and simple modelling. Hydrol. Process. 24, 2087–2097. https://doi.org/10.1002/HYP.7629

Ferguson, J., Vieli, A., 2020. Modelling steady states and the transient response of debris-covered glaciers. Cryosph. Discuss. [preprint]. https://doi.org/10.5194/tc-2020-228

Ferguson, J.C., Vieli, A., 2021. Modelling steady states and the transient response of debris-covered glaciers. Cryosph. 15, 3377–3399. https://doi.org/10.5194/tc-15-3377-2021

Filhol, S., Perret, A., Girod, L., Sutter, G., Schuler, T. V., Burkhart, J.F., 2019. Time-Lapse Photogrammetry of Distributed Snow Depth During Snowmelt. Water Resour. Res. 55, 7916–7926. https://doi.org/10.1029/2018WR024530

Foster, L.A., Brock, B.W., Cutler, M.E.J., Diotri, F., 2012. A physically based method for estimating supraglacial debris thickness from thermal band remote-sensing data. J. Glaciol. 58, 677–691. https://doi.org/10.3189/2012JoG11J194

Fowler, A.C., Mayer, C., 2017. The formation of ice sails. Geophys. Astrophys. Fluid Dyn. 111, 411–428. https://doi.org/10.1080/03091929.2017.1370092

Fugger, S., Fyffe, C., Fatichi, S., Miles, E.S., McCarthy, M., Shaw, T.E., Ding, B., Yang, W., Wagnon, P., Immerzeel, W., Liu, Q., Pelliccotti, F., 2022. Understanding monsoon controls on the energy and mass balance of Himalayan glacier (in review). Cryosph.

Fyffe, C.L., Brock, B.W., Kirkbride, M.P., Mair, D.W.F., Arnold, N.S., Smiraglia, C., Diolaiuti, G., Diotri, F., 2019. Do debris-covered glaciers demonstrate distinctive hydrological behaviour compared to clean glaciers? J. Hydrol. 570, 584–597. https://doi.org/10.1016/j.jhydrol.2018.12.069

Fyffe, C.L., Woodget, A.S., Kirkbride, M.P., Deline, P., Westoby, M.J., Brock, B.W., 2020a. Processes at the margins of supraglacial debris cover: Quantifying dirty ice ablation and debris redistribution. Earth Surf. Process. Landforms 45, 2272–2290. https://doi.org/10.1002/esp.4879

Fyffe, C.L., Woodget, A.S., Kirkbride, M.P., Deline, P., Westoby, M.J., Brock, B.W., 2020b. Processes at the margins of supraglacial debris cover: quantifying dirty ice ablation and debris redistribution. Earth Surf. Process. Landforms 45, 2272–2290. https://doi.org/10.1002/esp.4879

Gardelle, J., Arnaud, Y., Berthier, E., 2011. Contrasted evolution of glacial lakes along the Hindu Kush Himalaya mountain range between 1990 and 2009. Glob. Planet. Change 75, 47–55. https://doi.org/10.1016/j.gloplacha.2010.10.003

Gardelle, J., Berthier, E., Arnaud, Y., Kääb, A., 2013. Region-wide glacier mass balances over the Pamir-Karakoram-Himalaya during 1999-2011. Cryosphere. https://doi.org/10.5194/tc-7-1263-2013

Gardner, A.S., Moholdt, G., Cogley, J.G., Wouters, B., Arendt, A.A., Wahr, J., Berthier, E., Hock, R., Pfeffer, W.T., Kaser, G., Ligtenberg, S.R.M., Bolch, T., Sharp, M.J., Hagen, J.O., van den Broeke, M.R., Paul, F., 2013. A Reconciled Estimate of Glacier Contributions to Sea Level Rise: 2003 to 2009. Science (80-.). 340, 852–857. https://doi.org/10.1126/science.1234532

Gardner, A.S., Moholdt, G., Scambos, T., Fahnstock, M., Ligtenberg, S., Van Den Broeke, M., Nilsson, J., 2018. Increased West Antarctic and unchanged East Antarctic ice discharge over the last 7 years. Cryosphere 12, 521–547. https://doi.org/10.5194/tc-12-521-2018

Girona-Mata, M., Miles, E.S., Ragettli, S., Pellicciotti, F., 2019. High-Resolution Snowline Delineation From Landsat Imagery to Infer Snow Cover Controls in a Himalayan Catchment. Water Resour. Res. 55, 6754–6772. https://doi.org/10.1029/2019WR024935

Glazyrin, G., 1975. The formation of ablation moraines as a function of the climatological environment. Int. Assoc. Hydrol. Sci. 104, 106–110.

Goodsell, B., Hambrey, M.J., Classer, N.F., 2005. Debris transport in a temperate valley glacier: Haut Glacier d'Arolla, Valais, Switzerland. J. Glaciol. 51, 139–146. https://doi.org/10.3189/172756505781829647

Gulley, J., Benn, D.I., 2007. Structural control of englacial drainage systems in Himalayan debris-covered glaciers. J. Glaciol. 53, 399–412. https://doi.org/10.3189/002214307783258378

Gulley, J.D., Benn, D.I., Screaton, E., Martin, J., 2009. Mechanisms of englacial conduit formation and their implications for subglacial recharge. Quat. Sci. Rev. 28, 1984–1999. https://doi.org/10.1016/j.quascirev.2009.04.002

Hagg, W., Mayr, E., Mannig, B., Reyers, M., Schubert, D., Pinto, J., Peters, J., Pieczonka, T., Juen, M., Bolch, T., Paeth, H., Mayer, C., 2018. Future Climate Change and Its Impact on Runoff Generation from the Debris-Covered Inylchek Glaciers, Central Tian Shan, Kyrgyzstan. Water 10, 1513. https://doi.org/10.3390/w10111513

Hagolle, O., Huc, M., Villa Pascual, D., Dedieu, G., 2015. A Multi-Temporal and Multi-Spectral Method to Estimate Aerosol Optical Thickness over Land, for the Atmospheric Correction of FormoSat-2, LandSat, VENµS and Sentinel-2 Images. Remote Sens. 7, 2668–2691. https://doi.org/10.3390/rs70302668

Hambrey, M.J., Quincey, D.J., Glasser, N.F., Reynolds, J.M., Richardson, S.J., Clemmens, S., 2009. Sedimentological, geomorphological and dynamic context of debris-mantled glaciers, Mount Everest (Sagarmatha) region, Nepal. Quat. Sci. Rev. https://doi.org/10.1016/j.quascirev.2009.04.009

Han, H., Wang, J., Wei, J., Liu, S., 2010. Backwasting rate on debris-covered Koxkar glacier, Tuomuer mountain, China. J. Glaciol. https://doi.org/10.3189/002214310791968430

Herreid, S., 2021. What Can Thermal Imagery Tell Us About Glacier Melt Below Rock Debris? Front. Earth Sci. 0, 738. https://doi.org/10.3389/FEART.2021.681059

Herreid, S., Pellicciotti, F., 2020a. The state of rock debris covering Earth's glaciers. Nat. Geosci. 1–7. https://doi.org/10.1038/s41561-020-0615-0

Herreid, S., Pellicciotti, F., 2020b. Supplementary Information for Herreid and Pellicciotti, Nature Geoscience, 2020 (Version 1.0). Nat. Geosci. https://doi.org/http://doi.org/10.5281/zenodo.3866466

Herreid, S., Pellicciotti, F., 2018. Automated detection of ice cliffs within supraglacial debris cover. Cryosph. 12, 1811–1829. https://doi.org/10.5194/tc-12-1811-2018

Herreid, S., Pellicciotti, F., Ayala, A., Chesnokova, A., Kienholz, C., Shea, J., Shrestha, A., 2015. Satellite observations show no net change in the percentage of supraglacial debris-covered area in northern Pakistan from 1977 to 2014. J. Glaciol. 61, 524–536. https://doi.org/10.3189/2015JoG14J227

Hirschmüller, H., 2007. Stereo Processing by Semiglobal Matching and Mutual Information. IEEE Trans. Pattern Anal. Mach. Intell. 30, 328–341. https://doi.org/10.1109/TPAMI.2007.1166

How, P., Schild, K.M., Benn, D.I., Noormets, R., Kirchner, N., Luckman, A., Vallot, D., Hulton, N.R.J., Borstad, C., 2019. Calving controlled by melt-under-cutting: detailed calving styles revealed through time-lapse observations. Ann. Glaciol. 60, 20–31. https://doi.org/10.1017/aog.2018.28

Huggel, C., Kääb, A., Haeberli, W., Teysseire, P., Paul, F., 2002. Remote sensing based assessment of hazards from glacier lake outbursts: a case study in the Swiss Alps. Can. Geotech. J. 39, 316–330. https://doi.org/10.1139/t01-099

Hugonnet, R., McNabb, R., Berthier, E., Menounos, B., Nuth, C., Girod, L., Farinotti, D., Huss, M., Dussaillant, I., Brun, F., Kääb, A., 2021. Accelerated global glacier mass loss in the early twenty-first century. Nat. 2021 5927856 592, 726–731. https://doi.org/10.1038/s41586-021-03436-z

Huss, M., 2013. Density assumptions for converting geodetic glacier volume change to mass change. Cryosph. 7, 877–887. https://doi.org/10.5194/tc-7-877-2013

Huss, M., Bookhagen, B., Huggel, C., Jacobsen, D., Bradley, R.S., Clague, J.J., Vuille, M., Buytaert, W., Cayan, D.R., Greenwood, G., Mark, B.G., Milner, A.M., Weingartner, R., Winder, M., 2017. Toward mountains without permanent snow and ice. Earth's Futur. 5, 418–435. https://doi.org/10.1002/2016EF000514

Huss, M., Hock, R., 2018. Global-scale hydrological response to future glacier mass loss. Nat. Clim. Chang. 8, 135–140. https://doi.org/10.1038/s41558-017-0049-x

Huss, M., Sugiyama, S., Bauder, A., Funk, M., 2007. Retreat Scenarios of Unteraargletscher, Switzerland, Using a Combined Ice-Flow Mass-Balance Model. Arctic, Antarct. Alp. Res. 422–431.

Immerzeel, W.W., Kraaijenbrink, P.D.A., Shea, J.M., Shrestha, A.B., Pellicciotti, F., Bierkens, M.F.P., De Jong, S.M., 2014. High-resolution monitoring of Himalayan glacier dynamics using unmanned aerial vehicles. Remote Sens. Environ. 150, 93–103. https://doi.org/10.1016/j.rse.2014.04.025

Immerzeel, W.W., Lutz, A.F., Andrade, M., Bahl, A., Biemans, H., Bolch, T., Hyde, S., Brumby, S., Davies, B.J., Elmore, A.C., Emmer, A., Feng, M., Fernández, A., Haritashya, U., Kargel, J.S., Koppes, M., Kraaijenbrink, P.D.A., Kulkarni, A. V., Mayewski, P.A., Nepal, S., Pacheco, P., Painter, T.H., Pellicciotti, F., Rajaram, H., Rupper, S., Sinisalo, A., Shrestha, A.B., Viviroli, D., Wada, Y., Xiao, C., Yao, T., Baillie, J.E.M., 2020. Importance and vulnerability of the world's water towers. Nature 577, 364–369. https://doi.org/10.1038/s41586-019-1822-y

Inoue, J., Yoshida, M., 1980. Ablation and Heat Exchange over the Khumbu Glacier Ablation and Heat Exchange over the Khumbu Glacier"*.

IPCC, 2019. The Ocean and Cryosphere in a Changing Climate. Cambridge University Press. https://doi.org/10.1017/9781009157964

James, M.R., Robson, S., 2014a. Sequential digital elevation models of active lava flows from ground-based stereo time-lapse imagery. ISPRS J. Photogramm. Remote Sens. 97, 160–170. https://doi.org/10.1016/j.isprsjprs.2014.08.011

James, M.R., Robson, S., 2014b. Mitigating systematic error in topographic models derived from UAV and ground-based image networks. Earth Surf. Process. Landforms 39, 1413–1420. https://doi.org/10.1002/esp.3609

James, M.R., Robson, S., 2012. Straightforward reconstruction of 3D surfaces and topography with a camera: Accuracy and geoscience application. J. Geophys. Res. Earth Surf. 117, n/a-n/a. https://doi.org/10.1029/2011JF002289

Jarosch, A.H., Gudmundsson, M.T., 2012. A numerical model for meltwater channel evolution in glaciers. Cryosph. 6, 493–503. https://doi.org/10.5194/tc-6-493-2012

Jia, M., Li, D., Colombo, R., Wang, Y., Wang, X., Cheng, T., Zhu, Y., Yao, X., Xu, C., Ouer, G., Li, H., Zhang, C., 2019. Quantifying Chlorophyll Fluorescence Parameters from Hyperspectral Reflectance at the Leaf Scale under Various Nitrogen Treatment Regimes in Winter Wheat. Remote Sens. 11, 2838. https://doi.org/10.3390/rs11232838

Johnson, P.G., 1992. Stagnant Glacier Ice, St. Elias Mountains, Yukon. Geogr. Ann. Ser. A, Phys. Geogr. 74, 13. https://doi.org/10.2307/521466

Jouberton, A., Shaw, T.E., Miles, E.S., McCarthy, M., Fugger, S., Ren, S., Dehecq, A., Yang, W., Pellicciotti, F., 2022. Warming-induced monsoon precipitation phase change intensifies glacier mass loss in the southeastern Tibetan Plateau. PNAS (in Press.

Juen, M., Mayer, C., Lambrecht, A., Han, H., Liu, S., 2014. Impact of varying debris cover thickness on ablation: A case study for Koxkar Glacier in the Tien Shan. Cryosphere 8, 377–386. https://doi.org/10.5194/tc-8-377-2014

Kääb, A., Berthier, E., Nuth, C., Gardelle, J., Arnaud, Y., 2012. Contrasting patterns of early twenty-first-century glacier mass change in the Himalayas. Nature. https://doi.org/10.1038/nature11324

Kääb, A., Bolch, T., Casey, K., Heid, T., Kargel, J., Leonard, G., Paul, F., Raup, B., 2014. Glacier mapping and monitoring based on spectral data, in: Global Land Ice Measurements from Space. pp. 75–112.

Kamp, U., Byrne, M., Bolch, T., 2011. Glacier fluctuations between 1975 and 2008 in the Greater Himalaya Range of Zanskar, southern Ladakh. J. Mt. Sci. 8, 374–389. https://doi.org/10.1007/s11629-011-2007-9

Kargel, J.S., Leonard, G.J., Shugar, D.H., Haritashya, U.K., Bevington, A., Fielding, E.J., Fujita, K., Geertsema, M., Miles, E.S., Steiner, J., Anderson, E., Bajracharya, S., Bawden, G.W., Breashears, D.F., Byers, A., Collins, B., Dhital, M.R., Donnellan, A., Evans, T.L., Geai, M.L., Glasscoe, M.T., Green, D., Gurung, D.R., Heijenk, R., Hilborn, A., Hudnut, K., Huyck, C., Immerzeel, W.W., Jiang, L., Jibson, R., Kääb, A., Khanal, N.R., Kirschbaum, D., Kraaijenbrink, P.D.A., Lamsal, D., Liu, S., Lv, M., McKinney, D., Nahirnick, N.K., Nan, Z., Ojha, S., Olsenholler, J., Painter, T.H., Pleasants, M., Pratima, K.C., Yuan, Q.I., Raup, B.H., Regmi, D., Rounce, D.R., Sakai, A., Shangguan, D., Shea, J.M., Shrestha, A.B., Shukla, A., Stumm, D., Van Der Kooij, M., Voss, K., Wang, X., Weihs, B., Wolfe, D., Wu, L., Yao, X., Yoder, M.R., Young, N., 2016. Geomorphic and geologic controls of geohazards induced by Nepal's 2015 Gorkha earthquake. Science (80-.). 351. https://doi.org/10.1126/science.aac8353

Kendall, D.G., 1948. On the Generalized "Birth-and-Death" Process. Ann. Math. Stat. 19, 1–15.

https://doi.org/10.1214/aoms/1177730285

Keshava, N., Mustard, J.F., 2002. Spectral unmixing. IEEE Signal Process. Mag. 19, 44–57. https://doi.org/10.1109/79.974727

Kienholz, C., Rich, J.L., Arendt, A.A., Hock, R., 2014. A new method for deriving glacier centerlines applied to glaciers in Alaska and northwest Canada. Cryosph. 8, 503–519. https://doi.org/10.5194/tc-8-503-2014

King, O., Turner, A.G.D., Quincey, D.J., Carrivick, J.L., 2020. Morphometric evolution of Everest region debris-covered glaciers. Geomorphology 371, 107422. https://doi.org/10.1016/j.geomorph.2020.107422

Kirkbride, M.P., Deline, P., 2013. The formation of supraglacial debris covers by primary dispersal from transverse englacial debris bands. Earth Surf. Process. Landforms 38, 1779–1792. https://doi.org/10.1002/esp.3416

Kneib-Walter, A., Lüthi, M.P., Moreau, L., Vieli, A., 2021. Drivers of Recurring Seasonal Cycle of Glacier Calving Styles and Patterns. Front. Earth Sci. 9. https://doi.org/10.3389/feart.2021.667717

Kneib, M., Miles, E., Buri, P., Fugger, S., McCarthy, M., Shaw, T., Chuanxi, Z., Truffer, M., Westoby, M., Yang, W., Pellicciotti, F., 2022. Sub-seasonal variability of supraglacial ice cliff melt rates and associated processes from time-lapse photogrammetry. Cryosph. Discuss. [preprint]. https://doi.org/10.5194/tc-2022-81

Kneib, M., Miles, E.S., Buri, P., Molnar, P., McCarthy, M., Fugger, S., Pellicciotti, F., 2021. Interannual Dynamics of Ice Cliff Populations on Debris-Covered Glaciers from Remote Sensing Observations and Stochastic Modeling. J. Geophys. Res. Earth Surf. https://doi.org/10.1029/2021JF006179

Kneib, Marin, Miles, E.S., Buri, P., Molnar, P., McCarthy, M., Fugger, S., Pellicciotti, F., 2021. Data and Scripts for Interannual Dynamics of Ice Cliff Populations on Debris-Covered Glaciers from Remote Sensing Observations and Stochastic Modeling (Version 1.0). Zenodo. https://doi.org/10.5281/zenodo.4632840

Kneib, M., Miles, E.S., Jola, S., Buri, P., Herreid, S., Bhattacharya, A., Watson, C.S., Bolch, T., Quincey, D., Pellicciotti, F., 2020. Mapping ice cliffs on debris-covered glaciers using multispectral satellite images. Remote Sens. Environ. 112201. https://doi.org/10.1016/j.rse.2020.112201

Kopačková, V., Hladíková, L., 2014. Applying spectral unmixing to determine surface water parameters in a mining environment. Remote Sens. 6, 11204–11224. https://doi.org/10.3390/rs61111204

Kotchenova, S.Y., Vermote, E.F., Matarrese, R., Klemm, F.J., 2006. Validation of a vector version of the 6S radiative transfer code for atmospheric correction of satellite data. Part I: Path radiance. Appl. Opt. 45, 6762–6774. https://doi.org/10.1364/AO.45.006762

Kraaijenbrink, P.D.A., Bierkens, M.F.P., Lutz, A.F., Immerzeel, W.W., 2017. Impact of a global temperature rise of 1.5 degrees Celsius on Asia's glaciers. Nature. https://doi.org/10.1038/nature23878

Kraaijenbrink, P.D.A., Meijer, S.W., Shea, J.M., Pellicciotti, F., De Jong, S.M., Immerzeel, W.W., 2016a. Seasonal surface velocities of a Himalayan glacier derived by automated correlation of unmanned aerial vehicle imagery. Ann. Glaciol. 57, 103–113. https://doi.org/10.3189/2016AoG71A072

Kraaijenbrink, P.D.A., Shea, J.M., Litt, M., Steiner, J.F., Treichler, D., Koch, I., Immerzeel, W.W., 2018. Mapping Surface Temperatures on a Debris-Covered Glacier With an Unmanned Aerial Vehicle. Front. Earth Sci. https://doi.org/10.3389/feart.2018.00064

Kraaijenbrink, P.D.A., Shea, J.M., Pellicciotti, F., De Jong, S.M., Immerzeel, W.W., 2016b. Object-based analysis of unmanned aerial vehicle imagery to map and characterise surface features on a debris-covered glacier. Remote Sens. Environ. 186, 581–595. https://doi.org/10.1016/j.rse.2016.09.013

Lague, D., Brodu, N., Leroux, J., 2013. Accurate 3D comparison of complex topography with terrestrial laser scanner: application to the Rangitikei canyon (N-Z).

Laha, S., Kumari, R., Singh, S., Mishra, A., Sharma, T., Banerjee, A., Nainwal, H.C., Shankar, R., 2017. Evaluating the contribution of avalanching to the mass balance of Himalayan glaciers. Ann. Glaciol. 58, 110–118. https://doi.org/10.1017/aog.2017.27

Lee, Z., Carder, K.L., 2000. Band-ratio or spectral-curvature algorithms for satellite remote sensing? Appl. Opt. 39, 4377. https://doi.org/10.1364/ao.39.004377

Liu, Q., Mayer, C., Liu, S., 2015. Distribution and interannual variability of supraglacial lakes on debris-covered glaciers in the Khan Tengri-Tumor Mountains, Central Asia. Environ. Res. Lett.

Loriaux, T., Ruiz, L., 2021. Spatio-Temporal Distribution of Supra-Glacial Ponds and Ice Cliffs on Verde Glacier, Chile. Front. Earth Sci. 9. https://doi.org/10.3389/feart.2021.681071

Mallalieu, J., Carrivick, J.L., Quincey, D.J., Smith, M.W., James, W.H.M., 2017. An integrated Structure-from-Motion and time-lapse technique for quantifying ice-margin dynamics. J. Glaciol. https://doi.org/10.1017/jog.2017.48

Marzeion, B., Hock, R., Anderson, B., Bliss, A., Champollion, N., Fujita, K., Huss, M., Immerzeel, W.W., Kraaijenbrink, P., Malles, J.H., Maussion, F., Radić, V., Rounce, D.R., Sakai, A., Shannon, S., van de Wal, R., Zekollari, H., 2020. Partitioning the Uncertainty of Ensemble Projections of Global Glacier Mass Change. Earth's Futur. 8, e2019EF001470. https://doi.org/10.1029/2019EF001470

Matta, E., Giardino, C., Boggero, A., Bresciani, M., 2017. Use of Satellite and In Situ Reflectance Data for Lake Water Color Characterization in the Everest Himalayan Region. Mt. Res. Dev. 37, 16–23. https://doi.org/10.1659/mrd-journal-d-15-00052.1

Mattson, E.L., 1993. Ablation on debris covered glaciers: an example from the Rakhiot Glacier, Punjab, Himalaya. Intern. Assoc. Hydrol. Sci. 218, 289–296.

McCarthy, M., 2018. Quantifying supraglacial debris thickness at local to regional scales.

McCarthy, M., Miles, E., Kneib, M., Buri, P., Fugger, S., Pellicciotti, F., 2021. Supraglacial debris thickness and supply rate in High-Mountain Asia. https://doi.org/10.31223/X5WW5B

McCarthy, M., Pritchard, H., Willis, I., King, E., 2017. Ground-penetrating radar measurements of debris thickness on Lirung Glacier, Nepal. J. Glaciol. 63, 543–555. https://doi.org/10.1017/jog.2017.18

McFeeters, S.K., 1996. The use of the Normalized Difference Water Index (NDWI) in the delineation of open water features. Int. J. Remote Sens. 17, 1425–1432. https://doi.org/10.1080/01431169608948714

Messerli, A., Grinsted, A., 2015. Image georectification and feature tracking toolbox: ImGRAFT. Geosci. Instrumentation, Methods Data Syst. 4, 23–34. https://doi.org/10.5194/gi-4-23-2015

Mihalcea, C., Mayer, C., Diolaiuti, G., D'Agata, C., Smiraglia, C., Lambrecht, A., Vuillermoz, E., Tartari, G., 2008. Spatial distribution of debris thickness and melting from remote-sensing and meteorological data, at debris-covered Baltoro glacier, Karakoram, Pakistan, in: Annals of Glaciology. https://doi.org/10.3189/172756408784700680

Miles, E., McCarthy, M., Dehecq, A., Kneib, M., Fugger, S., Pellicciotti, F., 2021. Health and sustainability of glaciers in High Mountain Asia. Nat. Commun. 2021 121 12, 1–10. https://doi.org/10.1038/s41467-021-23073-4

Miles, E.S., Pellicciotti, F., Willis, I.C., Steiner, J.F., Buri, P., Arnold, N.S., 2016. Refined energy-balance modelling of a supraglacial pond, Langtang Khola, Nepal. Ann. Glaciol. https://doi.org/10.3189/2016AoG71A421

Miles, E.S., Steiner, J., Willis, I., Buri, P., Immerzeel, W.W., Chesnokova, A., Pellicciotti, F., 2017a. Pond dynamics and supraglacial-englacial connectivity on debris-covered Lirung Glacier, Nepal. Front. Earth Sci. 5. https://doi.org/10.3389/feart.2017.00069

Miles, E.S., Steiner, J.F., Brun, F., 2017b. Highly variable aerodynamic roughness length (z0) for a hummocky debris-covered glacier. J. Geophys. Res. Atmos. 122. https://doi.org/10.1002/2017JD026510

Miles, E.S., Steiner, J.F., Buri, P., Immerzeel, W.W., Pellicciotti, F., 2022. Controls on the relative melt rates of debris-covered glacier surfaces. Environ. Res. Lett. 17, 064004. https://doi.org/10.1088/1748-9326/ac6966

Miles, E.S., Watson, C.S., Brun, F., Berthier, E., Esteves, M., Quincey, D.J., Miles, K.E., Hubbard, B., Wagnon, P., 2018a. Glacial and geomorphic effects of a supraglacial lake drainage and outburst event, Everest region, Nepal Himalaya. Cryosph. 12, 3891–3905. https://doi.org/10.5194/tc-12-3891-2018

Miles, E.S., Willis, I., Buri, P., Steiner, J.F., Arnold, N.S., Pellicciotti, F., 2018b. Surface Pond Energy Absorption Across Four Himalayan Glaciers Accounts for 1/8 of Total Catchment Ice Loss. Geophys. Res. Lett. 45, 10,464-10,473. https://doi.org/10.1029/2018GL079678

Miles, E.S., Willis, I.C., Arnold, N.S., Steiner, J., Pellicciotti, F., 2017c. Spatial, seasonal and interannual variability of supraglacial ponds in the Langtang Valley of Nepal, 1999-2013. https://doi.org/10.1017/jog.2016.120

Miles, J., 2014. R Squared, Adjusted R Squared, in: Wiley StatsRef: Statistics Reference Online. John Wiley & Sons, Ltd, Chichester, UK. https://doi.org/10.1002/9781118445112.stat06627

Miles, K.E., Hubbard, B., Irvine-Fynn, T.D.L., Miles, E., Quincey, D.J., Rowan, A. V., 2020. Hydrology of debris-covered glaciers in High Mountain Asia. Earth-Science Rev. https://doi.org/10.1016/j.earscirev.2020.103212

Millan, R., Mouginot, J., Rabatel, A., Morlighem, M., 2022. Ice velocity and thickness of the world's glaciers. Nat. Geosci. 15, 124–129. https://doi.org/10.1038/s41561-021-00885-z

Milner, A.M., Khamis, K., Battin, T.J., Brittain, J.E., Barrand, N.E., Füreder, L., Cauvy-Fraunié, S., Gíslason, G.M., Jacobsen, D., Hannah, D.M., Hodson, A.J., Hood, E., Lencioni, V., Ólafsson, J.S., Robinson, C.T., Tranter, M., Brown, L.E., 2017. Glacier shrinkage driving global changes in downstream systems. Proc. Natl. Acad. Sci. 114, 9770–9778. https://doi.org/10.1073/pnas.1619807114

Minowa, M., Podolkyi, E.A., Sugiyama, S., Sakakibara, D., Skvarca, P., 2018. Glacier calving observed with time-lapse imagery and tsunami waves at Glaciar Perito Moreno, Patagonia. J. Glaciol. 64, 362–376. https://doi.org/10.1017/jog.2018.28

Mishra, N.B., Miles, E.S., Chaudhuri, G., Mainali, K.P., Mal, S., Singh, P.B., Tiruwa, B., 2021. Quantifying heterogeneous monsoonal melt on a debris-covered glacier in Nepal Himalaya using repeat uncrewed aerial system (UAS) photogrammetry. J. Glaciol. 1–17. https://doi.org/10.1017/JOG.2021.96

Mölg, N., Bolch, T., Walter, A., Vieli, A., 2019. Unravelling the evolution of Zmuttgletscher and its debris cover since the end of the Little Ice Age. Cryosph. 13, 1889–1909. https://doi.org/10.5194/tc-13-1889-2019

Mölg, N., Ferguson, J., Bolch, T., Vieli, A., 2020. On the influence of debris cover on glacier morphology: How high-relief structures evolve from smooth surfaces. Geomorphology 357, 107092. https://doi.org/10.1016/j.geomorph.2020.107092

Moore, P.L., 2021. Numerical Simulation of Supraglacial Debris Mobility: Implications for Ablation and Landform Genesis. Front. Earth Sci. 9. https://doi.org/10.3389/feart.2021.710131

Moore, P.L., 2018. Stability of supraglacial debris. Earth Surf. Process. Landforms 43, 285–297. https://doi.org/10.1002/esp.4244

Muñoz Sabater, J., 2019. ERA5-Land monthly averaged data from 1981 to present. Copernicus Clim. Chang. Serv. Clim. Data Store. https://doi.org/10.24381/cds.68d2bb30

Nainwal, H.C., Banerjee, A., Shankar, R., Semwal, P., Sharma, T., 2016. Shrinkage of Satopanth and Bhagirath Kharak Glaciers, India, from 1936 to 2013. Ann. Glaciol. 57, 131–139. https://doi.org/10.3189/2016aog71a015

Narama, C., Daiyrov, M., Tadono, T., Yamamoto, M., Kääb, A., Morita, R., Ukita, J., 2017. Seasonal drainage of supraglacial lakes on debris-covered glaciers in the Tien Shan Mountains, Central Asia. Geomorphology 286, 133–142. https://doi.org/10.1016/j.geomorph.2017.03.002

Neteler, M., Bowman, M.H., Landa, M., Metz, M., 2012. GRASS GIS: A multi-purpose open source GIS. Environ. Model. Softw. 31, 124–130. https://doi.org/10.1016/j.envsoft.2011.11.014

Nicholson, L., Benn, D.I., 2013. Properties of natural supraglacial debris in relation to modelling sub-debris ice ablation. Earth Surf. Process. Landforms 38, 490–501. https://doi.org/10.1002/esp.3299

Nicholson, L., Benn, D.I., 2006. Calculating ice melt beneath a debris layer using meteorological data. J. Glaciol. https://doi.org/10.3189/172756506781828584

Nicholson, L., Mertes, J., 2017. Thickness estimation of supraglacial debris above ice cliff exposures using a high-resolution digital surface model derived from terrestrial photography. J. Glaciol. 63, 989–998. https://doi.org/10.1017/jog.2017.68

Nicholson, L.I., McCarthy, M., Pritchard, H.D., Willis, I., 2018. Supraglacial debris thickness variability: Impact on ablation and relation to terrain properties. Cryosphere 12, 3719–3734. https://doi.org/10.5194/tc-12-3719-2018

Nuimura, T., Fujita, K., Yamaguchi, S., Sharma, R.R., 2012. Elevation changes of glaciers revealed by multitemporal digital elevation models calibrated by GPS survey in the Khumbu region, Nepal Himalaya, 1992-2008. J. Glaciol. https://doi.org/10.3189/2012JoG11J061

Ogilvie, I.H., 1904. The Effect of Superglacial Débris on the Advance and Retreat of Some Canadian Glaciers. J. Geol. 12, 722–743. https://doi.org/10.1086/621194

Orr, E.N., Owen, L.A., Saha, S., Hammer, S.J., Caffee, M.W., 2021. Rockwall Slope Erosion in the Northwestern Himalaya. J. Geophys. Res. Earth Surf. 126. https://doi.org/10.1029/2020JF005619

Ostrem, G., 1959. Ice Melting under a Thin Layer of Moraine, and the Existence of Ice Cores in Moraine Ridges. Geogr. Ann. 41, 228–230. https://doi.org/10.1080/20014422.1959.11907953

Paschalis, A., Molnar, P., Fatichi, S., Burlando, P., 2013. A stochastic model for high-resolution space-time precipitation simulation. Water Resour. Res. 49, 8400–8417. https://doi.org/10.1002/2013WR014437

Paul, F., Winsvold, S., Kääb, A., Nagler, T., Schwaizer, G., 2016. Glacier Remote Sensing Using Sentinel-2. Part II: Mapping Glacier Extents and Surface Facies, and Comparison to Landsat 8. Remote Sens. 8, 575. https://doi.org/10.3390/rs8070575

Pellicciotti, F., Stephan, C., Miles, E.S., Herreid, S., Immerzeel, W.W., Bolch, T., 2015. Mass-balance changes of the debris-covered glaciers in the Langtang Himal, Nepal, from 1974 to 1999. J. Glaciol. 61, 373–386. https://doi.org/10.3189/2015JoG13J237

Piermattei, L., Carturan, L., Guarnieri, A., 2015. Use of terrestrial photogrammetry based on

structure-from-motion for mass balance estimation of a small glacier in the Italian alps. Earth Surf. Process. Landforms 40, 1791–1802. https://doi.org/10.1002/ESP.3756

Planet Team, 2017. Planet Application Program Interface: In Space for Life on Earth. San Francisco, CA.

Pope, A., Rees, G., 2014. Using in situ spectra to explore landsat classification of glacier surfaces. Int. J. Appl. Earth Obs. Geoinf. 27, 42–52. https://doi.org/10.1016/j.jag.2013.08.007

Pritchard, H.D., 2019. Asia's shrinking glaciers protect large populations from drought stress. Nature 569, 649–654. https://doi.org/10.1038/s41586-019-1240-1

Quincey, D.J., Glasser, N.F., 2009. Morphological and ice-dynamical changes on the Tasman Glacier, New Zealand, 1990-2007. Glob. Planet. Change 68, 185–197. https://doi.org/10.1016/j.gloplacha.2009.05.003

Quincey, D.J., Glasser, N.F., Cook, S.J., Luckman, A., 2015. Heterogeneity in Karakoram glacier surges. J. Geophys. Res. Earth Surf. 120, 1288–1300. https://doi.org/10.1002/2015JF003515

Quincey, D.J., Richardson, S.D., Luckman, A., Lucas, R.M., Reynolds, J.M., Hambrey, M.J., Glasser, N.F., 2007. Early recognition of glacial lake hazards in the Himalaya using remote sensing datasets. Glob. Planet. Change 56, 137–152. https://doi.org/10.1016/j.gloplacha.2006.07.013

Racoviteanu, A.E., Nicholson, L., Glasser, N.F., 2021. Surface composition of debris-covered glaciers across the Himalaya using linear spectral unmixing of Landsat 8 OLI imagery. Cryosph. 15, 4557–4588. https://doi.org/10.5194/tc-15-4557-2021

Racoviteanu, A.E., Nicholson, L., Glasser, N.F., Miles, E., Harrison, S., Reynolds, J.M., 2022. Debris-covered glacier systems and associated glacial lake outburst flood hazards: challenges and prospects. J. Geol. Soc. London. 179. https://doi.org/10.1144/jgs2021-084

Radić, V., Bliss, A., Beedlow, A.C., Hock, R., Miles, E., Cogley, J.G., 2014. Regional and global projections of twenty-first century glacier mass changes in response to climate scenarios from global climate models. Clim. Dyn. 42, 37–58. https://doi.org/10.1007/s00382-013-1719-7

Ragettli, S., Bolch, T., Pellicciotti, F., 2016a. Heterogeneous glacier thinning patterns over the last 40 years in Langtang Himal, Nepal. Cryosphere. https://doi.org/10.5194/tc-10-2075-2016

Ragettli, S., Immerzeel, W.W., Pellicciotti, F., 2016b. Contrasting climate change impact on river flows from high-altitude catchments in the Himalayan and Andes Mountains. Proc. Natl. Acad. Sci. U. S. A. 113, 9222–9227. https://doi.org/10.1073/pnas.1606526113

Ragettli, S., Pellicciotti, F., Immerzeel, W.W., Miles, E.S., Petersen, L., Heynen, M., Shea, J.M., Stumm, D., Joshi, S., Shrestha, A., 2015. Unraveling the hydrology of a Himalayan catchment through integration of high resolution in situ data and remote sensing with an advanced simulation model. Adv. Water Resour. 78, 94–111. https://doi.org/10.1016/j.advwatres.2015.01.013

Rastner, P., Prinz, R., Notarnicola, C., Nicholson, L., Sailer, R., Schwaizer, G., Paul, F., 2019. On the Automated Mapping of Snow Cover on Glaciers and Calculation of Snow Line Altitudes from Multi-Temporal Landsat Data. Remote Sens. 11, 1410. https://doi.org/10.3390/rs11121410

Reid, T.D., Brock, B.W., 2014. Assessing ice-cliff backwasting and its contribution to total ablation of debris-covered Miage glacier, Mont Blanc massif, Italy. J. Glaciol. https://doi.org/10.3189/2014JoG13J045

Reid, T.D., Brock, B.W., 2010. An energy-balance model for debris-covered glaciers including heat conduction through the debris layer. J. Glaciol. https://doi.org/10.3189/002214310794457218

Reindl, D.T., Beckman, W.A., Duffie, J.A., 1990. Diffuse fraction correlations. Sol. Energy 45, 1–7. https://doi.org/10.1016/0038-092X(90)90060-P

Reynolds, J., 2000. On the formation of supraglacial lakes on debris-covered glaciers. IAHS-AISH Publ. 264, 153–161.

RGI Consortium, 2017. Randolph Glacier Inventory – A Dataset of Global Glacier Outlines: Version 6.0: Technical Report, Global Land Ice Measurements from Space, Colorado, USA. Digital Media. https://doi.org/https://doi.org/10.7265/N5-RGI-60

Rittger, K., Painter, T.H., Dozier, J., 2013. Assessment of methods for mapping snow cover from MODIS. Adv. Water Resour. 51, 367–380. https://doi.org/10.1016/j.advwatres.2012.03.002

Röhl, K., 2008. Characteristics and evolution of supraglacial ponds on debris-covered Tasman Glacier, New Zealand. J. Glaciol. https://doi.org/10.3189/002214308787779861

Röhl, K., 2006. Thermo-erosional notch development at fresh-water-calving Tasman Glacier, New Zealand. J. Glaciol. 52, 203–213. https://doi.org/10.3189/172756506781828773

Rounce, D.R., Hock, R., McNabb, R.W., Millan, R., Sommer, C., Braun, M.H., Malz, P., Maussion, F., Mouginot, J., Seehaus, T.C., Shean, D.E., 2021. Distributed global debris thickness estimates reveal debris significantly impacts glacier mass balance. Geophys. Res. Lett. e2020GL091311. https://doi.org/10.1029/2020GL091311

Rounce, D.R., King, O., McCarthy, M., Shean, D.E., Salerno, F., 2018. Quantifying Debris Thickness of Debris-Covered Glaciers in the Everest Region of Nepal Through Inversion of a Subdebris Melt Model. J. Geophys. Res. Earth Surf. 123, 1094–1115. https://doi.org/10.1029/2017JF004395

Rowan, A. V., Egholm, D.L., Quincey, D.J., Glasser, N.F., 2015. Modelling the feedbacks between mass balance, ice flow and debris transport to predict the response to climate change of debris-covered glaciers in the Himalaya. Earth Planet. Sci. Lett. https://doi.org/10.1016/j.epsl.2015.09.004

Rowan, A. V., Egholm, D.L., Quincey, D.J., Hubbard, B., King, O., Miles, E.S., Miles, K.E., Hornsey, J., 2021. The Role of Differential Ablation and Dynamic Detachment in Driving Accelerating Mass Loss From a Debris-Covered Himalayan Glacier. J. Geophys. Res. Earth Surf. 126, e2020JF005761. https://doi.org/10.1029/2020JF005761

Sakai, A., Fujita, K., 2010. Formation conditions of supraglacial lakes on debriscovered glaciers in the Himalaya. J. Glaciol. 56, 177–181. https://doi.org/10.3189/002214310791190785

Sakai, A., Nakawo, M., Fujita, K., 2002. Distribution Characteristics and Energy Balance of Ice Cliffs on Debris-covered Glaciers, Nepal Himalaya. Arctic, Antarct. Alp. Res. 34, 12–19. https://doi.org/10.1080/15230430.2002.12003463

Sakai, A., Nakawo, M., Fujita, K., 1998. Melt rate of ice cliffs on the Lirung Glacier, Nepal Himalayas, 1996. Bull. Glacier Res. 16, 57–66.

Sakai, A., Takeuchi, N., 2000. Debris-Covered Glaciers. IAHS Publ.

Salerno, F., Thakuri, S., D'Agata, C., Smiraglia, C., Manfredi, E.C., Viviano, G., Tartari, G., 2012. Glacial lake distribution in the Mount Everest region: Uncertainty of measurement and conditions of formation. Glob. Planet. Change 92–93, 30–39. https://doi.org/10.1016/j.gloplacha.2012.04.001

Salerno, F., Thakuri, S., Tartari, G., Nuimura, T., Sunako, S., Sakai, A., Fujita, K., 2017. Debris-covered glacier anomaly? Morphological factors controlling changes in the mass balance, surface area, terminus position, and snow line altitude of Himalayan glaciers. Earth Planet. Sci. Lett. 471, 19–31. https://doi.org/10.1016/j.epsl.2017.04.039

Sato, Y., Fujita, K., Inoue, H., Sunako, S., Sakai, A., Tsushima, A., Podolskiy, E.A., Kayastha, R., Kayastha, R.B., 2021. Ice Cliff Dynamics of Debris-Covered Trakarding Glacier in the Rolwaling Region, Nepal Himalaya. Front. Earth Sci. 9, 398.

https://doi.org/10.3389/FEART.2021.623623/BIBTEX

Scherler, D., 2014. Climatic limits to headwall retreat in the Khumbu Himalaya, eastern Nepal. Geology 42, 1019–1022. https://doi.org/10.1130/G35975.1

Scherler, D., Bookhagen, B., Strecker, M.R., 2011. Hillslope-glacier coupling: The interplay of topography and glacial dynamics in High Asia. J. Geophys. Res. Earth Surf. 116. https://doi.org/10.1029/2010JF001751

Scherler, D., Wulf, H., Gorelick, N., 2018. Global Assessment of Supraglacial Debris-Cover Extents. Geophys. Res. Lett. https://doi.org/10.1029/2018GL080158

Schwanghart, W., Scherler, D., 2014. Short Communication: TopoToolbox 2 – MATLAB-based software for topographic analysis and modeling in Earth surface sciences. Earth Surf. Dyn. 2, 1–7. https://doi.org/10.5194/esurf-2-1-2014

Shah, S.S., Banerjee, A., Nainwal, H.C., Shankar, R., 2019. Estimation of the total sub-debris ablation from point-scale ablation data on a debris-covered glacier. J. Glaciol. 65, 759–769. https://doi.org/10.1017/jog.2019.48

Shahgedanova, M., Stokes, C.R., Gurney, S.D., Popovnin, V., 2005. Interactions between mass balance, atmospheric circulation, and recent climate change on the Djankuat Glacier, Caucasus Mountains, Russia. J. Geophys. Res. D Atmos. 110, 1–14. https://doi.org/10.1029/2004JD005213

Sharp, R.P., 1949. Studies of superglacial debris on valley glaciers. Am. J. Sci. 247, 289–315. https://doi.org/10.2475/ajs.247.5.289

Shea, J.M., Wagnon, P., Immerzeel, W.W., Biron, R., Brun, F., Pellicciotti, F., 2015. A comparative high-altitude meteorological analysis from three catchments in the Nepalese Himalaya. Int. J. Water Resour. Dev. 31, 174–200. https://doi.org/10.1080/07900627.2015.1020417

Shean, D.E., Alexandrov, O., Moratto, Z.M., Smith, B.E., Joughin, I.R., Porter, C., Morin, P., 2016. An automated, open-source pipeline for mass production of digital elevation models (DEMs) from very-high-resolution commercial stereo satellite imagery. ISPRS J. Photogramm. Remote Sens. 116, 101–117. https://doi.org/10.1016/j.isprsjprs.2016.03.012

Smith, M.W., Vericat, D., 2015. From experimental plots to experimental landscapes: topography, erosion and deposition in sub-humid badlands from Structure-from-Motion photogrammetry. Earth Surf. Process. Landforms 40, 1656–1671. https://doi.org/10.1002/esp.3747

Stefaniak, A.M., Robson, B.A., Cook, S.J., Clutterbuck, B., Midgley, N.G., Labadz, J.C., 2021. Mass balance and surface evolution of the debris-covered Miage Glacier, 1990–2018. Geomorphology 373, 107474. https://doi.org/10.1016/j.geomorph.2020.107474

Steiner, J.F., Buri, P., Miles, E.S., Ragettli, S., Pellicciotti, F., 2019. Supraglacial ice cliffs and ponds on debris-covered glaciers: Spatio-temporal distribution and characteristics. J. Glaciol. 65, 617–632. https://doi.org/10.1017/jog.2019.40

Steiner, J.F., Gurung, T.R., Joshi, S.P., Koch, I., Saloranta, T., Shea, J., Shrestha, A.B., Stigter, E., Immerzeel, W.W., 2021. Multi-year observations of the high mountain water cycle in the Langtang catchment, Central Himalaya. Hydrol. Process. 35. https://doi.org/10.1002/hyp.14189

Steiner, J.F., Litt, M., Stigter, E.E., Shea, J., Bierkens, M.F.P., Immerzeel, W.W., 2018. The Importance of Turbulent Fluxes in the Surface Energy Balance of a Debris-Covered Glacier in the Himalayas. Front. Earth Sci. 6. https://doi.org/10.3389/feart.2018.00144

Steiner, J.F., Pellicciotti, F., Buri, P., Miles, E.S., Immerzeel, W.W., Reid, T.D., 2015. Modelling ice-cliff backwasting on a debris-covered glacier in the Nepalese Himalaya. J. Glaciol. 61, 889–907. https://doi.org/10.3389/2015JoG14J194

Stewart, R.L., Westoby, M., Pellicciotti, F., Rowan, A., Swift, D., Brock, B., Woodward, J., 2021.

Using climate reanalysis data in conjunction with multi-temporal satellite thermal imagery to derive supraglacial debris thickness changes from energy-balance modelling. J. Glaciol. 67, 366–384. https://doi.org/10.1017/jog.2020.111

Stokes, C.R., Popovnin, V., Aleynikov, A., Gurney, S.D., Shahgedanova, M., 2007. Recent glacier retreat in the Caucasus Mountains, Russia, and associated increase in supraglacial debris cover and supra-/proglacial lake development, in: Annals of Glaciology. pp. 195–203. https://doi.org/10.3189/172756407782871468

Tadono, T., Ishida, H., Oda, F., Naito, S., Minakawa, K., Iwamoto, H., 2014. Precise Global DEM Generation by ALOS PRISM. ISPRS Ann. Photogramm. Remote Sens. Spat. Inf. Sci. II–4, 71–76. https://doi.org/10.5194/isprsannals-II-4-71-2014

Thakuri, S., Salerno, F., Smiraglia, C., Bolch, T., D'agata, C., Viviano, G., Tartari, G., 2014. Tracing glacier changes since the 1960s on the south slope of Mt. Everest (central Southern Himalaya) using optical satellite imagery. Cryosph. 8, 1297–1315. https://doi.org/10.5194/tc-8-1297-2014

Thompson, S., Benn, D.I., Mertes, J., Luckman, A., 2016. Stagnation and mass loss on a Himalayan debris-covered glacier: processes, patterns and rates. J. Glaciol. https://doi.org/10.1017/jog.2016.37

Umbach, D., Jones, K.N., 2000. A Few Methods for Fitting Circles to Data, IEEE TRANSACTIONS ON INSTRUMENTATION AND MEASUREMENT.

Van Woerkom, T., Steiner, J.F., Kraaijenbrink, P.D.A., Miles, E.S., Immerzeel, W.W., 2019. Sediment supply from lateral moraines to a debris-covered glacier in the Himalaya. Earth Surf. Dyn. 7, 411–427. https://doi.org/10.5194/esurf-7-411-2019

Vermote, E.F., Tanré, D., Luc Deuzé, J., Herman, M., Morcrette, J.-J., 1997. Second Simulation of the Satellite Signal in the Solar Spectrum, 6S: An Overview, IEEE TRANSACTIONS ON GEOSCIENCE AND REMOTE SENSING.

Vikhamar, D., Solberg, R., 2003. Snow-cover mapping in forests by constrained linear spectral unmixing of MODIS data. Remote Sens. Environ. https://doi.org/10.1016/j.rse.2003.06.004

Vincent, C., Wagnon, P., Shea, J.M., Immerzeel, W.W., Kraaijenbrink, P., Shrestha, D., Soruco, A., Arnaud, Y., Brun, F., Berthier, E., Sherpa, S.F., 2016. Reduced melt on debris-covered glaciers: Investigations from Changri Nup Glacier, Nepal. Cryosphere. https://doi.org/10.5194/tc-10-1845-2016

Viviroli, D., Kummu, M., Meybeck, M., Kallio, M., Wada, Y., 2020. Increasing dependence of lowland populations on mountain water resources. Nat. Sustain. 3, 917–928. https://doi.org/10.1038/s41893-020-0559-9

Walz, S., 2021. DISTRIBUTION OF ICE CLIFFS ON DEBRIS-COVERED GLACIERS IN HIGH MOUNTAIN ASIA. University of Zürich.

Wangchuk, S., Bolch, T., 2020. Mapping of glacial lakes using Sentinel-1 and Sentinel-2 data and a random forest classifier: Strengths and challenges. Sci. Remote Sens. 2, 100008. https://doi.org/10.1016/j.srs.2020.100008

Watson, C.S., King, O., Miles, E.S., Quincey, D.J., 2018. Optimising NDWI supraglacial pond classification on Himalayan debris-covered glaciers. Remote Sens. Environ. 217, 414–425. https://doi.org/10.1016/j.rse.2018.08.020

Watson, C.S., Quincey, D.J., Carrivick, J.L., Smith, M.W., 2017a. Ice cliff dynamics in the Everest region of the Central Himalaya. Geomorphology 278, 238–251. https://doi.org/10.1016/j.geomorph.2016.11.017

Watson, C.S., Quincey, D.J., Carrivick, J.L., Smith, M.W., 2016. The dynamics of supraglacial ponds in the Everest region, central Himalaya. Glob. Planet. Change 142, 14–27.

https://doi.org/https://doi.org/10.1016/j.gloplacha.2016.04.008

Watson, C.S., Quincey, D.J., Smith, M.W., Carrivick, J.L., Rowan, A. V, James, M.R., 2017b. Quantifying ice cliff evolution with multi-temporal point clouds on the debris-covered Khumbu Glacier, Nepal. https://doi.org/10.1017/jog.2017.47

Watson, Quincey, D.J., Carrivick, J.L., Smith, M.W., 2016. The dynamics of supraglacial water storage in the Everest region, central Himalaya. Glob. Planet. Change 142, 14–27. https://doi.org/10.1016/j.gloplacha.2016.04.008

Wessels, R.L., Kargel, J.S., Kieffer, H.H., 2002. ASTER measurement of supraglacial lakes in the Mount Everest region of the Himalaya. Ann. Glaciol. 34, 399–408. https://doi.org/10.3189/172756402781817545

Westoby, M.J., Brasington, J., Glasser, N.F., Hambrey, M.J., Reynolds, J.M., 2012. "Structure-from-Motion" photogrammetry: A low-cost, effective tool for geoscience applications. Geomorphology 179, 300–314. https://doi.org/10.1016/j.geomorph.2012.08.021

Westoby, M.J., Rounce, D.R., Shaw, T.E., Fyffe, C.L., Moore, P.L., Stewart, R.L., Brock, B.W., 2020. Geomorphological evolution of a debris-covered glacier surface. Earth Surf. Process. Landforms 45, 3431–3448. https://doi.org/10.1002/esp.4973

Wijngaard, R.R., Steiner, J.F., Kraaijenbrink, P.D.A., Klug, C., Adhikari, S., Banerjee, A., Pellicciotti, F., van Beek, L.P.H., Bierkens, M.F.P., Lutz, A.F., Immerzeel, W.W., 2019. Modeling the response of the langtang glacier and the hintereisferner to a changing climate since the little ice age. Front. Earth Sci. 7, 143. https://doi.org/10.3389/feart.2019.00143

Willi, R., 2021. Determining the Influence of Supraglacial Debris on the Characteristics of Runoff from Glaciers in Switzerland. ETH Zürich.

Xie, F., Liu, S., Wu, K., Zhu, Y., Gao, Y., Qi, M., Duan, S., Saifullah, M., Tahir, A.A., 2020. Upward Expansion of Supra-Glacial Debris Cover in the Hunza Valley, Karakoram, During 1990 ~ 2019. Front. Earth Sci. 8, 308. https://doi.org/10.3389/feart.2020.00308

Yang, W., Zhao, C., Westoby, M., Yao, T., Wang, Y., Pellicciotti, F., Zhou, J., He, Z., Miles, E.S., 2020. Seasonal Dynamics of a Temperate Tibetan Glacier Revealed by High-Resolution UAV Photogrammetry and In Situ Measurements. Remote Sens. 2020, Vol. 12, Page 2389 12, 2389. https://doi.org/10.3390/rs12152389

Zemp, M., Frey, H., Gärtner-Roer, I., Nussbaumer, S.U., Hoelzle, M., Paul, F., Haeberli, W., Denzinger, F., Ahlstrøm, A.P., Anderson, B., Bajracharya, S., Baroni, C., Braun, L.N., Cáceres, B.E., Casassa, G., Cobos, G., Dávila, L.R., Delgado Granados, H., Demuth, M.N., Espizua, L., Fischer, A., Fujita, K., Gadek, B., Ghazanfar, A., Ove Hagen, J., Holmlund, P., Karimi, N., Li, Z., Pelto, M., Pitte, P., Popovnin, V. V., Portocarrero, C.A., Prinz, R., Sangewar, C. V., Severskiy, I., Sigurđsson, O., Soruco, A., Usubaliev, R., Vincent, C., 2015. Historically unprecedented global glacier decline in the early 21st century. J. Glaciol. 61, 745–762. https://doi.org/10.3189/2015JoG15J017

Zemp, M., Huss, M., Thibert, E., Eckert, N., McNabb, R., Huber, J., Barandun, M., Machguth, H., Nussbaumer, S.U., Gärtner-Roer, I., Thomson, L., Paul, F., Maussion, F., Kutuzov, S., Cogley, J.G., 2019. Global glacier mass changes and their contributions to sea-level rise from 1961 to 2016. Nature 568, 382–386. https://doi.org/10.1038/s41586-019-1071-0

Zhu, Z., Wang, S., Woodcock, C.E., 2015. Improvement and expansion of the Fmask algorithm: Cloud, cloud shadow, and snow detection for Landsats 4-7, 8, and Sentinel 2 images. Remote Sens. Environ. 159, 269–277. https://doi.org/10.1016/j.rse.2014.12.014